Removal of VOCs and H_2CO from air by nanoparticulate silica adsorbents or TiO_2 photocatalysts

Abdunaser Mabruk S Ewlad-Ahmed

September 2013

Removal of VOCs and H_2CO from air by nanoparticulate silica adsorbents or TiO_2 photocatalysts

Abdunaser Mabruk S Ewlad-Ahmed

Supervisor: Dr Lorraine T. Gibson

Department of Pure and Applied Chemistry
University of Strathclyde

A thesis submitted to the Department of Pure and Applied Chemistry, University of Strathclyde, in part fulfilment of the regulations for the degree of Doctor of Philosophy (Ph.D).

September 2013

Abstract

Constant concentrations of selected VOCs (toluene, ethylbenzene, cumene and dichlorobenzene) and formaldehyde (H_2CO) were successfully generated in separated sampling chambers. A commercially available sorbent (Tenax TA) and silica C_{18} cartridges impregnated with trapping solution were used to determine experimental masses "references masses" of VOCs and H_2CO, respectively, using selected sampling conditions. Mesoporous silica samples (MCM-41, MWD-MCM-41 and SBA-15) were synthesised under harsh conditions by traditional sol-gel methods. Extraction efficiencies of these adsorbents were compared to Tenax TA, and showed similar performances (64 to 69 %) for VOCs extraction. However, SBA-15 had slightly higher dynamic capacity due to its bimodal pore structure which includes microporores. Novel silica green nanomaterials (GNs) were synthesised using a bioinspired route; under mild conditions of natural pH and ambient temperature, rapid synthesis (15 min) and in all aqueous solutions. However produced GN materials have significantly lower surface areas (58 - 355 $m^2\ g^{-1}$) compared to MCM-41 (1014 $m^2\ g^{-1}$), they had similar or better extraction efficiencies (60 – 80 %) of MCM-41 due to their unique porosity including micropores. In addition they had comparable capacities per unit surface area with MCM-41.

A novel synthesis route "green" was applied to produce mesoporous silica (USG) with high surface area (up to 1100 $m^2\ g^{-1}$), pore size of 2.6 nm and large pore volume (1.00 $cm^3\ g^{-1}$) which are similar to MCM-41 properties. The new produced USG demonstrated a similar performance (60 %) and adsorption capacity for VOCs extraction compared with MCM-41. Furthermore all silica adsorbents were successfully functionalised with organic amine groups in order to examine their performance for H_2CO extraction. Results demonstrated that H_2CO was removed from air permanently by chemisorption on functionalized adsorbents.

Finally, porous TiO_2 thin films coated onto glass beads were used for VOCs degradation as the first time. The results indicated that the best performance of VOCs degradation (up to 80 %) was achieved by using smaller glass beads, at lower flow rate or an increase of coating number (thickness of films).

Acknowledgments

First of all, I would like to express my deepest sense of gratitude to my supervisor Dr. Lorraine Gibson for her supervising, patience guidance, encouragement and great advice throughout this study.

I am thankful to Dr. Siddharth V. Patwardhan for his generous assistance during the "Bridging the Gap" Award from the University of Strathclyde and Department of Chemical and Process engineering for financial support. To the analytical chemistry staff: Dr. Christine Davidson, Dr. Alison Nordon and Prof. David Littlejohn for their useful discussions and advice during the course of this study. To Dr. Pamela Allan and Craig King for their assistance and allowing me use their lab. To Ian Airdrie, Linsay and Gavin Bain for their assistance of BET isotherms analysis. To Denise Gilmour for doing the micro analysis and her very nice welcome when bringing the samples for analysis. To Margaret Wilson who always kindly looked after our chemicals orders. I am really very grateful to all the staff mentioned above as they helped me a lot in this project. To everyone in the Department of Pure and Applied Chemistry who provided technical assistance throughout the project.

I would also like to thank Prof. Michael Morris, and Prof Justin Holmes, their research groups at the Chemistry Department, University College Cork, Ireland who made my visit there so worthwhile and for their assistance of SAS-XRD and the TEM analysis for all our silica samples. To Dr. David J. Belton, School of Science and Technology, Nottingham Trent University for his assistance of microporsity analysis of GNs materials.

I also thank all members of the analytical chemistry postgraduate group for sharing experiences and knowledge and the excellent working atmosphere.

Finally, I take this opportunity to express my profound gratitude to my beloved parents (Mabruk Saleem Ewlad-Ahmed and Aisha Mohammed Saad), my wife (Fouzia Saad) and my sons (Mabrok), (Abd-ulmoeen) and (Moataz).

1 Introduction: Volatile Organic compounds in indoor air

1.1 Volatile Organic compounds in indoor air

Volatile organic compounds (VOCs) are the most common chemical pollutants in indoor air that should be controlled according to increasingly stringent environmental regulations. VOCs can be classified according to their chemical properties into the following chemical groups: aldehydes, aromatic hydrocarbons, aliphatic hydrocarbons, ketones, cyclo-alkanes, terpenes, halo-carbons, esters, alcohols, glycols, and glycoethers [1]. In addition they can also be classified consistent with their physical properties such as boiling point, carbon number, vapour pressure, etc. The World Health Organisation (WHO) working group on organic indoor air pollutants divided them according to their boiling point into 4 main categories: very volatile organic compounds (VVOC), volatile organic compounds (VOC), semi volatile organic compounds (SVOC) and organic compounds associated with particulate organic matter (POM) as summarized in Table 1.1.

Table 1.1 Classification of indoor organic pollutants (WHO, 1989)[2].

Category	Abbreviation	Boiling-point range*	Sampling media typically used in field studies
1	VVOC	< 0 to 50-100	Batch sampling; adsorption-on charcoal
2	VOC	50-100 to 240-260	Adsorption on Tenax TA, graphitised carbon black or charcoal
3	SVOC	240-260 to 380-400	Adsorption on polyurethane foam or XAD-2
4	POM	> 380	Collection on filters

* Polar compounds appear at the higher end of the range.

Furthermore VOCs can be divided according to their potential health effects (irritants, neurotoxins, carcinogens, etc.). Health awareness studies conducted on the cancer risk of VOCs demonstrated that about 70 % of the estimated cancer risk was due to exposure of polycyclic aromatic hydrocarbons, formaldehyde (H_2CO) and benzene [3, 4]. Formaldehyde vapour is given increased attention as an indoor air pollutant due to the potential impact on human health and comfort when present at high concentration (900 μg m^{-3}) [5]. As H_2CO is classified as a Group 1 probable human carcinogen [6], it is arguably the most widely studied aldehyde. A long-term exposure to lower levels of H_2CO vapour has been shown to cause irritation of the eyes and nose [7] and H_2CO vapour has been related to an increased risk of respiratory disease [8]. Despite being toxic and allergenic, H_2CO is still widely used in industrial processes to produce building materials and wood products; primarily due to its low cost and high reactivity [9].

VOCs are released as gases from solid, or liquid, sources which contain a variety of chemicals; some of these compounds may have short- and long-term adverse health influences. As many people spend the greater part of their lives indoors the risks to health may be greater due to indoor air pollution than the outdoor air [10].The possibility of health effects from exposure to pollutants depend on the types of VOCs present and their concentrations in indoor air.

1.2 Sources of indoor VOCs

A number of emissive VOC sources have been introduced to indoor air by building materials and human activities [11, 12]. Building materials release formaldehyde and aliphatic and aromatic hydrocarbons from materials such as wood-based products (ply-wood, particle board, medium-density, chip-board and fibreboard) [9, 13, 14]. Other sources of VOCs from building materials are associated with paints, gypsum, floor finishes, glues, carpets, household solvents, air fresheners and office equipment [15, 16]. Other important sources of VOCs in indoor air are related to human activities such as cleaning products, cooking, personal care agents, tobacco smoking and building renovation [17-19]. Externally generated pollution from combustion sources, for example vehicle exhaust and gas furnaces, also reduce the quality of

indoor air. In addition to these sources, the concentrations of VOCs in indoor air depend on outdoor levels, climate conditions, changes in temperature and relative humidity, as well as chemical reactions. For instance, ozone can react with unsaturated compounds in indoor air such as terpenes to produce substantial amounts of aldehydes (e.g., formaldehyde) [4]. As the main sources of VOCs are from materials and products typically used for construction or furniture, their concentrations indoors is usually 2 – 10 times higher than found outdoors [20, 21].

1.3 Sampling methods for indoor VOCs

Measurement procedures for monitoring levels of VOCs and formaldehyde in indoor air are usually divided into a sampling and an analytical step. The most common sampling methods used to sampling pollutants present in indoor air are conducted in either active or passive mode [22]. Both methods have long been used to collect pollutants from indoor air at the ppmv or ppbv levels. The selection of an appropriate sampling method depends on the objective of the investigation and the VOCs of interest [23, 24].

1.3.1 Active air sampling methods

In active sampling methods a specified volume air is drawn through a sampling tube which contains a suitable sorbent to trap the VOCs of interest. In this method, a pump is required to control the air flow rate usually at very low flow rates (< 100 cm^3 min^{-1}) and is normally used to collect average samples of air intermittently [25]. However, active sampling is usually performed when short-term averages are needed (normally 8 h sampling periods) [26]. Short-term samples are preferred when increased or variable concentrations are to be expected and the measurement is required in a short period of time [27]. The equipment has to be regularly checked and validated for stability of air volume and flow. Noise from the pump can also be disturbing during long-term sampling, and therefore a significant factor to consider if active sampling methods are to be used is the choice of an appropriate pump [25].

There is a wide range of adsorbents available for sampling indoor VOCs which can be classified into three broad categories: porous polymer-based sorbent (e.g. Tenax TA and Chromosorb), carbon-based sorbents (activated charcoal, graphitised carbon blacks, carbotraps, anasorb, carboxens and carbosieve) and silica gels. Porous polymer and carbon-based sorbents are the most widely used for indoor VOC sampling [28, 29]. Analytes retained on the sorption bed are released by thermal desorption or solvent extraction prior to analysis.

1.3.2 Passive air sampling methods

Passive sampling is based on the free flow of analyte molecules, where they diffuse from a high concentration (if present in air) to a lower concentration, which will be essentially zero at the surface of a trapping medium [24]. The air flow rate can be controlled by physical processes such as permeation through a membrane or diffusion through a static air layer [30]. The rate of flow is determined by the cross section of the passive sampling device, the distance between the adsorbent surface, the opening of the tube and by the properties of the compounds [25]. Since Palmes and Gunnison [31] developed modern passive samplers (tube-form sampler) in 1973 for quantitative diffusive sampling, a wide variety of sampling have been described, some of them depending on diffusion through an air-gap, some depending on permeation through a membrane and some using both techniques [30].

Two types of diffusive samplers are commonly used (badge-type and tube samplers) when long-term averages are needed (days or weeks). Badge–type samplers, with large cross sectional areas and short path lengths, suffer from severe restrictions because their pollutant collection rates are significantly affected by the speed of air and they are also unsuitable for thermal desorption. Activated carbon is a commonly used sorbent in badge-type devices due to its large specific area and solvent extraction is normally used for analyte desorption [32]. Tube-type diffusive samplers with a small cross-sectional areas and long diffusion lengths are compatible with thermal desorption and Tenax TA, Chromosorb, Chrompack are usually used as sorbents in these samplers. The first thermal desorption passive sampler was described by Brown (1981) [33].

The main advantages of passive sampling are that the equipment is simple and inexpensive because few analyses are needed during the monitoring period and the method of collection means that the sampling itself is more resistant to changes of environmental conditions such as wind and precipitation [23]. In addition it does not require bulky and expensive pumps that are subjected to regular checking and possible error in flow rate. Passive sampling can be used to collect several samples at the same time from high risk areas. Therefore, passive sampling becomes more attractive and acceptable in some situations [34]. The critical limitations of passive techniques are sorbent capacity and uptake rate in the case of high dosages, the response time and sensitivity in the case of low dosages [35]. The comparison of advantages and disadvantages of both sampling modes are outlined in Table 1.2[36].

Table 1.2 Advantages and disadvantages of active and passive sampling modes

Sampling technique	Advantages	Disadvantages
Active mode	Very effective enrichment. Large-volume samples can be collected. Ease of calibration. A large number of compounds can be separated as more than one sorbent is used.	High cost of a single measurement. Power equipment needs regular servicing. Energy is consumed. Transport of power equipment (pumps, ventilators) to the sampling site is troublesome.
Passive mode	Simple construction, small size. No need for a power source. Mean time-weighted concentration can be determined (the volume of air is unimportant). Useful for long-term sampling.	Poor sensitivity to short-term concentration changes. Enrichment less effective than with other techniques. Unsuitable for automation. Degree of enrichment dependent on ambient temperature and wind movements.

1.4 Detection techniques for VOCs and H_2CO vapour

1.4.1 The measurement of VOCs in indoor air

There are three different ways to analysis and determine VOCs in indoor air: use of a direct-reading instrument, no identification of specific analytes and by identification of individual VOCs. A direct-reading instrument is the most operationally simple method of analysis, which uses a chemical or biological detection system to analysis a mixture of VOCs without separation (thus detection is recorded as a 'total of VOCs') [37]. The no identification method is more instrumentally sophisticated as the trapped analytes are separated, although they are not individually measured and the sum the instrumental responses for the individual measured compounds is used to estimate the overall quantity of VOCs present [38]. The information obtained from direct-reading, or the no identification method, is often unsatisfactory because more details are normally required regarding VOCs therefore the chemical mixture has to be separated into its components using gas chromatography [39, 40].

Separation and identification of individual VOCs is the most complex, but more informative sampling method which is used to detect VOCs. The most common combination is to separate trapped components by gas chromatography and detect individual components by coupling the gas chromatograph (GC) to an appropriate detector such as a flame-ionisation detector (FID), an electron capture device (ECD) or a mass spectrometer (MS) [2, 41, 42]. The GC/MS provides the most conclusive qualitative and quantitative information, although a combination of FID and ECD has also been reported to permit the identification of compounds with widely different properties [43]. Nevertheless, GC/MS remains the most widely used technique for the characterisation of indoor VOCs. A total ion chromatogram is usually measured to obtain information on the ranges of compounds present and selected ion monitoring is performed to identify and monitor particular analytes [44].

VOCs which are adsorbed on the chosen sorbent first have to be transferred from the sorbent to the gas chromatograph. There are two methods for sample introduction into the GC: solvent extraction of the absorbed VOCs and injection of an aliquot of the extracted solution into the GC and thermal desorption of the trapped VOCs from the sorbent by a pure carrier gas, usually helium [41]. The main advantages and

disadvantages of both desorption techniques are summarized in Table 1.3. The desorbed compounds are re-concentrated and flash heated directly into GC column. Thermal desorption (TD) is the most sensitive method and often is applied; therefore TD-GC-MS is the most widely used technique for identification and monitoring of VOCs in indoor air.

Table 1.3 Advantages and disadvantages of desorption techniques [45]

Desorption techniques	Advantages	Disadvantages
Solvent extraction	Cheap, no specialist equipment needed, useful for liberating high-molecular weight compounds, samples can be analyzed repeatedly, and the best for thermally-labile compounds	Solvents are toxic and may give rise to interference, dilution of samples, and regeneration of sorbent bed before reuse
Thermal desorption	No sample-preparation step, sorbent reusable, eases of automation, no interference from a solvent, quantitative liberation of analytes, low levels of VOCs detectable, and short analysis time	Expensive, requires a high temperature, analytes may decompose at high temperatures, and non-volatile compounds may be lost, and requires thermally-resistant sorbents

1.4.2 Detection of formaldehyde

Several analytical methods exist to monitor H_2CO concentration in air. The most widely used methods include spectrophotometry [46], colorimetry [47, 48], high-performance liquid chromatography, HPLC, [49, 50], polarography [51] and gas chromatography [52, 53]. The formation of a derivative is normally required prior to separation and detection, and common reagents used include chromotropic acid [54, 55], pararosaniline [48, 56] or 2,4-dinitrophenylhydrazine [57].

Spectrophotometry is the most extensively used method for the detection of formaldehyde, however, there are a number of interferences and the method detection level is normally insufficient for occupational monitoring purposes [58]. The example of a colourimetric method is the chromotropic acid method which widely used for measurement of formaldehyde. In this method, air is passed through an adsorbent or an impinger charged with water [59]. Formaldehyde in the sample reacts with sulfuric acid and chromotropic acid to form a characteristic violet-coloured derivative which is determined spectrophotometrically [60]. The modified pararosaniline method is also commonly used as a colorimetric method since it gives an improvement in the sensitivity of the chromotropic acid method. In additional it is more reproducible, more specific and easier to use than the chromotropic acid procedure. Formaldehyde reacts with pararosaniline and sodium sulfide (Schiff's reagent) to produce a coloured solution which is determined by UV-VIS spectrometry [61].

It has been reported, however, that methods using these reagents provide poor limits of detection, are prone to interference by acetalydehyde and require strongly acidic conditions which are not suitable for the development of a solvent free device [62]. High-performance liquid chromatographic methods (HPLC) is the most sensitive method often used to monitor H_2CO vapour in indoor atmospheres, and the method normally involves derivatisation of formaldehyde with 2,4-dinitrophenylhydrazine (DNPH) prior to analysis, followed by separation and determination of the resultant formaldehyde hydrazone by ultraviolet (UV) spectroscopy [63, 64].

1.5 Typical concentrations of VOCs in indoor air:

Numerous studies have determined the levels of VOCs in indoor air in different types of buildings, which involve the study of residential and non-residential environments [4, 8-12]. Several hundred VOCs in indoor air have been detected and their adverse health effects on occupants specified. Although, according to many studies the levels of VOCs in indoor air are lower than their critical levels which may affect human health, the potential long term exposure to these compounds increases the risk on the occupant's health. Moreover, people generally spend about 70 % of their time

indoors and so they are in contact with indoor pollutants more so than outdoor. In many indoor sites a level of pollution that is ten times higher than corresponding outdoor site [65]. Table 1.4 shows a range of monoaromatic hydrocarbons (MAHCs) and formaldehyde which appeared in numerous papers studying VOCs levels in indoor and outdoor air. Monoaromatic hydrocarbons (MAHCs), including benzene, toluene, ethylbenzene, xylene (BTEX), cumene and dichlorobenzene (DCB), form an important group of air pollutants in urban areas [66].

Table 1.4 The average concentrations (μg m^{-3}) of monoaromatic hydrocarbons and formaldehyde monitored in selected studies.

Compound	Japan Ref. [9]	UK Ref.[10]	Australia Ref. [11]	USA Ref. [12]	Canada Ref. [4]	Poland Ref. [8]
Benzene	……	13.90	7.00	4.10	1.22	……
Toluene	21.00	38.40	14.00	15.3	26.47	24.00
Ethylbenzene	11.20	2.30	1.80	9.70	2.69	4.00
o-xylene	……	1.9	8.9	11.2	33	……
Cumene	……	……	……	……	0.88	……
DCB	78.10	0.10	31.00	2.97	0.58	……
Formaldehyde	120.10	……	……	19.60 Ref. [67]	……	……

1.6 Removal of VOC from indoor air by solid materials

In general, there are three methods that could be used to improve the indoor air quality; source control, increased ventilation, and air cleaning. Sources of VOCs are often ungovernable and increased ventilation might even lead to more pollution from the outdoor environment. Thus, air cleaning remains to be the most practical option to improve the indoor air quality by adsorption or photocatalysis using active solid

materials [68]. The adsorption of VOCs on adsorbents is the main traditional method used to remove VOCs from indoor air. Adsorption process depends on the transition of pollutants from the gaseous phase to a solid phase. On the other hand photocatalysis uses solid materials (photocatalysts) activated by ultra violet (UV) or visible light to oxidize VOCs to H_2O and CO_2 [69]. Photo-degradation of VOCs can also be achieved by advanced oxidation processes (AOP) such as thermal oxidation destruction [70] or photocatalytic oxidation (PCO) [71].

Over the last 20 years the removal of VOCs from indoor environments by adsorption has been widely studied compared to photocatalysis. Using the Science Direct search engine, results showed that a total of 6169 papers were published with keyword (adsorption + VOCs), between 1995 and 2013 (May). Whereas with (photocatalysis + VOCs) number of papers reported was approximately 800 papers as illustrated in Figure 1.1. It was shown that the adsorption techniques were extensive used to extract VOCs from air. In contrast photodegradation of VOCs was applied less and for both techniques the number of publications in the field increased year to year until recently.

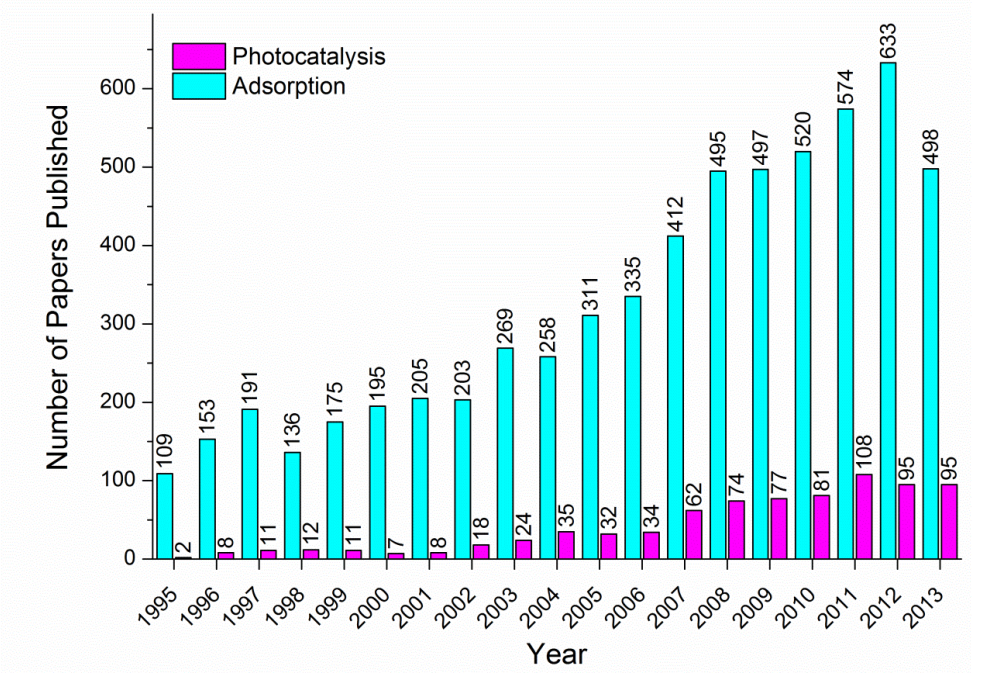

Figure 1.1 The number of papers published verses year for adsorption or photocatalysis of VOCs

1.6.1 Conventional adsorbents used to extract VOCs

Numerous porous materials have been used as sorbents to reduce the concentration of VOCs present in indoor air. These sorbents include silica gel, alumina, zeolite molecular sieves, carbon molecular sieves, graphitized carbon blacks, styrene and acrylate polymers and Tenax. The selection of a suitable sorbent depends on the nature and concentrations of VOCs in the air, ambient conditions (temperature, humidity and pressure), the type of sampling, the type of analytical equipment available and the recovery of VOCs [72]. The recovery depends on the breakthrough volume, chemical adsorption and the desorption efficiency [73]. The most common sorbents available for sampling of VOCs are given in Table 1.5. Most of them are used for active sampling, although some have furthermore been used for passive sampling. All sorbents have limitations when covering a wide range of VOCs and some are suitable for specific VOCs of interest. Therefore, multiple sorbents are required to cover a large mixture of VOCs [74]. The most common sorbents currently used are silica gel, active carbon and porous polymers.

1.6.1.1 Tenax TA

In the literature Tenax TA (Poly-2,6-diphenylphenylene oxide), with a high thermal stability up to 350 °C, is the most often used and best evaluated sorbent for VOCs sampling; thus it tends to be the default choice for most research groups monitoring indoor air [2]. However, Tenax TA has a low surface area (about 35 m^2 g^{-1}) and low adsorption capacity which can limit its applications for removing VOCs presented at high concentrations. It is suitable for both desorption techniques (thermal desorption or solvent extraction). The monomeric unit of Tenax TA is illustrated in Figure 1.2 [25].

Table 1.5 Sorbents used to adsorb VOCs from indoor air [4, 35, 74]

Sorbent	**Compounds Sampled**	**Main Advantages and Disadvantages**
Tenax TA	- most non-polar VOCs - terpenes - slightly polar VOCs - aldehydes > C5 - (acids > C3)	- low background - well investigated - some decomposition products (benzaldehyde, acetophenone)
Carbotrap	- most non polar VOCs - slightly polar VOCs	-low background -reactions of some compounds (i.e. aldehydes, terpenes)
Activated carbon	- most non-polar VOCs - slightly polar VOCs	-high capacity -reactions of some compounds
Porapak Q	- most non-polar VOCs - slightly polar VOCs	-high background -low thermal stability
Organic molecular Sieves (e.g. Carboxen 563, 564)	- polar and non-polar VOCs	-water adsorption

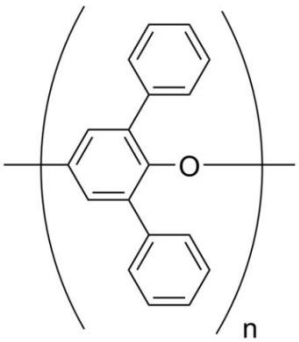

Figure 1.2 The monomeric unit of Tenax TA

1.6.1.2 Activated carbons (ACs)

Activated carbons are powdered, granular or monolith formed carbons with a highly developed surface area and porosity, containing very small graphite crystallites and amorphous carbon. The structure of AC is composed of three groups, namely micropores, mesopores and macropores. The micropores usually account for over 95% of total surface area of ACs. The pore diameters are usually less than 1 nm, the volumes of micropores range from 0.15 up to 0.6 cm g^{-1} and form a very large surface area up to 3000 m^2 g^{-1} [75].

ACs is conventionally produced from a wide range of organic materials by a thermal method (dry distillation) to form carbonised organic precursors, which can be activated to increase the pore volume either thermally or chemically [76]. The pores structure of ACs strongly depends on the nature of the precursors, conditions of their thermal treatment and the physical/chemical activation process used [75]. Activated carbons are commonly used for removal of VOCs from air due to their high efficacy in the adsorption processes and low costs of fabrication. However, it is most suited to solvent extraction as it may decompose at the high temperatures required for thermal desorption.

1.6.1.3 Silica gel (SiO_2)

Silica gel can be also used as catalyst support [77] and a sorbent for VOCs [78]. The silica gel is a porous material of high surface area and is formed by irregular particles (amorphous) of silica [79]. It has a structure which consists of tetrahedral units of SiO_4 connected by siloxane bridges Si–O–Si [80]. The silica surface under normal conditions is covered with reactive silanol groups SiOH [79]. Silica gel is commercially available at relatively low cost and with varied dimensions such as surface area and pore size.

1.6.2 Mesoporous Materials

Inorganic porous materials have been used widely as heterogeneous catalysts and adsorption media for the collection of pollutants due to their large specific surface

area and high adsorption capacity [81, 82]. The classification of a porous materials is usually given by their pore size dimension [83], these porous materials were classified by the IUPAC into three classes [84, 85]:

- Microporous materials, their pores size are < 2 nm

- Mesoporous materials, their pores size are 2 – 50 nm

- Macroporous materials, their pores size are > 50 nm

Since discovering a new family of mesoporous molecular sieves (M41S) in 1992 by Beck *et al*. [81], numerous studies have been reported focusing on methods used for synthesis, characterization of M41S materials and their applications [86-88]. These materials have demonstrated their unique advantages for gas or liquid adsorption due to the distinctive structure of the mesopores material: highly ordered pores, a narrow pore size distribution, large pore volumes, high surface areas of >1000 m^2 g^{-1} [89, 90], open pore structure and reliable desorption performance [91, 92]. The silica mesoporous materials contain silanoxy bridges (≡Si-O-Si≡) in their framework and silanol functional groups (≡Si-OH) distributed on the surface as a result of incomplete condensation. [93].

MCM-41 is the most famous member of the M41S family and together with SBA-15 are the most commonly used mesoporous materials for VOCs adsorption. Preparation methods used to synthesis MCM-41 and SBA-15, or to modify their physicochemical properties, will be described in detail in Sections 5.1.1 and 5.1.2, respectively. In addition the diversity of MCM-41 and SBA-15 as potential adsorbents for VOC and H_2CO removal will be also discussed in Section 5.1.3.

1.6.3 Photocatalysts used for VOCs degradation

Generally, semiconductors oxides or sulfides such as TiO_2, ZnO, ZnS, CdS, Fe_2O_3, Al_2O_3 and SnO_2 are the most commonly used photocatalysts. Of these conventional TiO_2 photocatalysts are the most important and widely used for VOCs degradation, but only under UV irradiation due to its wide band gap of 3.2 eV [94]. Since Fujishima *et al.* (1972) discovered the phenomenon of the photo-induced water

cleavage to TiO_2 electrode [95], there has been increasing interest in its environmental applications. In the subsequent three decades, a wide range of potential applications of photcatalytic oxidation (PCO) to air purification have been reported, demonstrating that the most POC reactors commonly uses nano-titania (TiO_2) catalysts and ultraviolet (UV) light for VOC degradation [96]. The preparation methods of TiO_2 photocatalysts, improvement of its photocatalytic activation and degradation of VOCs by the PCO technique and modified TiO_2 photocatalysts will be described in detail in Chapter 8.

1.7 Factors effecting the adsorption of VOCs from indoor air

The adsorption of VOCs from indoor air onto surfaces is affected by several factors such as temperature, relative humidity, the chemical nature and gas phase concentration of the VOC and material properties such as chemical structure, specific surface area and pore size [97]. Colombo *et al.* (1993) reported that the adsorption of the most compounds tended to increase with a decrease in analyte boiling point [98]. Popa *et al.* [99] studied the adsorption of toluene and a mixture of six VOCs in paint and painted gypsum and found the adsorption of most compounds tended to increase with a decrease in analyte vapour pressure. Moreover, the adsorption capacity for toluene as a single compound was slightly larger than as part of mixture.

Another factor that may affect the adsorption of the VOCs on materials is the relative humidity (RH). The study of the effect of the present of water vapour on the adsorption of VOCs can be found in many papers, but with different conclusions [100]. For example, Won *et al.* (2001) observed that the increased RH levels lead to reduced adsorption capacities of some VOC on building materials [101], whereas Colombo *et al.* (1993) reported no significant influence of RH on VOC adsorption by carpet [98]. Zhang *et al.* showed that the RH may decrease the adsorption of some VOC on building materials but increase the adsorption of others [102]. Moreover, the adsorption has been shown to decrease with an increase in temperature from 23 °C to 35 °C [103]. The ranges of factors that may influence the adsorption of VOCs from indoor air onto sorbent surfaces are summarized in Table 1.6.

Table 1.6 Factors influencing the adsorption of VOCs on sorbents

	Factor	Effect of adsorption	Ref.
1	Physical properties of VOCs	Adsorption of VOCs increased with increased vapour pressure and decreased boiling point.	[104, 105]
2	Physical properties of sorbent	The greater the specific area, the larger the VOCs adsorption.	[106]
3	Air temperature	The adsorption and desorption rate at 35 °C was higher than at 23 °C. Desorption rate increased more rapidly than the adsorption rate, the VOCs adsorption decreased with an increase in temperature of 23 °C to 35 °C.	[103]
4	Air velocity	The higher air velocity, the higher desorption rate.	[58]

1.8 Aims and objectives

This work presented here aims to develop methods used to reduce concentrations of volatile organic compounds (VOCs) and formaldehyde (H_2CO) vapour from indoor air in order to enhance air quality. Herein, monoaromatic hydrocarbons (MAHCs), including toluene, ethylbenzene, cumene and dichlorobenzene, in addition to H_2CO were selected as targets due to their potential impact on human health and comfort. Moreover, the target application areas in this work were to remove the selected VOCs or H_2CO by, primarily adsorption, or photocatalysis.

A key aim of the work was to examine the performance of conventional mesoporous materials such as MCM-41 and SBA-15 for VOCs adsorption; these materials were prepared under harsh conditions. Furthermore the chemisorption of H_2CO after

modifying them with organic amine groups was investigated for formaldehyde removal.

A second key objective was to prepare mesoporous sorbents using a green synthesis routes in order to enhance conventional preparation conditions. This novel route has developed to provide a new possible approach for a rapid and green preparation method for the production of mesoporous sorbents. Also in order to examine the performance of these mesoporous sorbents for VOCs or H_2CO removal, their extraction efficiencies were compared with conventional MCM-41.

Finally the use of titanium dioxide (TiO_2) photocatalysts (powder or films) activated by the UV irradiation were assessed for removal of VOCs from indoor air.

Therefore the thesis has been divided into 9 chapters. Chapter 1 provides an outline of the literature on sources of VOCs and H_2CO, conventional sampling methods and sorbents used for monitoring their indoor levels, determination techniques used. Chapter 2 and 3 present an overview of instrumental and experimental methods employed in this work. Chapter 4 includes full details about the validation of methods used to determine VOCs or H_2CO. Chapter 5 demonstrates the high performance of mesoporous silicate materials (MCM-41 or SBA-15) for VOCs, and chemisorption of H_2CO by functionalized NH_2-MCM-41 or NH_2-SBA-15. Chapter 6 presents the production of novel silica green nanomaterials (GNs) using a bioinspired synthesis route, reporting the first applications of GNs sorbents as VOCs and H_2CO scavengers. Chapter 7 reports a novel method for synthesising mesoporous silica materials using a green route which includes a rapid production of mesoporous materials under mild conditions and with similar performance for VOCs and H_2CO compared to conventional mesoporous materials. Chapter 8 demonstrates a simple design for the photocatalytic oxidation (PCO) reaction of VOCs using TiO_2 photocatalysts (powder or films). Finally, Chapter 9 presents the thesis conclusions and the future work.

2 Theory of Methods and Instrumental Techniques

2.1 N_2 adsorption technique [107]

The adsorption-desorption of molecules on surfaces of solid materials is a commonly used method for characterization of porous materials. Due to its inertness, N_2 is often used as an adsorbate. Much information about the porosity of the materials can be obtained from the shape of the adsorption-desorption isotherms and the total surface area of the sample can also be calculated.

The gas/N_2 adsorption technique, especially the Brunauer-Emmett-Teller (BET) isotherm model describes the dependence of an adsorbed gas against the partial pressure of the gas above a surface at a fixed temperature. Whenever a gas is in contact with a solid there will be an equilibrium established between the molecules in the gas phase and the corresponding adsorbed species (molecules or atoms) which are bound to the surface of the solid. Figure 2.1 shows the four stages which can occur on the surface of porous materials during the adsorption process [108].

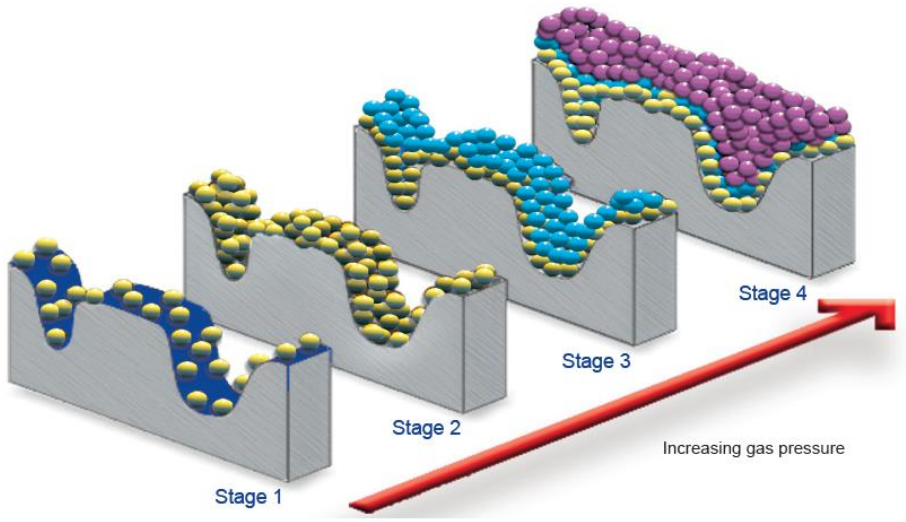

Figure 2.1 Adsorption stages on porous material.[108]

It can be seen that at low gas pressure, stage 1, the isolated sites on the adsorbent begin to adsorb gaseous molecules. All isolated sites will be covered as the gas pressure increases (stage 2) producing one layer of molecules on the adsorbent surface (monolayer). At stage 3, further increases in gas pressure will result in multi-layer coverage. At this stage the surface area can be calculated according to the BET

equation. Finally at stage 4, a further increase of the gas pressure will cause complete coverage of the sample and fill all the pores. At this stage, the Barret-Joyner-Halenda (BJH) calculation can be used to determine pore diameter, volume and distribution.

2.1.1 Classification of adsorption isotherms and hysteresis loops [73, 107, 109]

Adsorption isotherms have been classified by IUPAC into six different categories and the hysteresis loops into four types as seen in Figure 2.2. Type I is associated with microporous solids with relatively small external surfaces. The limiting gas molecule uptake is governed by the accessible micropore volume rather than by the internal surface area. Type II isotherms are typical for aggregated powders which have no ordered pore structure obtained for non-porous or macroporous adsorbents. Type III, V and VI are uncommon isotherms, but are obtained in special cases. Type IV isotherms are typical for porous structures which contain mesopores.

Hysteresis loops can appear in the multilayer range of physisorption isotherms type IV and V and are usually associated with capillary condensation. The different hystereses that can be formed correspond to the different pore shapes in the material. For example H1 loops are found for material with spherical pores of approximately the same size, i.e., the materials have well-defined structures and narrow pore size distributions. Type H2 loops are formed with ‘ink bottle’ shaped pores, which is typical for materials with complex structures containing interconnected networks of pores with different size and shape. Type H3 loops and H4 loops are produced by slit-shaped pores or narrow slit-like pores by microporous materials [73].

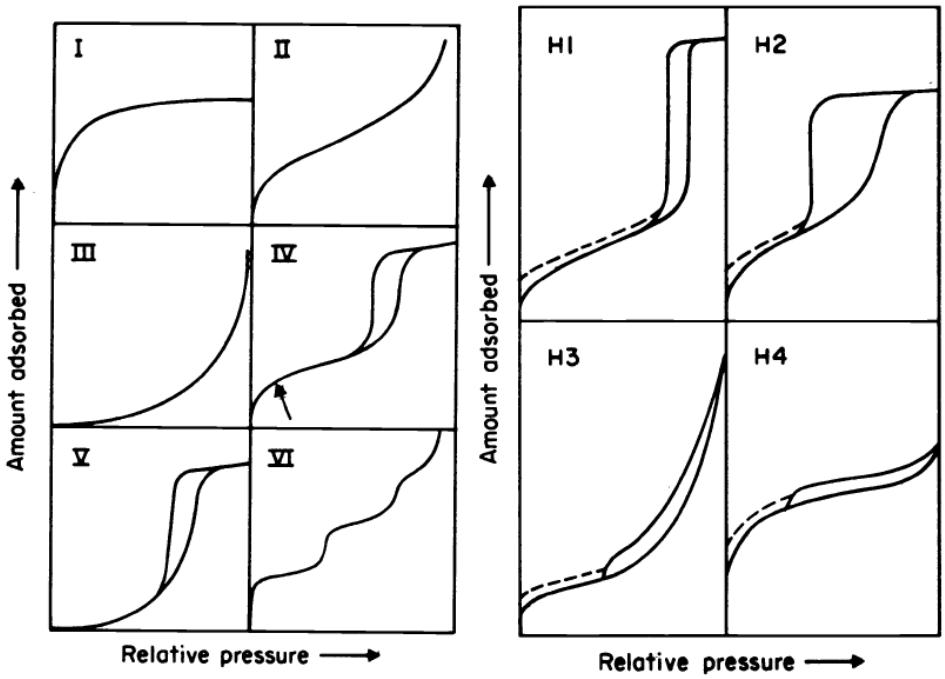

Figure 2.2 Different types of isotherms and hysteresis loops [73]

Ordered mesoporous materials typically have Type IV isotherms, where the steep slope of the curve, at intermediate partial pressure, is due to the filling of the mesopores. The slope of the curve at lower pressures is due to monolayer adsorption at the high internal surface area and the plateau above the steep slope is due to adsorption at the external surface. Mesoporous materials such as MCM-41 usually have isotherms containing no hysteresis loop as they typically possess a very narrow pore size distribution (see Figure 2.3). On the other hand, SBA-15 has a slightly broader pore size distribution which gives a H3 hysteresis loop in the isotherm [110, 111].

Generally, nitrogen isotherms for mesoporous materials consist of five distinct regions as shown in Figure 2.3; region I is due to monolayer adsorption of nitrogen on the external surface and inside the mesopores and appears at very low relative pressures (p/p_o). Region II indicates the partial pressure region where multilayers are formed and data collected at this stage can be used to calculate the adsorbent's surface area. At region III the volume of nitrogen adsorbed increases sharply due to

condensation of nitrogen inside the mesopores; this capillary condensation pressure can be applied to determine the pore volume and pore size distribution. Region IV is associated with multilayer adsorption of nitrogen at the external surface of the adsorbent material. The very shallow slope of this region indicates that the external surface area of the material is small. Finally, at relative pressures close to 1 a volume of nitrogen adsorbed with a small hysteresis loop (region V) can be assigned to condensation of nitrogen within the interstitial voids of the porous material [110].

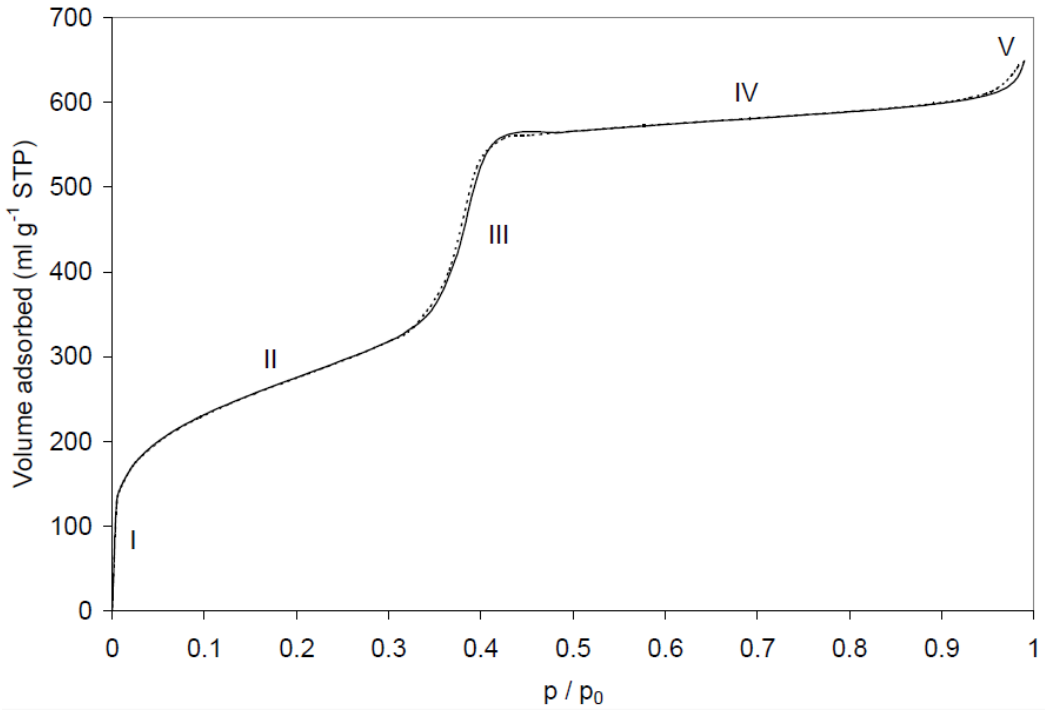

Figure 2.3 A typical nitrogen isotherm for mesoporous materials [110].

2.1.2 Determination of specific surface area using BET isotherms [112]

The specific surface area (m^2 g^{-1}) of porous materials can be determined from the theory proposed by Brunauer, Emmett and Teller in 1938, which is expressed by the BET equation (Equation 2.1) [113]:

$$\frac{V}{V_m} = \frac{C(\frac{P}{p_0})}{\left[1 + (C-1)\left(\frac{P}{p_0}\right)\right]\left[1 - \left(\frac{P}{p_0}\right)\right]}$$ **Equation 2.1**

The BET equation is considered classical in the original meaning of this word, i.e. every possible proposed improvement of methodology, or calculations, in the determination of specific surface areas will use BET as a reference. Therefore, for the determination of monolayer capacity (V_m) the BET Equation 2.1 is conveniently expressed in the linear form (Equation 2.2):

$$\frac{(\frac{P}{P_0})}{V(1 - \left(\frac{P}{P_0}\right))} = \frac{1}{CV_m} + \frac{(C-1)(\frac{P}{P_0})}{CV_m}$$ **Equation 2.2**

Where:

V = volume of gas adsorbed per gram of adsorbent at vapour pressure P.

V_m = the monolayer capacity of the surface.

P_o = the saturation gas pressure at the temperature used.

C = constant.

Thus, the BET plot of $(P/P_o)/ [V (1-(P/P_o)]$ versus (P/P_o) provide straight lines at a low pressure range, usually $0.05 < (P/P_o) < 0.25$ depending on the sample. From such linear plots, with slope $s = (C-1)/CV_m$ and intercept $t = 1/CV_m$. By solving simultaneous equations, two unique values of V_m and C can be obtained from Equation 2.3 Equation 2.4, respectively:

$$V_m = \frac{1}{(s + t)}$$ **Equation 2.3**

$$C = \left(\frac{S}{t}\right) + 1$$ **Equation 2.4**

Derivation of the monolayer capacity (V_m) from the above equation allows the subsequent calculation of the surface area, *S* (see Equation 2.5), by estimation the volume of the adsorbed monolayer V_m, if N_2 is used as the adsorptive gas, which is usually the case, then according to reference [114]

$$S\ (m^2 g^{-1}) = 4.356\ V_m\ (cm^3 g^{-1})$$ **Equation 2.5**

2.1.3 The t-plot method

The t-plot method is used to determine the specific surface area and volume of micropores in the presence of mesopores. The experimental isotherm is transformed into a *t-plot* in the following manner: the amount adsorbed, *V*, is replotted against thickness, *t*, compared to the standard *t-curve* for non-porous materials at the corresponding p/p_0.

Multi-layer formation is modelled mathematically to calculate a layer "thickness, t" as a function of increasing relative pressure (p/p_o). The resulting t-curve is compared with the experimental isotherm in the form of a t-plot. That is, experimental volume adsorbed is plotted versus statistical thickness for each experimental p/p_0 value. The linear range lies between monolayer and capillary condensation. The slope of the t-plot (V/t) is equal to the "external area", i.e. the area of those pores that are not micropores. Mesopores, macropores and the outside surface is able to form a multi-layer, whereas micropores which have already been filled cannot contribute further to the adsorption process.

The surface areas and volumes were determined by using the *t*-method of Halsey for micropore volume in the presence of mesopores (Equation 2.6):

$$t(\text{Å}) = a\left[\frac{1}{ln(\frac{p_0}{p})}\right]^{\frac{1}{b}}$$ **Equation 2.6**

Where,

t = statistical adsorbed film thickness

a = Pre-exponential term = 6.0533 for nitrogen

b = Exponential term = 3.0 for nitrogen

p_0/p = Reverse of Relative pressure

Typically, materials with micropores and mesopores show two linear regions of monolayer formation where the intersection is a measure of the pore diameter (2*t*). The upper linear region represents the mesopore slope from which the mesopore surface can be determined using the above equation and the lower linear region represents the total pore slope. The micropore surface S_μ is the difference between the BET surface and the *t* area S_t, and it can be calculated from Equation 2.7:

$$S_\mu = S_{BET} - S_t$$ **Equation 2.7**

2.1.4 Determination of pore size [112]

The Barrett-Joyner-Halenda (BJH) method [115] for calculating pore size distributions is based on a model of the adsorbent as a collection of cylindrical pores. The theory accounts for capillary condensation in the pores using the classical Kelvin equation since it is closely related to an equation originally proposed by Lord Kelvin [116], for a cylindrical pore the Kelvin equation is given in Equation 2.8 by:

$$\ln\left(\frac{P}{P_0}\right) = \frac{2\gamma\bar{V}}{rRT}$$ **Equation 2.8**

Which gives the dependence of P/P_0 on the pores radius r. Where γ is the surface tension of the liquid and $\bar{V}$ is the molar volume of the condensed liquid contained in a narrow pore of radius r. R is the gas constant and T is the temperature. In this equation γ and $\bar{V}$ are assumed independent of r. Using nitrogen as adsorptive gas at its boiling temperature (77 K). The Kelvin equation can be written as seen in Equation 2.9:

$$r_k = \frac{4.15}{\log\left(\frac{P}{P_0}\right)} \, A^{\circ}$$ **Equation 2.9**

Where r_k indicates the radius into which condensation occurs at the required relative pressure. This radius, called the Kelvin radius or the critical radius, is not the actual pore radius since some adsorption has already occurred on the pore wall prior to condensation, leaving a centre core of radius r_k. Conversely, an adsorbed film remains on the wall during desorption, when evaporation of the centre core takes place. Barrett-Joyner-Halenda (BJH) [115] takes this under consideration and produces another equation based on the thickness of the adsorbed film when condensation or evaporation occurs, then the actual pore radius r_p, is given by Equation 2.10:

$$r_p = r_k + t$$ **Equation 2.10**

Where:

r_p = actual radius of the pore.

r_k = Kelvin radius of the pore.

t = thickness of the adsorbed film.

2.1.5 Determination of pore volume and average pore radius [117]

The total specific pore volume is defined as the liquid volume at a certain P/P_o ratio (usually at P/P_o = 0.95: after the condensation step). In this case, the amount of adsorbed gas reflects the adsorption capacity and the total specific pore volume can be calculated by converting the amount adsorbed into a liquid volume assuming that the density of the adsorbate is equal to the bulk liquid density at saturation. Then the pore volume, V_p. is given by Equation 2.11:

$$V_p = \frac{W_a}{p_l}$$ **Equation 2.11**

Where W_a is the adsorbed amount (g) and p_l is the liquid density at saturation. Assuming that no surface exists, other than the inner walls of the pores, and that the pore is of cylindrical geometry the average pore radius (*a.p.r*) can be calculated from the ratio of the total pore volume and the BET surface area from the following Equation 2.12:

$$a.p.r = \frac{2V_p}{S_{BET}}$$ **Equation 2.12**

The total surface area S_{BET} can be calculated from the BET method described above.

2.2 Chromatography

Chromatography is a term used to describe the separation of components in a sample by distributing them between two phases; the stationary and mobile phase, usually in a chromatographic column. By separating the sample into individual components, it is easier to identify and measure the quantities of the various sample components. There are numerous chromatographic techniques and corresponding instruments such as gas chromatography (GC) and high performance liquid chromatography (HPLC).

2.2.1 Gas Chromatography [118-120]

In GC, the components of a gaseous or vaporised sample are separated by being distributed between a mobile gaseous phase and a stationary phase held in a column. Compounds or molecules must have sufficient volatility and thermal stability; in the gas or vapour phase at 400-450 °C and they must not decompose to be suitable for GC analysis. Separation of analytes is often performed by GC and the rate of migration of each component depends on specific analyte-stationary phase interactions.

Gas liquid chromatography (GLC) is in widespread use in all fields of science and its name is usually shorted to gas chromatography (GC). It is based on the partitioning of analytes between a gaseous mobile phase and a liquid phase immobilised on the surface of an inert solid packing or on the wall of capillary tubing. The mobile phase in GC is called the carrier gas. Helium is the most common carrier gas although nitrogen and hydrogen can be used with the choice of carrier gas being dictated by the type of detector used. Liquid or gaseous samples are conventionally introduced into the injection port using a syringe (in manual or automatic injection mode). In the case of air samples collected onto sorbent tubes, they are introduced into the chromatography by heating the sorbent tube in a thermal desorption unit (TDU).

The TDU is used to extract adsorbed VOCs from a sorbent packed sampling tube using a pure carrier gas, usually helium at specified temperatures [121]. Before desorption is performed it is important to leak test the system to ensure that the tube has been sealed correctly and the TDU system is leak-tight. The sampling tube is also purged with He as the carrier gas at ambient temperature to remove any water vapour and oxygen from the sampling tube [23]. Then the VOCs are desorbed using an optimised temperature programme. After thermally desorbing the VOCs from the sampling tube they are re-concentrated on a cold trap (containing Tenax TA) at – 30 °C before the sample is finally transferred to a GC column for separation. herein the cold trap is rapidly heated from – 30 °C to 300 °C to provide fast transfer of the analytes onto the GC column [122, 123]. The procedure of the sample path through a typical thermal desorption process is illustrated in Figure 2.4.

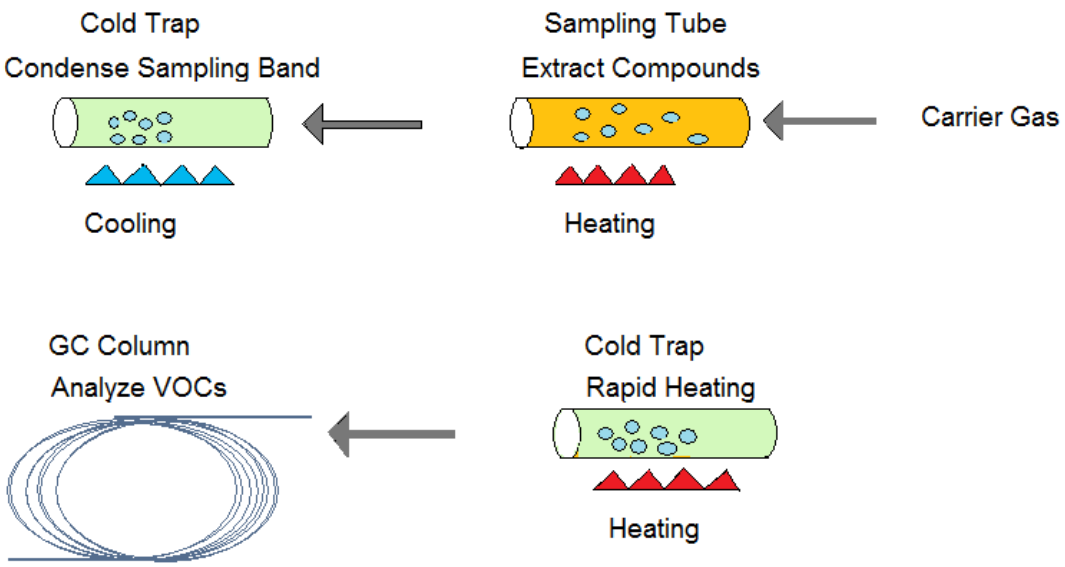

Figure 2.4 Illustration of VOC desorption in a TDU

The analytes pass from the TDU into the gas chromatograph via an inert transfer line and are passed into the column which is held at a temperature controlled by an oven. Solutes travel through the column at a rate that is primarily determined by their physical properties, the temperature and the composition of the stationary phase inside the column. The fastest moving solutes exit (or elute) from the column first, followed by the remaining solutes in a specific order. In general separation of the analytes occurs through differences in boiling point and relative affinities for the stationary phase. A larger proportion of lower boiling point analytes exists in the carrier gas, compared to the stationary phase, therefore these analytes will move down the column quickly with the carrier gas and elute faster than higher boiling point analytes.

There are two main types of column in common use in GC; the conventional packed column or the capillary column. Packed columns, usually made of glass or stainless steel, have an internal diameter of 2 to 4 mm, are 1 to 4 m long and are packed with particles or a solid support that is coated with a thin layer (0.5 to1µm) of the stationary liquid phase. Packed columns have significantly lower resolving powers than capillary columns and as a result are more commonly used in industrial and research applications. Capillary columns are made of fused silica, which can be coiled easily and so the length of capillary columns ranges from 10 - 100 m. They

have a smaller internal diameter than packed columns. There are two basic types: wall-coated open tubular (WCOT) and support-coated open tubular (SCOT) capillary columns. The liquid stationary phase is coated on, and supported by, the walls of the tube. The original capillary columns had a very thin liquid film of 0.2 - 1 mm thickness coated on smooth metal or glass surface. Such columns (SCOT), a layer of celite or other supports is adsorbed onto the tubing wall and the liquid phase is adsorbed onto the celite. Capillary columns can provide very high resolution compared with packed columns.

The desirable properties of a liquid stationary phase for GC columns include low volatility (ideally, their boiling point should be at least 100 °C higher than the maximum operating temperature for the column), thermal stability and chemical inertness. The most widely used stationary phases for both packed and capillary columns for GC are listed in Table 2.1 in order of increasing polarity. Most of them are polydimethyl siloxane based which have the general structure as shown in Figure 2.5. Hydrocarbon-type stationary phases and dialkyl siloxanes are non-polar, whereas stationary phases contain functional groups such as –CN, -CO and –OH are polar phases.

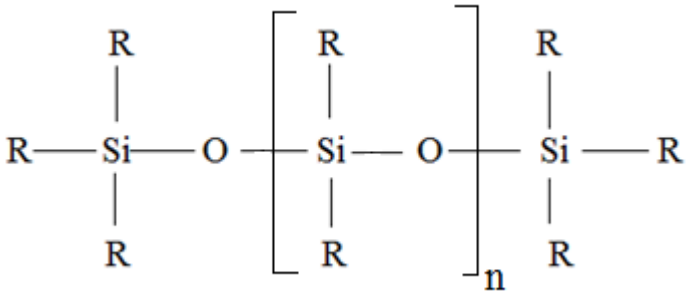

Figure 2.5 General structure of liquid stationary phase

Table 2.1 Some common liquid stationary phases for the GC

Stationary phase	Common trade Name	Maximum Temp. ^{0}C	Common Applications
Polydimethyl siloxane	OV-1, SE-30	350	Nonpolar phase, hydrocarbons, Poly aromatic, sreroids
5 % Phenyl-polydimethyl siloxane	OV-3, SE-52	350	Fatty acid methyl esters, alkaloids, halogenated compounds, drugs
50 % Phenyl-polydimethyl siloxane	OV-17	250	Drugs, sreroids, pesticides, glycols
50 % Triflouropropyl-polydimethyl siloxane	OV-210	200	Chlorinated aromatics, nitro-aromatics, alkyl-benzene
Polyethylene glycol	Carbowax 20M	250	Free acids, alcohols, ethers, glycols
50 % Cynopropyl-polydimethyl siloxane	OV-275	240	Free acids, alcohols, rosin acids, fatty acids

The polarity of analytes containing common functional groups listed in increasing order of polarity are as follows: aliphatic hydrocarbons < olefins < aromatic hydrocarbons < halides < sulfides < ethers < nitro compounds < esters < aldehydes, ketones < alcohols, amines < amides < carboxylic acids < water. To have a reasonable retention time on the separation column, analytes must show some solubility with stationary phase. The separation principle of column is based on the basic theory of "like dissolve like". In other words, non-polar stationary phases are used for the analyses of non-polar compounds and polar stationary phases provide the most effective separation of polar compounds. Interaction between non-polar compounds and a nonpolar stationary phases is by physical adsorption (Van der Waals forces) and this interaction is increased by the increasing the hydrophobicity of analyte. Polar molecules can interact with the stationery phase in the column by three different interactions: dipole (π-π), acid-base interactions and H-bonding. Separations are determined by differences in the overall effects of these interactions.

Column temperature selection [124, 125] is an important variable that must to be controlled, thus the column used in GC instrument is normally housed in a thermostated oven. The appropriate temperature selection in GC is a compromise between several factors. *The injection temperature* should be relatively high, consistent with the thermal stability of the sample, to get the sample into the column in a small volume. *The column* temperature is a compromise between speed, sensitivity and efficiency of separation. The analytes' migration rates are directly related to the column temperature. In some samples, which contain analytes of similar physical properties, use of a high column temperature could lead to very poor separation due to the sample components spending most of their time in the gas phase and so they elute quickly. Equally if column temperatures are too low analytes may take too long time in the stationary phase and elute from the column slowly. Therefore a procedure known as *temperature programming* is used to analyse samples which contain a large number of analytes of different boiling point. By altering the oven temperature during the chromatographic process, best analyte resolution can be obtained.

After separation the analytes are individually passed on to the detector. The ideal detector for GC should have adequate sensitivity, stability, reproducibility, a linear response for solutes of interest, a temperature range from room temperature to at least 400 °C, a high reliability and ease use, and permit the selective and non-destructive analysis of sample. *The detector temperature* must be higher than the column to prevent condensation of the sample components. The sensitivity of the thermal conductivity detector deceased as its temperature is increased therefore it should be kept at the minimum required. There are many detectors used in conjunction with GC such as, flame ionization, infrared, thermal conductivity and, most commonly, mass spectrometry which is described below.

The mass spectrometer (MS) is one of the most powerful detectors for GC which is normally used in analytical chemistry to determine the molecular weight of an analyte or to identify unknown organic compounds in a sample [118, 124, 126]. All mass spectrometers consist of three regions; the ion source (ionizer), the mass analyser and the detector as described below and illustrated in Figure 2.6.

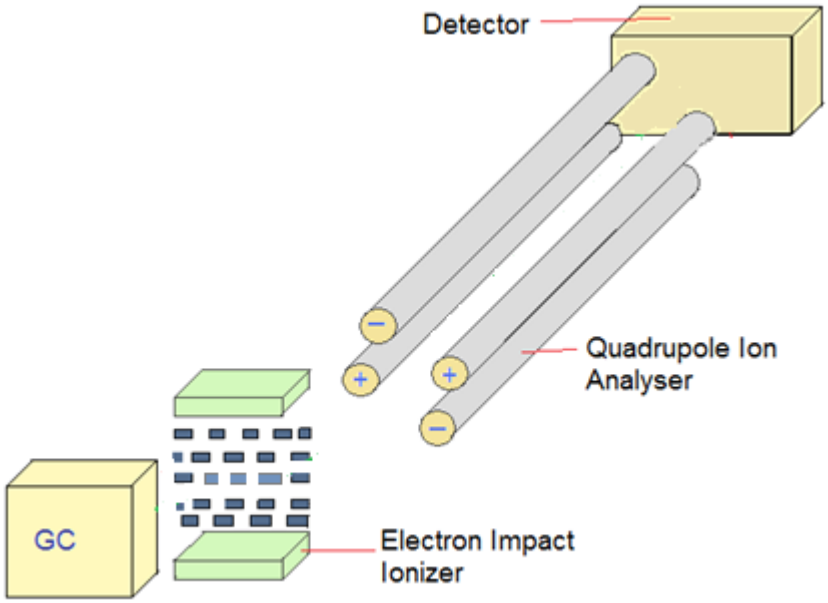

Figure 2.6 The schematic of a mass spectrometer [118].

The starting point of mass spectrometric analysis is the formation of gaseous ions in an ion source. Electron-impact "Electron Ionization" (EI) and chemical ionisation sources are used to produce gaseous ions in the mass spectrometric system and most modern mass spectrometers are designed so that electron-impact ionisation and chemical ionisation can be carried out interchangeably [125]. A high-energy electron beam (70 eV) is applied in the ion source which normally operates at 2 x 10^{-5} Torr with 1.0 cm^3 min^{-1} He flowing into the manifold for electron ionisation, or 3 x 10^{-4} Torr for chemical ionisation. A large change of pressure between the end of the GC column and ion source causes the expansion of the gas flow to several litres per minute, therefore large pumps are required to remove the excess gas and to maintain the vacuum inside the source near optimum pressure for ionisation [127].

During ionisation positive ions are produced as shown below.

$$M + e^- \rightarrow M^+ + 2\,e^-$$

Where *M* is the analyte molecule and M^+ is called *molecular ion* or *parent ion*. The molecular ions are produced in different energy states and the internal energy (rotational, vibrational, and electronic) is dissipated by fragmentation reactions,

producing fragments with lower mass. These lower mass fragments are themselves ionised or converted to ions by further electron bombarding. An example of the ionisation process for methanol in the ion source is given below.

$$CH_3OH + e^- \longrightarrow CH_3OH^{\bullet+} + 2\,e^-$$

The charged methanol ion, which contains an unpaired electron, is normally unstable and will breakdown into smaller pieces (fragments).

$$CH_3OH^{\bullet+} \text{ (molecular ion)} \longrightarrow CH_2OH^{+} \text{ (fragment ion)} + H^{\bullet} \quad \textbf{or}$$

$$CH_3OH^{\bullet+} \text{ (molecular ion)} \longrightarrow CH_3^{+} \text{ (fragment ion)} + {}^{\bullet}OH$$

The positively charged ions that are created will pass through the MS and uncharged atoms will be removed before reaching the detector.

In the ion analyser [118, 128] molecular ions and fragment ions are accelerated by manipulation of the charged particles through the mass spectrometer. Uncharged molecules and fragments are pumped away. Various spectrometers are based on magnetic sectors in which ions pass through magnetic field and are deflected based on their (m/z) ratio. The mass analyser used throughout the course of this investigation was the quadrupole mass analyser.

The quadrupole uses the stability of the trajectories in oscillating electric fields to separate the ions based upon their m/z ratio. Quadrupole analysers are made up of four rods with circular or hyperbolic section. These rods are arranged in pairs to which an alternating radiofrequency (RF) and DC potential is applied. The oscillating field allows a range of m/z ratios to pass through, while any ions with a m/z ratio higher or lower than this preselected range are unable to pass through and collide with the poles, see Figure 2.6. The quadrupole mass spectrometer is ideally used as a GC detector due to it is compact and relatively inexpensive, complete scan is achieved in the duration of a GC peak, and simply by scanning voltage.

There are a number of different detectors for use with the mass spectrometer; however they can generally be divided into two categories. The first of which involves the direct measurement of the charges which reach the detector, for example photographic plate and Faraday cage detectors. The other category of detectors involves increasing the intensity of the signal such as the array detector and the photomultiplier detector.

The most common detector is the photomultiplier which was used during the course of this investigation. The photomultiplier detector consists of two conversion dynodes, a photomultiplier and a phosphorescent detector. This detector enables the detection of both positive and negative ions. When operated in the positive mode the secondary ions are accelerated towards the negatively charged dynode, while in negative mode the ions are accelerated towards the dynode which carries the positive potential. The secondary electrons given off are then accelerated towards the phosphorescent screen, which is coated in a thin layer of aluminium conductor to avoid the accumulation of a charge. At the phosphorescent screen the electrons are converted to photons, which are then detected by the photomultiplier.

2.2.2 High-Performance Liquid Chromatography (HPLC) [118, 128]

In LC the mobile phase is a liquid solvent containing the sample as a mixture of solutes. HPLC modes can be classified by the separation mechanism or by the type of stationary phase to: liquid–liquid (partition) chromatography, liquid-solid (adsorption), ion-exchange, size-exclusion, affinity, or chiral chromatography. The HPLC apparatus consists of four principles parts; mobile-phase supply system, sampling injection system, column and detector.

The mobile supply [128, 129] contains a pump to provide the high pressures required and usually contains some means of providing gradient elution (i.e. changing concentrations of eluent or filling with a range of solvents of polarities and mixing in a buffer volume). The solvents must be pure and be degased. The requirements for liquid chromatographic pumps include; i) a working maximum pressure range of 6000 psi, ii) a pulse-free flow, iii) the ability to alter flow rates from 1 to 10 cm^3 min^-

[1], iv) flow rate reproducibility better than 0.5 % and v) it must be chemically inert to common solvents (stainless steel and Teflon seals must be used). There are two basic types of pumps in common use; constant volume pumps and constant pressure pumps.

The constant pressure pump consists of some device for direct pressurisation of the mobile phase with an inert gas giving a reliable pulse-free flow. They are of low cost and are simple to use however they are not as accurate as constant volume pumps. The delivered flow rate from a constant pressure pump is very sensitive to changes in solvent viscosity and changes in column permeability hence they are generally unsuitable for gradient elution. The constant volume pumps provide a more precise analysis and they are particularly useful when gradient elution is used. There are two major types of constant pressure pumps used in the HPLC instruments called syringe type pumps and reciprocating pumps.

The syringe pump [129] has a plunger which is driven by a stepping motor through a gear box and the rate of delivery from the syringe is controlled by varying the voltage on the motor. The main advantage of the syringe type pumps is that it is capable of providing a pulse-free flow at high pressure and the flow rate independent of the operating pressure. The reciprocating pump [129] is used in almost all commercial HPLC instruments and consists of a small cylindrical chamber that is filled and then emptied by back-and-front motion of a piston. The pumping motion produces a pulsed flow which appears as baseline noise on the chromatogram, therefore the pulses must to be subsequently damped. Advantages of reciprocating pumps are small internal volume (35-400 μL), high output pressure (up to 10,000 psi), adaptability to gradient elution and a constant flow rate independent of column back-pressure and solvent viscosity.

For maximum efficiency on a chromatographic column the sample should be introduced, ideally, as an infinitely narrow band. A typical injection system using a sampling loop is illustrated in Figure 2.7 [118, 128, 129]. This injection system consists of a stainless steel ring with six different ports, one to the column. A movable Teflon cone within the ring has three open segments, each of which connects a pair of external ports. Two of the ports are connected by an external

sampling loop of fixed volume. In one configuration, the cone permits direct flow of effluent onto the column and the loop can be filled with the sample. The cone can be then rotated 30° to make the sample loop a part of the moving stream, which sweeps the sample into the column. Samples of few microliters (for example 20 μL) can be injected at the fixed pressure.

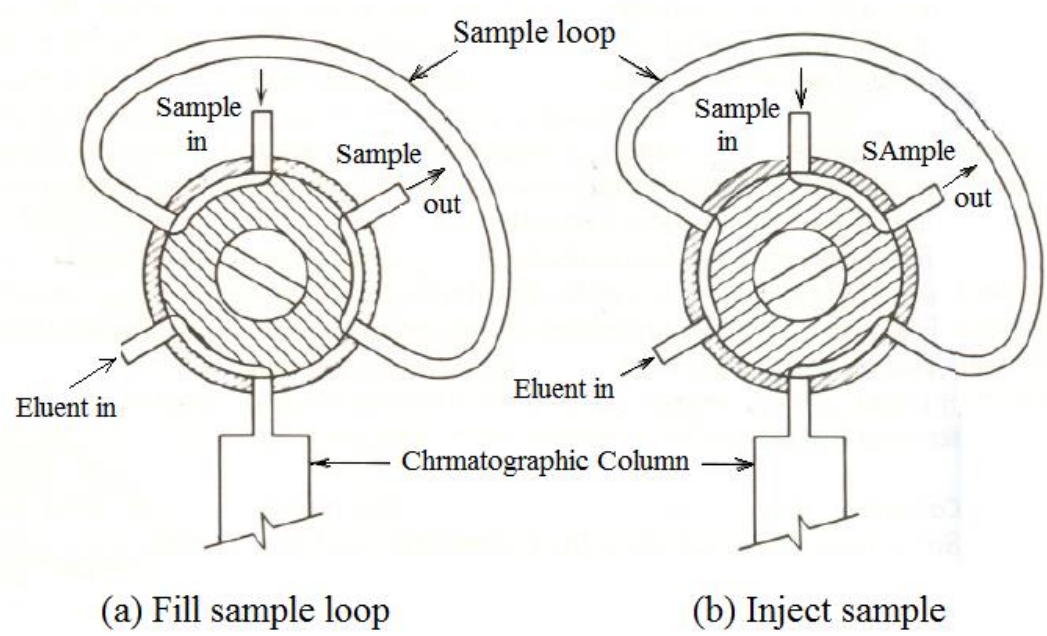

Figure 2.7 Sample loop injector for liquid chromatography [128]

Liquid chromatography columns [118, 129] are usually constructed from stainless steel tubing, although glass and polymer tubing can be used. Most analytical columns range in length from 5 to 25 cm and have inside diameters of 3 to 5 mm. The most common particle size of the solid support is 3 to 5 μm and columns can provide efficiencies of 40,000 to 70,000 plates /m. In general, the smaller particle diameter of adsorbents, or solid supports, used in the column the greater separation efficiency. To minimize stagnant pools in the column, the pores of the support must be completely filled with stationary phase. Solid adsorbents should be activated by heating and after the packing the mobile phase should be passed through the column for at least 2 h at a flow rate of 0.5 cm^3 min^{-1} to remove entrained air and allow the adsorbents to equilibrate with the mobile phase. Silica is the most common bonded-phase packing

in partition chromatography, the silica particles are often coated with thin organic films that are chemically or physically bonded to the surface.

Most of bonded-phase packings are prepared by reacting an organochlorosilane with the –OH groups formed on the surface silica by hydrolysis in hot dilute HCl, producing an organosiloxane with a straight chain hydrocarbon whose chain length is dictated by the selected derivatising agent used. Most commonly octyl- or octyldecyl groups (-R) are used. For alter the polarity of the column the silica surface can be bonded with organic functional groups such as aliphatic amines, ethers, nitriles or aromatic hydrocarbons. According to the relative polarities of the mobile and stationary phases, partition chromatography can be further sub-divided into two types; normal-phase or reversed-phase chromatography.

Normal-phase chromatography is based on a highly polar stationary phase, such as triethylene glycol or water, and a relatively non-polar mobile phase such as hexane or *i*-propyl ether. Whereas in reversed-phase chromatography the stationary phase is non-polar, usually a hydrocarbon and the mobile phase is a relatively polar solvent such as water, or acetonitrile. It has been estimated that more than 75 % of all liquid chromatography separations are currently performed with reversed-phase bonded (octyl- or octyldecyl) stationary phases and aqueous mobile phases containing methanol or acetonitrile. During separation of a range of components by reversed-phase chromatography the most polar components will be eluted first and increasing the mobile phase polarity will increase the elution time.

The order of polarities of common mobile phase solvents is water > acetonitrile > methanol > ethanol > tetrahydrofuran > propanol > cyclohexane > hexane. The polarity of stationary phase should be matched roughly with that of the analyte and mobile phase for more successful separation. When the polarities of analyte and mobile phase are matched but are different from that of stationary phase, the stationary phase cannot compete successfully for the sample components and retention times become too short for practical applications. In contrast, if the polarities of the analyte and stationary phase are too alike, retention times become inordinately long.

Ideal detectors [128, 129] for liquid chromatography should have similar characteristics of ideal gas chromatography detectors outlined in Section 2.2.1 except that it does not necessary have to operate over a wide temperature range. The most widely used detectors for LC applications include refractometry and ultraviolet (UV) detectors. Refractometry measures the bulk properties of both the sample and the mobile phase. Ultraviolet (UV) detectors measure the property of solute in the sample without removal of mobile phase before detection. These detector types are the most widely used detectors for liquid chromatography and are based on the absorption of ultraviolet and visible radiation.

UV-VIS spectrometry [128, 130] is used to measure the molecular absorbance of a molecule in the ultraviolet visible region of the spectrum. Absorbance measurements based upon UV-VIS radiation find widespread application for the quantitative determination of a large variety of inorganic and organic species. A single-beam instrument consists of, the radiation sources, a filter or monochromator for wavelength selection, matched cells that can be alternately placed in the radiation beam, photodetector, amplifier and readout device as shown in Figure 2.8.

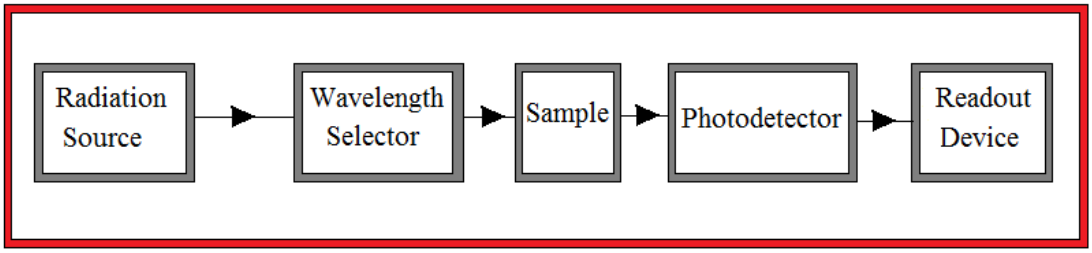

Figure 2.8 Basic instrumentation for UV-VIS spectrometry.

The fraction of radiation absorbed by a solution of an absorbing analyte can be quantitatively related to its concentration [128, 130]. When an absorbing species is placed in the beam of radiation the sample absorbs some of the beam and allows part of the beam to pass through and be detected. The beam of the light that strikes the sample can be absorbed, transmitted, scattered or reflected as illustrated in Figure 2.9.

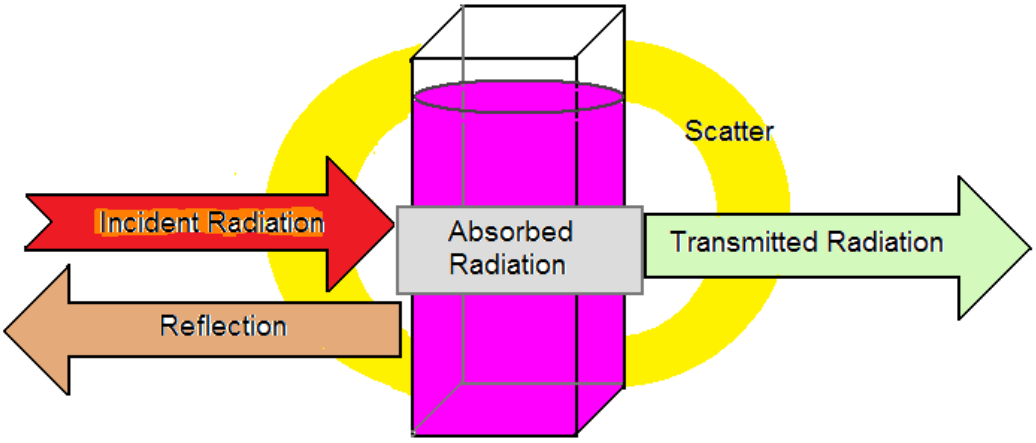

Figure 2.9 Interactions of the radiation and matter in UV-VIS spectrometry

The amount of monochromatic radiation absorbed by a sample is described by Beer's law. Incident radiation of radiant power P_0 passes through a solution of absorbing species at concentration C and path length b, and the transmitted radiation has radiant power P, which measured by the detector. The molecular absorption is based on the measurement of the transmittance T or the absorbance A of solution contained in UV transparent cells having a path length of b cm. Typically, the concentration C of the absorbing analyte is linearly related to absorbance as given in Equation 2.13.

$$A = -\log T = \log \frac{P_0}{P} = \in b\, c$$

Equation 2.13

Where $\in$ is the molar absorbance value in L mol^{-1} cm^{-1}. This equation is a mathematical representation of Beer's law.

The transmittance and absorbance cannot be measured directly because some of the beam was absorbed by the sample and some was passed through the sample, in addition, part of the beam was scatted by large molecules or was reflected. Therefore, the power of the beam transmitted by analyte solution is usually compared with the power of the beam transmitted by an identical cell containing only solvent

(blank). The true experimental transmitted and absorbance is then obtained by Equation 2.14.

$$A = -\log T = \log \frac{P_{solvent}}{P_{solution}} = \log \frac{P_0}{P}$$ **Equation 2.14**

Where P_o and P here refer to the power of radiation after it passed through cells containing solvent (blank) and the analyte, respectively [131].

The absorption of ultraviolet or visible radiation by molecules results in the transition of an electron from the ground state to an exited energy state. Species containing unsaturated bonds generally exhibit useful absorption peaks because the electrons are not strongly held within double and triple bonds. Unsaturated organic functional groups that absorb in UV or visible regions of the electromagnetic spectrum are known as chromophores. Non-bonding electrons in the saturated organic compounds containing heteroatom, such as oxygen, nitrogen, sulfur or halogens can be excited by UV radiation.

Many UV detectors are simple interference devices that can measure the absorbance at only a few selected wavelengths. The more expensive detectors have a monochromator that allows selection of a particular wavelength. In general, UV detectors in HPLC-UV or UV-vis spectrometry instruments consist of source of radiation, monochromator, cell, window and filter, detector, amplifier and readout device as illustrated in Figure 2.10.

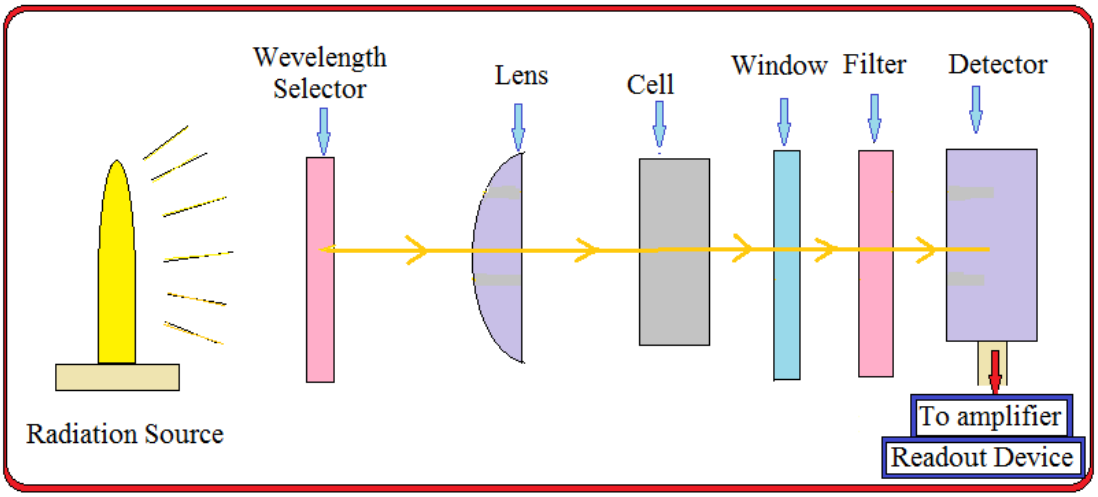

Figure 2.10 Schematic diagram of the UV absorbance detectors

Irradiation from the UV source is passed through the wavelength selector (monochromator) to obtain the required wavelength. The lens focuses the radiation to strike the cell, having passed through the sample cell the light passes through window and filter before striking the detector photocell. The signals generated are proportional to the intensity of the light. These signals are pre-amplifier and then fed to the readout recorders which provide quantitative data of measured analye.

The source should have a readily detectable output of radiation over the wavelength region for which the instrument is designed to operate. The radiation sources used for ultraviolet region are low-pressure hydrogen or a medium-pressure mercury vapour lamp, which can be used from 185 to 375 nm. In UV-vis spectrometry two sources of radiation are typically used to cover the required wavelength range. A hydrogen, or deuterium lamp and tungsten filament are used to provide the instrument with the appropriate light in UV and visible regions. The sources must provide a sufficient radiant energy over the required wavelength region, and maintain a constant intensity over the measurement time. The radiation emitted by each sources is passed through the filter, or monochromator, to obtain the selected wavelength of radiation. After the monochromatic radiation is passed through the sample cell, the transmitted radiation has to be detected.

The cell holding the sample must to be transparent in the wavelength region being measured. The cells used in UV-visible spectrometers are usually quartz cuvettes 1 cm long (internal distance between parallel walls).

Detectors [128, 132] used in UV-vis spectrometry also depend on the wavelength region to be measured and normally a phototube, photomultiplier tube or a diode array detector is used. The phototube (or photocell) consists of a photoemissive cathode and an anode, where a high voltage is impressed. When a photon enters the window of the tube and strikes the cathode an electron is emitted and attracted to the anode creating a current flow that can be amplified and measured. The response of the photoemissive material used is wavelength dependent and different phototubes are available for different regions of the spectrum. The photomultiplier tube detector is more sensitive for the UV-vis regions of the electromagnetic spectrum and is essentially constructed of several phototubes which are built into one envelope. When a primary electron is emitted from the photoemissive cathode by a photon it is accelerated toward the next photoemissive electrode where it releases secondary electrons. This, in turn, is accelerated to the next electrode where each electron releases a further electron, and so on, up about 10 stages of amplification. The electrons are finally collected by the anode. The diode array detector is used in spectrometers that record an entire spectrum simultaneously. It consists of a series of hundreds of silicon photodiodes positioned side-by-side on a single silicon crystal or chip. It has an associated capacitor which collects and integrates the photocurrent generated when photons strike the photodiode. The spectral response of a silicon diode array is that of silicon, about 180 to 1100 nm, covering regions of radiation from UV to near infrared, which is wider than for photomultiplier tubes, with high quantum efficiency.

2.2.3 Chromatographic principles and selectivity factors [128]

When an analyte (solute) is injected onto chromatographic column equilibrium is rapidly established as the analyte distributes (or partitions) between the stationary X_s and X_m mobile phases.

$$X_m \quad \rightleftharpoons \quad X_s$$

The distribution equilibrium is described by distribution coefficient as shown in Equation 2.15:

$$K_m \quad = \quad \frac{[X]_s}{[X]_m} \qquad \textbf{Equation 2.15}$$

Where $[X]_s$ and $[X]_m$ are the concentrations of analyte *X* in the stationary or mobile phases at equilibrium. The Distribution coefficient K_m is a constant and is known as the partition coefficient in this case. Analytes with a large partition coefficient value will be retained more strongly by the stationary phase than those with a small value, meaning that the analyte will spend a longer time in the chromatographic column before eluting. The time required for the separation, or the time of analyte peak to appear on the chromatogram, is known as the analyte retention time(t_R).

Each analyte will have a specific retention time according to its interaction with the stationary phase and the flow rate of the mobile phase. This time should be longer than the time required for the mobile phase to traverse the column or the time it would take for an unretained analyte to appear; defined by the so-called void time (t_M). The difference between the retention time and void time ($t_R - t_M$) is called the adjusted retention time (t_R'). The capacity factor or retention factor, K_A is used to describe the rate of analyte flows through the column and this factor can be expressed as given in Equation 2.16:

$$K_A = \frac{t_R - t_M}{t_M} = \frac{t'_R}{t_M}$$ **Equation 2.16**

The retention factor (K_A) value is used to estimate the capability of the column for the separation of target analytes. For example if the K_A value is less than 1 the analyte will pass too quickly through the column and when the K_A value is too high (about 20) the analyte will take a very long time to pass the column. Usually preferable K_A values lie in the range 1 – 5 [133]. To examine the ability of a column to separate two species (analytes A and B for example) the selectivity factor (α) as given in Equation 2.17 can be assessed:

$$\alpha = \frac{K_B}{K_A}$$ **Equation 2.17**

Where K_B and K_A are the retention factors for the two species (B and A). For efficient separation the selectivity factor should be greater than 1 [133].

The Theoretical Plate and Column Efficiency in Chromatography [128]

Several factors influence the separation efficiency of a column which can be expressed in terms of the number of theoretical plates in a column. In the simplest of terms, the theoretical plates can be envisaged as a number of separate layers in a column; each separate layer interacting with the analyte of interest. Thus a theoretical plate represents a single equilibrium step. In fact the plates do not really exist but the information which could be obtained from an assumption of the theoretical plates (see Figure 2.11) is useful to estimate the column efficiency. For high separation efficiency, a large number of theoretical plates are required.

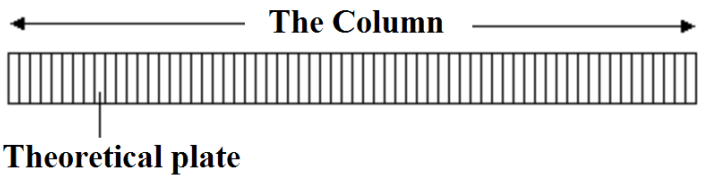

Figure 2.11 The assumption of theoretical plates inside the column.

The number of theoretical plates, N, in a column can be calculated from a chromatogram using the expression in Equation 2.18.

$$N = \frac{5.55\ t_R^2}{w_{0.5}^2}$$ **Equation 2.18**

Where $w_{0.5}$ is the peak width measured at height of half-height of the peak. The height equivalent to a theoretical plate (HETP) is the length of a column (L) divided by the number of theoretical plates (see Equation 2.19).

$$HETP = \frac{L}{N}$$ **Equation 2.19**

2.3 Powder X-ray diffraction (PXRD) [134, 135]

X-ray diffraction is an important and powerful method for the investigation of materials. This method is based on the scattering of X-rays by the electrons of atoms. The wavelengths of X-rays are similar to interatomic distances and so the X-rays scattered by different atoms will interfere destructively or constructively, in the latter case giving rise to diffracted beams. In the case of crystalline samples, sharp diffraction phenomena result.

The principle of the XRD technique is shown in Figure 2.12, where monochromatic X-rays with wavelength λ are reflected from parallel crystal planes, with an incident angle θ between the beam direction and the planes with distance d between lattice planes.

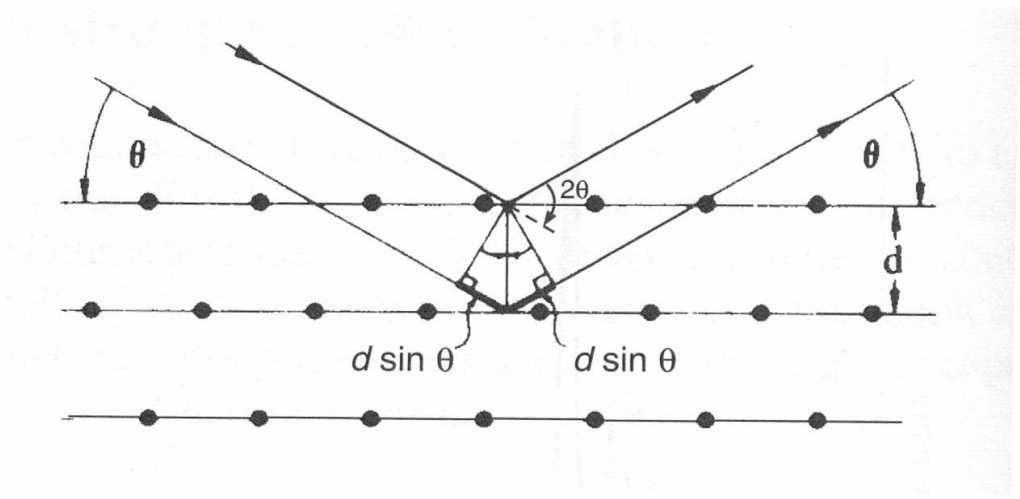

Figure 2.12 Geometry for interference of a wave scattered from two planes separated by spacing, *d[134]*.

It can be shown that X-rays reflected from two adjacent parallel planes will be in the same phase and interfere constructively when the following condition is met, which is known as the Bragg equation (Equation 2.20). The geometry of the corresponding diffraction events can be described by Bragg's law, which combines a measure of the lattice of the crystal structure, namely the distance *d* between lattice planes, the wavelength λ of the X-ray radiation and the diffraction angle θ:

$$2d\ sin\,\theta\ =\ n\,\lambda \qquad \textbf{Equation 2.20}$$

Where *n* is an integer (the reflection order) and *d* is the interplanar spacing. The intensity of the diffracted X-ray beam is therefore dependent upon θ and *d*, so by measuring the diffraction intensity at different values of 2θ, the interplanar distances in the crystal may be investigated. The Bragg equation treats diffraction as the reflection of X-rays at the lattice planes; correspondingly, a diffraction event is usually called a reflection. By analysing the geometry of the diffracted beams, information can be gained on the geometry of the lattice of the structure under

investigation. By further analysing the intensity distribution of the reflections, information on the positions of the atoms can be obtained. This is usually carried out by measuring X-ray reflections on a single-crystal and forms the basis of X-ray single-crystal structural analysis [136].

Mesoporous materials have an amorphous structure in the pore walls, so there are no diffraction peaks due to ordered crystal structure. However, as there is a long-range order in the pore structure, diffraction peaks at low 2θ values are observed, with corresponding *d*-values in the pore size range. An X-ray beam with an exact angle is directed onto a smooth surface of the sample. If the material has any long range periodicity the X-ray beam will, at some angles, be reflected and collected by a detector.

The "*d*" value is often expressed as "d_{hkl}", where h, k and l are the Miller indices for the respective crystal planes, which describe the direction of the crystal plane in three dimensional spaces. For some structures the (hkl) values of a crystal plane may be expressed as a direction vector that is orthogonal to the plane. The values of h, k and l then correspond to the x, y and z values of the vector, respectively. A given set of planes with indices h, k, and l cut the a-axis of the unit cell in h sections, the b axis in k sections and the c axis in l sections. A zero indicates that the planes are parallel to the corresponding axis.

2.4 Transmission Electron Microscopy [137]

Transmission electron microscopy (TEM) is an imaging technique which uses high energy electrons accelerated to nearly the speed of light to provide a highly magnified view of the micro- and nanostructure of materials. The TEM technique consists of four parts: electron source, electromagnetic lens system, sample holder, and imaging system. The electron source consists of a cathode and an anode. The cathode is a tungsten filament which emits electrons when being heated. A negative cap confines the electrons into a lightly focused beam. The beam is then accelerated towards the specimen by the positive anode. Electrons at the rim of the beam will fall onto the anode while the others at the centre will pass through the small hole of the anode. The electron source works like a cathode ray tube. Electromagnetic lens

system: after leaving the electron source, the electron beam is firmly focused using electromagnetic lens and metal apertures. The system only allows electrons within a small energy range to pass through, so the electrons in the electron beam will have a well-defined energy.

The sample holder is a platform equipped with a mechanical arm for holding the specimen and controlling its position. When an electron beam passes through a thin-section specimen of a material, electrons are scattered. A sophisticated system of electromagnetic lenses focuses the scattered electrons into an imaging system which consists of another electromagnetic lens system and a screen. The electromagnetic lens system contains two lens systems, one for refocusing the electrons after they pass through the specimen, and the other for enlarging the image and projecting it onto the screen. The screen has a phosphorescent plate which illuminations when being hit by electrons forming an image in a way similar to photography.

2.5 Fourier Transform Infrared Spectroscopy (FTIR) [118, 128, 138]

FTIR spectroscopy is an analytical technique widely used for the identification of wide range of solids, liquids and gases. However, in many cases some form of sample preparation is required in order to obtain a good quality spectrum. Traditionally IR spectrometers have been used to analyse samples by means of transmitting the infrared radiation directly through the sample. Where the sample is in the solid form the intensity of the spectral features is determined by the thickness of the sample and typically this sample thickness cannot be more than a few tens of microns. The FTIR spectra obtained can be used as a characteristic finger print of the whole compound, or features of the FTIR spectrum can be used to assign chemical structures to the observed molecule. FTIR spectrometer normally contains an interferometer which causes interference in the incident beam using a moving mirror and beam splitter (Figure 2.13). The beams then recombine to produce a complex model of frequencies which can be measured by a suitable detector to produce a signal (interferogram). Fourier transform is used to convert the interferogram into the conventional FTIR spectrum,

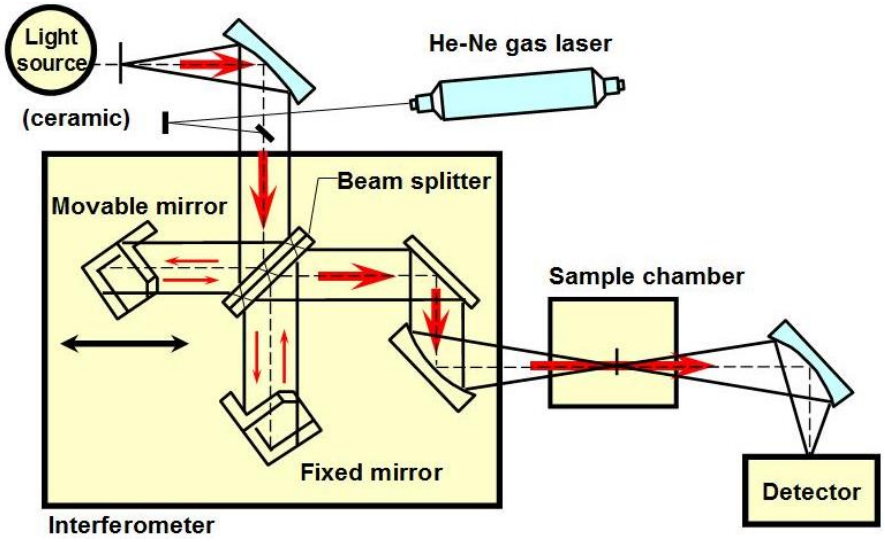

Figure 2.13 Diagram of the Michelson Interferometer used in an FTIR Spectrophotometer [138].

Electromagnetic (EM) radiation can be absorbed by molecules and this process can cause three types of quantized transitions to occur according to the quantum energy of the radiation. In addition to electronic transitions, molecules exhibit two other types of transitions; vibrational transitions and rotational transitions. The relative energy levels of these transition processes are in order electronic > vibrational > rotational transitions. However IR radiation is not energetic enough to cause electronic transitions as seen with UV and visible light; it can however induce transitions in the vibrational and rotational states of a molecule. As the alteration of a molecule's rotational state needs low energy this process occurs at the far IR region of the electromagnetic spectrum.

Absorption of IR radiation can either be transformed into kinetic energy, as a result of collisions, or released again as a photon. Traditionally IR spectrometers have been used to analyse materials by means of transmitting the infrared radiation directly through the sample. The spectrometer is used to measure the radiation intensity as a function of the wavelength of the light behind a sample. At the vibrational

frequencies of the molecules an intensity decrease is obtained and a transmittance, or absorbance, spectrum is measured.

To absorb infrared light there must be a change in the dipole moment (polarity) of the molecules and diatomic molecules must have a permanent dipole (polar covalent bond in which a pair of electrons is shared unequally). A molecule can vibrate in many ways, and each vibration is referred to as a vibrational mode. For molecules which contain N atoms, the number of expected vibrational modes can be calculated. For example, linear molecules demonstrate 3N – 5 degrees of vibrational modes, whereas nonlinear molecules have 3N – 6 degrees of vibrational modes (also called vibrational degrees of freedom). For example it can get an idea of the nature of vibrational states by picturing a bond in a molecule as vibrating spring with atoms attached to both ends as seen in Figure 2.14. Molecules can vibrate in six different ways: symmetric and asymmetric stretching, scissoring, twisting, rocking and wagging:

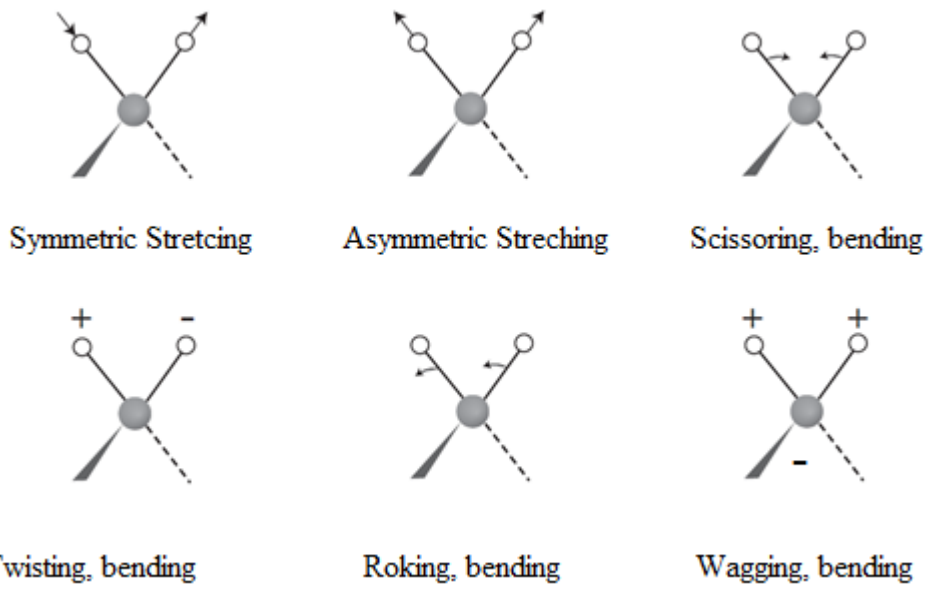

Figure 2.14 Stretching and bending vibrational modes of molecules. The (+) and (-) indicate motion out or into of the page, respectively [118].

The stretching of a bond in a molecule, caused by absorption of IR radiation, can be described by the use of a model which was suggested by Hooke and is known as Hooke's Law. In this approximation, two atoms and the connecting bond are treated as a simple harmonic oscillator composed of 2 masses (atoms) joined by a spring (see Figure 2.15):

Figure 2.15 Hooke's law models [139].

According to Hooke's law, the frequency of the vibration of the spring is related to the mass and the force constant of the spring, k, by the Equation 2.21:

$$\nu = \frac{1}{2\pi}\sqrt{\frac{k}{m}} \qquad \textbf{Equation 2.21}$$

Where k is the force constant, m is the mass and ν is the frequency of the vibration.

Some limitations apply to this theory because the bond in the molecule does not behave exactly as a spring, as it cannot be compressed beyond a certain point. Removing this limitation leads to a molecule following an anharmonic oscillating as seen in Figure 2.16.

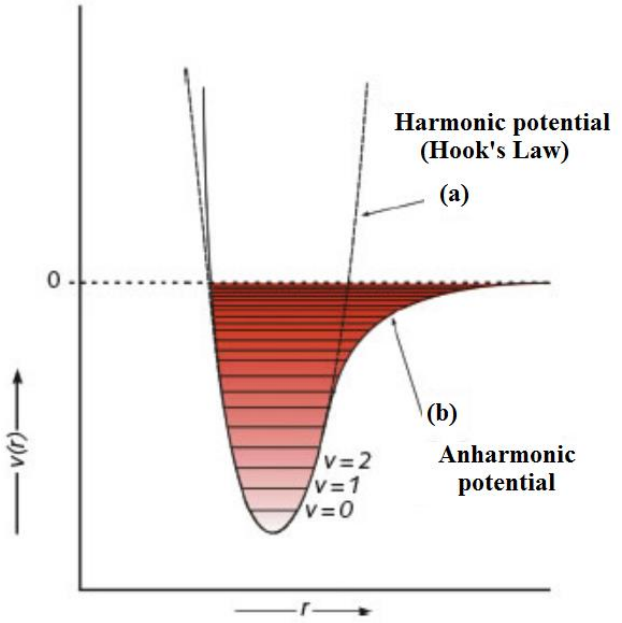

Figure 2.16 Effect of increasing energy on the bond length (r) and energy levels (v) [139].

In this case, the molecule's energy levels become more closely spaced as the interatomic distance of the atoms increase. This allows transitions to occur at smaller energy. Therefore, overtones can be different, (lower) in energy, to those obtained by the harmonic oscillator theory. The following equation has been derived from Hooke's law. For the case of a diatomic molecule:

$$\bar{\nu} = \frac{1}{2\pi c}\sqrt{\frac{f(m_1 + m_2)}{m_1 m_2}} \qquad \textbf{Equation 2.22}$$

Where $\bar{\nu}$ is the vibrational frequency (cm^{-1}), m_1 and m_2 are the mass of atoms 1 and 2, respectively, in g, c is the velocity of light (cm/s) and f is the force constant of the bond (dyne/cm).

2.5.1 Attenuated total reflectance (ATR)-FTIR spectroscopy

The combination of infrared spectroscopy with the theories of reflection has made advances in surface analysis possible. Specific IR reflectance techniques may be divided into the areas of specular reflectance, diffuse reflectance, and internal reflectance. The latter is often termed as attenuated total reflectance technique, which is today the most widely used FTIR sampling tool. ATR generally allows qualitative or quantitative analysis of samples with little or no sample preparation, which greatly speeds up sample analysis time. The main advantage of ATR sampling comes from the very thin sampling path-length and depth of penetration of the IR beam into the sample. This is in contrast to traditional FTIR sampling by transmission where the sample must be diluted with an IR transparent salt, pressed into a pellet or pressed to a thin film, prior to analysis to prevent total absorption of IR.

Attenuated total reflection operates by measuring the changes that occur in a totally internally reflected infrared beam when the beam comes into contact with a sample (see Figure 2.17). An infrared beam is directed onto an optically dense crystal with a high refractive index at a certain angle. This internal reflectance creates an evanescent wave that extends beyond the surface of the crystal into the sample held in contact with the crystal. It can be easier to think of this evanescent wave as a bubble of infrared that sits on the surface of the crystal. This evanescent wave protrudes only a few microns (0.5 - 5 μm) beyond the crystal surface and into the sample. Consequently, there must be good contact the sample and the crystal surface. In regions of the IR spectrum where the sample absorbs energy, the evanescent wave will be attenuated or altered. The attenuated energy from each evanescent wave is passed back to the IR beam, which then exits the opposite end of the crystal and is passed to the detector in the IR spectrometer. The system then generates an infrared spectrum.

Two requirements must be met for the successful analysis of samples by this technique; the sample must be in direct contact with the ATR crystal and the refractive index of the crystal must be significantly greater than that of the sample. There are a number of crystal materials available for ATR, with zinc selenide (ZnSe) and germanium being commonly used. A diamond crystal with a ZnSe lens reflection

ATR plate is a relatively low cost ATR crystal material and is therefore often ued to analyse samples.

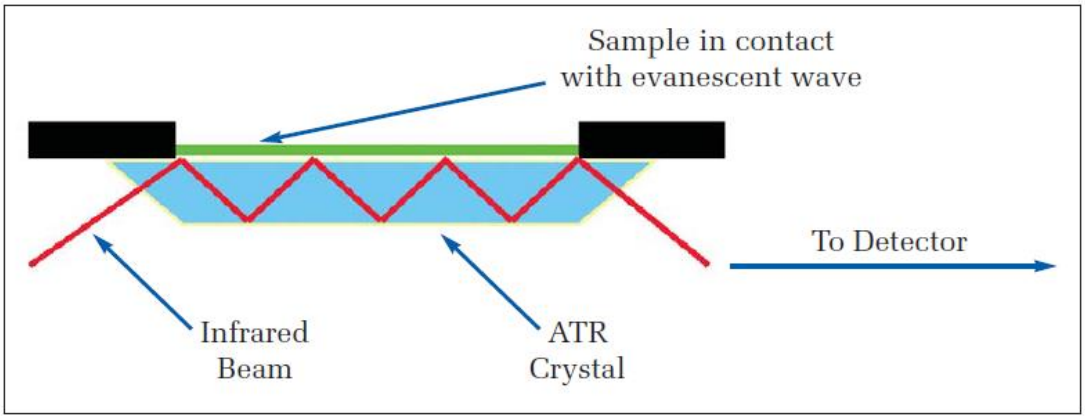

Figure 2.17 A multiple reflection ATR system.

2.6 Carbon, Hydrogen, Nitrogen,(CHN) Elemental Analysers [140]

A CHN elemental analyser is a fast technique which is used to estimate the quantities (%) of carbon, hydrogen or nitrogen in a sample (see Figure 2.18). The basic principle of the technique is based on applying very high temperature to the sample (1000 $^{\circ}$C) in a high oxygen environment causing combustion. During the combustion process, any carbon, hydrogen or nitrogen present in the sample will be converted to carbon dioxide (CO_2) water (H_2O) or nitrogen oxides (NO_x), respectively, and other by-products. Any other elements present in the sample will also be converted to their corresponding combustion products, for example chloride or sulfur will be converted to hydrogen chloride and sulfur dioxide, which are removed by scrubbing chemicals inside the combustion tube.

The combustion products are introduced into a combustion chamber (furnace) using an inert gas and they are passed over very high purity copper at a temperature of approximately 600 $^{\circ}$C in a reduction tube. The main function of the heated copper is to remove any extra oxygen gas remaining in the sample after combustion and to convert nitrogen gas into nitrogen dioxide (NO_2). All gases produced are then passed

through adsorbent traps in order to remove all gases other than CO_2, H_2O and NO_2. To determine the identities of adsorbed gases, the sorbent traps are heated and the effluent is introduced into the gas chromatography (GC) column for separation. A thermal conductivity detector can be used to detect the eluted analytes. Quantification of the elements requires calibration and is achieved using high purity 'micro-analytical standard' compounds such as acetanilide and benzoic acid.

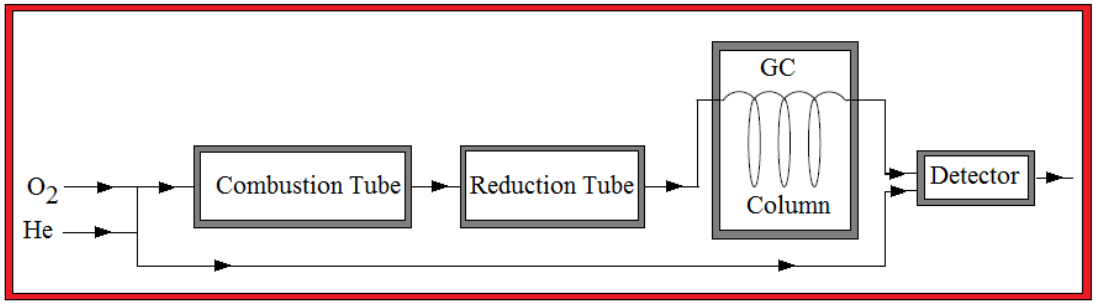

Figure 2.18 Basic instrumentation for CHN Elemental Analysers

3 Experimental and Safety

3.1 Synthesis of mesoporous adsorbent materials

3.1.1 MCM-41 preparation

MCM-41 was prepared by altering the method reported by Ritter *et al.* [141]. In this work hexadecyltrimethylammonium bromide (CTAB, Aldrich) was used as a structure directing agent. A mixture (208 cm^3 and 96 cm^3) of distilled water and aqueous ammonia (NH_3 35 %, Fisher Scientific), respectively, was warmed to 35 ^{0}C, and 8.8 g of CTAB was added under stirring to obtain a clear solution. Then 40 cm^3 of tetraethoxysilane (TEOS, 98 %, Aldrich) was gently added under continuous stirring for 3 h. The produced gel was aged in a sealed container at room temperature for 24 h. The solid product (hereafter referred to as as-synthesised MCM-41, or As-MCM-41) was obtained after filtration, washing with distilled water and drying in air at ambient temperature before being calcined at 500 ^{0}C for 5 h to remove the CTAB template. The calcined material will hereafter be referred to as C-MCM-41.

A second template extraction procedure was also used where CTAB was removed from the silica framework using a modified microwave digestion (MWD) method that has been reported by Tina *et al.* [142]. A mixture of hydrogen peroxide (H_2O_2) and nitric acid (HNO_3) was used as oxidative agents. Approximately 0.3 g of As-MCM-41 was dissolved in a mixture of 5 cm^3 of 65-68 wt. % HNO_3 (Riedel-de Haen) and 1.5 cm^3 of 30 % H_2O_2 (Sigma Aldrich, Gillingham, UK) in a pressure vessel. The microwave (Model 5, CEM Corporation, Buckingham Industrial Park, UK) was programmed at an operating power of approximately 1600 W. The temperature and pressure applied inside the microwave were controlled to be lower than 200 ^{0}C and 1.3 MPa, respectively. The working frequency and voltage of the microwave was 2450 MHz and 220 V for 15 min. The solid material produced, MWD-MCM-41, was obtained after filtration, washing with distilled water and drying in air at room temperature.

3.1.2 SBA-15 preparation

SBA-15 was produced by modifying the method reported by Zhao *et al.* [143], using non-ionic surfactants as structure-directing agents. In a typical preparation, 4 g of a surfactant tri-block copolymer, Pluronic P123, $PEO_{20}PPO_{70}PEO_{20}$ (BASF Corporation, 3000 Continental Drive), was dissolved in 60 cm^3 of distilled water and 120 cm^3 of 2 M hydrochloric acid (HCl, 37 %, Sigma Aldrich) solution in a glass bottle under stirring at room temperature. This surfactant solution was then heated to 40 ^{0}C prior to the addition of 11.3 g of tetraethylorthosilicate (TEOS, 98 %, Aldrich) and the mixture was left under stirring for 24 h at 40 ^{0}C before being placed in an oven at 60 ^{0}C for 5 days. The solid produced was filtered, washed with distilled water and dried overnight at 60 ^{0}C before it was calcined at 550 ^{0}C for 24 h. The resulting solid had a ratio of SiO_2: 0.0032 P123: 4.4 HCl: 144 H_2O.

3.1.3 Functionalisation of MCM-41 and SBA-15

Functionalisation of sorbents (MCM-41 and SBA-15) was achieved using the post synthesis grafting process (PSG) reported by Lim *et al.* [144]. 3-aminopropyltrimethoxysilane was used as a functional organic amine group as shown in Figure 3.1. Briefly, 5 g of each material, (C-MCM-41, MWD-MCM41, or SBA-15) were pre-treated at 120 ^{0}C for 2 h then immediately immersed into 50 cm^3 of toluene (Sigma-Aldrich) in a 250 cm^3 flask and 10 cm^3 of 3-aminopropyltrimethoxysilane (97 %, Fluka) was added to the mixture which was refluxed for 4 h. The product was filtered, washed with 100 cm^3 of ethanol (Sigma-Aldrich) and dried at 80 ^{0}C in an oven for 1 h. The derivatised materials will be referred to as NH_2-C-MCM-41, NH_2-MWD-MCM-41 or NH_2-SBA-15.

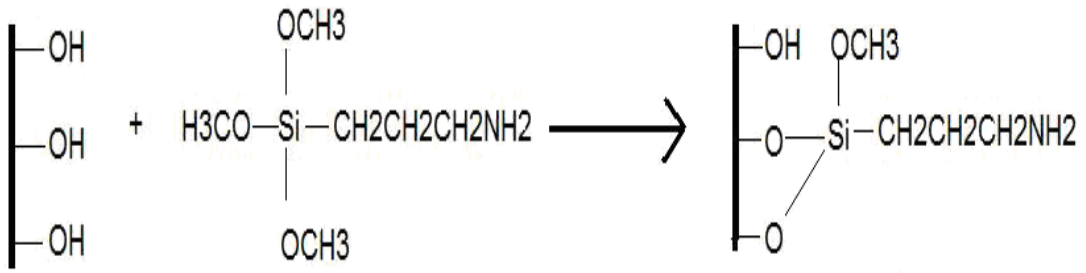

Figure 3.1 Schematic of modification of silica materials by organic amine group.

3.2 Characterisation of materials

3.2.1 Small angel scattering (SAS)-XRD

SAS-X-ray diffraction (XRD) profiles were recorded on a Philips X'Pert Diffractometer, equipped with a Cu Kα radiation source and accelerator detector. Incident and reflected Stoller slits of 0.2^0 were used with a programmable divergent slit (a constant 10 mm sample footprint). A sample block was placed directly above the centre of the sample at about 0.3 mm from the substrate plane. This reduced low angle scatter allowing more accurate low angle operation. Care was also taken to place the sample surface at the axis of rotation of the goniometer. This was achieved by placing the sample below the straight through beam and raising it until the beam of intensity was attenuated by 50%. Ideally, when the samples were rotated both clockwise and anti-clockwise, the straight through beam intensity was lowered equally. These experimental conditions were required for the low angle data to be quantified properly.

3.2.2 BET isotherm

Textural properties, such as surface area, pore size and pore size distribution, of the materials were measured by nitrogen adsorption-desorption isotherms on a Micromeritics ASAP 2420 surface area and porosity analyser. A gas adsorption sampling tube was weighed before and after addition (300 - 400 mg) of each sample to obtain the accurate weight, then the sample tube was attached to the degas port of a gas adsorption instrument and degassed prior to analysis for 6 h at 200 ^{0}C. Experimental points obtained at a relative pressure (P/P_0) of 0.05 – 0.25 were used to calculate the Brunauer–Emmett–Teller (BET) surface area. A 30-point BET surface area plot was used to calculate the average pore size distribution of the materials using the Barret–Joyner–Halenda (BJH) model and the total pore volume was calculated at P/P_0 equal to 0.99. Desorption isotherms were used to calculate the pore diameters.

The micropore measurements were performed on a Quantachrome Autosorb-1 which measures equilibrium pressure after the addition or removal of nitrogen from the

system. The measurements were made using the adsorption branch at minimum relative pressure of 10^{-5}. Using nitrogen as the adsorbate allows pores down to 7 Å to be measured. However when adsorption was found in pores smaller than this, the instrument was unable to determine the absolute diameter as the adsorption under these conditions doesn't represent completely covered surfaces due to the spatial constraints on the nitrogen molecules. The surface areas and volumes were determined using the *t*-method of Halsey for micropore volume in the presence of mesopores (see Equation 2.6 and Equation 2.7 in Section 2.1.3).

3.2.3 ATR-FTIR spectra

Infrared spectra were obtained in the 4000–400 cm^{-1} region with a resolution of 4 cm^{-1}, by accumulating 32 scans using an attenuated total reflectance (Diamond with ZnSe lens reflection ATR plate) Fourier Transform Infrared (ABB, MB3000 FTIR) spectrometer. After the crystal area was cleaned and the background collected, the powdered sample was placed onto the small diamond crystal area. The sample height was not more than a few millimetres high and just enough sample was used to cover the crystal area. Once the solid was placed on the crystal area, the pressure arm was positioned over the crystal/sample area. Force was applied pushing the sample onto the diamond surface and a software package using a 'Preview Mode' allowed the quality of the spectrum to be monitored in real-time while fine tuning the exerted force. The pressure was applied until the strongest spectral bands had an intensity which extended beyond 70 % transmittance, T, namely from a baseline at % T down to 70 % T. This was very easy to achieve with the soft samples and fine powders used here.

3.2.4 Elemental microanalysis

Elemental analysis was carried out using an Exeter Analytical CE440 elemental function to provide the functional group (carbon and nitrogen) and hydrogen content of the studied materials. The sample to be analysed was weighed accurately inside a small tin capsule, which was introduced to combustion tube (analyser's furnace). The

capsule combusts at 950 °C in a high oxygen environment, then the combustion temperature was elevated to above 1800 ^{0}C. At this temperature the sample was vaporised and completely combusted to form CO_2, H_2O, N_2, N_xO_x and others gaseous by-products. After combustion the sample gases flowed through a reduction tube which removed unused oxygen and converted oxides of nitrogen to N_2. A small portion of this mixture was allowed to flow through a series of thermal conductivity cells (detector), where the quantities of each gas CO_2, H_2O and N_2 were recorded.

3.2.5 TEM

Transmission electron microscopy (TEM) images were collected on a JEOL JEM 2100 TEM operating at 200 kV. Samples were prepared for TEM by dispersing a small quantity of the solid materials in ethanol and placing a drop of the mixture on a carbon-coated copper grid.

3.3 Generation of known concentrations of VOCs or H_2CO in environmental chambers

3.3.1 Dynamic atmospheric chambers

Dynamic atmospheric chambers [145] were used to generate constant concentrations of VOCs (toluene, ethylbenzene (EB), cumene and dichlorobenzene (DCB)), or H_2CO, in a flowing air stream that passed through a sampling chamber. The dynamic atmospheric system involved a temperature controlled oven which contained VOC or H_2CO sources, an air compressor, two air streams and a 20 dm^3 sampling chamber as shown in Figure 3.2. An air compressor (Jun Air 122-50) provided the dynamic system with two separate air streams; each stream was directed to a different Kin-Tec sampling chamber which contained a temperature controlled oven. The two Kin-Tec chambers housed an oven where the VOC or H_2CO sources were located. Both environmental chambers (one for VOC generation and one for H_2CO generation) were set up in a similar way as follows (also see Table 3.1 and

Figure 3.3 for a list of each analyte's physical properties):

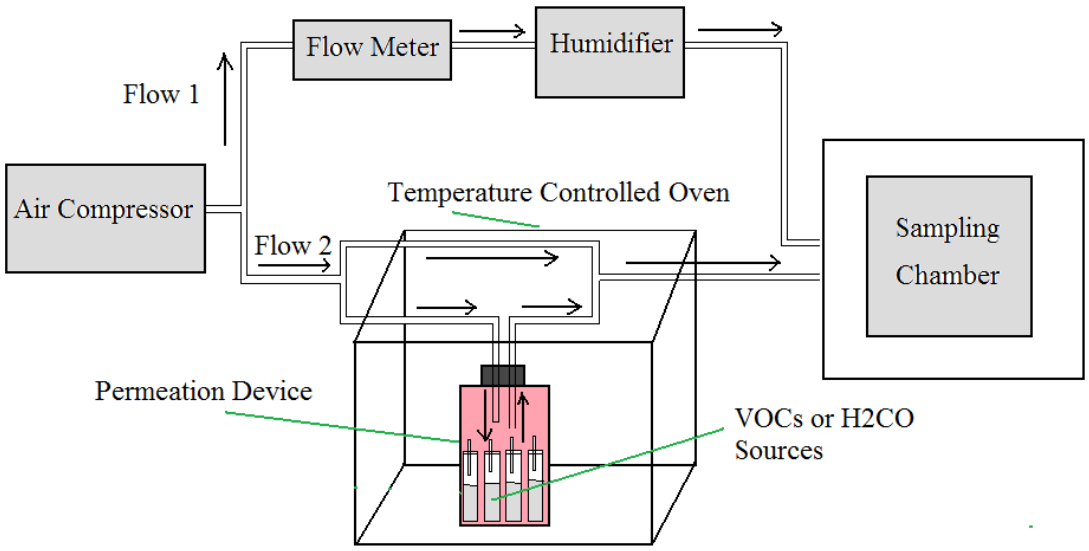

Figure 3.2 Dynamic atmospheric chamber system

Flow 1 provided the sampling chamber with humidified air at high-relative humidity (H-RH of 80 %) after passing through a humidification system. Whereas flow 2 entered directly into the temperature controlled oven (Kin-Tek Laboratories Inc. Model 491 M-B), and passed over a permeation device which contained the VOC or H_2CO sources. In the VOC set-up four GC autosampler vials (with silicon seal tops) were used to hold 1 cm^3 each of toluene, EB, cumene or DCB, as shown in Figure 3.4a. The GC vials were closed and the lids, containing a silicon septum, were pieced with a GC syringe needle (18 gauge). This produced a controlled permeation source as the vapours diffused at a constant rate from the source through the needle into the flowing stream. In the H_2CO set up a known mass of solid paraformaldehyde (powder, 95 %, Sigma-Aldrich) was used as the H_2CO source and it was held inside a permeation tube holder (see Figure 3.4b). When heated the paraformaldehyde emitted H_2CO from the permeation tube at a controlled rate.

Table 3.1 Physical properties of selected VOCs. [146, 147]

VOC	Liquid density/ g cm^{-3} at 25 ^0C	Boiling Point/ ^0C	Vapour Pressure /mm Hg at 20 ^0C	Molecular Weight	Source
Toluene (99.5%)	0.87	111	22	92.14	Fisher Scientific
EB (99 %)	0.87	136	10	106.17	Sigma-Aldrich
Cumene (99 %)	0.86	154	8	120.2	ACROS Organics
DCB (99 %)	1.3	180	1.2	147	Aldrich Chemical

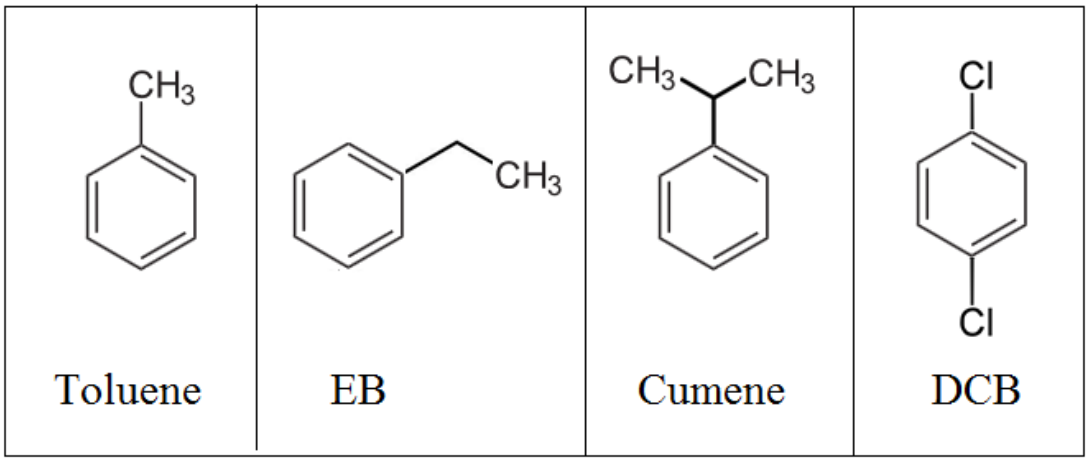

Figure 3.3 Formula structure of target VOCs in this research.

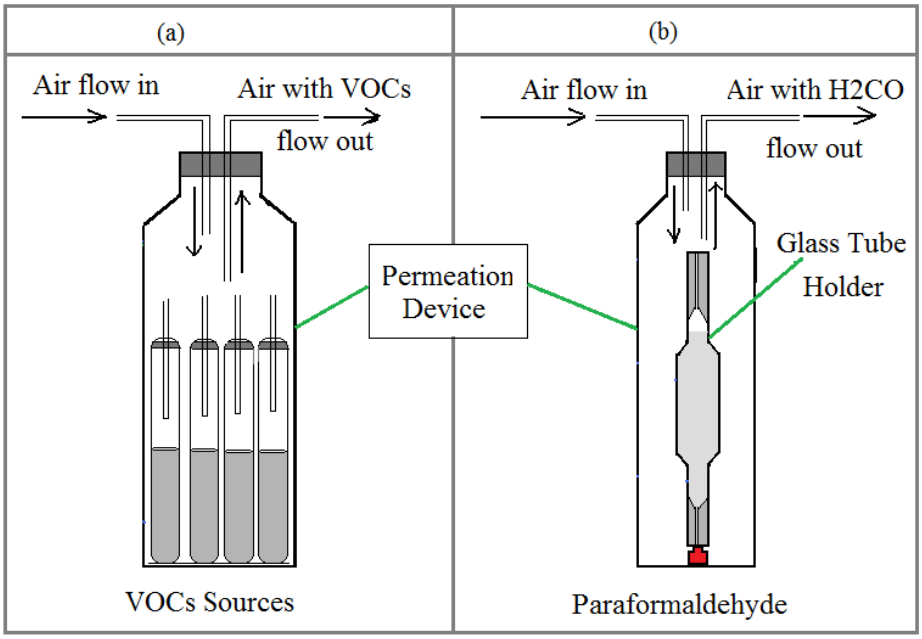

Figure 3.4 Permeation Devices a) VOCs Source and b) H_2CO source.

3.3.2 Determination of the theoretical concentration of VOCs, or H_2CO vapour, produced in environmental chambers

The theoretical concentrations of VOCs and H_2CO generated in each chamber were calculated by Equation 3.1:

$$C = \frac{K_0 E}{F}$$ **Equation 3.1**

Where C is the pollutant concentration (ppm), E is the emission rate (ng min^{-1}) and F is the flow rate of air passing through the permeation device (cm^3 min^{-1}). The pollutant emission rate depends on the temperature of oven, with increased emission at higher oven temperatures. The K_0 value is used to convert the gas unit concentration from mg cm^{-3} to parts per million (ppm or µg g^{-1}). The value of K_0 is the inverse density of the gas of interest and so depends on the temperature of the environmental chamber within which the gas will reside. In simple terms the K_0 value is the molar volume of the gas at specific temperature divided by its molecular weight. The molar volume (V) was calculated using the ideal gas equation (Equation 3.2).

$$PV = nRT$$ **Equation 3.2**

Where R is the gas constant (0.0821 L atm mol^{-1} K^{-1}), T is temperature (K), P is pressure (I atm) and n =1. The molar volume (V) was given by Equation 3.3.

$$V = \frac{nRT}{P}$$ **Equation 3.3**

The K_0 values were calculated at 25 ^{0}C by using Equation 3.4 for the VOCs and H_2CO.

$$K_0 = \frac{24.46(L)}{MW(g)}$$ **Equation 3.4**

Thus, K_0 values were calculated for toluene, EB, cumene, DCB and H_2CO as 0.265, 0.230, 0.204, 0.166 or 0.815 L g^{-1}, respectively.

3.3.3 Preparation of sorbent packed tubes

The studied sorbents were packed into sampling tubes. Two types of sampling tubes (3.5 inches in length and 5 mm internal diameter) were used: stainless steel for VOC collection or glass tubes for H_2CO collection. The sorbent materials were first pressed into a disc (using a KBr press), crushed and sieved to 60 - 80 mesh prior to use. As the prepared sorbents were fine powders, when placed directly into a sorbent tube it was difficult to pass air through the tube at 100 cm^3 min^{-1}. Therefore to reduce the back pressure the powdered sorbent (100 mg) was mixed with 1500 mg of glass beads (750 – 1000 μm), held between two plugs of glass wool (see Figure 3.5). After it was packed one end of the sorbent tube was connected to a nitrogen cylinder via a mass flow controller. Nitrogen gas was flushed through the sorbent tube at a flow rate of 100 cm^3 min^{-1} for 5 min. Finally, the prepared VOC sorbent tubes were conditioned using a thermal desorption unit (TDU) at 320 °C for 15 min. Glass tubes could not be conditioned by the TDU because of the pressures used to hold the tube during the leak test; therefore sorbents were conditioned before they were loaded into the glass tubes.

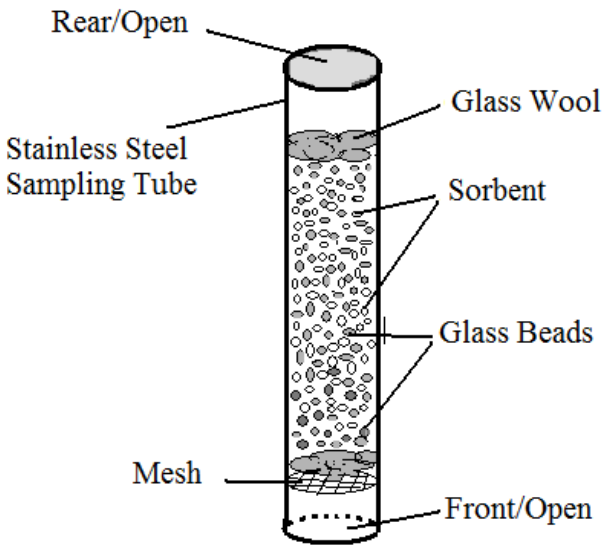

Figure 3.5 Packed sorbent and glass beads into sampling tube

3.4 VOC pollutant concentrations generated and determination of trapped VOC concentrations.

Determination of VOC concentrations generated in the environmental chamber was achieved by connecting a commercially available sampling tube containing Tenax TA to a sampling port in the chamber. The sampling tubes were conditioned using a thermal desorption unit (TDU) at 320 °C for 15 min prior to use. A known volume of air (cm^3) was passed over the tube by controlling the air flow rate (cm^3 min^{-1}), using an SKC sidekick pump, for a set period of time of (min). A schematic diagram of the VOC collection set up is given in

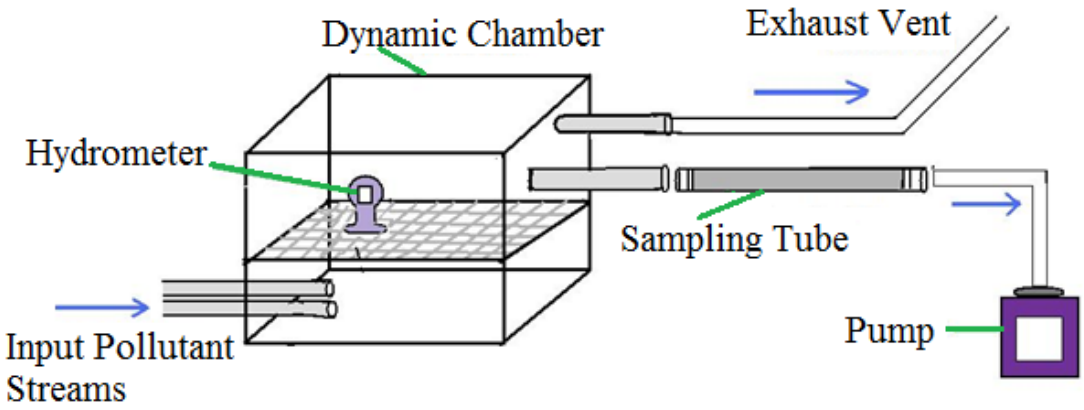

Figure 3.6. The masses (ng) of pollutants trapped by the Tenax TA sampling tube were determined by TD-GC-MS (see section 3.4.1) allowing the VOC concentrations (mg cm^{-3}) to be determined by dividing the mass collected by the volume of air sampled.

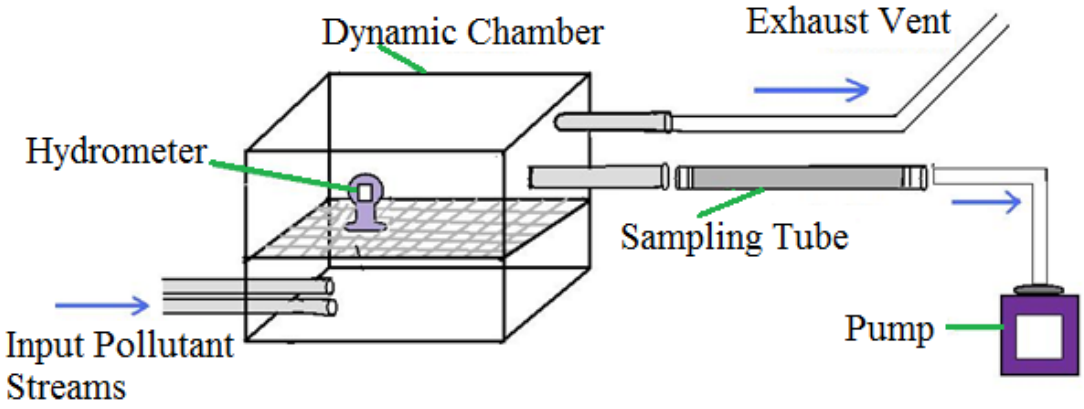

Figure 3.6 Sampling set up to collect VOCs from sampling chamber

The flow rate of air that passed over the VOC sources was 200 cm^3 min^{-1} and the oven temperature was set to 25 ^{0}C giving emission rates of 13643, 7221, 4939 or 3130 ng min^{-1} and values of K_0 were calculated as 0.265, 0.230, 0.204 or 0.166 of toluene, EB, cumene or DCB, giving theoretical VOC concentrations (see Equation 3.1) of 34.05, 18.02, 12.38 or 7.81 mg m^{-3}, respectively. Since the flow rate of polluted air coming out the sampling chamber was 100 cm^3 min^{-1} for 1 min, the expected masses of analytes trapped by the sampling tube were 3405, 1802, 1238 or 781 ng.

3.4.1 Analysis of VOC sampling tubes using TDU-GC-MS

A thermal desorption unit (TDU), gas chromatograph (GC) and mass spectrometer (MS) were used as to quantitatively analyse the VOCs trapped in sampling tubes. The TDU, a Perkin Elmer Turbo Matrix TD, was coupled to a Perkin Elmer GC and Turbo Mass Gold MS. The TDU operating conditions used to thermally desorb the

VOCs from sampling tube are given in Table 3.2 and the GC conditions, and column, used to separate the analytes are given in Table 3.3. Finally the MS operating conditions are outlined in Table 3.4.

Table 3.2 Operating conditions of the TDU for the desorption of VOCs

Desorb flow	19 cm^3 min^{-1}
Desorb temperature	300 ^0C
Cold trap sorbent	Tenax TA
Cold trap temperature	Held at -30 ^0C, Ramped at 99 ^0C s^{-1} to 300 ^0C, Held at
Split ratio	1 %

Table 3.3 Operating conditions of the GC for the separation of analytes

Inlet Line temperature	180 ^0C
Oven Temperature	65 ^oC
Heating Rate	65 ^0C for 5 min, Ramped to 90 ^0C for 8 ^0C min^{-1} held 90 ^0C for 1.87 min
Column	Perkin Elmer, SMS Elite, (dimethylpolysilicane (5% diphenyl)) 30 m 0.25 mm i.d.
Carrier Gas	Helium
Carrier Gas Flow	1 cm^3 min^{-1}

Table 3.4 Operating conditions of the MS for the detection of analytes

Electron Energy	Trap Emission	Multiplier	Scan Run Time	Scan Time	Inter Scan Delay	m/z range (amu)	Solvent Delay
70 eV	70 eV	350 V	10 min	0.2 s	0.1 s	50-300	min

3.4.2 Preparation of standard solutions of VOCs and calibration of TDU-GC-MS

Standard solutions containing each VOC were used to calibrate the TDU-GC-MS for the quantitative analysis of analytes. A stock solution (60 ng μL^{-1}) was prepared by dissolving known amounts of toluene, EB, cumene or DCB in methanol (99 %, Fluka) to 100 cm^3 using a volumetric flask. Prior to desorption, each conditioned Tenax sampling tube was loaded with increasing volumes of the methanolic standard solution together when an internal standard (o-xylene: 5 μL of 60 ng μL^{-1}), therefore 6 mg of each analyte and internal standard was added to a 100 cm^3 flask to prepare the stock solution. To covert the analyte mass to volume, the liquid density for each VOC was used and the volumes added to prepare the stock solution are given in Table 3.5.

Table 3.5 The required volume of VOC to prepare standard solutions

Compound	Density g cm^{-3}	Required volume μL
Toluene	0.87	6.9
EB	0.87	6.9
Cumene	0.86	7
DCB	1.3	4.6
o-xylene	0.879	6.8

The direct-injection method modified by Idris *et al.* [145] was used to calibrate the instrument. This involved the use of a Perkin Elmer GC 8000 injection port, which was modified as shown in Figure 3.7 to facilitate efficient liquid sample introduction onto sampling tubes. An adaption union was used to connect the tube directly to the injection port of the GC. The injected analytes were transferred onto tubes using helium as a carrier gas. After injection of the standard solution, helium gas was passed over the sampling tube for 2 min at a flow rate of approximately 100 cm^3 min^{-1}. To obtain analyte standard curves 1, 3, 5, 7 or 9 µL of the stock solution was injected into a series of conditioned sampling tubes together with 5 µL of the internal standard. Calibrant tubes were analysed using the TDU-GC-MS conditions outlined above. The internal standard curves for each analyte were prepared using the peak area ratio of analyte: internal standard.

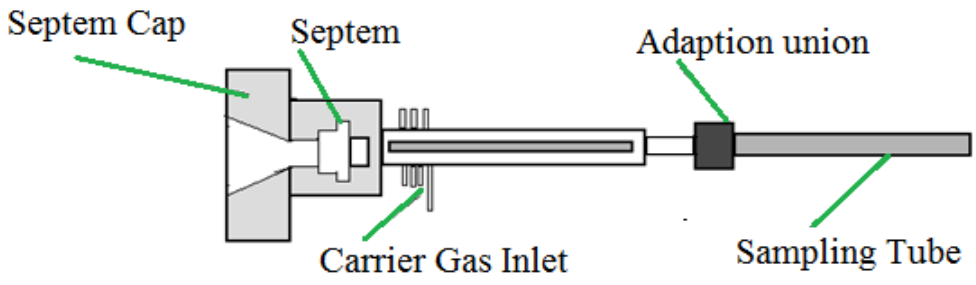

Figure 3.7 Schematic of the modified Perkin Elmer GC 8000 injection port

3.5 H_2CO vapour concentration generated in the environmental chamber, analysis and calibration.

To generate a high concentration of H_2CO vapour the rate of air passing over the H_2CO permeation device was 200 cm^3 min^{-1} and the temperature of oven was set to 80 °C; providing an emission rate of 6845 ng min^{-1}. Using a K_0 value of 0.815 L g^{-1} gave a theoretical concentration of 14.5 mg m^{-3}. To generate H_2CO vapour at lower concentration the temperature of the oven was reduced to 50 °C; all other operating

parameters remained unchanged. At this lower temperature the emission rate of H_2CO reduced to 541 ng min^{-1} giving a theoretical H_2CO conc of 1.4 mg m^{-3}.

3.5.1 Colorimetric method used to determine H_2CO vapour concentration in air

H_2CO vapours exiting the chamber were pulled, using an SKC sidekick pump, through an impinger containing 10 cm^3 of distilled water and 2 cm^3 of Schiff's reagent (see Figure 3.8). Schiff's reagent was prepared as reported by Miksch *et al.* [61] and consisted of a mixture of pararosaniline in hydrochloric acid with sodium sulfite solution. The stock solution of 0.2 mM pararosaniline was prepared by dissolving 0.06 g of pararosaniline ($C_{19}H_{17}N_3$, Sigma-Aldrich) in 0.63 M hydrochloric acid (HCl, 37 %, Sigma-Aldrich) in a 1 L volumetric flask which was made up to 1 L with distilled water. The sodium sulfite solution (0.4 M) was prepared daily by dissolving 2.5 g of sodium sulfite (Na_2SO_3, Fisons) in distilled water in a 50 cm^3 volumetric flask, then it was made up to the market with distilled water.

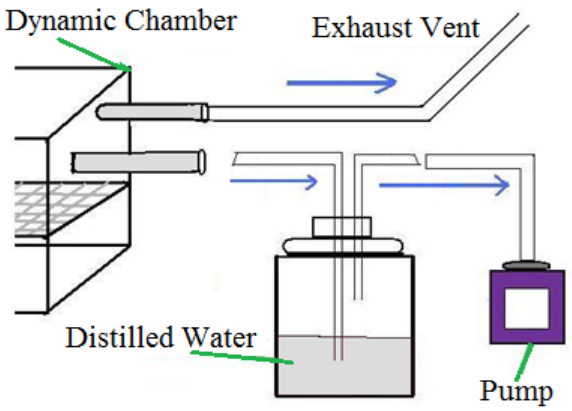

Figure 3.8 Sampling set up to collect high concentrations of H_2CO using an impinger with Schiff's reagent.

Pararosaniline was combined with dilute HCl to immediately produce a colourless solution as illustrated in Figure 3.9. Previous studies [61, 148] proposed that protonation of the pararosaniline (A) resulted in the cationic species represented by

the canonical forms for the resonance structure (D). In contrast to the previous theories where chloride was suspected as the nucleophile in the reduction, Gibson *et al.* [48] reported that water acts at the central carbon atom, and in turn, loss of a proton delivers the hydrated species (E) which is a colourless intermediate, and is stable in air at room temperature for several months.

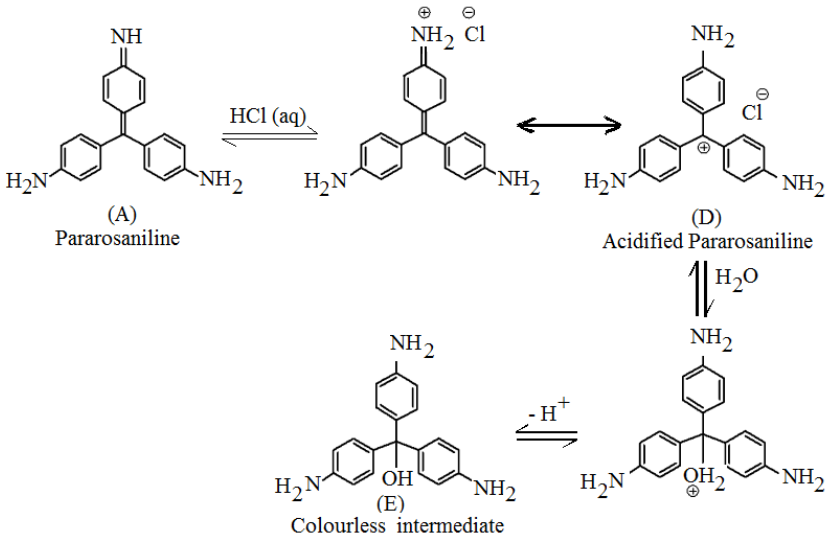

Figure 3.9 Disruption of pararosaniline chromophore due to nucleophilic attack by water in acidic conditions[48]

To prepare Schiff's reagent 1 cm^3 of each solution (pararosaniline and sodium sulfite) was added to 10 cm^3 of distilled water. When formaldehyde containing air passed through the reagent the colourless intermediate reacted with the analyte to produce the sulfonic acid product shown in Figure 3.10.

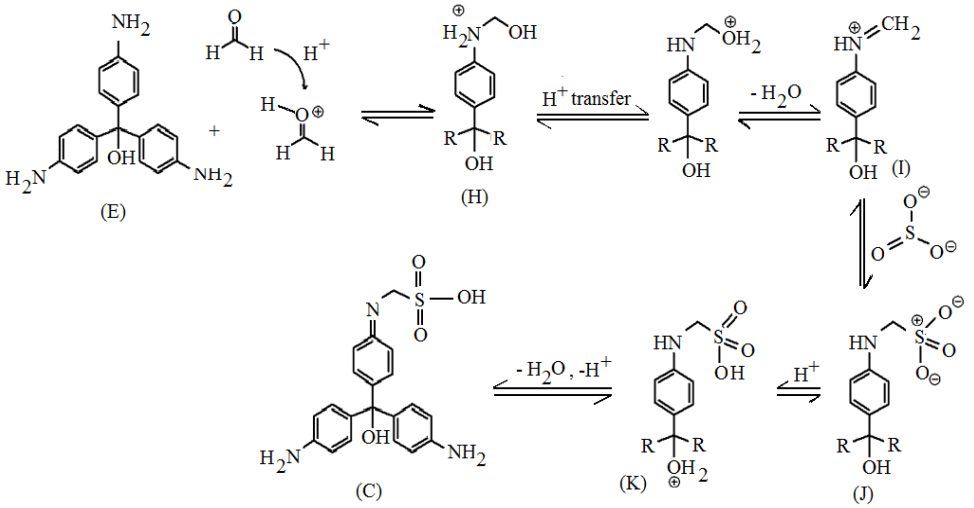

Figure 3.10 The reaction mechanism between the hydroxyl-intermediate with formaldehyde and sulfite[48]

The final solution was stored at room temperature for 1 h before the absorbance was measured by UV-vis spectrometry using an UV-visible (UV-vis) spectrophotometer (S. I. Photonics Inc, Tucson, Arizona USA, Model 420) over 400 – 700 nm. The sample solution and blank solution (water plus Schiff's reagent) were placed in 10 mm cells and analysed using UV-vis spectroscopy (operating parameters are given in Table 3.6) The tungsten source used in the instrument was a 10 watt quartz- halogen lamp with approximately 3100 ^{0}K, and the deuterium source was a high-intensity, lamp.

Table 3.6 Specification for UV-VIS spectrophotometer (S. I. Photonics, Inc Model 420)

Specification	Instrument Details
Wavelength range	200 – 980 nm
Lamps	Deuterium lamp; Halogen lamp
Spectral Bandwidth	1.2 nm
Wavelength range Accuracy	1.2 nm

Photometric range	0.002 – 3.00 Au
Photometric Accuracy	0.005 Au
Baseline stability (at 300 nm and 600 nm)	< 0.005 Au/hour
Stray light	< 0.02 %

Formaldehyde standard solutions were prepared by dilution of 2.5 mM H_2CO stock solution which was prepared by dissolving 37.2 µL of formalin (H_2CO solution, 37 wt. % in H_2O, contains 10 -15 % methanol, Sigma- Aldrich) in distilled water in a 200 cm^3 volumetric flask, then the solution was made up to mark by distilled water. To convert the concentration (mM) of the stock solution to ppm (mg L^{-1}), the required weight (mg) of formalin used to prepare the stock solution was calculated by Equation 3.5.

$$mM = \frac{wt\ (mg)}{MW \times V_L}$$ **Equation 3.5**

Where MW is molecular weight of H_2CO and V is the volume of solution (L).

Wt (mg) = 2.5 x 30.03 x 0.200 L

= 15 mg

15 mg in 200 cm^3 ≡ 75 mg L^{-1} (75 ppm)

The concentration of formalin was 37 wt. %, the net required weight was:

Wt (mg) = 15 x 100/37

= 40.5 mg

To convert the weight (mg) to required volume (V) of formalin, the density of formalin (d, 1.09 g cm^{-3}) was used

d = 1.09 g cm^{-3} ≡ 1090 mg cm^{-3}

$$V = \frac{40.5\ mg}{1090\ mg\ cm^{-3}} = 0.0372\ cm^3$$

0.0372 $cm^3 \equiv$ 37.2 μL

Thus, 37.2 μL of formalin was dissolved in 200 cm^3 to obtain the stock solution (75 ppm). The standard solutions of H_2CO were prepared by diluting 10, 20, 30, 40 cm^3 of the stock solution to 50 cm^3 for each by distilled water in four 50 cm^3 volumetric flasks to obtain calibrant solutions with concentrations of 15, 30, 45 and 60 ppm, respectively. 10 cm^3 of each calibrant was placed into a small glass bottle, then 1 cm^3 of pararosaniline and sodium sulfite solutions were added. When sampling air from the environmental chamber, 10 cm^3 of distilled water was used to collect the H_2CO vapour. Then 1 cm^3 of each pararosaniline solution and sodium sulfite were added to H_2CO solution. All solutions were kept at least one h before being analysed by UV-vis spectroscopy to ensure the reaction was completed and the obtained coloured solutions were at their maximum intensities. Calibration curves of absorbance versus concentration were used to determine the concentration of H_2CO trapped by the impinger in sampling experiments. The mass (μg) of H_2CO collected was divided by the volume (cm^{-3}) of air sampled to obtain the formaldehyde concentration in the flowing stream (μg cm^{-3}).

3.5.2 Chromatographic method of analysis used to determine low H_2CO vapour concentrations in air

Vapours exiting the chamber were pulled through Sep-Pak Plus C18 cartridges (Waters) impregnated with a 0.8 cm^3 trapping solution of 10 mM 2, 4-dinitrophenyl hydrazine (DNPH) using an SKC sidekick pump calibrated to 100 cm^3 min^{-1} for a 60 min collection period (see Figure 3.11). The trapping solution was prepared by dissolving approximately 100 mg of doubly recrystallised 2,4-DNPH (Aldrich, 97%) in a solution that contained 49.5 cm^3 of acetonitrile (Rathburn) and 0.5 cm^3 of orthophosphoric acid (BDH Laboratory supplier, 85%). The solution was slightly heated (approximately 40 °C) to promote dissolution of 2, 4-DNPH. F vapours were derivatised and collected as F-DNPH.

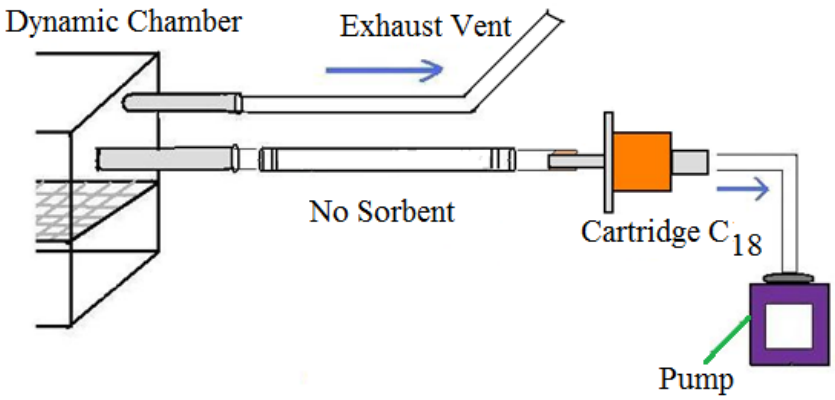

Figure 3.11 Sampling set up to collect H_2CO onto DNPH-modified Sep-Pak cartridges

To calibrate the method a stock solution of F-DNPH (200 µg cm^{-3}) was prepared by dissolving 10 mg of F-DNPH (Supelco, 99.95 %) in 50 cm^3 acetonitrile. Standard solutions of F-DNPH were prepared by dilution of the stock solution in acetonitrile at different concentrations to obtain 6 sets of calibrant solutions (2, 4, 8, 12, 16 or 20 µg cm^{-3}). After sampling, trapped F-DNPH was eluted from the cartridge using 3 cm^3 of acetonitrile (Fisher Chemical). The extracted derivative was filtered (anotop IC 20 µm filters, Whatman) prior to determination of F-DNPH by liquid chromatography (LC) coupled to a direct wavelength uv detector using the operating conditions listed in Table 3.7.

Table 3.7 Operating conditions of the LC-UV-vis detector

Parameter	Condition
Column	C_{18} ODS column 150 x 4.6 mm
Eluent	70: 30 Water: Acetonitrile
Flow rate	1.5 mL min^{-1}
Pressure	≈ 1500 PSI
Temperature	Ambient

Detector Wavelength	360 nm
Detector Range	0.2 nm

Measured F-DNPH concentrations (µg cm^{-3}) were multiplied by the volume (cm^3) of acetonitrile used to extract F-DNPH to determine the trapped F-DNPH mass (µg). This mass was divided by molecular weight of F-DNPH (210.15) to give the number of micromoles which were collected and since there is an equimolar reaction between F and DNPH (see Figure 3.12) this was taken to represent the number of F micromoles trapped by the reagent. The trapped mass was then calculated by multiplication by the MW of formaldehyde (30.03).

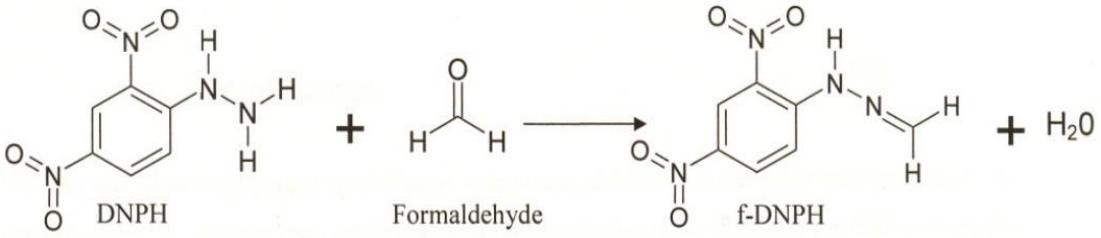

Figure 3.12 Scheme of reaction between DNPH and H_2CO to produce F-DNPH

3.6 Calculations used to assess the performance of sorbents for extraction of selected VOCs or H_2CO.

To examine the extraction efficiency of each sorbent for removal of target pollutants from the flowing stream a tube loaded with sorbent material was positioned as illustrated in Figure 3.13. An example is given for the collection of F vapours at low concentration however a similar set up was used for VOCs and F vapour at high concentration by replacing the SKC cartridge with a Tenax TA sampling tube or the Schiff's reagent impinger. In the VOC experiment a flow rate of 100 cm^3 min^{-1} was used for 1 min, whereas F vapours were collected for 60 min. Chambers were equilibrated and the air was sampled in replicate using Tenax TA sampling tubes, the

pararosanaline impinge or the 2,4-DNPH loaded Sep-Pak cartridge. Pollutant masses (denoted $mass_{nosorb}$) were determined as given above. Then sorbent loaded tubes were placed directly before the sampling device and the experiments were repeated using the same experimental conditions. Pollutant masses that passed through the sorbents and were collected by the sampling device were denoted $mass_{sorb}$. The efficiencies of each sorbent to extract the target pollutants were then calculated using Equation 3.6.

$$\text{Extraction Efficiency} = \frac{Wt_{sorb}}{Wt_{nosorb}} \times 100$$

Equation 3.6

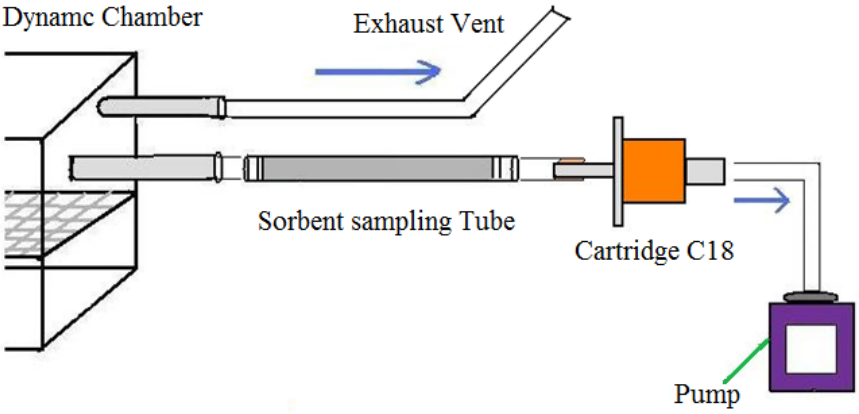

Figure 3.13 Sampling set up to collect H_2CO by Cartridge C_{18} with sorbent tube in-line

The breakthrough volume (BTV) was also used to determine the efficacy of synthesised sorbents, where breakthrough is defined as the point at which 5 % of the analyte in the flowing stream is measured by the sampling device. The first experiment undertaken was to sample an atmosphere containing the theoretical generated concentrations (34.1, 18, 12.4, or 7.8 mg m^{-3}) of toluene, EB, cumene and

DCB, respectively, at 100 cm^3 min^{-1} for 1 min. The masses (M_1) for each VOCs trapped by different sorbents in tube 1 were then measured for the 100 cm^3 aliquot.

Different sampling times were used to introduce higher analyte masses onto each sorbent. To determine breakthrough, the analytes trapped by the sampling tube were measured (M2) and the percentages of analytes that had broken through the sorbent calculated as given in Equation 3.7, where M_E is the pollutant mass that passed over the sorbent tube.

$$VOCs\ or\ H2CO\ BT\ \% = \frac{M_2}{M_E} \times 100 \qquad \textbf{Equation 3.7}$$

Breakthrough was reported when the % age of VOCs or H_2CO measured in sampling tubes exceeded 5 % of the total mass passing over the sorbent.

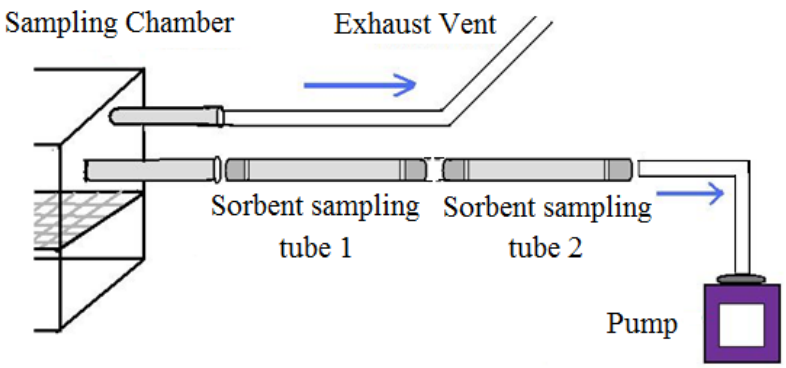

Figure 3.14 Schematic of breakthrough set up

3.7 Safety

All chemical substances used in this work were performed in a safe and controlled manner, according to the experimental risk assessments. The substances, and their hazards associated, used in the experimental methods are listed in Table 3.8. Due to their hazardous chemical properties, a laboratory coat and safety glasses were worn at all times and the substances were handled with gloves in a fume cupboard and stored in appropriate vented locations.

Table 3.8 Hazardous substance associated with experimental methods

Substance	Toxic	Carcinogenic	Mutagenic	Harmful	Flammable	Corrosive	Irritant
Toluene				√	√		
Ethylbenzene				√	√		
Cumene							√
Dichlorobenzene				√			
o-Xylene	√				√		
Tetraethylorthosilicate (TEOS)				√	√		√
Tetramethylammonium Hydroxide (TMAOH)	√			√		√	
Cetyltrimethylammonium bromide (CTAB)	√						√
Hydrochloric Acid						√	√
Ethanol					√		
Methanol	√				√		
Formaldehyde	√			√	√		√
Pararosaniline				√			√
Sodium Sulfite							√
Nitric Acid				√		√	
Hydrogen Peroxide				√		√	
Formalin	√				√		√

Paraformaldehyde		√		√			√
Sodium metasilicate				√		√	
Pentaethylenehexamine						√	
Tetraethylenepentamine						√	
Titanium (IV) isoprpoxide					√		
Poly(ethylene glycol)-block poly(propylene glycol)-block poly(ethylene glycol) (P123)	√						

4 Validation of methods used to determine VOCs or H_2CO

4.1 Calculation of theoretical concentrations of VOCs generated inside dynamic sampling chamber

The theoretical concentrations C (mg m^{-3}) of VOCs were calculated using Equation 3.1 (given in section 3.3.2) which depended on the air flow (F) rate, cm^3 min^{-1}, that passed over the permeation sources, the pollutant emission (E) rate, ng min^{-1}, and the value K_0 which is a constant for each VOC under study.

4.1.1 Calculation of VOCs emission rates released in permeation device

The pollution emission rates of individual permeation sources containing a 1 cm^3 aliquot of each VOC sources were calculated. The permeation vials were weighed before being placed inside the permeation device in the temperature controlled oven which was set to 25 °C and the air flow rate passing over permeation device was set to 200 cm^3 min^{-1}. The air continued to pass over the heated permeation sources for known periods of time. Each permeation source was then removed from the oven, cooled to room temperature and weighed before being replaced back into the oven. The emission rates (ng min^{-1}) of the in-house prepared permeation devices were determined by dividing the masses (ng) of analyte lost from the permeation source over time (min) as shown in Equation 4.1.

$$E = \frac{mass\ loss\ (ng)}{time\ (\text{min})} \qquad \textbf{Equation 4.1}$$

The emission rates for toluene, ethylbenzene (EB), cumene and dichlorobenzene (DCB) were determined by Idris [149] using the same permeation device, oven, and permeation source (vials containing 1 cm^3 of each VOC standard), under the same conditions (flow rate of air passed over the sources 200 cm^3 min^{-1}at 25 °C). Weight losses were measured weekly for 6 weeks and the resulting average weight losses (ng min^{-1}) are given in Table 4.1.

Table 4.1 The average of VOCs emission rates ng min^{-1}[149]

VOCs	Toluene	EB	Cumene	DCB
Average of weight loss (g/week)	0.1375	0.0728	0.0498	0.0316
Error of weight Loss (g/week)	0.004	0.0041	0.0028	0..0049
Average of weight loss (ng/min)	13643	7221	4939	3130

4.1.2 Calculation of theoretical concentrations of VOCs

The theoretical concentrations ppm (µg g^{-1}) of VOCs generated in the atmospheric chamber system were calculated using Equation 3.1 (given in section 3.3.2), and the average emission rates (E) of each VOC given in Table 4.1. The flow rates (F) of air passed over the sources of VOCs (200 cm^3 min^{-1}) was combined with humidified air which was also set at flow rate of 200 cm^3 min^{-1}. Therefore the final concentrations calculated by divided concentrations of VOCs in the air stream by a factor of 2 (see Table 4.2)

Table 4.2 The theoretical concentrations of VOCs generated in sampling chamber

VOCs	Emission ng min^{-1}	K_0 L g^{-1}	Flow rate cm^3 min^{-1}	Conc. in air stream/ µg g^{-1}	Conc. in sampling chamber/ µg g^{-1}
Toluene	13643	0.265	200	18.077	9.038
EB	7221	0.230	200	8.304	4.152
Cumene	4939	0.204	200	5.038	2.519
DCB	3130	0.166	200	2.598	1.299

The concentration of each VOC in sampling chamber ppmw (µg g^{-1}) was converted to ppmv (µg L^{-1}) which is equivalent to mg m^{-3} by using their calculated densities

(see Table 4.3). The density of pollutant was calculated by using Equation 4.2 which was obtained from the ideal gas equation (see Equation 3.2 given in Section 3.3.2).

$$D = \frac{PMW}{RT}$$ **Equation 4.2**

Where D is the density of gas (g L^{-1}), P is the pressure (1 atm), MW is the molecular weight, R is the gas constant (0.0821 L atm mol^{-1} K^{-1} and T is the temperature (K).

Table 4.3 Theoretical concentrations of VOCs generated in sampling chamber

VOCs	Concentration in sampling chamber/ µg g^{-1}	Gaseous density g L^{-1}	Concentration in sampling chamber / mg m^{-3}
Toluene	9.038	3.767	34
EB	4.152	4.340	18
Cumene	2.519	4.914	12
DCB	1.299	6.010	7.8

4.2 Analysis of VOCs using TDU-GC-MS

4.2.1 Calibration of TDU-GC-MS using internal standard curves

The TDU-GC-MS was calibrated for a quantitative analysis of toluene, EB, cumene and DCB using the standard solutions prepared as described in section 3.4.2 which were injected onto sampling tubes using the direct-injection method discussed in section 3.4.2. Tenax TA was used as a reference sorbent to calibrate the instrument, and to validate the sampling method used to extract VOCs in air.

Different volumes (1, 3, 5, 7 or 9 µL) of the standard solution (60 ng μL^{-1}) were injected into 5 sets of conditioned calibrant sampling tubes (Tenax TA), and followed by injection of 5 µL of the o-xylene internal standard (at 60 ng μL^{-1}). Then the calibrant tubes were analysed by TDU-GC-MS and the peak areas obtained for each analyte were plotted against weight (ng) of VOC injected into the calibrant tubes to obtain the regression data shown in Figure 4.1.

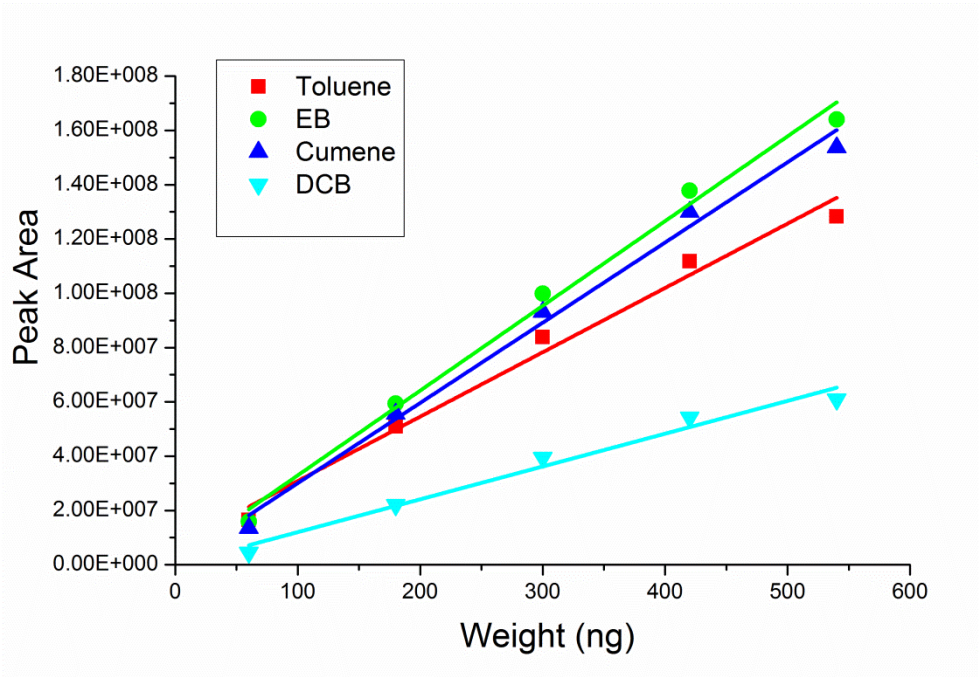

Figure 4.1 Standard curves of VOCs obtained by using peak area

Linear regression analysis was performed and the results obtained are summarised in Table 4.4. Since the accepted criteria of correlation coefficient was 0.9900, the correlation coefficients (0.9700 - 0.9898) produced were below that criteria. The confidence interval of intercept for all VOCs had not included zero, therefore the data were thought to be non-linear.

Table 4.4 Statistical evaluation of linearity of different concentrations of VOCs

VOCs	Slope	Intercept	Correlation Coefficient	Standard Error on Slope	Standard Error on Intercept
Toluene	237077	7160440	0.9791	17292	5960150
EB	312306	1695260	0.9898	15807	5448380
Cumene	295674	470409	0.9884	16015	5519850
DCB	120898	-61305	0.9700	10594	3651320

An internal standard method of calibration was then used to improve the calibration of the instrument by enhancing the linearity. The peak areas of each analyte mass obtained from the resultant SIR chromatograms were divided by the peak area of the

internal standard. Using a 5 µL injection volume, a constant mass of 300 ng of internal standard was injected onto each calibrant tube, whereas the masses of injected analytes increased from 60 to 540 ng. The EI chromatograms obtained for the calibrant tubes are given in Figure 4.2.

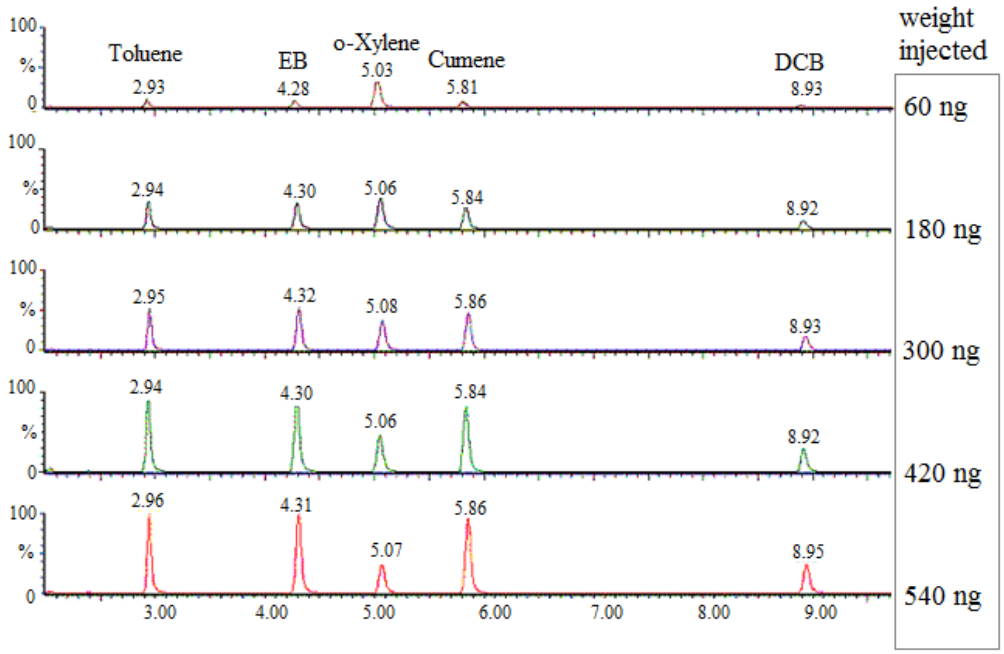

Figure 4.2 EI chromatograms for VOCs standard solutions and internal standard injected onto Tenax TA

The internal standard curve for VOCs was obtained for calibrant tubes loaded with Tenax TA as shown in Figure 4.3. Linear regression analyses and the correlation coefficients for the analytes were shown to improve by use of the internal standard calibration method (see Table 4.5). The correlation coefficients for all analytes were in the accepted criteria of > 0.9900, and all analytes had a confidence interval of the intercept which included zero. All sampling tubes were subsequently spiked with the internal standard prior to analysis.

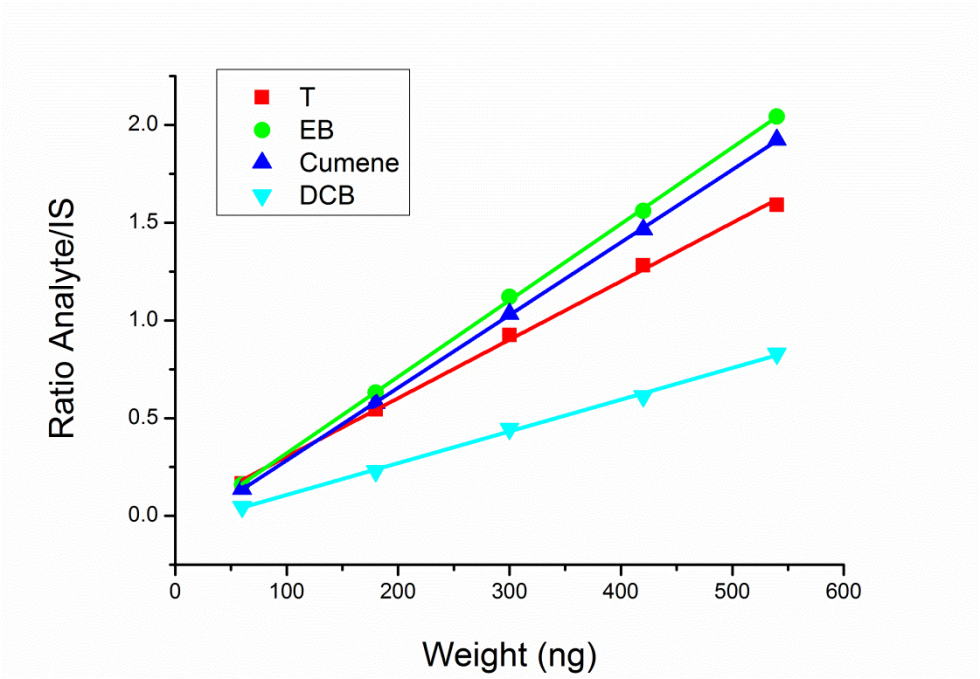

Figure 4.3 Standard curves of VOCs obtained by using analyte/ internal standard peak area ratio

Table 4.5 Statistical evaluation of linearity of different concentrations of VOCs injected onto Tenax TA .

VOCs	Slope	Intercept	Correlation Coefficient	Standard Error on Slope	Standard Error on Intercept
Toluene	0.0030	0.0042	0.9992	0.00007	0.0243
EB	0.0039	- 0.0705	0.9999	0.00003	0.0114
Cumene	0.0037	- 0.0880	0.9999	0.00002	0.0065
DCB	0.0016	- 0.05490	0.9993	0.00004	0.0121

4.2.2 Use of different sorbents for calibration tubes

Samples of MCM-41 were prepared using the method described in section 3.1.1 and for comparison the surfactant was removed from the silica framework by calcination or by microwave producing C-MCM-41 or MWD-MCM-41, respectively. Samples of SBA-15 were prepared as described in section 3.2.1.

Different sampling tubes containing 100 mg of each sorbent (C-MCM-41, MWD-MCM-41 or SBA-15) were prepared and loaded into commercially available stainless steel sampling tubes as described in section 3.3.3. Different volumes (2, 4, 6, 8 or 10 µL) of the standard solution containing (60 µg mL^{-1}) of toluene, EB, cumene and DCB were injected into the conditioned sorbent loaded tubes, together with a known volume (5 µL) of internal standard (60 µg mL^{-1}). The sorbent tubes loaded with VOC solutions were then analysed by TDU-GC-MS using the operating conditions outlined in section 3.4.1. The results obtained allowed regression curves to be calculated for each sorbent (see Figure 4.4 for SBA-15, Figure 4.5 for C-MCM-41 or Figure 4.6 for MWD-MCM-41).

The results indicated that the correlations between VOC masses and peak area ratios were linearly related for all three sorbent tubes. The regression data (summarised in Table 4.6) demonstrated that the intercept value for most of analytes had confidence intervals that included zero. However, values of correlation coefficients for most of the analytes were below the accepted criteria of < 0.9900 for all sorbents. More importantly, it was observed that the analytes had different adsorbing behaviours on the different adsorbent tubes. For example, toluene had a correlation coefficient value of 0.9883 and 0.5065 for C-MCM-41 and MWD-MCM-41 while EB or cumene had values below the accepted criteria just for MWD-MCM-41 or C-MCM-41, respectively. In contrast DCB had values of correlation coefficient below that accepted criteria for all sorbents.

These results were unexpected as it was thought that calibration slopes would be similar as the analytes could be efficiently loaded onto, and removed from, each sorbent by thermal desorption. However the results clearly demonstrated a different response (slope) for the analytes for all three sorbents. To investigate further the sorbents were used to collect VOCs from the atmospheric chamber using the same sampling conditions. Furthermore these results indicated that the direct-injection method used to introduce the known masses of VOCs and the internal standard (IS) onto sampling tubes need to be further validated.

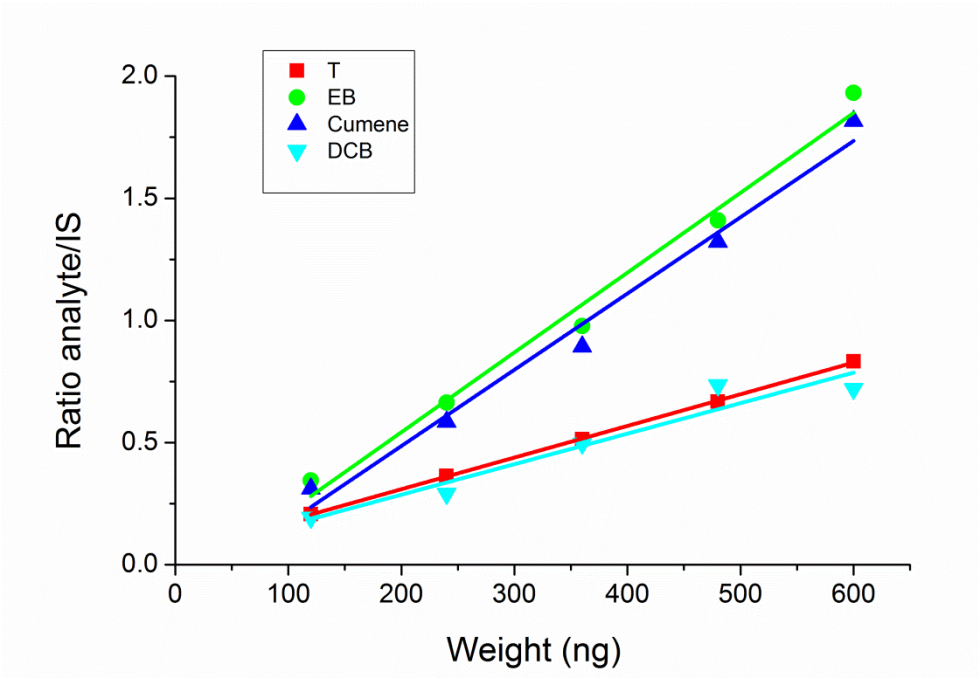

Figure 4.4 Standard curves obtained by using analyte/ internal standard peak area ratio for VOCs trapped on SBA-15

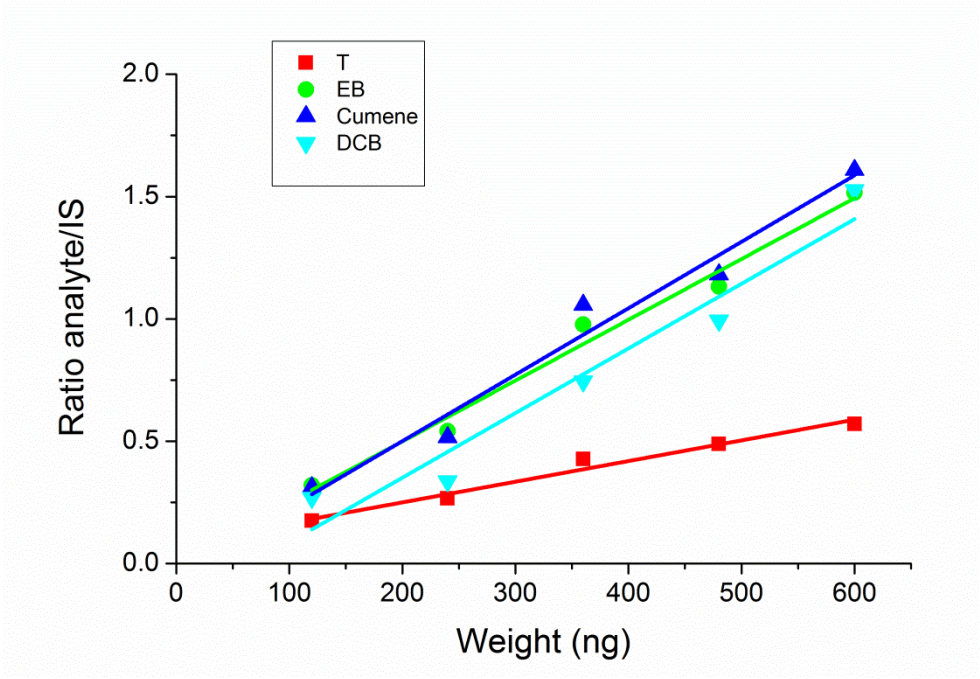

Figure 4.5 Standard curves obtained by using analyte/ internal standard peak area ratio for VOCs trapped on C-MCM-41

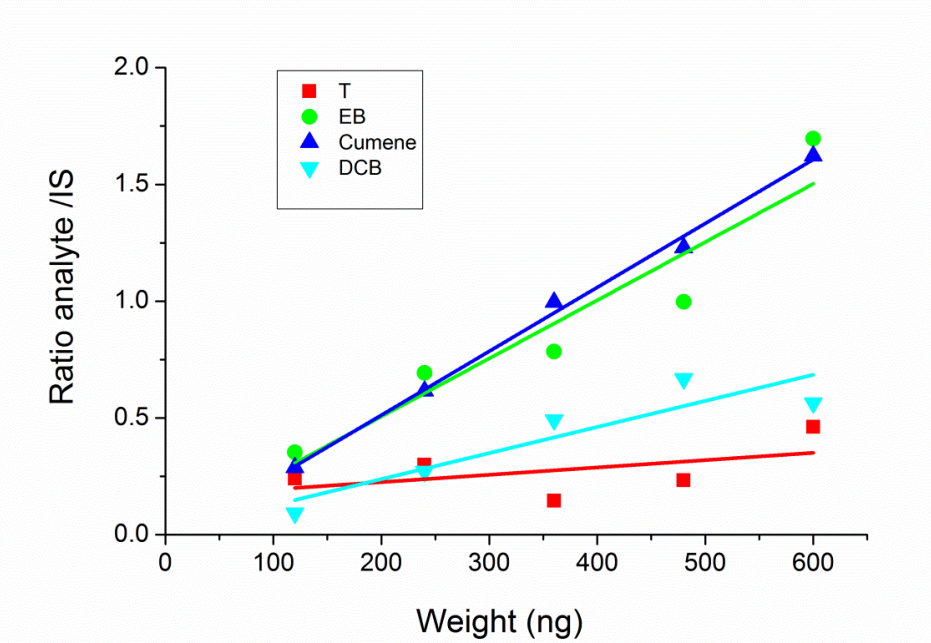

Figure 4.6 Standard curves obtained by using analyte/ internal standard peak area ratio for VOCs trapped on MWD-MCM-41

Table 4.6 Statistical evaluation of linearity of different concentrations of VOCs injected onto different sorbents

Sorbent	VOCs	Toluene	EB	Cumene	DCB
SBA -15	Slope	0.0013	0.0033	0.0031	0.0013
	Intercept	0.0503	-0.1110	-0.1385	0.0372
	Correlation Coefficient	0.9999	0.9932	0.9919	0.9656
C-MCM-41	Slope	0.0008	0.0025	0.0027	0.0026
	Intercept	0.0812	0.0025	-0.0424	-0.1776
	Correlation Coefficient	0.9883	0.9919	0.9857	0.9736
MWD-MCM-41	Slope	0.0003	0.0025	0.0027	0.0011
	Intercept	0.1628	0.0079	-0.0350	0.0147
	Correlation Coefficient	0.5065	0.9463	0.9978	0.9100

4.2.3 Comparison of experimentally calculated masses of VOCs with their theoretically generated values

The theoretical concentrations of toluene, EB, cumene and DCB generated in the atmospheric chamber system were 34, 18, 12 or 7.8 mg m^{-3}, respectively. Tenax TA was used to sample the polluted air at a rate of 150 cm^{-3} min^{-1} for 30 s, therefore the theoretical masses of each VOC expected to be trapped in collected samples of air were 2554, 1352, 928 or 585 ng, respectively. Three sets of experiments were used to compare the measured masses trapped by sampling tubes with the theoretically derived values and each experiment used 4 sampling Tenax TA tubes. The masses trapped by each sampling tube were determined by internal standard regression.

The results listed in Table 4.7 indicated that the masses trapped by Tenax TA in all experiments were lower than the theoretically expected masses (by approximately a factor of 2). To ensure that the calculated masses were determined correctly, the masses were recalculated for all experiments and repeated over a period of four months before being compared again with the theoretical masses. The results again showed that the experimentally calculated masses trapped by sampling tubes were lower than the theoretical masses by approximately a factor of 2, indicating that repeatable results were achieved with % RSD values below 7 % for all experiments. The exact reasons for analyte losses in the chamber were not clear however the atmospheric sampling system used was not desilinised and it was likely that there will be analyte losses due to adsorption in the tubing and onto the walls of the chamber. In addition there may also be some leaks from the chamber. It was therefore concluded that the VOC concentrations would need to be experimentally determined rather than relying on theoretically calculated values. What was important to note was the stability of the concentrations generated. Here the system set up was developed in-house using general purpose materials. The permeation vials were prepared in-house using simple GC vials and syringe needles to control pollutant flow. Flow rates to the chamber were controlled with mass flow control meters. With this simple set up it was possible to generate a dynamic flowing stream of air contaminated with known masses of VOCs at a constant concentration for a period of at least four weeks. This system was therefore thought to be valid for use

when determining the efficiency of VOC sorbents if experimental VOC concentrations were measured before and after the sorbent test.

Table 4.7 The repeatability and the reproducibility of determination of trapped masses using Tenax sampling tubes

VOCS	T / ng	EB / ng	Cumene / ng	DCB / ng
Exp1	1193	557	446	218
Exp2	1117	498	441	216
Exp3	1102	498	435	211
Average Weight Trapped	1137 ± 49	518 ± 35	441 ± 6	215 ± 5
% RSD	4.3	6.8	1.3	2.2
Theoretical Mass Applied	2554	1352	929	586

4.2.4 Validation of direct-injection method used for calibration by different sorbents

To investigate the variety of calibration results that were obtained when different sampling sorbents were used to calibrate the TDU-GC-MS, sorbent tubes loaded with MWD-MCM-41 were chosen to trap VOCs from polluted air coming out of the atmospheric chamber. A sampling flow rate of 100 cm^3 min^{-1} for different sampling times of 20, 40, 60 and 80 s was used. The expected masses of VOCs trapped from the polluted air passing through the sorbent tubes are listed in Table 4.8.

Table 4.8 Masses of VOCs expected to be trapped by MWD-MCM-41 at different sampling times

Expected (theoretical) mass	Sampling time			
	20 s	40 s	60 s	80 s
Toluene (ng)	1135	2270	3405	4540
EB (ng)	601	1201	1802	2402
Cumene (ng)	413	825	1238	1651
DCB (ng)	260	521	781	1042

The internal standard solution (IS) was injected onto each sampling tube before analyses by TDU-GC-MS. The peak area of each analyte was divided by the peak area of the IS to obtain the ratio, which was plotted against the sampling time (see Figure 4.7). The curves indicated that the peak areas of analytes increased with an increase of sampling time indicating a high capacity of MWD-MCM-41 for trapping VOCs from the polluted air compared to the capacities achieved when methanolic standard solution were injected onto the same sorbent tubes (note masses of VOC in air were set to match masses of VOCs in methanolic solutions). Since the masses of VOCs collected from contaminated air were much higher than those of methanolic standard solutions, it was thought that a potential competition between methanol and the analytes, for the sorbent, may have caused significant decreased capacities when using the direct injection method to introduce known masses of VOCs, and the IS, onto the sorbent sampling tubes. The VOCs in methanol appeared to easily breakthrough silica sampling tubes without being retained, whereas in air, the capacity of MCM-41 for VOCs was much greater.

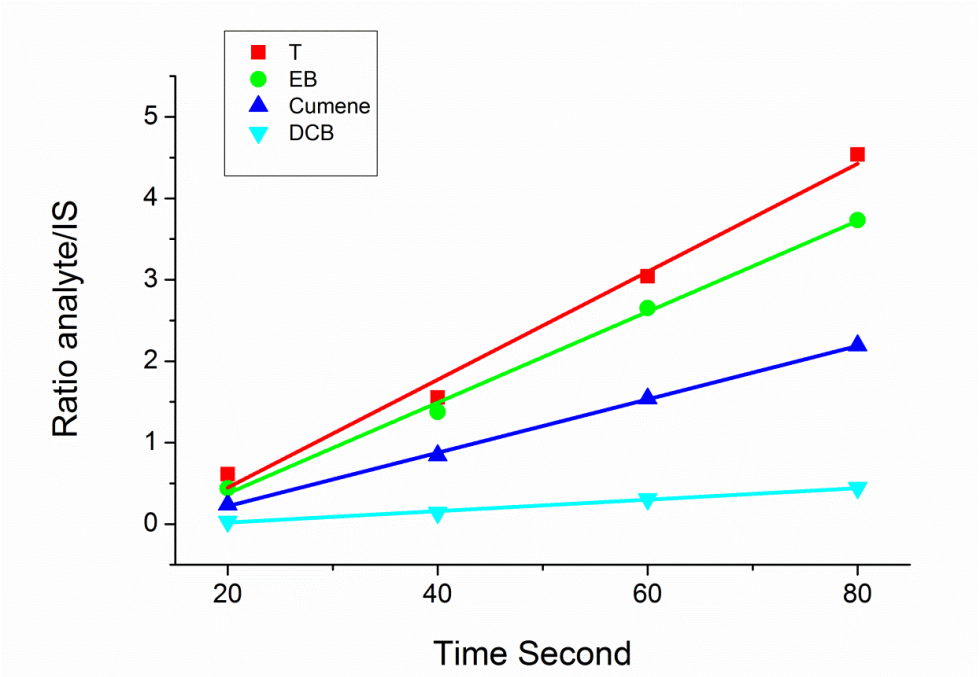

Figure 4.7 Use MWD-MCM-41 to trap the VOCs from atmospheric chamber at different sampling time

These results were thought to be important as they indicated that the direct injection sampling method cannot be used to calibrate silica sorbent tubes as methanol interfered with the analyte-stationary phase interactions on the surface of the siliceous materials. Further confirmation of the inaccuracies determined by direct-injection of methanolic standard solutions onto silica adsorbent tubes was achieved by examination of the breakthrough of VOCs masses. Sorbent tubes filled with MWD-MCM-41, C-MCM-41 or SBA-15 were connected to the direct injection port as described in section 3.5.3, then conditioned Tenax TA tubes were placed in-line immediately after the sorbent tubes. The direct-injection method was used to inject 10 µL of a standard solution containing 600 ng of each VOC followed by 5 µL of the IS. Masses of VOCs collected by the Tenax TA tubes were divided by masses retained on the sorbent tubes to provide breakthrough values of each VOC, as summarised in Table 4.9. The results demonstrated that more than 50 % toluene or 30 % of EB or IS masses were desorbed from all siliceous sorbents when direct-injection method was used to inject methanolic solutions of VOCs and IS, confirming the effect of methanol on the adsorption of analytes on these sorbents.

Table 4.9 Breakthrough of VOCs through using direct-injection method.

VOCs Sorbent	Toluene % BT	EB % BT	IS % BT	Cumene % BT	DCB % BT
MWD-MCM-41	65	41	40	5	2
C-MCM-41	58	33	27	13	3
SBA-15	51	29	31	11	2

To obtain accurate results of VOCs trapped on siliceous sorbents by direct injection, it was necessary therefore to select sampling tubes filled with Tenax TA for calibrating the TDU-GC-MS instrument. The calibrant sampling tubes containing Tenax TA were conditioned before they were injected with different volumes of VOCs standard solutions contained 60, 180, 300, 420 or 540 ng of VOCs, followed by injection of 5 µL of IS onto each calibrant tube as described in section 4.2.1. Ratios of analyte/IS peak areas were plotted against masses of VOCs injected onto tubes to obtain calibration curves. Linearity was achieved indicating that in the case of Tenax TA methanol has no interference with the sorbent allowing the VOCs to be successfully retained in the sampling tube. Therefore VOC masses trapped in all silica sorbent tubes were calculated by calibration curves using Tenax TA.

4.2.5 Using Tenax TA as a reference to collect analytes in a 100 cm^3 volume of air

Tenax TA was used to trap the VOCs (toluene, EB, cumene and DCB) from the sampling chamber at the chosen sampling conditions to calculate masses of VOCs that presented in 100 cm^3 of contaminated air. Four Tenax TA sampling tubes were conditioned prior to collect the VOCs from polluted air under the same conditions. The flow rate of polluted air passing through sampling tubes was set at 100 cm^3 min^{-1} for 1 min. The samples were directly analysed by TDU-GC-MS, avoiding the injection of internal standard (IS) by direct-injection method which may lead to breakthrough of trapped masses. The resultant peak areas of each analyte were used to calculate masses of VOCs trapped on sampling tubes. In this case, the TDU-GC-

MS was calibrated by injecting different volumes (1, 3, 5, 7 or 9 µL) of VOCs standard solutions containing (60, 180, 300, 420 or 540 ng) onto conditioned calibrant tubes filled with Tenax TA, again no injection of IS was needed. The calibrant tubes were analysed by the TDU-GC-MS, and the obtained peak areas were plotted against masses (ng) of injected VOCs to get calibration curves as shown in Figure 4.8. The linear regression analyses and the correlation coefficients for the analytes were summarised in Table 4.10 demonstrated that all analytes had the correlation coefficients in the accepted criteria (> 0.9900).

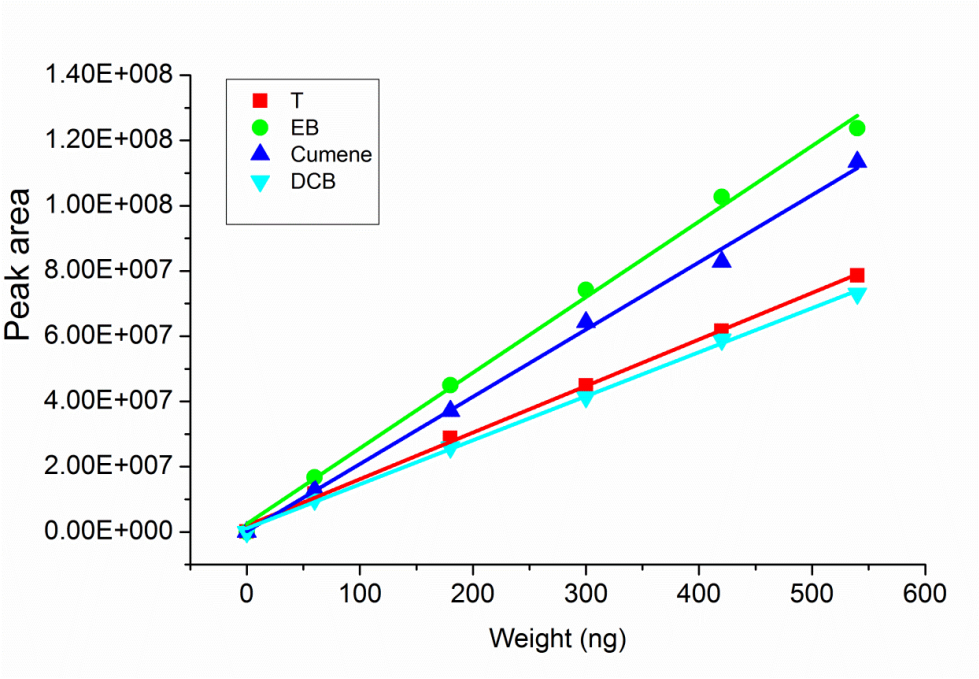

Figure 4.8 Standard curves of VOCs by peak area obtained on Tenax TA.

Table 4.10 Statistical evaluation of linearity of different concentrations of VOCs injected onto Tenax TA

VOCs	Slope	Intercept	Correlation Coefficient	Standard Error on Slope	Standard Error on Intercept
Toluene	142747	1924240	0.9983	2670	839984
EB	231732	2485280	0.9963	6340	1994690
Cumene	206192	207566	0.9967	5316	1672480
DCB	135029	1109140	0.9987	2219	698201

The masses of VOCs trapped on each sampling tube were determined by their peak areas and standard regression curves obtained by TDU-GC-MS instrument (see Table 4.11). The results demonstrated that the relative standard deviation (%RSD) values of calculated masses were below 7 % for all analytes measured by 4 sampling tubes. The averages of calculated masses 2109, 404, 479 or 494 ng for toluene, EB, cumene or DCB respectively, were used as "reference masses" to determine extraction efficiency of siliceous sorbents that used to sample the VOCs from contaminated air under the same conditions (flow rate at 100 cm^3 min^{-1} for 1 min).

Table 4.11 Reference masses of VOCs collected from 100 cm^3 air by Tenax TA.

VOCs Experiments	Toluene Masses (ng)	EB Masses (ng)	Cumene Masses (ng)	DCB Masses (ng)
S1	2113	399	459	453
S2	2090	402	477	485
S3	2137	406	488	514
S4	2097	411	492	525
Average (ng)	2109 ±21	404 ±5	479 ±15	494 ±32
% RSD	1.00	1.3	3.1	6.4

4.3 Calculation of theoretical concentration of H_2CO generated inside dynamic sampling chamber

The theoretical concentrations C (mg m^{-3}) of H_2CO vapour generated in the dynamic chamber were calculated by using Equation 3.1 described in section 3.3.2. The theoretical concentration was depended on the air flow (F) rate cm^3 min^{-1} that passed over the permeation source, the H_2CO emission rate (E) ng min^{-1} which depended on the temperature of oven, and a value K_0 which is a constant.

4.3.1 Calculation of H_2CO emission rate released in permeation device

The H_2CO emission rates of the permeation glass tube holder containing paraformaldehyde as a source of H_2CO had to be calculated at different selected oven temperatures. The glass tube holder was weighed before being placed inside a permeation device in the temperature controlled oven. The temperature oven was set to 80 °C to generate a high concentration of H_2CO vapour or at 50 °C to generate lower formaldehyde concentrations. The air flow rate passing over the permeation device was set to 200 cm^3 min^{-1} and continued to pass over the heated permeation source for known periods of time, then the permeation source was removed from the oven, cooled to room temperature and weighed before being replaced back into the oven.

The emission rate E (ng min^{-1}) was calculated by Equation 4.1 as described in section 4.1.1. The weight losses (ng) were measured weekly over one month for each temperature, divided by the time (min) of each week to obtain the E and the average values for E are given in Table 4.12. The results indicated that the weight losses of H_2CO vapour were constant for both temperatures. Indeed as a general rule of thumb it is expected that reaction rates will double for every 10 °C increase in temperature. These emission rates roughly follow this general rule. The data given in Table 4.12 confirm the ability to produce stable stream of polluted air at high or low concentration of H_2CO by using the dynamic chamber system.

Table 4.12 The average emission rates of H_2CO at 50 °C and 80 °C

Oven temp / °C	Weight loss / g week^{-1}				Weight loss / g week^{-1}	E / ng min^{-1}
	Week 1	Week 2	Week 3	Week 4		
80	0.070	0.068	0.067	0.071	0.069	6845
50	0.0053	0.0054	0.0056	0.0053	0.0054	541

4.3.2 Calculation the theoretical concentration of H_2CO vapour

The theoretical concentrations ppm (µg g^{-1}) of H_2CO generated in the atmospheric chamber system was calculated using Equation 3.1 as described in section 3.4.2, and average emission rates (E) of H_2CO given in Table 4.12. The flow rates (F) of air passed over the source of H_2CO was set at 200 cm^3 min^{-1} and was combined with humidified air (flow rate 200 cm^3 min^{-1}). Therefore the calculated concentrations of H_2CO in the air stream were then divided by a factor of 2 (see Table 4.13).

Table 4.13 The theoretical concentrations of H2CO generated in sampling chamber at 50 and 80 °C

Oven temp / °C	E / ng min^{-1}	K_0 / L g^{-1}	Flow rate / cm^3 min^{-1}	Conc. in air stream/ µg g^{-1}	Conc. in chamber/ µg g^{-1}
50	541	0.815	200	2.2	1.1
80	6845	0.815	200	28	14

The concentration of H_2CO in the sampling chamber ppmw (µg g^{-1}) was converted to ppmv (µg L^{-1}) units which is equivalent to mg m^{-3} using the vapour phase density (see Table 4.14). The density of pollutant was calculated by using Equation 4.2 (see

section 4.1.2) which was obtained from the ideal gas equation (see Equation 3.2 in section 3.3.2).

Where D is the density of gas (g L^{-1}), P is the pressure (1 atm), MW is the molecular weight, R is the gas constant (0.0821 L atm mol^{-1} K^{-1} and T is the temperature (K).

Table 4.14 Theoretical concentrations of VOCs and formaldehyde generated in sampling chambers

Oven temp / ºC	Conc. in sampling chamber / µg g^{-1}	Gaseous density / g L^{-1}	Conc. in sampling chamber / mg m^{-3}
50	1.1	1.227	1.4
80	13.947	1.227	17.11

4.3.3 Comparison of experimentally calculated masses of H_2CO with its theoretically generated values

Paraformaldehyde was used as the source of H_2CO vapour produced in the atmospheric system when the permeation oven temperature was set to 80 or 50 ºC. Using the measured emission rate values of 6845 or 541 ng min^{-1}, the theoretical concentrations of H_2CO vapour generated in the sampling chamber were calculated to be 17 or 1.4 mg m^{-3}, at 80 or 50 ºC, respectively.

To compare the theoretical concentration of H_2CO generated at the high concentration (17 mg m^{-3}) with the experimental concentration applied for each experiment, the temperature of oven was set to 80 ºC, four experiments were applied at different sampling times 45, 60, 90 and 120 min and the flow rate of sampled air was set at 200 cm^{-3} min^{-1}. The theoretical masses of H_2CO that should be trapped could then be calculated for each experiment as given in Table 4.15.

Table 4.15 The theoretical masses of H_2CO applied at different sampling times

Experiments	Conc. of H_2CO in chamber / mg m^{-3}	Flow rate / cm^3 min^{-1}	Sampling time / min	Theoretical Masses / µg
Exp. 1	17	200	45	154
Exp. 2	17	200	60	205
Exp. 3	17	200	90	308
Exp. 4	17	200	120	411

The H_2CO vapour in polluted air was sampled by 10 cm^3 of distilled water for the selected sampling time and followed by adding Schiff's reagents to obtain coloured solution which was detected by colorimetric method as described in section 3.5.2. The resultant absorbance was used to calculate the experimental masses of H_2CO vapour collected in each experiment by using the standard calibration curve (see section 4.4.1.1). Each experiment was repeated three times and the average masses trapped were compared with the expected theoretical masses (see Table 4.16).

The results showed that the theoretical masses were lower than the calculated masses applied in all experiments. The reason of that is not known; therefore the use of calculated masses was more accurate to determine H_2CO collected from sampling chamber because they depend on the calibration curve which was obtained by using standard solutions of H_2CO. Furthermore the results showed that the calculated masses were increased with increased sampling times (see Figure 4.9).

Although this sampling method of H_2CO was not optimised (i.e. the chamber was not desilinised and the molarity of the standard solutions used was not confirmed by back titrations) the experimentally calculated values were thought to be similar to the expected values.

Table 4.16 Comparison of theoretical masses and applied masses of H2CO generated in sampling chamber at different sampling times

Experiment Time / min	S_1 Mass / µg	S_2 Mass / µg	S_3 Mass / µg	average	% RSD	Theoretical masses /µg
45	142	143	139	141 ± 2	1.47	154
60	242	233	239	238 ± 5	1.93	205
90	392	406	396	398 ± 7	1.81	308
120	538	542	548	543 ± 5	0.93	411

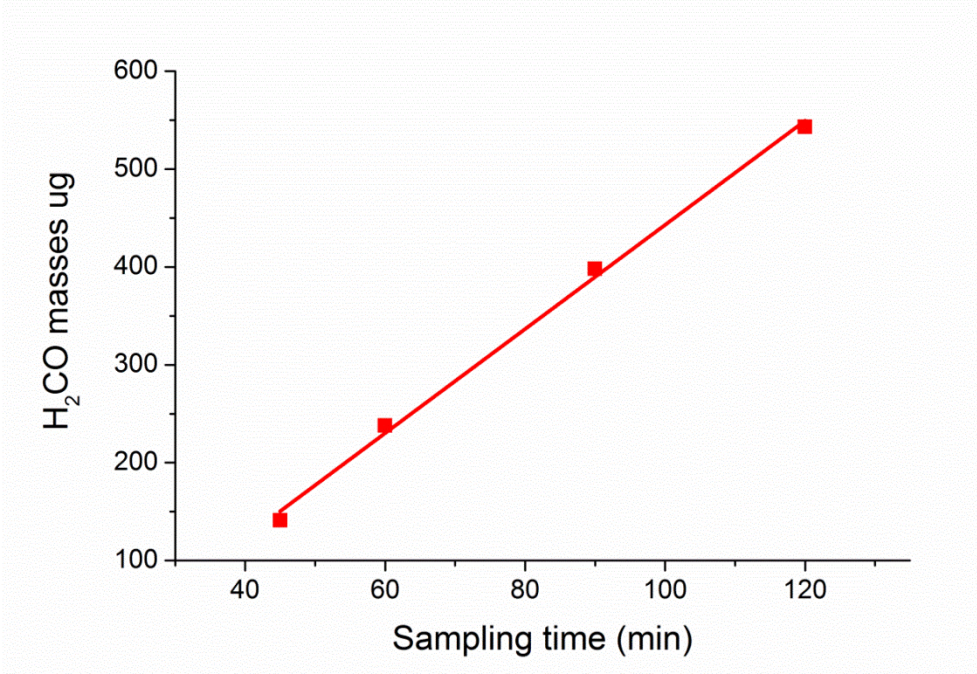

Figure 4.9 Tapped masses of H_2CO with increasing sampling times

The experimental values indicated that a good agreement of experimentally calculated concentrations with the theoretical data was achieved at the lower end of the sampling scale; however the accuracy of the experiments decreased as the sampling times increased. These experiments demonstrate that the sampling chamber

can be used to generate atmospheres contaminated with H_2CO vapour at concentrations that were close to estimated values. However to ensure the accuracy is achieved the concentrations generated would have to be determined experimentally.

The accuracy of the sampling procedure was also examined at lower concentration (1.4 mg m^{-3}) of H_2CO generated by decreasing the permeation oven temperature to 50 °C. The collection method was altered slightly by adding Schiff's reagents to the distilled water prior to collection of H_2CO vapour. This change was implemented because it was noted that the coloured solutions were not stable when Schiff's reagent was added to aqueous solutions of low H_2CO concentrations.

Two experiments were used to collect H_2CO from the sampling chamber and each experiment used four solutions of Schiff's reagent (1 cm^3 of each reagent) added to 10 cm^3 of distilled water. The sampling rate was also reduced to 100 cm^3 min^{-1} and the sampling time was set to 60 min. The absorbance value of the coloured solution was measured at 560 nm by colorimetry approximately one hour after H_2CO vapour was bubbled through the impinger. The absorbance values obtained were used to calculate the experimentally trapped masses of H_2CO by calibration curve (see Table 4.17). The results indicated that the modified method may be repeatable and reproducible for collection of H2CO vapour in the impinger.

However, the results were repeatable; they indicated that the masses of trapped H_2CO vapour had been excessively high. Theoretically it was expected that 8 µg of H_2CO would have been trapped in the impinger, yet experimentally 240 µg of was measured. Reasons why there was such a large discrepancy were not known; therefore this method was recommended to collect H_2CO vapour generated at high concentration only.

Table 4.17 The calculated masses of H_2CO generated at low concentration

Experiments	S_1 Mass / µg	S_2 Mass / µg	S_3 Mass / µg	S_4 Mass / µg	average	RSD / %
Exp1	225	240	277	223	241 ± 25	10.37
Exp2	236	262	258	244	250 ± 12	4.84
Average	231	251	268	234	246 ± 19	7.61

H_2CO vapour generated in atmospheric chamber at low concentration (1.4 mg m^{-3}) was sampled using silica C18 cartridges impregnated with 0.8 cm^3 of a trapping solution, consequent of low accuracy when the impinger method was used. 6 sampling cartridges were used to sample H_2CO vapour from contaminated air at a flow rate of 100 cm^3 min^{-1} for different sampling time (10, 20, 30, 40, 50 or 60 min). H_2CO vapour trapped as F-DNPH was eluted from cartridges using 3 cm^3 of acetonitrile and the extracted derivative was determined by the LC-UV-vis instrument as described in section 3.5.2. The masses (µg) of H_2CO vapour trapped on cartridges were quantitatively calculated by calibration curve as described in section 3.5.2, and compared to their expected masses (see Table 4.18). The results demonstrated that most of the experimental masses trapped at different sampling time were similar to their corresponding theoretical masses. Furthermore the measured masses increased with increased sampling times (see Figure 4.10).

The experiment used to sample H_2CO vapour for 60 min was selected to examine the repeatability of the sampling method. 4 sampling cartridges were applied to sample volume (6 dm^3) of contaminated air that expected to include 8 µg of H_2CO. Sampling cartridges were eluted by acetonitrile to extract F-DNPH derivative prior to determination by the calibrated LC-UV-vis instrument. The masses of H_2CO trapped on sampling cartridges were again calculated from calibration curve obtained by F-DNPH standard solutions. The average of calculated masses was 8.1 with a relative standard division (% RSD) value of 1.2 confirming repeatability of the method.

Moreover this method demonstrates a high accuracy for the collection and determination of H_2CO generated at low concentration (1.4 mg m^{-3}), therefore it will be used to study the sorbents performance for extracting H_2CO from indoor air.

Table 4.18 Comparison of expected and trapped masses of H2CO.

Sampling time (min)	Expected Masses (µg)	Trapped Masses (µg)	Recovery %
10	1.35	1.7	126
20	2.70	2.9	107
30	4.05	4.0	99
40	5.40	5.4	100
50	6.75	6.2	92
60	8.10	8.12	100

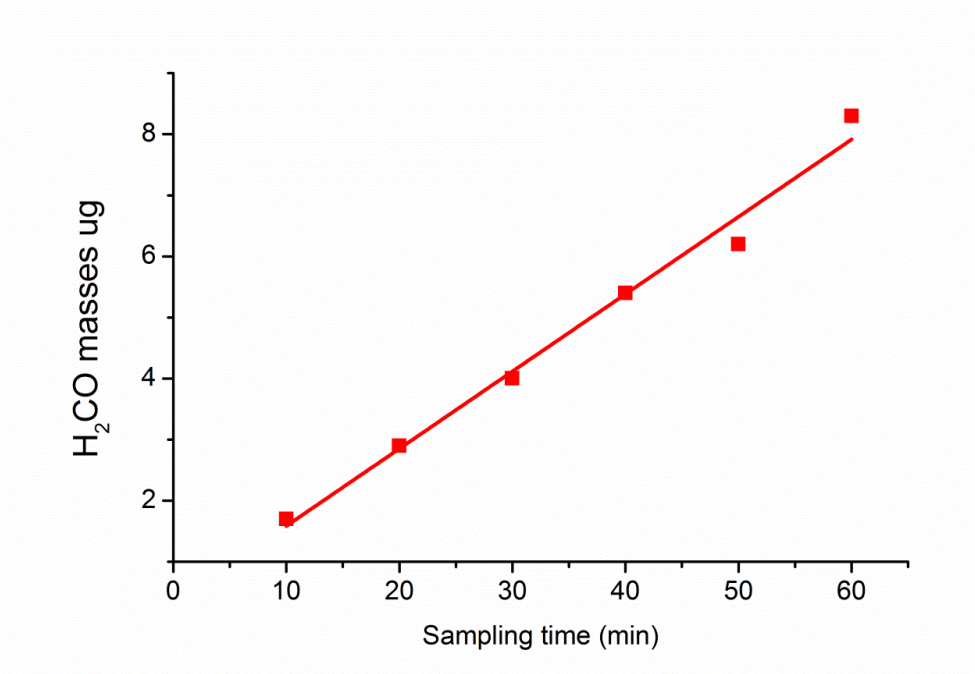

Figure 4.10 The increase of the masses of H_2CO collected by cartridge with increasing of sampling times

4.4 Detection of H_2CO vapour

4.4.1 Use UV-VIS Spectroscopy

The coloured solutions of H_2CO vapour that had reacted with Schiff's reagent in the impinger was analysed by UV-vis spectrophotometry under the instrumentation and technical specifications detailed in Table 3.6 (see section 3.5.1).

4.4.1.1 Calibration of UV-VIS spectroscopy by standard curve

Before the UV-vis spectroscopy was used to detect samples of H_2CO vapour collected from the atmospheric chamber system, the instrument was calibrated using standard solutions of aqueous phase H_2CO prepared as described in section 3.5.1. Schiff's reagent (a pararosaniline and sodium sulfite solution) were added to each solution to produce a coloured product which could be measured spectrophotometrically at 560 nm by the instrument as described in section 3.5.1.

The standard solutions of H_2CO used to obtain a standard calibration curve contained 15, 30, 45, 60 or 75 mg L^{-1} of aqueous H_2CO. Approximately 10 cm^3 of each solution was used in calibration solutions which meant that calibrant solutions contained 150, 300, 450, 600 or 700 μg, respectively, of H_2CO. The obtained intensities of absorbance were plotted against masses (μg) contained in resultant coloured solutions to obtain the standard calibration curves given in Figure 4.11. The results demonstrated that the signal intensity at 560 nm increased linearly with increased H_2CO masses contained in the standard solutions. Linear regression analysis was performed, the correlation coefficients was 0.9975, in the accepted criteria of > 0.9900, and the standard calibration curve had a confidence interval of intercept with included zero ($y = 0.0013x - 0.0274$).

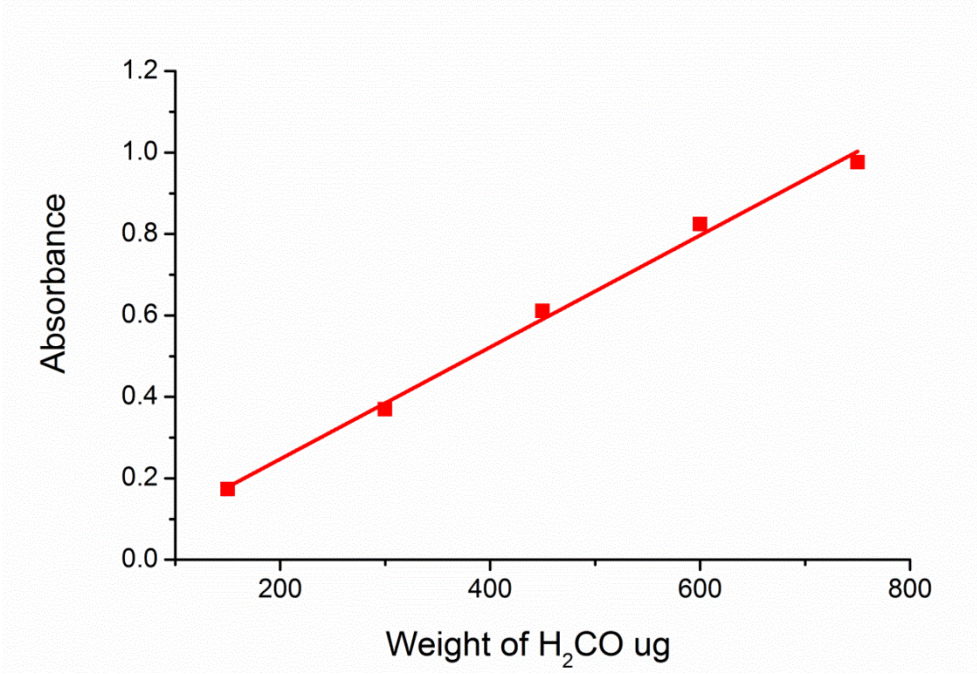

Figure 4.11 Standard calibration curve of H_2CO standard solutions

To determine range of concentrations that would provide a linear response, solutions containing higher masses of H_2CO were prepared giving solutions that contained masses in the range 150 -1500 µg). The signal intensity of the standard solutions was measured at 560 nm and the resultant values were plotted against the masses of H_2CO present in standard solutions (see Figure 4.12). The curve showed that the standard calibration curve could be used to calculate concentrations of H_2CO in collected samples at 75 ppm (750 µg) as the highest value.

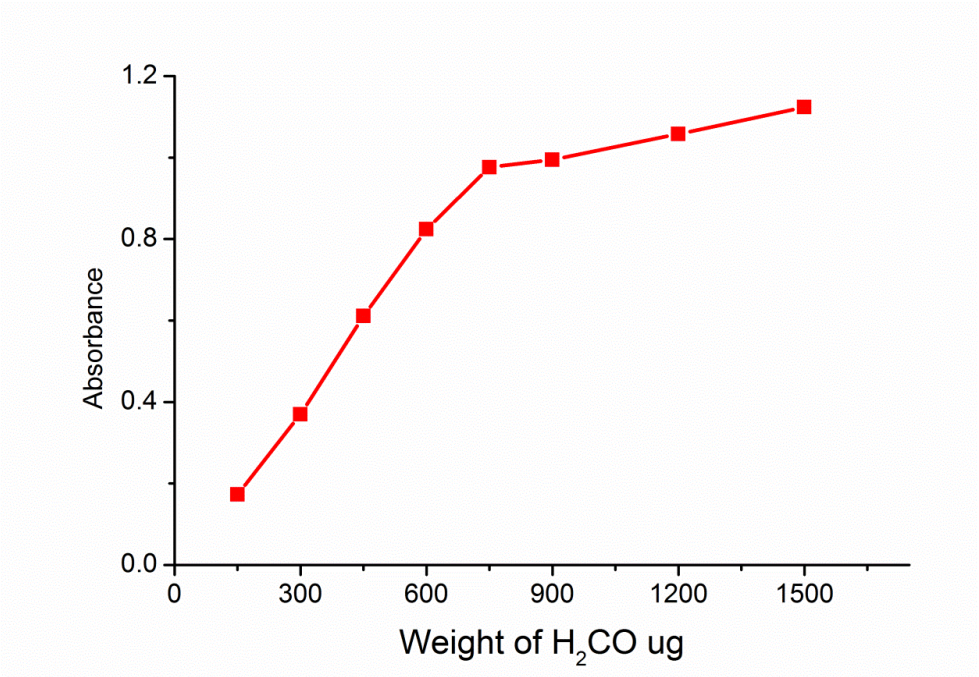

Figure 4.12 Limitation of UV-VIS calibration for determining H_2CO in collected samples

4.4.1.2 Determination of the coloured solution stability

To determine an appropriate time for detecting samples of H_2CO after adding Schiff's reagents, the absorbance of the resultant coloured solution was measured by UV-vis spectroscopy at different times. H_2CO was collected in 10 cm^3 distilled water, 1 cm^3 of pararosaniline solution was added to the sample of H_2CO followed by 1 cm^3 of sodium sulfite solution. Then the absorbance of the resultant coloured solution was immediately measured by the UV instrument every 30 s for 120 min. The results were plotted against time periods of after addition of Schiff's reagents (Figure 4.13). The curve demonstrated that the absorbance values, and hence colour of the product produced, were stable 60 min after addition of Schiff's reagent. Therefore the appropriate time to measure solutions used to trap H_2CO vapour was thought to be approximately 60 min after addition of the reagents.

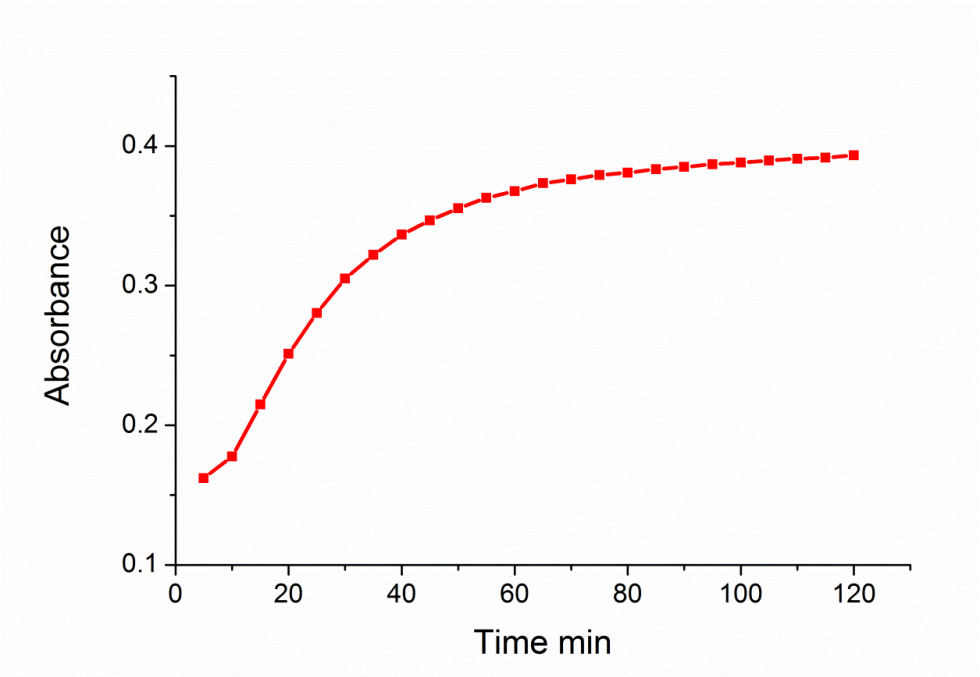

Figure 4.13 The relation between the absorption and the period of time after adding Schiff's reagents

4.4.2 Use of the LC-UV-vis detector for H_2CO determination

The LC coupled to the UV-vis detector was used to determine H_2CO vapour that generated at low concentration (1.4 mg m^{-3}) in dynamic chamber. The H_2CO collected by silica C_{18} cartridges impregnated with trapping solution of DNPH was detected as F-DNPH by the LC-UV-vis under conditions that summarised in Table 3.7 (see section 3.5.2).

4.4.2.1 Calibration of LC-UV by standard curve

Before the LC-UV-vis detector was used to detect samples of H_2CO vapour collected by sampling cartridges which loaded with trapping solution of 2,4-DNPH, the instrument was calibrated using standard solutions of F-DNPH prepared as described in section 3.5.2. Approximately 20 µL of each set of standard solutions (2, 4, 8, 12, 16 or 20 µg cm^{-3}) were injected into LC injection port using LC micro syringe and analysed as described in section 3.5.2. The calibration experiment was repeated 3

times and the results (summarised in Table 4.19) demonstrated that all sets of standard solutions had a % RSD < 3.5, confirming a high repeatability of instrument for H_2CO detection. The averages of F-DNPH peak areas were plotted against their concentrations (µg cm^{-3}) to obtain the calibration curve (see Figure 4.14).

The results showed that the peak areas increased linearly with increased concentrations of standard solutions. Linear regression analysis was achieved with an accepted correlation coefficient (0.9976) and a confidence interval of intercept that included zero (y = 162865x + 27841). This linear regression equation will applied to calculate concentrations of detected F-DNPH which converted to masses of H_2CO vapour collected from dynamic chamber by sampling cartridges for all experiments used to study the extraction of H_2CO vapour generated at low concentrations.

Table 4.19 Repeatability of the LC-UV for calibration by F-DNPH

Conc. (µg cm^{-3})	Exp.1 Peak area	Exp.2 Peak area	Exp.3 Peak area	Average of Peak area		% RSD
2	347354	343068	339612	343345	3878	1.13
4	674174	651135	671278	665529	12549	1.89
8	1369090	1312629	1304199	1328639	35284	2.66
12	1933999	1932644	1942953	1936532	5602	0.29
16	2598243	2470305	2625695	2564748	82934	3.23
20	3370286	3399509	3347252	3372349	26190	0.78

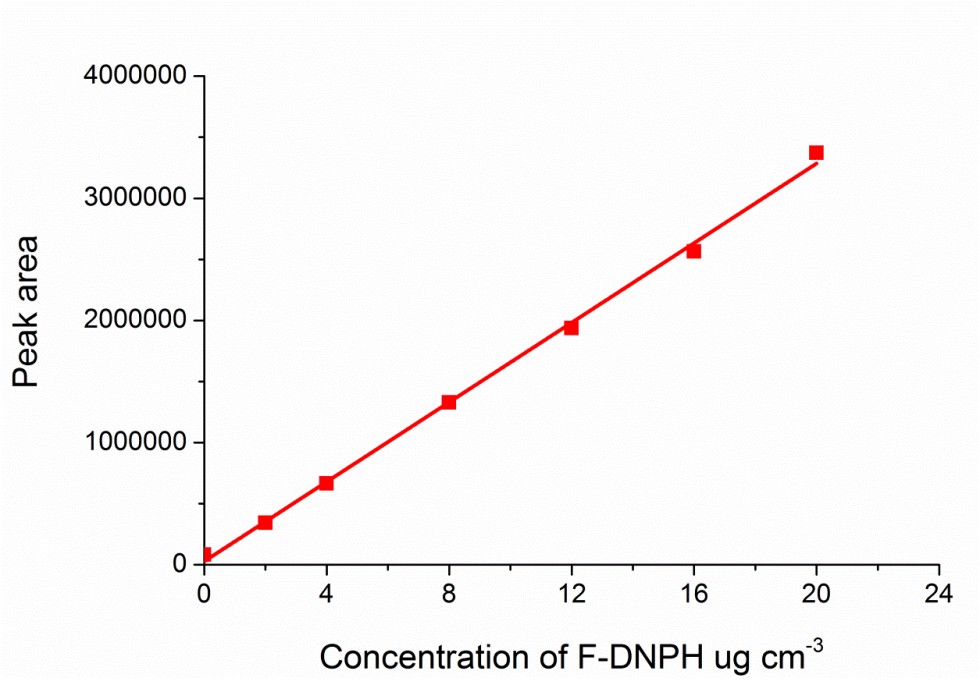

Figure 4.14 Standard curve of F-DNPH standard solutions at low concentrations

4.4.2.2 Calculation of experimental concentration of H_2CO generated in camber by sampling cartridges

C18 Cartridges impregnated with 0.8 cm^3 of a trapping solution (2,4- DNPH) were used to sample H_2CO vapour from contaminated air at flow rate of 100 cm^3 min^{-1} for 60 min. Then each sampling cartridge was washed with 3 cm^3 of acetonitrile to extract the F-DNPH derivative which was then detected by the calibrated LC-UV-vis instrument. The resultant peak areas of F-DNPH were analysed by the linear regression equation obtained from external calibration curve to convert to concentrations (µg cm^{-3}) which were converted to masses of H_2CO vapour trapped by cartridges as described in section 3.5.2. As an example of that, to calculate masses of H_2CO trapped on sampling cartridges at different sampling time (10, 20, 30, 40, 50 or 60 min), concentrations (µg cm^{-3}) of F-DNPH were calculated as given in Table 4.20, then converted to trapped masses of H_2CO (µg) as showed in Table 4.21.

Table 4.20 Use calibration curve for calculation the concentration of F-DNPH

Sampling Time min	Peak area of F-DNPH	intercept	Slope	F-DNPH / µg cm^{-3}
10	618006	27841	162865	3.97
20	1073898	27841	162865	6.76
30	1491798	27841	162865	9.33
40	2023672	27841	162865	12.60
50	2327600	27841	162865	14.46
60	3057027	27841	162865	18.94

Table 4.21 Convert of F-DNPH conc. to masses of H_2CO (µg)

F-DNPH / µg cm^{-3}	Elution volume / cm^3	Masses F-DNPH / µg	MW F-DNPH	µmoles F-DNPH	MW of H_2CO	Masses of H_2CO / µg
3.97	3	11.90	210.15	0.057	30.03	1.7
6.76	3	20.29	210.15	0.097	30.03	2.9
9.33	3	27.99	210.15	0.133	30.03	4
12.60	3	37.79	210.15	0.180	30.03	5.4
14.46	3	43.39	210.15	0.206	30.03	6.2
18.94	3	56.82	210.15	0.270	30.03	8.12

4.5 Conclusions

The validation of methods used to collect and determine VOCs and H_2CO generated in the atmospheric dynamic chambers was required before the silica sorbents could be examined for VOCs or H_2CO scavengers. The results demonstrated that constant

concentrations of VOCs and H_2CO were generated in dynamic atmospheric chambers using in-house prepared permeation vials and permeation devices. Permeation vials were shown to provide constant emission rates (E) of VOCs for up to 6 weeks, whereas paraformaldehyde stored in permeation device was used to provide a constant (E) of H_2CO for even longer times. The flow rate (F) of air that passed through permeation devices and over VOCs or H_2CO sources was set at 200 cm^3 min^{-1}. For generation of VOCs, when the temperature of controlled oven was set to 25 ^0C, the constant emission rates (E) of VOCs were measured, and the theoretical concentrations were calculated to 34, 18, 12 and 7.8 mg m^{-3} for toluene, EB, cumene and DCB, respectively. In contrast, H_2CO could be generated at high or low concentrations according to the oven temperature. When the temperature was set to 80 ^0C the concentration was calculated to 17 mg m^{-3}, whereas when it was set to 50 ^0C, the concentration was 1.4 mg m^{-3}.

Sampling tubes loaded with Tenax TA was shown a provide a valid method for calibration of the TDU-GC-MS instrument by a direct injection method. In contrast, the use of silica sorbents for instrument calibration by direct injection method demonstrated significant breakthrough of target VOCs due to a competition between methanol and the analytes of interest. Therefore Tenax TA was used throughout this work as calibrant and reference sampling tubes, even when different silica sorbents were used to collect VOCs from contaminated air. Tenax sampling tubes were then used to sample VOCs from sampling chamber under the selected conditions (flow rate 100 cm^3 min^{-1} for 1 min) and results demonstrated the method was successfully validated and was shown to be repeatable and reproducible. The average of VOCs masses collected by Tenax sampling tube were 2109, 404, 479 and 494 ng of toluene, EB, cumene and DCB, respectively. These masses will be used as a "references masses" to examine the performance of studied silica sorbents for VOCs adsorption.

A colorimetric method was successfully used to determine the H_2CO vapour concentration generated in a flowing air stream. UV-vis spectrometry and standard solutions of H_2CO were used to calibrate the instrument. The results demonstrated that the most suitable time for development of the coloured solution was 60 min after addition of the Schiff's reagent to the formaldehyde containing solutions. However,

low stability of coloured solution was observed when the method was used to collect H_2CO generated at low concentration, suggesting that the colorimetric method could only be used to determine the concentration of H_2CO generated at high concentration.

The H_2CO vapour generated at low concentrations was collected by C18 cartridges loaded with a 2,4-DNPH trapping solution and the hydrazine derivative was analysed by LC-UV –vis. The flow rate of polluted air at 100 cm^3 min^{-1} with a sampling time of 60 min was shown to provide ideal conditions giving average collected H_2CO masses of 8.1 µg. Therefore using these conditions, this mass was used as the "references H_2CO mass" when examining the extraction efficiencies of studied silica sorbents for H_2CO removal.

5 Use mesoporous silica for extraction of VOCs and H_2CO from indoor air

5.1 Introduction

MCM-41 is regarded as one of the most suitable model adsorbents of the M41S family of materials and is often used to confirm the theoretical estimation of an equilibrium adsorption in cylindrical pores [92]. MCM-41 is an amorphous silica material with a regularly ordered pore arrangement consisting of a hexagonal array of uniform mesopores [82, 150]. The material has a very narrow pore-size distribution which can be controlled by selected of an appropriate surfactant that acts as a template where the silica will arrange around [151] or by selecting an applicable method for removing the template from network of as-made materials such as microwave digestion [152, 153].

SBA-15 is another commonly used mesoporous materials which has attracted much attention as an adsorbent due to its excellent thermal stability, variable pore sizes, and tailored particle morphology [154]. A novel material, SBA-15, was first synthesised by the research group led by Zhao *et al.* [155] using poly(alkylene oxide) block copolymers and low molecular weight nonionic ethylene oxide surfactants in acidic media. SBA-15, obtained through triblock copolymer templating, has a well-ordered 2D hexagonal array consists of the primary mesopore channels connected by complementary micropores walls to form bimodal pore system which increases the applicability of the material for use as an adsorbent or a catalyst [156].

5.1.1 Methods of MCM-41 preparation

MCM-41 mesoporous materials are generally synthesised using the original preparation method reported by Beck *et al.* [157] in water under alkaline conditions. The original synthesis method has also been altered by many groups enhance, or alter, the material's physicochemical properties or to reduce preparation time. A list of different preparation methods are outlined in Table 5.1. In general terms the material can be produced using a variety of silica sources such as tetraethyl orthosilicate (TEOS) and organic ionic surfactants, such as cetyltrimethylammonium bromide (CTAB), in alkaline solution over a broad time/temperature regime to form an ordered organic–inorganic composite material [158]. The mechanism of the inorganic–organic composites formation is thought to be based on electrostatic

interactions between the positive charged on surfactant micelles and the negative charged silicate species as illustrated in Figure 5.1[159].

Numerous studies have investigated mechanisms for the formation of MCM-41; Figure 5.2 illustrates two main pathways: pathway 1 indicates formation by liquid crystal phases and pathway 2 using silica anions. The number of different pathways discussed is as a result of changes in surfactant properties and depends on the concentration of the surfactant in water and the presence of other ions. In pathway 2, MCM-41 was synthesised at low surfactant concentrations below the critical micelle concentrations [83, 160]. Beck and co-workers (1992) suggested that the formation of these materials is by a liquid-crystal templating (LCT) mechanism. The organic surfactants arrange themselves in liquid crystal phases independently of the inorganic crystallization, then the silica precursor polymerizes around the self-assembled. In support of LCT mechanism the structure and pore dimension of MCM-41 materials are closely linked to the properties of surfactant such as, chain length and concentration [160, 161].

Table 5.1 Modification methods used to prepare MCM-41

No.	Surfactant	pH adjustment	Silica source	Condensation time and temperature	Method of template removing	Characterisation			Ref.
						BET surface area ($m^2\ g^{-1}$)	pore volume V_p ($cm^3\ g^{-1}$)	Pore size (nm)	
1	CTAB + TEAOH	H_2SO4 at PH 9.5-10	Sodium silicate	98 h at 96 ^{0}C	Calcined at 560 ^{0}C for 10 h	1516	1.29	3.0	[162]
2	CTAB	NaOH	TEOS	96 h at 100 ^{0}C	SFE at 85 ^{0}C and 90 bar	1250	0.78	2.79	[163]
3	CTAB	NaOH	Kromasil	144 h at 115 ^{0}C	Calcined at 550 ^{0}C for 5 h.	845	0.83	3.1	[164]
4	CTAB	H_2SO_4	Sodium silicate	49 h at 100 ^{0}C	Calcined at 550 ^{0}C for 6 h.	1018	0.81	2.45	[165, 166]
5	CTAB	TMAS	TEOS	48 h at 150 ^{0}C	Calcination at 540 ^{0}C for 7 h	1040	-----	3.70	[157]
6	CTAB	diethylamine	TEOS	72 h at 100 ^{0}C	Calcination at 550 ^{0}C for 6 h	1012	0.91	2.73	[49, 167]

7	CTAB	TAAB & sulfuric acid	fumed silica	168 h at 100 ^{0}C	Calcination at 550 ^{0}C for 6 h	1136	0.61	2.26	[168]
8	MTAB	sodium hydroxide	sodium silicate	1 h Microwave at 100 ^{0}C	Calcination at 550 ^{0}C for 6 h	1020	0.745	2.10	[169]
9	CTAB	aqueous ammonia	TEOS	12 h at 90 ^{0}C	Calcination at 550 ^{0}C for 5 h	1070	0.85	3.19	[170]
10	CTACl	aqueous ammonia	TEOS	24 h at 100 ^{0}C	Solvent extraction ethanol/HCl	1003	0.35	2.50	[171]
11	HDTMAB	sodium hydroxide	TEOS	10 h at 100 ^{0}C	Solvent extraction ethanol/HCl	1070	0.664	2.42	[172]
12	CTAB	TEAOH [k]	sodium silicate	96 h at 96 ^{0}C	supercritical fluid extraction (SFE)	1332	0.81	2.92	[163, 173]
13	CTAB	aqueous ammonia	TEOS	4 h at 35 ^{0}C	Calcination at 550 ^{0}C for 5 h	813	0.69	2.53	[153]
14	CTAB	aqueous ammonia	TEOS	4 h at 35 ^{0}C	Microwave digestion at 200 ^{0}C	760	6.74	0.99	[153]

*Abbreviations in this table were: Cetyl trimethyl ammonium bromide (CTAB), tetramethylammonium silicate (TMAS), tetraethyl orthosilicate (TEOS), tetraalkylammonium bromide (TAAB), cetyl trimethylammonium chloride (CTACl), hexadecyltrimethylammonium bromide (HDTMAB), tetraethylammonium hydroxide (TEAOH) and Myristyltrimethylammonium bromide (MTAB).

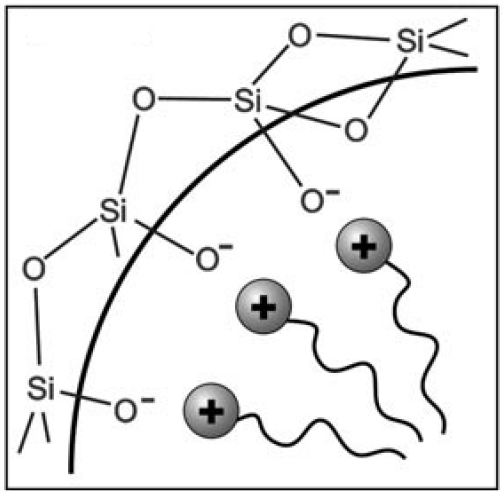

Figure 5.1 Electrostatic interactions between silicate anions on the surface of the micelles [159]

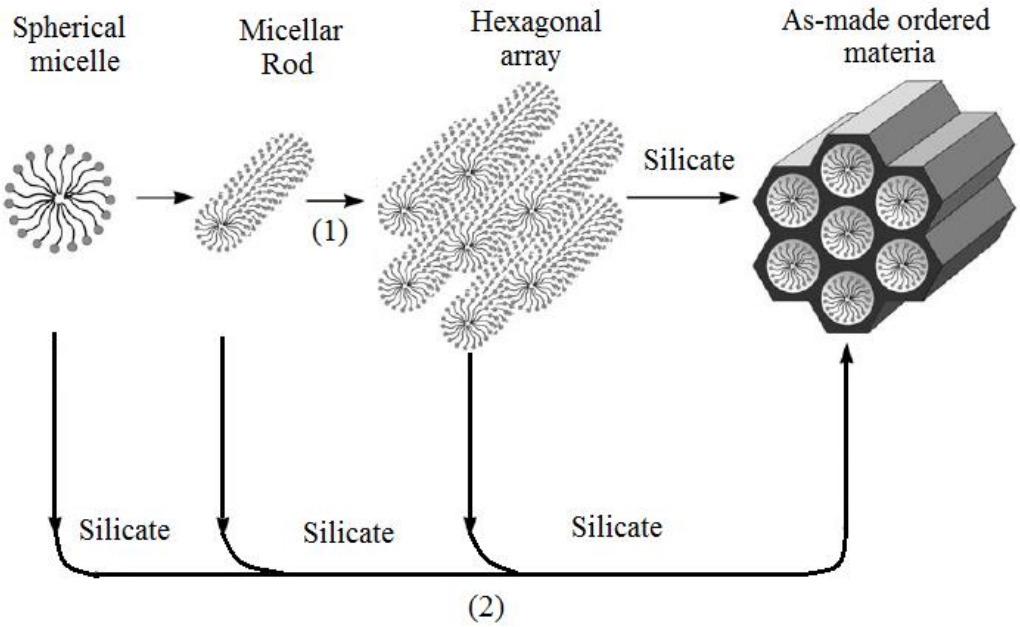

Figure 5.2 Two possible mechanistic pathways for formation of MCM-41: (1) liquid crystal phase and (2) silica anion [83].

The organic template is removed from the as-synthesised materials by calcination, solvent extraction, or microwave digestion (MWD) to obtain porous materials (see Figure 5.3). As-synthesised products are typically calcined at 550 ^{0}C for 5 h [164], or dissolved in mixture of nitric acid and hydrogen peroxide as the oxidative agents using a microwave at 200 ^{0}C to remove the organic template leaving the porous silica network [153, 174]. The nature of the organic surfactant, including the length of the carbon chain, the aqueous concentration, the mole ratio of surfactant:silica, and reaction conditions are all significant factors in determining the nature of the final MCM-41 product formed.

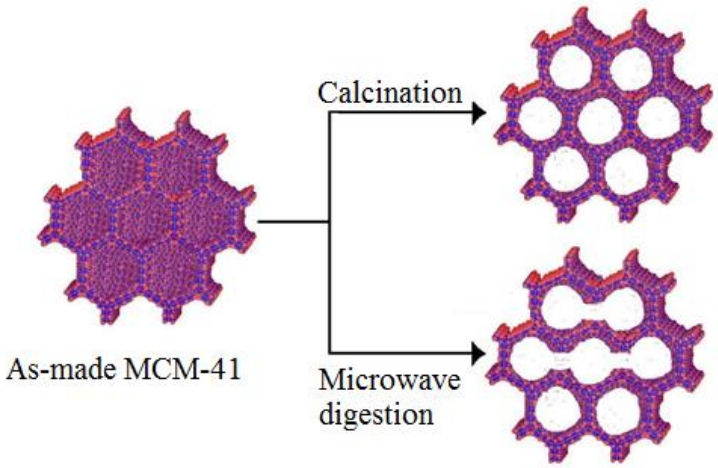

Figure 5.3 Schematic of template removal from as-made MCM-41 by calcination and microwave digestion[153].

5.1.2 SBA-15 preparation method

SBA-15 is an ordered mesoporous silica structure, synthesized from silica sources in the presence of amphiphilic triblock copolymers. Pluronic P123 (EO_{20} $PO_{70}EO_{20}$) and Pluronic F127 (EO_{106} $PO_{70}EO_{106}$) are the most common block lengths used as templating agents. The presence of external PEO blocks as hydrophilic portions and the internal PPO as hydrophobic blocks leads to the construction of micelles with a hydrophobic PPO core surrounded by hydrophilic PEO blocks. TEOS, tetramethyl orthosilicate, or sodium silicates are used as a typical silica source in the SBA-15 preparation. The organic structure-directing agents can be easily removed by calcination at 140 °C for 3 h, or refluxing in ethanol (EtOH) [143, 175]. Under acidic conditions, and at room temperature, alkyl-ethylene oxide often favours the formation of cubic silica phases, whereas poly (alkylene oxide) triblock copolymers tend to form the hexagonal mesoporous silica structures. Different mesoporous structures include, cubic, three-dimensional hexagonal, and lamellar structures [155]. The SBA family can be synthesis by using different lengths of block and copolymer chains. For example, a cubic mesoporous silica phase (SBA-11) was synthesized in the presence of $C_{16}EO_{10}$ surfactant species, with high surface area 1070 m^2 g^{-1} and pore size of 2.5 nm, while $C_{18}EO_{10}$ was used to syntheses three-dimensional

hexagonal mesoporous silica structures (SBA-12). In addition, novel cubic mesoporous silica (SBA-16) can be synthesised using a large chain EO group, such as $EO_{106}PO_{70}$ EO_{106} with a surface area of 740 m^2 g^{-1}, and pore size of 5.4 nm. The typical poly (alkylene oxide) triblock copolymers are $EO_{20}PO_{70}$ EO_{20} which are used to synthesis highly ordered hexagonal structures (SBA-15) with a high surface area (690 – 1040 m^2 g^{-1}), large pore size 4.6 - 30 nm, unusually large pore volume of up to 2.5 cm^3 g^{-1}, and silica wall thicknesses ranging from 3.1 – 6.4 nm [143].

In general, the synthesis of solid powder SBA-15 was achieved by dissolving the template polymer in an acidic solution and adding a silica source. The mixed solution is aged at a temperature which is slightly above room temperature for 20 to 24 h and heated up to 80 to 100 ^{0}C either in a conventional oven or in a microwave oven for an appropriate time. The precipitated solids are centrifuged, washed and dried.

5.1.3 Use of mesoporous silicates for extraction of VOCs and H_2CO from indoor air

Mesoporous silicas with high surface areas have excellent adsorbent properties, due to its uniform pore size, open pore structure and dependable desorption performance; all necessary factors when selecting an appropriate sorbent for the removal of VOCs from indoor air [91, 176]. The use of mesoporous materials as adsorbents has many advantages as they can be used to adsorb VOCs at room temperature with high capacity, they can be reactivated easily with hot air (120-150 ^{0}C), they can be used to preconcentrate recovered VOCs by 3-10 times and they can be used to trap a wide range of VOCs [177].

Sorbents most commonly used to adsorb VOCs include, Tenax TA, Carbotrap, activated charcoal, silica gel, MCM-41 and SBA-15 [178]. However, silica gel and activated charcoal are rarely encountered where high thermal desorption is required because their high activities can lead to sample degradation at high desorption temperatures. Conversely, Tenax TA has limited applications for adsorption of VOCs at high concentrations due to its low surface area (about 35 m^2 g^{-1}) and low adsorption capacities [122]. Wu *et al.* [179] compared the adsorption properties of

mesoporous silica MCM-41 and microporous carbon molecular sieves for VOCs (more than 50 target compounds with size varying C_2-C_{12}). The results demonstrated that carbon sorbents quantitatively absorbed a wider range of the VOCs from C_2-C_{12} while MCM-41 sorbents adsorbed significantly larger molecules from C_8-C_{12}. In addition, the thermal desorption temperatures required to release the trapped VOCs (C_8-C_{12}) from MCM-41 were at moderate temperatures of 150 ^{0}C, whereas the microporous carbon sorbents required higher desorption temperatures of 300 ^{0}C for sufficient recovery [179]. Serrano *et al.* [180] compared the adsorption properties of mesoporous MCM-41 and SBA-15 for the removal of toluene and isopentane from air, and used a thermal desorption technique. The results showed that the MCM-41 and SBA-15 were capable of adsorbing toluene and isopentane in significant amounts. The best combination of amount adsorbed, adsorption strength and hydrophobicity was obtained by MCM-41(H-sg) prepared by sol-gel method whereas MCM-41(H-ht) obtained by a hydrothermal treatment presents a very weak interaction with toluene and isopentane, which leads to low adsorption amounts for these compounds.

In contrast, a different behaviour was observed for pure silica SBA-15 adsorbent for these compounds, it led to small adsorption amounts but with a high strength of interaction between the adsorbent and adsorbate. These results related to presence of microporous SBA-15 walls with connecting mesoporous channel structures. The adsorption was limited by the small microporous area available, although the location of the adsorbate molecules within these micropores occurs with a stronger interaction than in the case of the mesopores [180].

Functionalisation of mesoporous silica, such as MCM-41 and SBA-15, by inorganic-organic groups has been used to modify the adsorption properties of mesoporous materials, to increase their surface area and hydrothermal stability and to lead to a greater adsorption selectivity of compounds [181]. Lim *et al.* [144] prepared the vinyl-functionalised mesoporous silica (v-MCM-41) and compared the hydrothermal stability with conventional MCM-41. The results showed that the hydrothermal stability of v-MCM-41 in water was higher than conventional MCM-41 due to increased channel wall thickness and hydrophobicity. Many inorganic-organic

groups can be used for functionalisation of mesoporous materials for example organic amine has been used as a functional group to adsorb carbonyl compounds (C=O) such as H_2CO [182]. However less is known about the ability of mesoporous materials to remove H_2CO vapour and of the few studies that have been published [183-185] limited data was provided to support the sampling and extraction methods used.

Further, recent modifications in the preparation methods of MCM-41 and SBA-15 present several major advantages including low temperature synthesis, a broad ranged and controllable pore widths and increased thermal stability. Functional groups can be introduced onto the silica surface to increase the adsorption performance of mesoporous silica for specific targets such as H_2CO. Table 5.2 illustrates the diversity of MCM-41 and SBA-15 as potential VOC and H_2CO scavengers.

Table 5.2 Physical properties of mesoporous silica used to adsorb VOCs or H_2CO from indoor air.

Sorbent	S_{BET} ($m^2\ g^{-1}$)	V_p ($cm^3\ g^{-1}$)	BJH Dp (nm)	Functional Group	Adsorbates	Ref.
MCM-41	1065	0.73	2.3	Pure Silica	Toluene, isopentane	[186]
MCM-41	1030	----	2.9	Pure Silica	C_7–C_{12}	[179]
MCM-41	1060	0.87	----	Pure Silica	Benzene, n-hexane	[155]
MCM-41	1086	0.86	3.5	Pure Silica	Dichloromethane, benzene	[187]

MCM-41	734	0.76	----	Pure Silica	Ethane, Ethylene	[188]
SBA-15	594	0.85	6.4	Pure Silica	Toluene, isopentane	[180]
SBA-15	501	1.14	8.2	Pure Silica	Cyclohexane, benzene	[189]
SBA-15	577	1.03	5.6	Me-SBA-15	Cyclohexane, benzene	[189]
SBA-15	354	0.41	----	Vinyl-SBA-15	Benzene, n-hexane	[182]
SBA-15	698	1.2	----	Pure Silica	Benzene	[190]
MCM-41	1111	0.67	2.51	APTES-MCM-41	H_2CO	[183]
MCM-41	937	0.54	2.38	AEAPMDMS-MCM-41	H_2CO	[183]
MCM-41	777	0.53	2.33	TMSPDETA-MCM-41	H_2CO	[183]

*Abbreviations used in this table were: 3-aminopropyltriethoxysilane (APTES), N(b-aminoethyl) g-aminopropylmethyl dimethoxysilane (AEAPMDMS), and N1-(3-(trimethoxysilyl)-propyl) diethylenetriamine (TMSPDETA).

Since the main aims of this chapter were to first use amino functionalised mesoporous materials for chemisorption of H_2CO vapour from indoor air in addition to employing non functionalized materials as VOCs scavengers, the aims of this chapter can be broken down as follows:

i) synthesis of two types of mesoporous materials, MCM-41 and SBA-15 with high surface area and larger pores,

ii) examination of adsorption extraction performances for selected VOCs from polluted air and comparison of efficacies to commercial Tenax TA,

iii) to functionalise mesoporous materials by an organic amine group to enhance their adsorption properties toward H_2CO extraction,

iv) to investigate the chemisorption of H_2CO on NH_2-sorbents and

v) to examine the efficiency of functionalized materials for H_2CO extraction in passive sampling mode.

5.2 Experimental

5.2.1 Synthesis of mesoporous silicates (C-MCM-41, MWD-MCM-41, SBA-15)

As-made MCM-41 was prepared as described in Section 3.1.1, and the surfactant CTAB was removed from the silica framework of as-MCM-41 by calcination at 500 ^{o}C for 5 h or microwave digestion (as outlined in Section 3.1.1) to produce C-MCM-41 or MWD-MCM-41 respectively. SBA-15 was prepared as described in Section 3.1.2.

5.2.2 Functionalization of C-MCM-41, MWD-MCM-41, SBA-15

Sorbents (C-MCM-41, MWD-MCM-41 or SBA-15) were functionalized by the post synthesis grafting process as outlined in Section 3.1.3, using 3-aminopropyltrimethoxysilane as a functional organic amine group to produce NH_2-C-MCM-41, NH_2-MWD-MCM-1 or NH_2-SBA-15, respectively. These modified-sorbents were used to chemisorb H_2CO from air.

5.2.3 Characterisation of mesoporous silicates

All materials were characterized as described in Section 3.2. SAS-XRD was used to examine the periodicity of the material structure. Surface area, pore size and pore distribution were measured by nitrogen adsorption-desorption isotherms (BET isotherm). Further characterisations were carried out by ATR-FTIR spectroscopy and microanalysis to confirm the removal of organic templates from as-made materials and the presence of the amino group after functionalization.

5.2.4 Set up of dynamic atmospheric systems

Two dynamic atmospheric systems were used to generate constant concentrations of the selected VOCs or H_2CO vapour in separate sampling chamber as illustrated in Figure 3.1 (see Section 3.3.1). The first sampling chamber contained 34, 18, 12 and 7.8 mg cm^{-3} of toluene, EB, cumene or DCB, respectively, whereas the second chamber contained 1.4 mg cm^{-3} of H_2CO.

5.2.5 VOCs sampling method set up

Sampling tubes loaded with different sorbents (C-MCM-41, MWD-MCM-41 or SBA-15) were prepared and conditioned by the thermal desorption unit TDU as described in Section 3.3.3 prior to VOC collection. The flow rate of contaminated air exiting from the sampling chamber was set to 100 cm^3 min^{-1} for all experiments and the experimental masses expected to be present in a 100 cm^3 aliquot of contaminated air were measured by sampling tubes loaded with Tenax TA "as a reference sorbent". Masses of 2109, 404, 479 or 494 ng of toluene, EB, cumene or DCB, respectively were trapped. These masses will be used as "reference masses" to examine the performance of studied sorbents for VOCs adsorption.

5.2.6 H_2CO sampling method set up

5.2.6.1 Active sampling mode

In active sampling mode, functionalised and non-functionalised sorbents were conditioned at 120 °C for 2 h before they were mixed with glass bead and loaded into glass tubes to prepare sampling tubes (see Section 3.3.3). The flow rate of

contaminated air was set to100 cm^3 min^{-1} and the sampling time was selected to be 60 min for all experiments. Silica cartridges impregnated with a 2,4-DNPH trapping solution were used to collect H_2CO vapour from the exiting air and the masses of H_2CO were determined by LC-UV-vis. The average detected masses (8.12 μg) were used as expected or "reference" masses that were used to compare extraction efficiencies of the different sorbents for H_2CO adsorption.

5.2.6.2 Passive sampling mode

H_2CO vapour was generated inside an environmental chamber at 1.4 mg m^{-3} and left overnight prior to addition of sorbents. Sampling cartridges impregnated with 2,4-DNPH trapping solution were used to remove 500 cm^3 of contaminated air from the chamber immediately prior to sorbent addition (see Figure 5.4a), and the mass of H_2CO present in the air sample was determined as approximately 1.2 μg by the LC-UV-vis instrument. MWD-MCM-41, SBA-15, NH_2-MWD-MCM-41 or NH_2-SBA-15 were all added to the chamber and assessed for the passive extraction of formaldehyde vapour from air. In the first experiment, MWD-MCM-41 was pre-treated at 120 ºC for 2 h and 100 mg of the sorbent was immediately placed inside the chamber as shown in Figure 5.4b and left to passively adsorb H_2CO vapour. Subsequent decreases in H_2CO concentration, which were attributed to sorbent extraction, were determined by analyses of further 500 cm^3 aliquots of air (see Figure 5.4c). Concentrations were recalculated after each aliquot of air was removed from the chamber to correct for dilution and measurements were taken at 5, 10, 15, 20, 25, 30 or 35 min after sorbent addition. The experiments were repeated under the same conditions for each sorbent (SBA-15, NH_2-MWD-MCM-41 or NH_2-SBA-15) and the chamber was reconnected to the permeation device and left overnight again to ensure that the generation of H_2CO concentration was constant before each experiment. A control experiment was also measured with no sorbent inside the chamber to measure the decrease of H_2CO concentration after each 500 cm^3 aliquots of air.

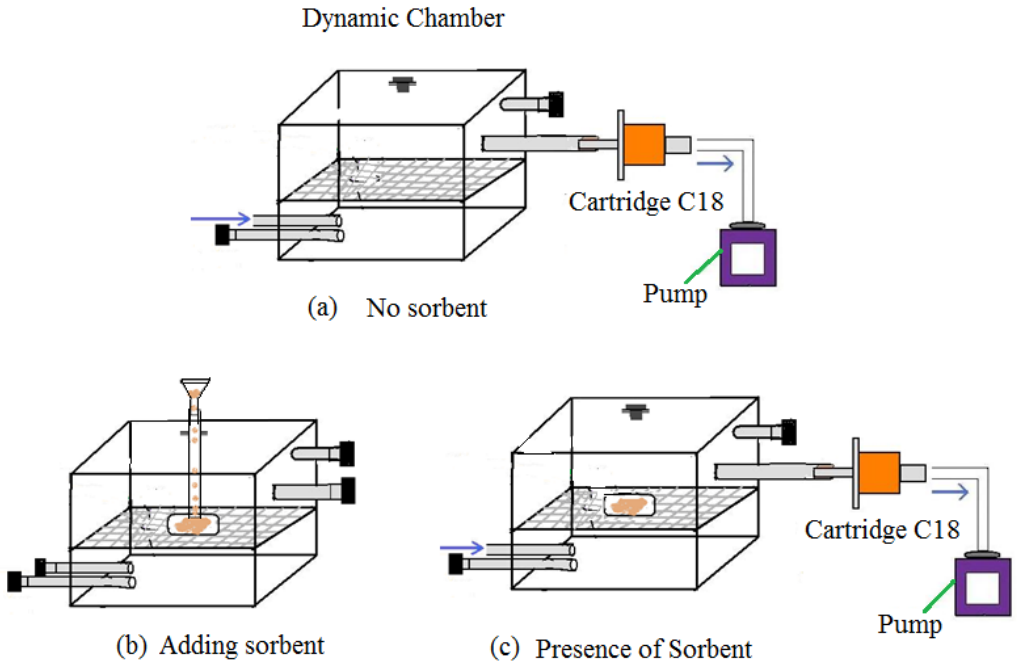

Figure 5.4 Set up of passive sampling mode illustrating sampling scheme when (a) no sorbent was added, (b) the addition of sorbent to the sampling chamber and (c) sampling with sorbent present.

5.3 Results and discussion

5.3.1 Sorbents characterisation by XRD and N_2 adsorption isotherm

The SAS-XRD patterns of SBA-15, MWD-MCM-41 or C-MCM-41 samples are shown in Figure 5.5. All adsorbents had the typical (100) diffraction peak at a 2θº angle of 0.925 or 2.27 for SBA-15 or C-MCM-41 and MWD-MCM-41 with an intensity of approximately 16700, 10300 or 6000, respectively. The patterns of C-MCM-41 and SBA-15 had weaker peaks assignable to (110) or (200) reflections, confirming their increased periodicity. The ordering of pores in C-MCM-41 and SBA-15 was confirmed by the TEM as indicated in Figure 5.6. In contrast, pore ordering was not apparent in the TEM micrograph for MWD-MCM-41 indicating that the harsh conditions used during microwave digestion significantly reduced the periodicity of the pores in the material.

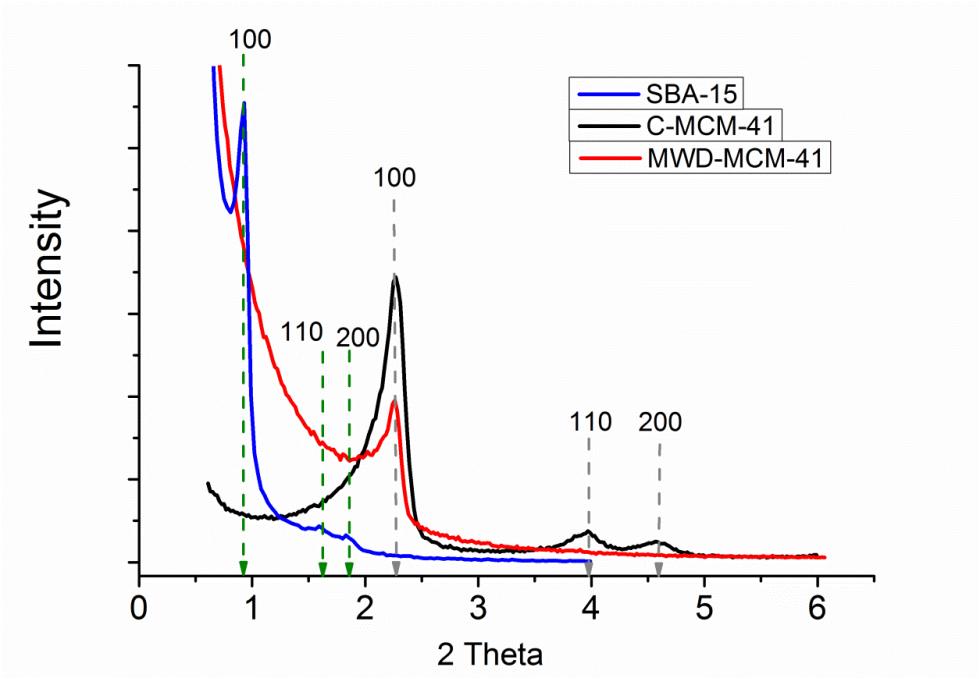

Figure 5.5 SAS-XRD patterns of C-MCM-41, MWD-MCM-41 and SBA-15

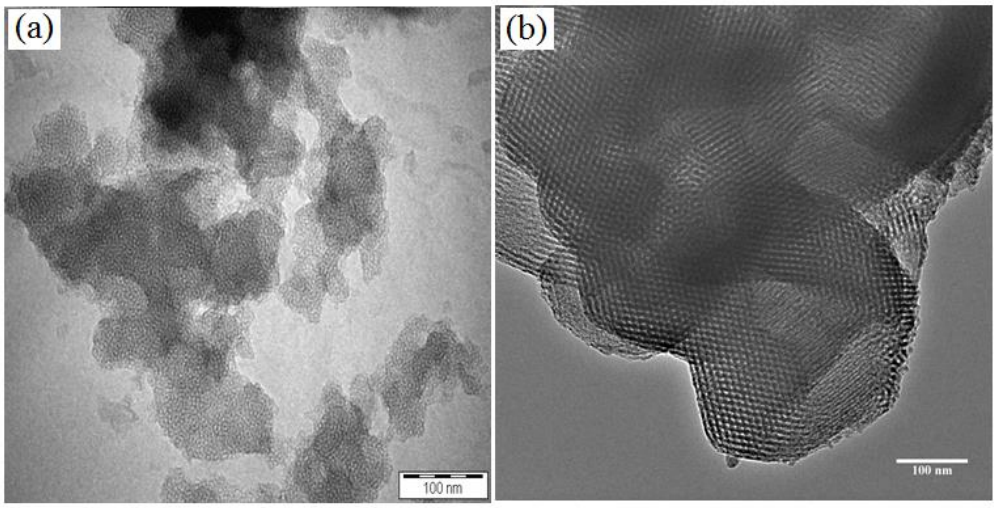

Figure 5.6 Representative TEM images of (a) MCM-41 and (b) SBA15

N_2 sorption isotherms provided the physicochemical properties of prepared materials before and after functionalization as summarised in Table 5.3. The results showed that surface areas of C-MCM-41 and SBA-15 were measured at 1014 ± 4.6 and 644 ± 7.9 m^2 g^{-1}, respectively, which are in agreement with data commonly reported in the literature, (for example 1050 m^2 g^{-1} [170] and 678 m^2 g^{-1} [165] for C-MCM-41

and SBA-15). Interestingly the results demonstrated that surface area of MCM-41 was significantly reduced (from 1014 ± 4.6 to 760 ± 1.1 m^2 g^{-1}) when microwave digestion was used to remove the organic template from network of as-MCM-41. There was also a significant increase in the average pore size from 2.7 to 6.74 nm (see Figure 5.8) when microwave digestion was used to remove the template.

Table 5.3 Physical characterisation data of modified and non-modified mesoporous adsorbents.

Sorbents	BET Surface Area (m^2 g^{-1})[a]	Pore Size (nm)[b]	Pore Volume (cm^3 g^{-1})[c]
C-MCM-41	1014 ± 4.6	2.7	0.82
NH_2-C-MCM-41	824 ± 19.7	2.2	0.32
MWD-MCM-41	760 ± 1.1	6.74	0.99
NH_2-MWD-MCM-41	173 ± 1.7	N/A	0.25
SBA-15	644 ± 7.9	6.93	0.82
NH_2-SBA-15	127 ± 0.7	6.1	0.24

[a] Calculated by BET model from sorption data at range 0.05-0.25 of relative pressure.

[b] Calculated by BJH model from the sorption branches of isotherm.

[c] Calculate from N_2 adsorbed at a relative pressure P/P_0 of 0.99.

N/A no clear size seen, only broad line (See Figure 5.10)

The N_2 sorption isotherms for C-MCM-41, MWD-MCM-41 and SBA-15 (Figure 5.7) illustrated that a typical type IV isotherm was measured for all adsorbents confirming their mesoporosity. However, capillary condensation steps for MWD-MCM-41 was observed at a slightly higher relative pressure of 0.55- 0.70 compared to C-MCM-41 at 0.28- 0.39. This indicated that the high pressure induced in the microwave resulted in pore wall tear-down leading to the production of larger pores with a wider pore size (see also Figure 5.8). C-MCM-41 had an isotherm which did not contain hysteresis loop which indicates the production of a material with a narrow range of well-defined pores; this was confirmed by the pore distribution plot as given in Figure 5.8.

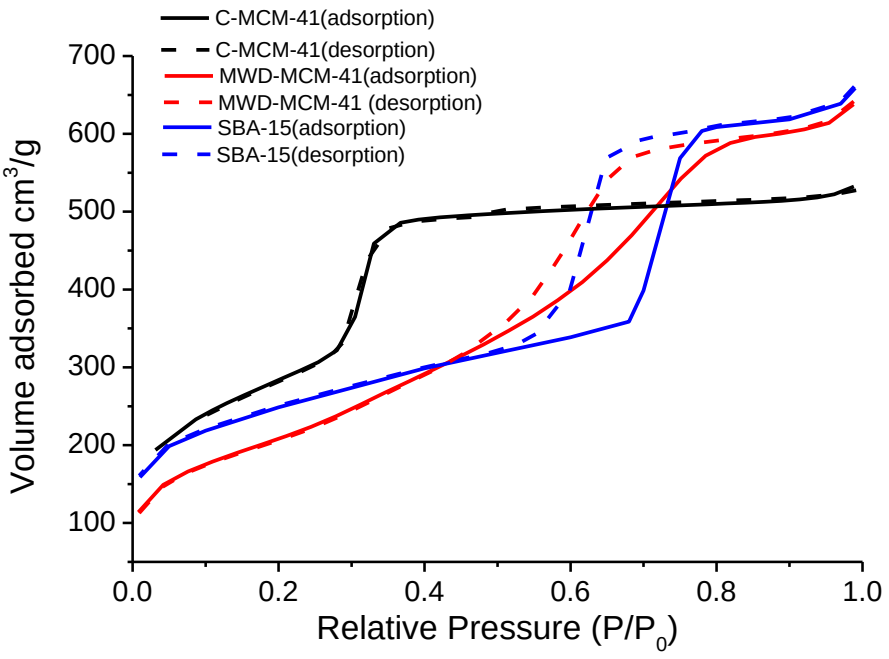

Figure 5.7 Nitrogen adsorption isotherms of C-MCM-41, MWD-MCM-41 and SBA-15

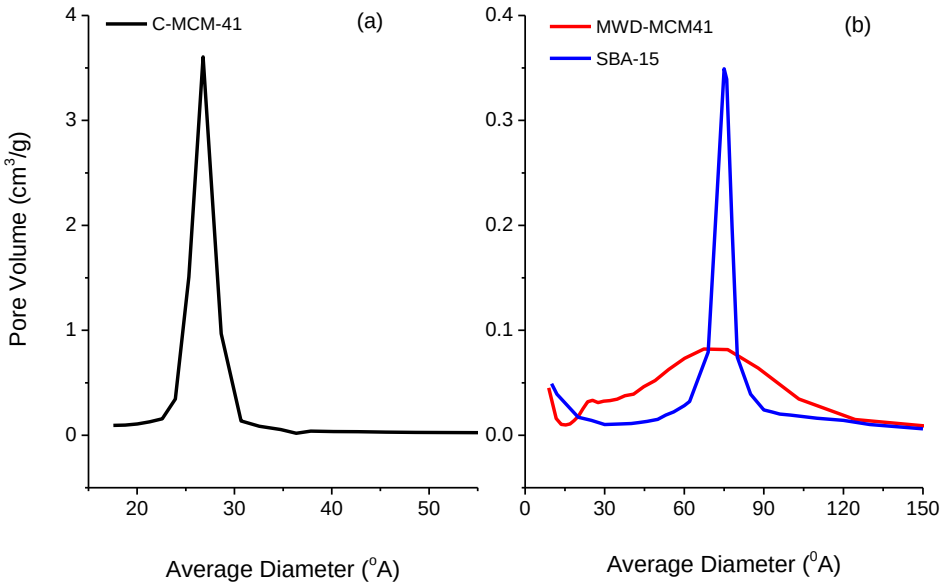

Figure 5.8 BJH pore size distribution patterns of (a) C-MCM-41, (b) MWD-MCM-41 and SBA-15.

The physicochemical properties of functionalized materials (NH_2-C-MCM-41, NH_2-MWD-MCM-41 and NH_2-SBA15) obtained from N_2 sorption isotherms

(summarised in Table 5.3) demonstrated a slight decrease of C-MCM-41 surface area (1014 to 824 m^2 g^{-1}) after functionalisation by amino organic group producing NH_2-C-MCM-41. In contrast, significant reductions of MWD-MCM-41 and SBA-15 surface areas (760 ± 1.1 to 173 ± 1.7 m^2 g^{-1} or 644 ± 7.9 to 127 ± 0.7 m^2 g^{-1}, respectively) were observed (see also Figure 5.9). Since all materials were functionalised using the same procedure and reagents, the greater reduction in surface areas were thought to be related to the larger pore sizes which allowed a greater coverage of functional groups on the internal surface of the pores. Successful functionalisation was also confirmed by examination of the ATR-FTIR spectra and elemental microanalysis (See Section 5.3.2).

Measured isotherms for NH_2-C-MCM-41 and NH_2-SBA-15 were similar to those previously measured for materials prior to functionalisation; this implies that the materials retained their structure (isotherm type IV, pore size) as shown in Figure 5.9 and Figure 5.10. In contrast the structure of MWD-MCM-41 was altered after functionalisation as confirmed by plotting the pore distribution as shown in Figure 5.10. Interestingly the SAS-XRD patterns of functionalized materials (NH_2-C-MCM-41, NH_2-MWD-MCM-41 and NH_2-SBA15) shown in Figure 5.11 demonstrated that all adsorbents had similar patterns after functionalisation. They possed the typical (100) diffraction peak at a 2θº angle of 0.75 with an intensity of approximately 16000. In addition reflections assignable to the (110) reflection at a 2θº angle of 2 with a significant intensity of approximately 5000 and a weak reflection (200) at a 2θº angle of 3, were also present confirming their high periodicity. Overall the results confirmed the production of functionalised adsorbents with alteration of their initial structures as result of recrystallization during the functionalisation processes.

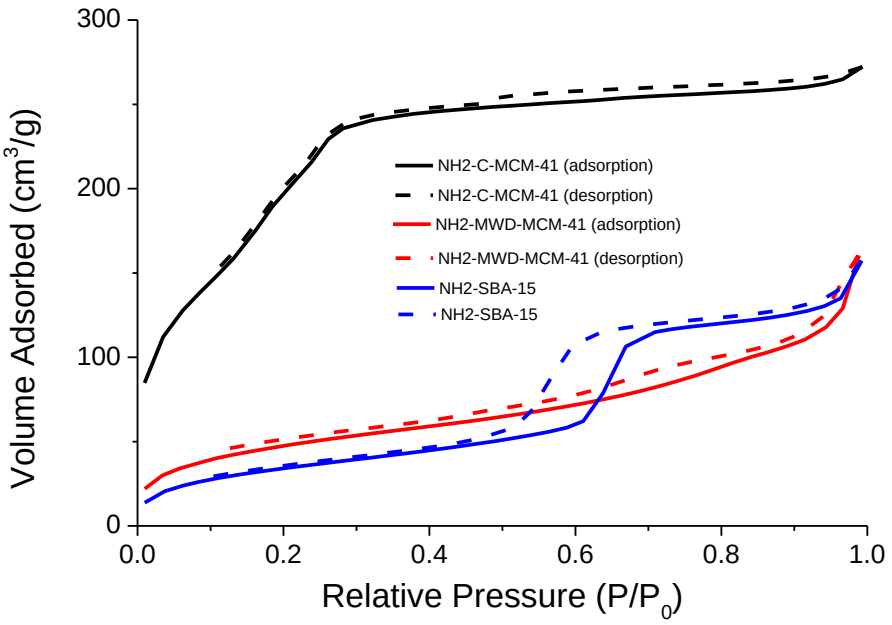

Figure 5.9 Nitrogen adsorption isotherms of NH_2-C-MCM-41, NH_2-MWD-MCM-41 and NH_2-SBA-15.

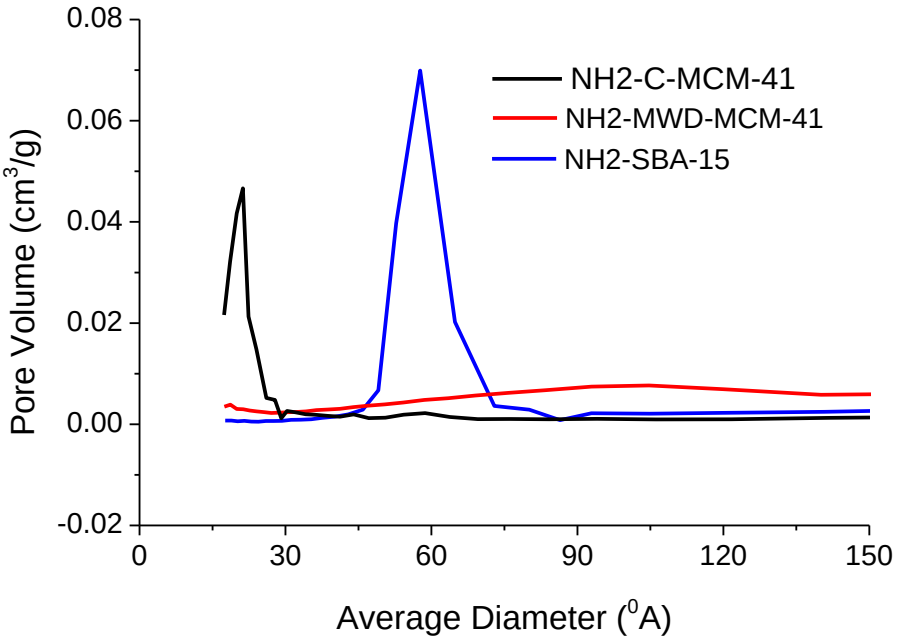

Figure 5.10 BJH pore size distribution patterns of NH_2-C-MCM-41, NH_2-MWD-MCM-41 and NH_2-SBA-15.

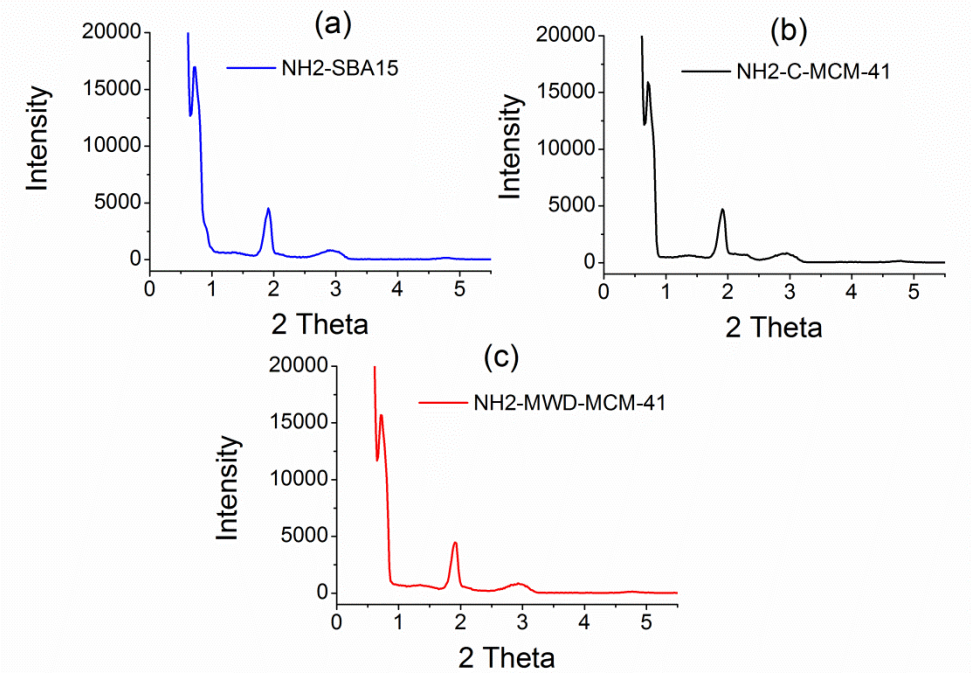

Figure 5.11 SAS-XRD patterns of (a) NH_2-SBA-15, (b) NH_2-C-MCM-41 and (c) NH_2-MWD-MCM-41.

5.3.2 ATR-FTIR spectra and elemental analysis of mesoporous silica samples

The ATR-FTIR spectra of silica samples (Figure 5.12), confirmed successful synthesis and functionalization of silica materials. The formation of silica materials was confirmed by the presence of peaks i-iii in Figure 5.12a which contained similar features expected of a silica material associated with the inorganic backbone; such as a large broad band between 1000 and 1250 cm^{-1} (i) and band at 800 cm^{-1} (iii) that were assigned to the Si–O–Si stretching and a band at 950 cm^{-1} (ii) which is assigned to the Si-OH. It was observed that the intensity of silanol groups bands for functionalised materials were considerably smaller compared to their original counterparts. Successful functionalisation of silica materials with amino groups was confirmed by the presence of peaks which appeared in the spectra at 1560 cm^{-1} and 1480-1490 cm^{-1} (v and vi in Figure 5.12b). These peaks were assigned to N-H and C-N respectively, were not evident in the spectra of the unmodified materials. The band

measured between 1635-1645 cm^{-1} (iv), which was present in all materials before and after functionalisation, was assigned to a water bending mode.

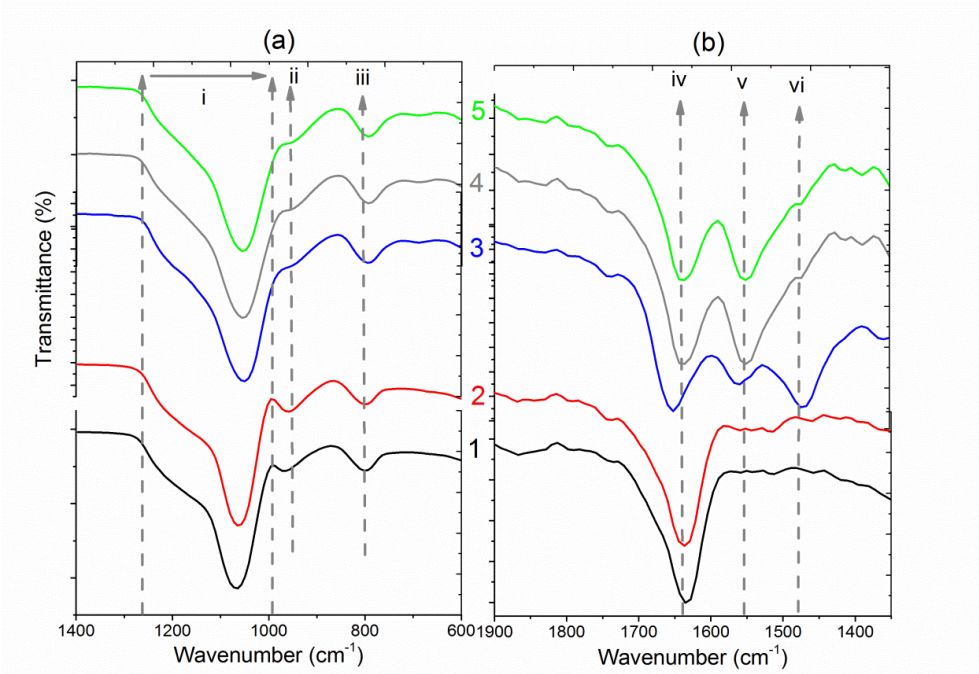

Figure 5.12 FT-IR spectra of MWD-MCM-41 (1), SBA-15 (2), NH_2-SBA-15 (3), NH_2-C-MCM-41 (4) and NH_2-MWD-MCM-41 (5) showing silica formation (a) and amine functionalisation (b).

The spectroscopic results were supported by elemental analysis summarised in Table 5.4. The percentage of nitrogen (% N) was measured at 1.81, 2.79 or 2.21 % for NH_2-C-MCM-41, NH_2-MWD-MCM-41 or NH_2-SBA-15 respectively. These percentages were used to estimate the degree of surface functionalisation (L_0) using the equation reported by Damian *et al.* [191]. The calculated values of L_0 (Table 5.4) demonstrated that a highest degree of functionalisation (L_0 = 1.99) was achieved for MWD-MCM-41, followed by SBA-15 (L_0 = 1.58), whereas the C-MCM-41 had the lowest degree at (L_0 = 1.29); despite possessing the highest surface area (1014 m^2 g^{-1}) of all materials. Hence the low degree of functionalization of C-MCM-41 could be attributed to its small pore size (2.7 nm) compared to the other materials. Since MWD-MCM-41 and SBA-15 had similar pore size and surface area, the difference in their degree of functionalisation (L_0) was attributed to the wider pore size distribution present in MWD-MCM-41 allowing greater accesses to the inner pores.

Table 5.4 Elemental analysis data recorded for the silica samples.

Silica materials	% C	% H	% N	$L_{0\,/}$ mmol g^{-1} [a]
As-MCM-41	22.48	5.14	1.26	-
C-MCM-41	Trace/Nil	0.50	Trace/Nil	-
NH_2-C-MCM-41	5.81	1.97	1.81	1.29
MWD-MCM-41	Trace/Nil	0.52	Trace/Nil	-
NH_2-MWD-MCM-41	8.2	2.32	2.79	1.99
SBA-15	Trace/Nil	Trace/Nil	Trace/Nil	-
NH_2-SBA-15	6.9	1.66	2.21	1.58

[a] Functionalisation degree (L_0 mill moles of nitrogen per gram of functionalised silica)

5.3.3 Use C-MCM-41, MWD-MCM-41 and SBA-15 for VOCs extraction

Before examining extraction efficiencies, or the dynamic capacities of the adsorbents for VOC extraction, the TDU-GC-MS was calibrated by standard solutions of selected VOCs using calibrant tubes which loaded with Tenax TA as described in Section 4.2.1. The resultant calibration curve for each VOC was used to calculate its masses adsorbed on studied adsorbents. Furthermore sampling tubes loaded with Tenax TA were used to determine experimental masses of VOCs generated in sampling chamber using an air flow rate of 100 cm^3 min^{-1} and a sampling time of 1 min, as outlined in Section 4.2.5. The sampling tubes were analysed by TDU-GC-MS and collected masses of VOCs were calculated using their calibration curves. The average of masses 2109, 404, 479 and 494 ng of toluene, EB, cumene and DCB, respectively, were used as "reference masses" to examine extraction efficiencies or dynamic capacities of adsorbents under study.

5.3.3.1 Effect of methanolic solution on masses of VOCs trapped on MCM-41

To investigate the influence of methanolic solutions on masses of VOCs trapped by MCM-41 adsorbents, two experiments for each adsorbent were used to collect VOCs

from sampling chamber. The contaminated air was sampled at flow rate of 100 cm^3 for 1 min for each sample under taken. In the first experiment, VOCs were collected by 3 sampling tubes (n=3) each containing C-MCM-41 or MWD-MCM-41, and each sampling tube was immediately analysed by the TDU-GC-MS without addition of the methanolic IS solution. A further set of 3 sampling tubes containing each adsorbent were then used to collect the VOCs under the same sampling conditions, and prior to analysis the direct-injection method was used to inject 5 µL of the methanolic IS solution. In this second set of experiments, sampling tubes loaded with Tenax TA were also placed after sorbent tubes to examine analyte breakthrough. The analytes collected by Tenax TA were measured by the TDU-GC-MS and the masses were calculated as (lost masses) which used to determine the breakthrough (% BT) of each VOC when direct injection method was applied.

For both MCM-41 adsorbents, the average calculated masses (n=3) summarised in Table 5.5 demonstrated that masses of all VOCs detected without injection of IS were significantly higher than that masses detected after injection of IS by direct-injection method. Interestingly breakthrough (% BT) of the VOCs were measured at approximately 30 % for C-MCM-41 (except for DCB which was slightly higher at 40 %), confirming the deleterious influence of introducing methanolic solutions onto Tenax TA loaded with VOC. Breakthrough was even higher for MWD-MCM-41 when used to collect VOCs under the same sampling conditions, the methanolic solution introduced with the IS gave breakthrough values a factor of 2 higher than for C-MCM-41. Therefore to permit accurate detection of VOCs collected by siliceous adsorbents it was recommended to avoid introducing a methanolic internal standard solution onto sampling tubes.

Table 5.5 Effect of methanolic solution on masses of VOCs trapped on MCM-41

Sorbents	C-MCM-41			
VOCs	T masses (ng)	EB masses (ng)	Cumene masses (ng)	DCB masses (ng)
Average without IS ± SD	1263 ± 52	247 ± 10	321 ± 8	414 ± 34
Average with IS ± SD	905 ± 60	178 ± 29	247 ± 39	240 ± 41
Average of lost masses ± SD	358 ± 40	69 ± 24	74 ± 32	174 ± 42
% BT	28 ± 3	28 ±10	23 ± 10	42 ± 10
Sorbents	MWD-MCM-41			
VOCs	T masses (ng)	EB masses (ng)	Cumene masses (ng)	DCB masses (ng)
Average without IS ± SD	1330 ± 120	277 ± 10	316 ± 12	421 ± 18
Average with IS± SD	758 ± 92	122 ± 13	136 ± 23	122 ± 13
Average of lost masses ± SD	572 ± 186	155 ± 13	180 ± 20	299 ± 24
% BT	43 ± 10	56 ± 4	57 ± 7	71 ± 4

5.3.3.2 Extraction efficiency of mesoporous adsorbents for VOCs adsorption

Sampling tubes loaded with C-MCM-41 or MWD-MCM-41 were used to examine their performance for VOCs extraction using the dynamic chamber. For all experiments, the flow rate of contaminated air was set at 100 cm^3 min^{-1} and sampling time was 1 min. Conditioned sampling tubes were used to sample 100 cm^{-3} of contaminated air, and the experiment was repeated 3 times (n=3). All samples were analysed by the calibrated TDU-GC-MS. Masses of VOCs adsorbed on each sample

were calculated from their obtained peak areas and calibration curves as described in Section 4.2.1 (see Table 5.6).

The average masses of VOCs collected by MCM-41 adsorbents, and their "references masses" collected by calibrant Teanx tubes under the same conditions were applied in Equation 3.5 (see Section 3.6) to obtain the extraction efficiencies of MCM-41 adsorbents. Whereas the extraction efficiency of SBA-15 was measured as reported by Idris [149]. The average masses of VOCs collected by SBA-15 were again compared to their masses collected by Tenax TA to provide extraction efficiencies for SBA-15 as given in Table 5.6.

The results showed that MCM-41 adsorbents had a similar performance for extracting VOCs (64 to 67 %) with slightly higher performance for DCB (83 to 85 %). Whereas different efficiencies were observed for SBA-15 which had higher efficiencies (80 and 96 %) for EB and cumene and but slightly lower values for toluene and DCB (56 and 69 %), respectively, when compared to MCM-41.

Table 5.6 Extraction Efficiencies of MCM-41 and SBA-15 adsorbents for VOCs

Sorbents	C-MCM-41				
VOCs	T	EB	Cumene	DCB	Total
Average ± SD	1263 ± 52	247 ± 10	321 ± 8	414 ± 34	2245
% RSD	4.13	4.00	2.52	8.13	
Ext. Eff. %	60	61	67	83	64
Sorbents	MWD-MCM-41				
Average ± SD	1330 ±	277 ± 10	316 ± 12	421 ± 18	2344
% RSD	9.02	3.47	3.65	4.31	
Ext. Eff. %	63	69	66	85	67
Sorbents	SBA-15 [149]				
Ext. Eff. %	56	80	96	69	69
% RSD	0.2	2.7	0.8	0.2	

5.3.3.3 Dynamic adsorption capacity of sorbents (Breakthrough)

The breakthrough and dynamic capacity of C-MCM-41 and SBA-15 were examined as described in Section 3.6 by passing the same contaminated air stream through sorbent tubes at 100 cm^3 min^{-1} for longer sampling times. The first sampling tube loaded with the studied sorbent was connected to a sampling port on the permeation chamber and a second sampling tube loaded with Tenax TA was connected in line immediately after the first sampling tube. The masses of VOCs passing through sorbent tubes were collected by Tenax TA sampling tubes which were analysed as outlined in Section 3.4.1. The breakthrough values for each VOC are shown in Figure 5.13 and were calculated by Equation 3.6 as the mass of VOC that passed through the sorbent tube divided by the mass of VOC trapped by the sampling tube, expressed as a percentage (see Section 3.6). By convention, breakthrough was defined when percentage values were greater than 5 %.

The results in Figure 5.13 indicated that toluene was the first analyte to exceed the breakthrough value for both sorbents. At a sampling flow rate of 100 cm^3 min^{-1}, the breakthrough of toluene occurred after sampling 1 or 1.3 dm^3 of contaminated air by C-MCM-41 or SBA-15, respectively. However C-MCM-41 had a higher surface area (1014 ± 4.6 m^2 g^{-1}) compared to SBA-15 (644 ± 7.9 m^2 g^{-1}), the results (Figure 5.13) demonstrated a slightly higher capacity for SBA-15 which was thought to be derived from the intrinsic pore connections between long 1D-mesopore channels and complementary micropores in its a bimodal pore system [91]. It is expected that a presence of micropores in pore network leads to the strong adsorption of VOCs (green arrows) and, moreover, an additional diffusivity of the adsorbed VOCs through the mesoporous (light brown arrows) as illustrated in Figure 5.14.

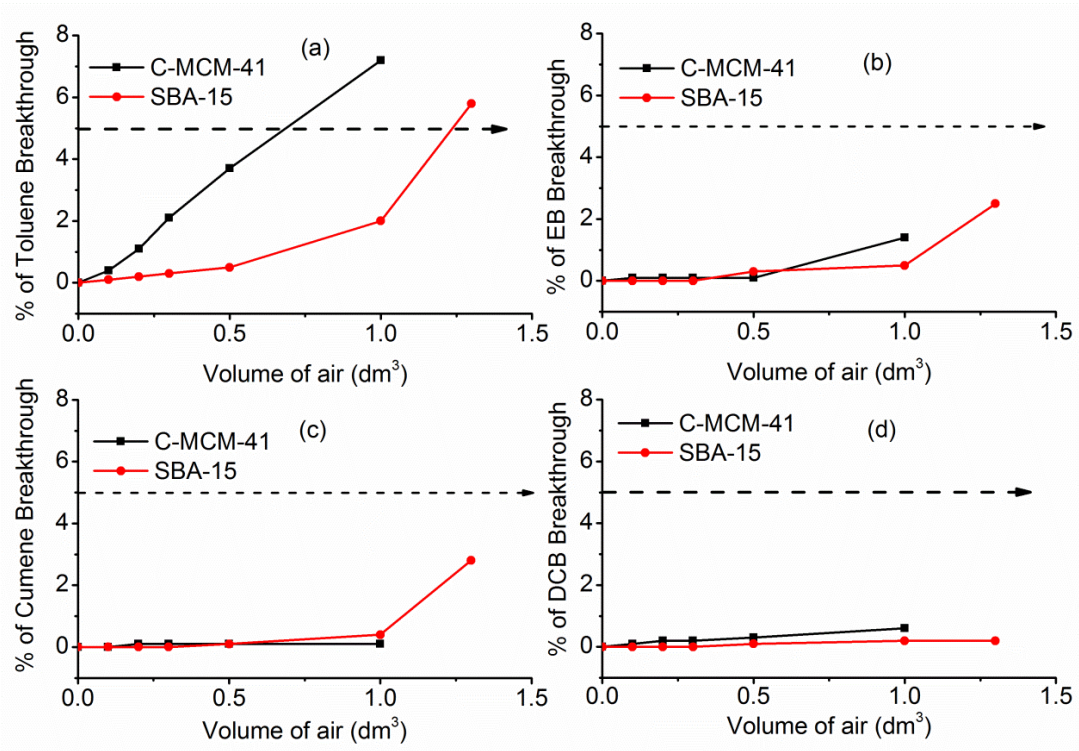

Figure 5.13 Calculated breakthrough volumes for toluene (a), EB (b), cumene (c) and DCB (d) on C-MCM-41 and SBA-15

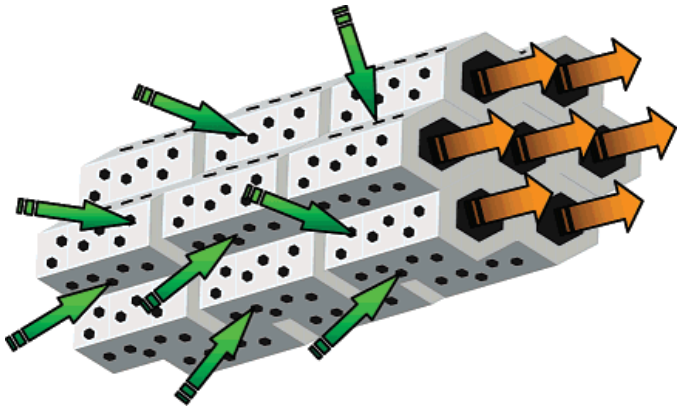

Figure 5.14 Schematic representation showing the effect of the bimodal pore system on VOC adsorption in SBA-15 [91].

When the concentration of analyte adsorbed on 1g of adsorbent was measured as masse per unit volume of air sampled at point of breakthrough (ng/cm^3), C-MCM-41 showed the highest dynamic adsorption capacity compared to SBA-15 (Figure 5.15).

However, SBA-15 had a higher capacity when normalised according to surface area (SA) as masses of VOCs trapped by surface of adsorbent (ng/m^2) see also Figure 5.15. These results provided some initial information required for understanding the dynamic adsorption of VOCs by mesoporous materials which relate to the complicated material characteristics (surface area, pore volume and pore structure).

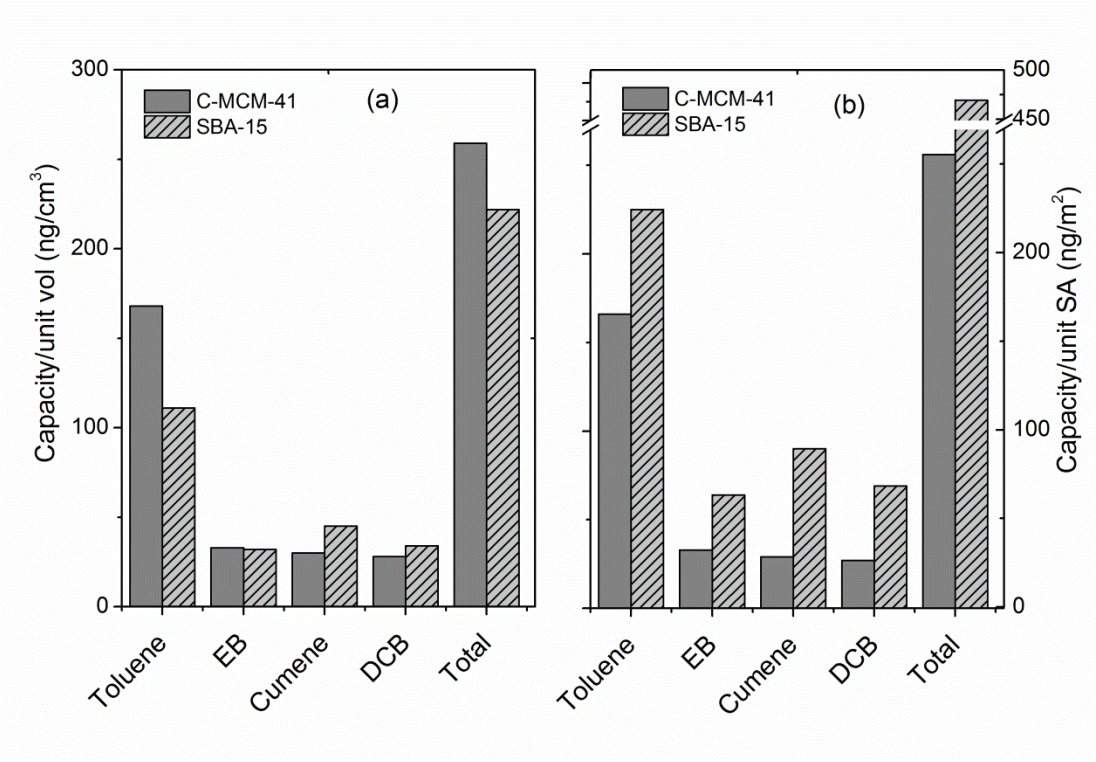

Figure 5.15 Capacity of C-MCM-41 and SBA-15 normalised a) unit volume and b) surface area

5.3.4 Use mesoporous sorbents for H_2CO extraction

5.3.4.1 Assessment of sorbents for H_2CO extraction in dynamic mode

Before determination of sorbent extraction efficiencies, H_2CO masses collected by 2,4-DNPH cartridges were determined using a flow rate of 100 cm^3 min^{-1} and sampling time 60 min. Sampling cartridges were washed by acetonitrile to extract F-DNPH derivate prior to detected by calibrated LC-UV-vis instrument, and masses of

collected H_2CO vapour concentrations were calculated as described in Section 4.4.2.2. Repeated sampling (n=4) of the chamber with the chosen conditions provided an average mass of 8.1 µg with an RSD value of 4.6 %.

5.3.4.1.1 Sorbents extraction efficiencies and capacities when used in active mode

Sorbent tubes loaded with non-functionalised sorbents (MWD-MCM-41 and SBA-15) and functionalised sorbents (NH_2-MWD-MCM-41 or NH_2-SBA-15), were used to extract H_2CO vapour from the dynamic system. To assess the efficiency of these sorbents for H_2CO extraction, a sampling tube was placed immediately before the hydrazine trapping cartridge (see Figure 3.11 in Section 3.6). Sorbents were placed in-line and experiments were repeated (n= 3). Sorbent efficiencies were calculated by using measured masses (wt_{nosorb} and wt_{sorb}) as given in the equation 3.5 in Section 3.6. Functionalised sorbents (NH_2-MWD-MCM-41 and NH_2-SBA-15) gave high performance values of 96 % for the extraction of H_2CO vapour from 1.4 mg m^{-3} of contaminated air, as illustrated in Figure 5.16 whereas non-functionalised sorbents (MWD-MCM-41 and SBA-15) had lower extraction efficiencies at approximately 70 %.

Furthermore dynamic capacities of selected sorbent were determined by measuring H_2CO breakthrough (see Figure 5.17). The results demonstrated that H_2CO breakthrough occurred rapidly for non-functionalised sorbents MWD-MCM-41 or SBA-15 with breakthrough values of 31or 33 %, respectively. In stark contrast when materials were grafted to incorporate amine functionality sorbent breakthrough was not observed after the 60 min sampling time (6 dm^3 of contaminated air was sampled at 1.4 mg m^{-3}). When the sampling volume of contaminated air was increased to 12, 18 or 24 dm^3; still no breakthrough was observed indicating that 100 mg of NH_2-sorbents could be used to clean H_2CO from 24 dm^3 of air even if present at elevated concentration (1.4 mg m^{-3}).

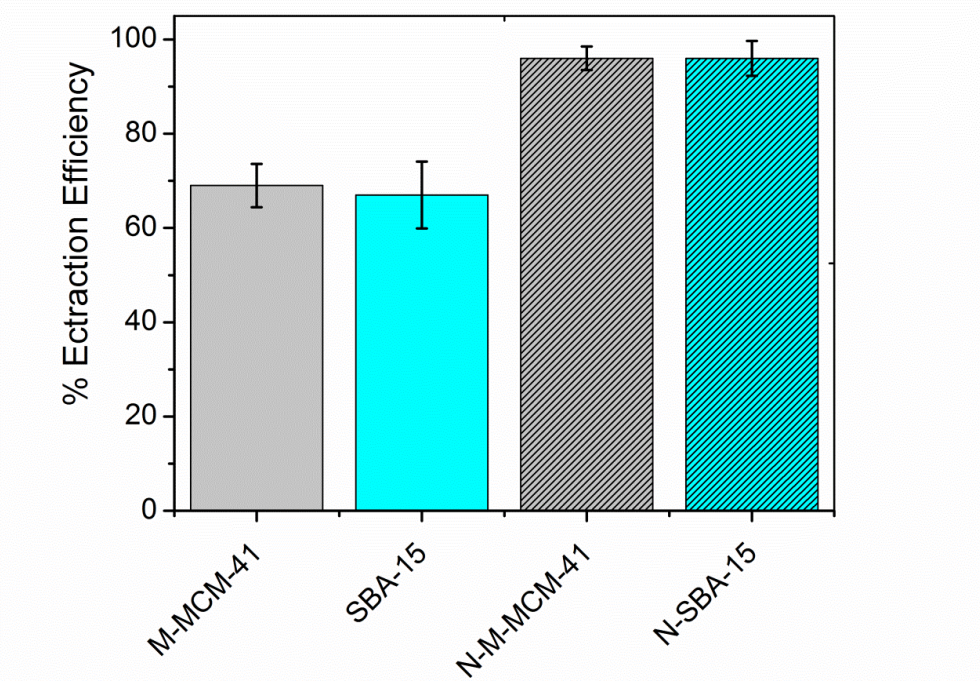

Figure 5.16 Extraction efficiency of sorbents for H_2CO adsorption. Error bars indicate the % relative standard deviation value (n = 3)

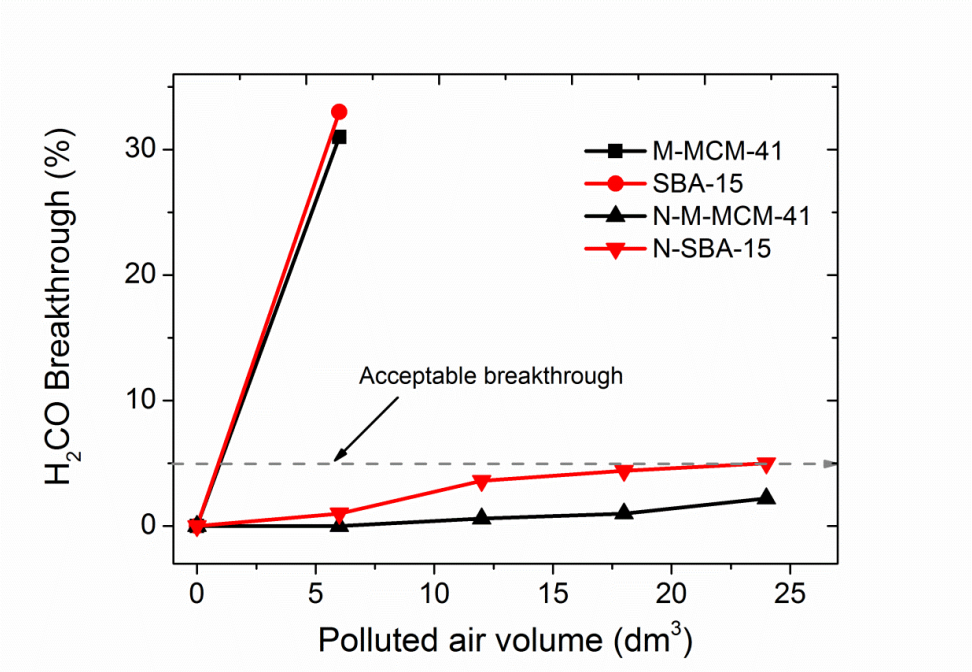

Figure 5.17 Calculated breakthrough volumes for H_2CO on sorbents with and without amine functionalization during their assessment

5.3.4.1.2 Investigation of chemisorption removal of H_2CO

To investigate the adsorbate-adsorbent interaction and to ensure H_2CO was permanently removed from the air (by chemisorption), the masses of H_2CO adsorbed on sampling tubes loaded with MWD-MCM-41, SBA-15, NH_2-MWD-MCM-41 or NH_2-SBA-15 were back flushed with air for 60 min at 100 cm^3 min^{-1}. The recovered masses were collected by hydrazine sampling cartridges and mass percentages remaining on the sorbent tubes were calculated (see Figure 5.18). The results demonstrated that, of the small amount of H_2CO collected by MWD-MCM-41 or SBA-15 45, 65 % was removed as air passed through the sorbent. Perhaps more importantly NH_2-MWD-MCM-41 or NH_2-SBA-15 loaded with H_2CO bound the target strongly through chemisorption (see Figure 5.19), resulting in its permanent removal from air.

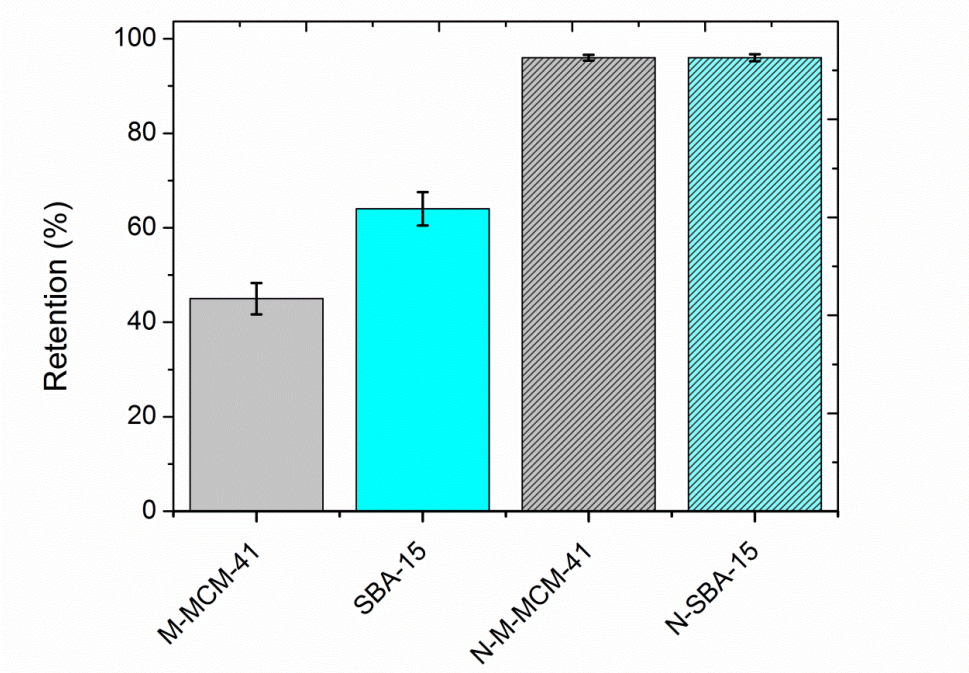

Figure 5.18 Retention of H_2CO adsorbed on different sorbents. Error bars indicate the % relative standard deviation value (n = 3).

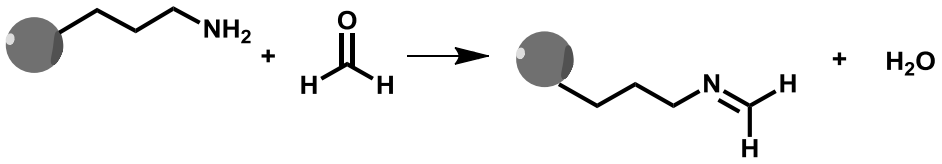

Figure 5.19 Schematic diagram for reaction of H_2CO on amino functionalised sorbents

5.3.4.1.3 Air polluted with H_2CO and VOCs

To prove the potential utility of the NH_2-sorbents as H_2CO environmental scavengers the efficacy of the materials were assessed for H_2CO extraction in the presence of VOCs; as would typically be the case when used to clean an indoor air environment. The chamber conditions were altered so that the environment contained 17, 9.1, 6.2 or 3.9 mg m^{-3} of toluene, EB, cumene and DCB respectively, in addition to H_2CO vapour at 0.7 mg m^{-3}. The polluted air was passed through sorbent tubes filled with MCM-41, SBA-15, NH_2-MCM-41 or NH_2-SBA-15 at a flow rate 100 cm^3 min^{-1} for 60 min. Hydrazine sampling cartridges were placed in line after sorbents tube to collect masses of H_2CO that passed through the sorbents. The presence of VOCs in the flowing stream had no detrimental effect on the masses of H_2CO adsorbed by NH_2-sorbents (see Table 5.7 and Figure 5.20). To further validate this result the pollutant masses passing through NH_2-sorbent were increased by a factor of 3 (sampling time of 180 min); still no H_2CO breakthrough was observed for NH_2-based sorbents (see also Table 5.7).

Table 5.7 Effects of VOCs on adsorption of H_2CO on studied sorbents

sorbent	Sampling time / min	H_2CO on cartridge / µg	Mass trapped by sorbents / µg	Breakthrough %
MCM-41	60	1.0	3.1	24
SBA-15	60	0.7	3.4	17
NH2-MCM-41	60	0.9	3.2	5.0
	180	0.4	11.9	3.3
NH2-SBA-15	60	0.2	3.9	4.9
	180	0.2	12.1	2.7

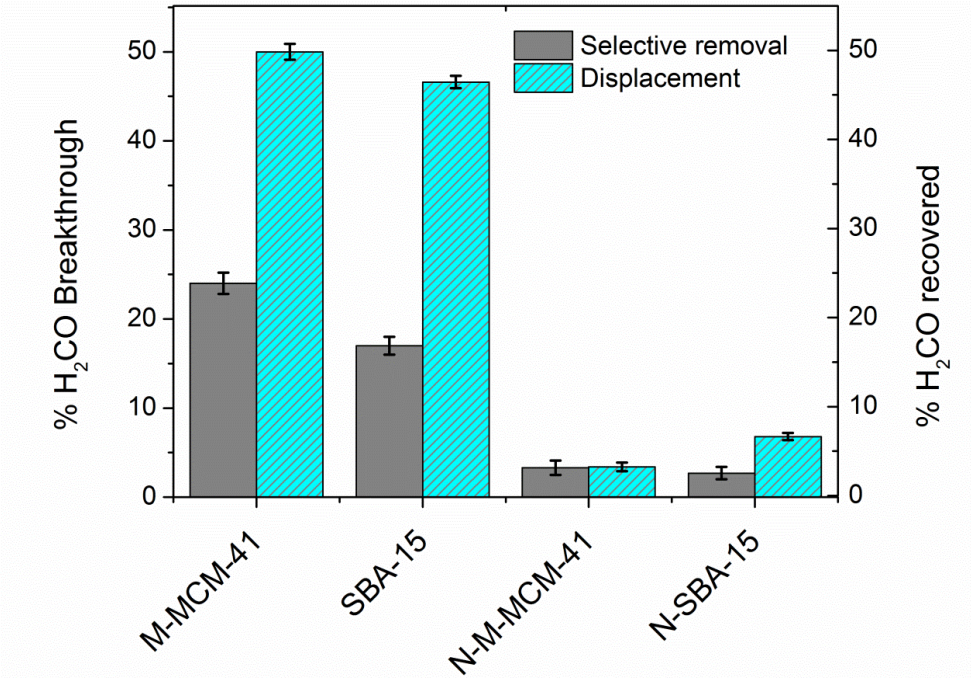

Figure 5.20 Effects of VOC on H_2CO removal. Left axis shows selective removal of H_2CO (% breakthrough) from a mixture of H_2CO and VOC. Right axis shows displacement of pre-adsorbed H_2CO by VOC (% H_2CO recovered). Error bars indicate the % relative standard deviation value (n = 3)

5.3.4.2 Assessment of sorbents for H_2CO extraction in passive mode

Sorbents, MWD-MCM-41, SBA-15, NH_2-MWD-MCM-41 and NH_2-SBA-15 were used to sample H_2CO vapour generated at 1.4 mg m^{-3} in a chamber by passive mode. The initial mass of H_2CO trapped by sampling cartridges, prior to sorbent addition, was 1.3 µg (n = 5); this sampling period will be referred to as t_0. Immediately after the initial sample was drawn (500 cm^3 of air contaminated) from the chamber, a small sampling port (1.1 cm in diameter) was opened and 100 mg of sorbent was added to the chamber (see Figure 5.4). The environment was re-sampled 7 times using 5 min sampling periods, the extraction potentials of NH_2-MWD-MCM-41 or NH_2-SBA-15 were compared to the materials prior to functionalisation. A control experiment was also measured without addition of a sorbent into chamber (no-sorbent) to ensure that reduction of H_2CO concentration was due to presence of sorbent.

The final percentage ratio of masses measured at t_7 / t_0 % (relative [H_2CO] %) were obtained (see Figure 5.21). Unmodified materials indicated a final reduction in H_2CO mass to 80 % which, being comparable to the control experiment, indicated that neither sorbent was useful for passive extraction of H_2CO from air. Mass ratios decreased significantly lower than 80 % for functionalised materials; to 50 or 25 % after a short sampling time before being stable at approximately 40 or 25 % for NH_2-SBA-15 or NH_2-MWD-MCM-41, respectively. However, as the experiment progressed no further reduction of H_2CO in the chamber was observed. It appeared that when used in passive mode, the amine-sorbents caused significant reduction in H_2CO concentration but not to a zero-concentration level. These results suggested that use of functionalised silica materials would be effective in museum cabinets to reduce H_2CO to below threshold concentrations (but not to zero concentration level) potentially protecting susceptible objects from vapour attack.

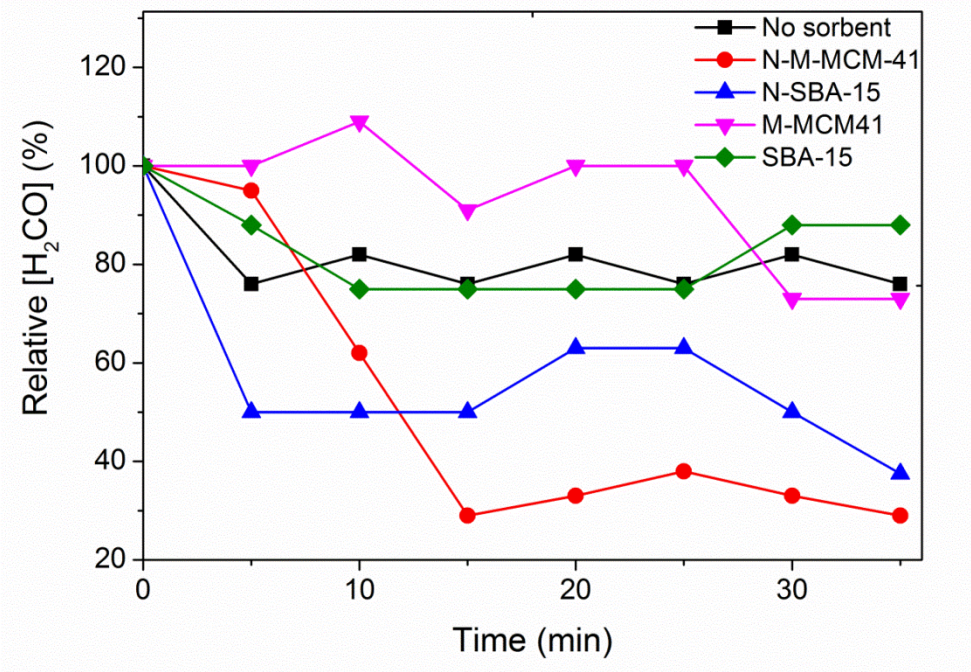

Figure 5.21 Relative concentration of H_2CO remaining on sorbents after 35 min in passive sampling mode

5.4 Conclusions

The aims of this chapter were to synthesis and functionalise mesoporous silica (MCM-41 and SBA-15), and to examine the adsorptive properties of these materials for the removal of VOCs and H_2CO from indoor air. The extraction efficiencies for VOCs were compared to the commercially available sorbent, Tenax TA. The performance of functionalised materials for the extraction of H_2CO was examined in both active and passive sampling mode.

The results demonstrated a similar performance of MCM-41 adsorbents (C-MCM-41 or MWD-MCM-41) whereas a slightly different performance was measured for SBA-15 with a higher extraction efficacy for EB and cumene but lower extraction of toluene and DCB. The dynamic capacities of C-MCM-41 and SBA-15 for VOCs adsorption were measured and the results showed that SBA-15 had a slightly higher capacity compared to C-MCM-41 in spite of C-MCM-41 possessing a higher surface area by a factor of 1.6. It was thought that the presence of the bimodal pore structure in SBA-15 lead to strong adsorption of VOCs. On the other hand, when the dynamic

capacity of adsorbents was measured as weight of adsorbed VOCs per volume of sampled air, the results showed that MCM-41 had a higher capacity than SBA-15, indicating that both of mesoporous materials can potentially be used as VOCs scavengers.

Furthermore MWD-MCM-41 and SBA-15 were selected to examine their performance for extracting H_2CO vapour from indoor air. This work presents the first detailed study of meso-silica materials used in dynamic and passive mode for H_2CO adsorption. Active sites (amine groups) were necessary before silica materials could extract H_2CO from air permanently. Chemisorption was evident in displacement experiments ensuring that H_2CO was removed from the air permanently. For best performance dynamic mode use is recommended although passive application of the materials will still permit a significant reduction of pollutants in indoor air, but not to nonzero levels.

Despite the high performance of mesosilica materials for the removal of selected VOCs and H_2CO from a contaminated air stream it was recognised that the methods used to prepare the materials are complex, lengthy, costly and involve the use of organic reagents which themselves can be classified as pollutants. Therefore alternative silica adsorbent platforms were assessed using bioinspired silica synthesis routes which involve rapid preparation processes and more environmentally friendly reagents at near-neutral pH. These bio-inspired silica materials and their use for remediation of polluted air will be discussed in the next chapter. Their performance will be compared to the benchmark mesosilica materials which have been assessed in this chapter.

6 Synthesis of novel green nanomaterials (GNs) for VOCs and H_2CO extraction

6.1 Introduction

6.1.1 Biosilicification

Biological silica formation has been defined accurately as ‘‘the movement of silicic acid from environments in which its concentration does not exceed its solubility (< 2 mmol/L) to intracellular or systemic compartments in which it is accumulated for subsequent deposition as amorphous hydrated silica” [192]. The biosilicification process in diatoms combines condensation of diluted solutions of silica precursors (i.e. silicic acid) and control of the morphology. It appears that diatoms (microalgae) produce large quantities of porous, hierarchically ordered and nanostructured silica over several length scales ranging from nanometre to micrometre dimensions [193]. These silicates were produced by a complex biologically controlled process entirely under environmentally friendly conditions with remarkable regulation of biosilica formation [194]. The outstanding features of biological silica formation compared to synthetic silica are: ornate and hierarchical controlled structures, mild conditions (nature pH ≈ 7 and room temperature), environment-friendly - all-aqueous solutions- (‘‘green’’), and involvement of organic components [195].

6.1.2 From biological silica to bioinspired synthesis

In order to understand how biosilicification materials are biologically formed in *“vivo”* and to mimic this knowledge for formation of bioinspired silica in *“vitro”* experiments, detailed studies have been conducted using organic biomolecules such as proteins, polysaccharides and small amines under mild physicochemical conditions [196-200]. Such methods utilise analogues (natural or synthetic) of biomolecules, called “additives” which possess the key functionalities required for silica formation under mild conditions; thus producing green nanomaterials (GN) [201, 202]. To date, wide ranging additives including proteins, enzymes, polymers and small molecules have been investigated for the controlled synthesis of silica-based GN [201].

Research publications in the areas of biological and bioinspired silica indicate that significant progress has been made in the last 10–15 y. Using the Science Direct

search engine, it was observed that from 2000 to date (March 2013) 1203 papers were accessed using biological + bioinspired as keywords. Using the keywords 'bioinspired silica' the number of papers published totalled 480 papers. Figure 6.1 demonstrates that the number of 'bioinspired silica' articles published over the last three years was approximately 66 - 70 % of those reported using 'biological + bioinspired' keywords. Interestingly the growth of research outcomes, especially in the area of bioinspired silica, looks set to continue as indicated by a rapid increase of papers focussed on this topic of research during the first 3 months of 2013.

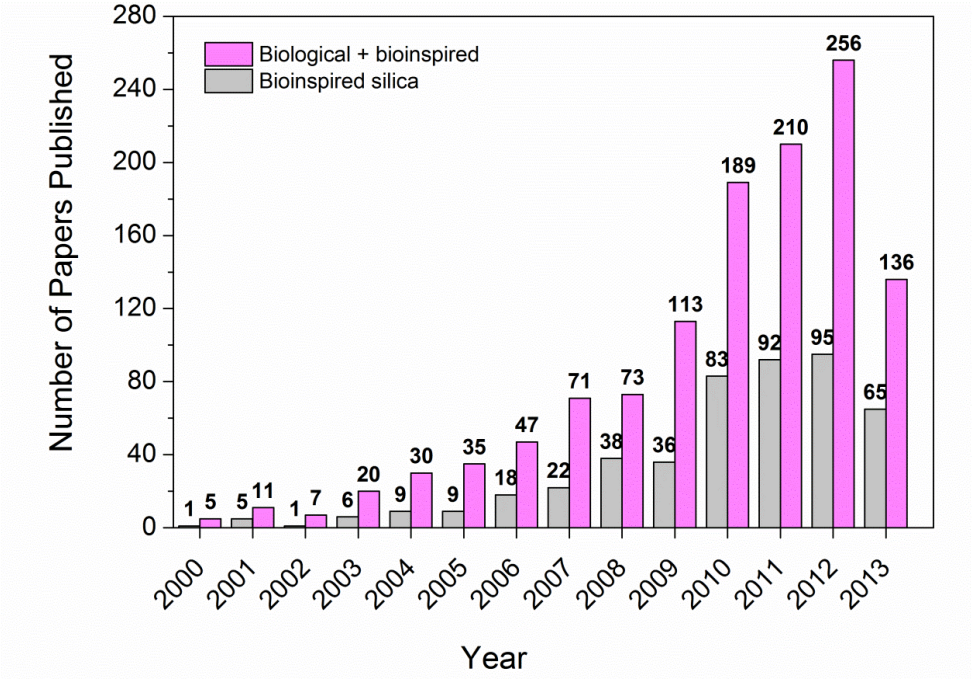

Figure 6.1 The number of papers published each year for 'biological + bioinspired' and 'bioinspired silica' articles. Data obtained using keywords in a Science Direct search from 2000 to date (March 2013).

6.1.3 Bioextracted and synthetic additives

Several research groups reported that biomolecules additives "bioextracts" have shown an ability to control silica formation in aqueous systems in *"vitro"* and under the similar conditions of silica deposition in *"vivo"* [203, 204]. These biomolecules, thought to be responsible for biosilicification processes, have been isolated from diatoms, or sponge, and their composition and structure were studied to mimic gained information for developing bioinspired synthetic schemes of silica formation [205, 206]. For example Sumper *et al.* have shown that some isolated proteins, silaffins, a set of cationic polypeptides, can condense aqueous silicic acid to silica particles in *"vitro"* [196]. Stucky *et al.* have utilised synthetic polypeptides for silica formation and obtained similar results [207].

Furthermore, silicatein, a protein found in the silica spicules of the sponge, and polyamines found in various diatoms, have been proposed to be responsible for biosilicification [208]. A series of polyamines with propylamine backbones of varying levels of methylation is one of the major organic components that has been isolated from siliceous diatom shells [209]. These polyamines have been applied to mimic the biological process for the rapid precipitation of silica spheres in several hundreds of nanometres in diameter from silicic acid solutions [210, 211].

Due to the complex nature of bioextracted additives, the ability to extract the silica product with high purity and characterisation of the product often proves difficult at times. Therefore their analogues, synthetic additives, have been utilized to mimic silica formation in *"vitro"*. A significant number of investigated rules that govern silica formation in the presence of additives have been identified, including the presence of cationically charged moieties; or the importance of additives self-assembly prior to and during silica polymerisation. Several studies had been reported using synthetic additives such as polymers, block co-polymers or small amines for silica formation in order to further investigations of their effects on silica polymerisation [212-214]. These synthetic additives offer significant advantages such as the ability to investigate mechanisms that governs the complex process of silica formation and control of properties (e.g. structure and assembly) of produced silica. An example of synthesised additives is small amines; Belton *et al.* reported the

successful synthesis of a series of linear methylated propylamines with variety of levels of methylation and amine lengths in order to study the influence of these amines on silica formation [201, 211].

6.1.4 Bioinspired silica

Bioinspired silica is the progress of synthesis routes that produce novel silica-based materials under mild synthetic conditions; neutral pH ≈ 7, ambient temperature in aqueous solution using a range of precursors with varying concentration. In addition silica precipitation is rapid and the methods allow significant control of the silica morphology in the product [202]. For example, rapid precipitation of spherical silica particles from silicic acid at concentrations 30 mM within 30 s was achieved by small amines such as ethyl- or propylamines containing 6 to 7 amine repeated units [211].

Moreover, by adapting the additive chemistry during preparation a wide range of structures can be prepared with different silica morphologies including spherical particles, hollow particles, fibres, sheets, films/coatings, hollow tubes, porous gels. Some examples of the morphologies produced by a) proteins + polyamines [215], b) polyethyleneimine [216] and complex hybrid materials using polymers and small amines for c) hollow nanofibres [217] d) hollow nanoparticles [201], are shown in the micrographs given in Figure 6.2.

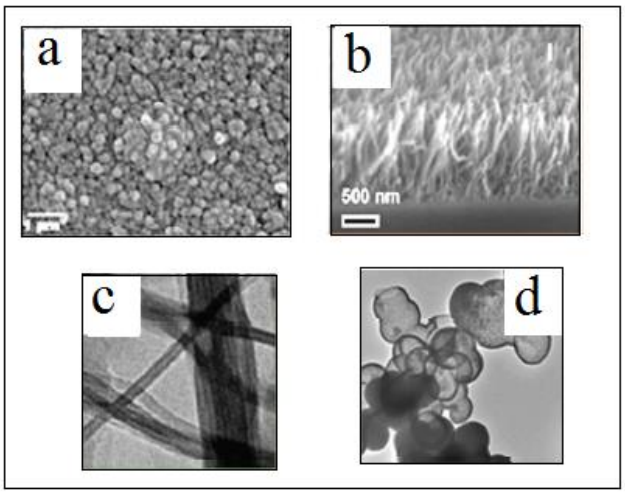

Figure 6.2 Reproduced images of selected examples of structures and morphologies including: (a), (b) coatings, (c) hollow nanofibres and (d) hollow nanoparticles. All these were produced using bioinspired chemistry [195].

It is essential to control the porosity and surface area of silica materials used in adsorption, catalysis, fillers and composites. For example, the sol–gel synthesis method has been adapted to generate a range of porous and hybrid hierarchical silica structures with high porosity and surface area (>700 m^2 g^{-1}), such as MCM- and SBA-silica, but the materials are produced under harsh conditions using time consuming multistep methods [155, 157, 218]. In contrast bioinspired routes have been used to produce silica surface area ranges of < 10 - 1030 m^2 g^{-1} and pore sizes of < 2 to 60 nm [206, 219, 220]. For example, Coradin *et al.* have used amino acid as an additive to synthesis silica with a high surface areas (> 500 m^2 g^{-1}) and an unique bimodal distribution of pores consisting of mesopores (2.5–3.5 nm) and meso-to-macropores ranging between 10–100 nm under mild conditions [220].

Silica has also been precipitated by propylamines which are analogous to the amines found in diatoms and sponges, producing materials with low surface areas < 10 m^2 g^{-1} [202, 213]. Many experimental studies have shown that short alkylamines such as poly (ethyleneamine) can also induce rapid condensation of silicic acid producing silica spheres, and their properties thought to be related to the number of amine units

present [213, 221, 222]. Belton *et al.* have used linear ethyleneamine (EA) of between 1 and 5 repeat ethyleneamine units to condense monosilicic acid at 30 mM, and ratio 1:1 of Si: N [213], demonstrating that most of these amines are able to generate silica with varying morphology and surface area.

6.1.5 Silica precursors (silicic acid)

Orthosilicic acid, $Si(OH)_4$, is a weak acid ($pK_a \approx 9.8$) in soluble form, consisting of a silicon atom tetrahedrally coordinated to four hydroxyl groups [223]. In water at 25 °C the silica is stable for long periods of time at concentrations below 100 ppm, however when the concentration exceeds the solubility amorphous solid phase, at 100-200 ppm, it undergoes auto-polycondensation reactions [205]. The early stage of orthosilicic acid condensation includes the formation of dimers, then trimers and oligomers, which condense forming silica particles as shown in Figure 6.3 [224].

The molecular mechanism for the condensation process is thought to involve the reaction of un-ionised $Si(OH)_4$ and ionised $Si(OH)_3O^-$ or two un-ionised molecules of silicic acid (see top section in Figure 6.3) to form dimers, depending on the pH of the reaction medium. Furthermore the condensation process is thought to be activated by condensing produced anionic silicate species with un-charged monomers to form small oligomeric species which leads to particle growth by aggregation, by Ostwald ripening and/or by 'necking' between combined particles [200, 225]. This process is thought to increase the siloxane (Si-O-Si) bonds to a maximum number and decrease uncondensed Si(OH) groups to minimum; then oligomers cyclise to aggregate particles with a higher density of silanol groups which are more acidic and, therefore, more highly ionised [226]. The rate of aggregation depends on pH, temperature and particle concentration. Interestingly the silica particles bear a negative charge in solution even at the circumneutral pH which applies important rules in particles aggregation. Smaller species dissolve and release silicic acid that re-precipitates in solution at the point of contact between particles 'necking' [227].

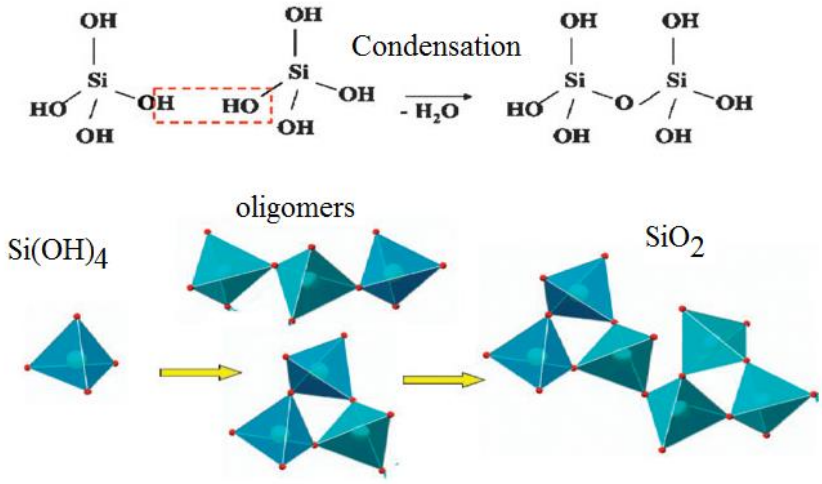

Figure 6.3 Scheme of silicic acid condensation forming of silica [224].

The colorimetric molybdate method has been extensively used to study the kinetics of silica polymerisation by measuring the concentration of orthosilicic acid in solution, reporting multiple-order reaction ranging from first to fifth order [228]. At the later stage of polymerisation, larger oligomers were formed by addition of monomer to trimers or larger oligomers, and the concentration of orthosilicic acid in solution was in equilibrium with silicic acid on the particle surface. The silicic acid was continually dissolved and re-precipitated to approach the solubility limit of amorphous silica [226]. Further growth of silica oligomers was achieved even at the solubility limit and at this stage the reaction order could not be assigned due to loss of orthosilicic acid from solution. Despite the multiple-orders of reaction for silica formation, it was reported that the rate of oligomerisation has been affected by factors such as the concentration of orthosilicic acid, pH, temperature, and the presence of additives [226, 229].

Orthosilicic acid has also been polymerised from solution, in the presence of biomolecules as additives at mild conditions [43]. Such additives are able to affect the oligomerisation of silica and control their properties such as particle size, pore structure, surface area and aggregation. Furthermore the involvement of additives in the formation and dissolution of silica alters the species stability shifts the

equilibrium between produced silicates and orthosilicic acid [230]. For example Belton *et al.* reported that particle stabilisation occurred in the presence of a high concentration (30 mM) of pentaetylenehexamine (PEHA) when used as an additive, suggesting that the mechanism of silicic acid condensation in presence of PEHA was thought to include the production of water as the leaving group as illustrated in Figure 6.4 [213].

At pH 7 it was expected that not all of the amine groups available in polyethyleneamine will be protonated due to increasing resistance for protonation when neighbouring amine groups were charged [231]. The electrostatic attraction between deprotonated silanol groups on the surface of the silica particles and positive charged amines on polyamine chain brought uncharged amines into close contact with silanol groups on the surface as shown in Figure 6.4a. The resultant deprotonated silanol groups will attack the silicon in silicic acid which, in turn, have silanol group that will attack the charged amine at the same time (b), producing a growth of silica particles by adding a molecule of silicic acid and reproducing the polyamine after loss of a water molecule as shown in step (c).

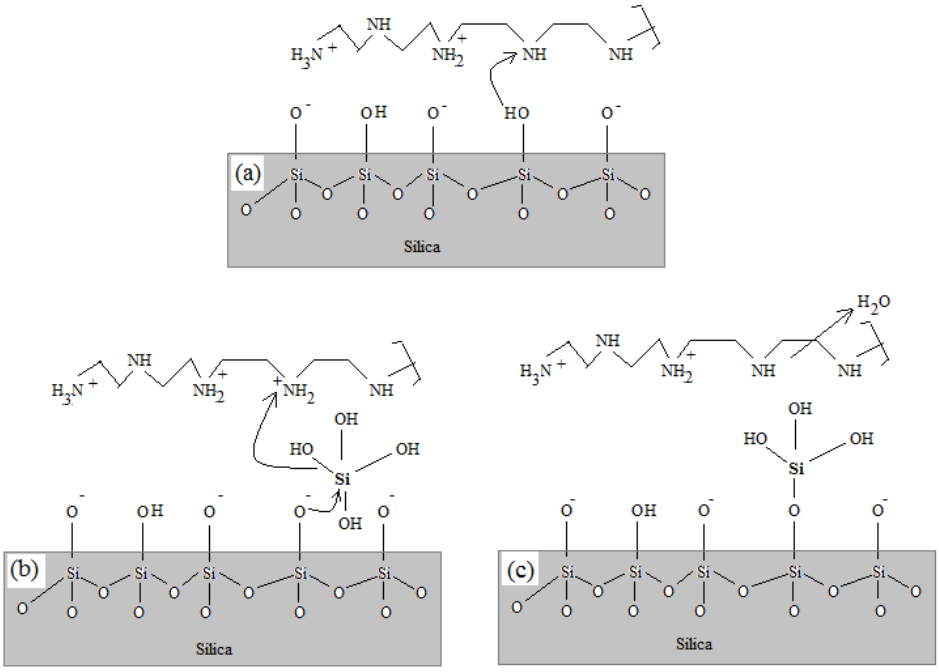

Figure 6.4 Schematic of mechanism for silicic acid condensation in presence of PEHA as an additive (represented from Ref. [213])

In addition the presence of polyamine with long chains such as PEHA and at high concentration (30 mM) will increase the aggregation rate of silica formation by extending the amine chains in the bulk solution allowing them to connect the neighbouring particle as illustrated in Figure 6.5 [213].

Orthosilicic acid can also be precipitated at supersaturated concentrations (typically 30 or 100 mM) using bioinspired biomolecules such as polyethyleneamine as additives [200, 222]. In vitro, aqueous orthosilicic acid at mild conditions, circumneutral pH, ambient temperature and the presence of additives permit silicate particle condensation to form a gel network by a suggesting stages of process: polymerization of monomer of silicic acid to small particles, particle growth, and finally, formation of branched particle networks resulting in gelation [232].

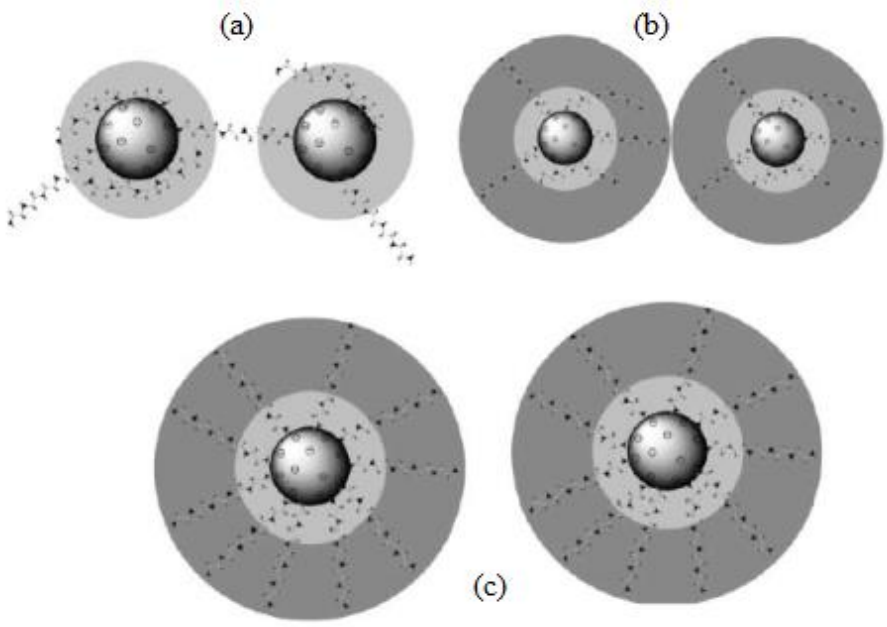

Figure 6.5 Schematic representation of the effect of PEHA on silica formation; (a) particle bridging, (b) forming double layer around silica particle and (c) particle stabilisation at high concentration of PEHA

The condensation of silicic acid by biomolecules is also effected by factors such as pH, temperature, and precursor concentration of the model condensing system.

However, the suitability and exact chemistry of silicate speciation at a selected pH, time and concentration of silicic precursors are not always fully known [232]. Many silicic acid precursors such as tetraethylorthosilicate (TEOS) [233], glycol modified alkoxysilanes [234], and sodium silicate solutions [212] have been used to produce bioinspired silica.

6.1.6 Applications

In recent years, there has been an exciting growth in biologically inspired silica synthesis research, with *in vitro* experiments leading to the development of bioinspired green nanomaterials (GNs) with reaction processes that can control their properties such as surface area and particle size [211]. These materials have started appearing in a range of applications such as catalysis and biocatalysis, coatings, hybrid materials, sensors [235, 236], and drug delivery [237] due to the ease of synthesis of biologically inspired materials [195]. For example Millner, Chaniotakis and their respective co-workers have reported that the improvement of electrochemical biosensors properties such as thermal stability, protection against protease attack and operative life were achieved after using a bioinspired route to synthesis carbon nanofibre (CNF) electrodes containing silica-enzyme coatings nanocomposites. In addition these biosensor systems demonstrated a greater sensitivity with a linear and faster response when compared to silica-enzyme systems without the CNF [236, 238]. Sano *et al.* reported that bioinspired silica synthesis methods can be utilised to develop an anticancer drug delivery system by hydrolysing silica in aqueous solution and thereby immobilising protein onto silica to form a protein-silica composite which slowly releases the protein, sustaining the its activity for a longer time [237].

Herein this work reports the first application of GNs silica as VOCs and H_2CO scavengers. Of particular importance here for gas adsorption is the ability of certain additives to control the porosities of GN silica, which potentially could have an impact on selective adsorption that is typically required in VOC removal. For example, it has been shown that short alkylamines, such as ethyleneamines, when used as additives, were able to enhance the kinetics of GN formation, while also

controlling their porosity; the additive architecture and chemistry was found to be crucial [211, 213]. Therefore, this part of study aims to generate tailored GN adsorbents by applying the fundamental knowledge of GN synthesis. Advantages of bioinspired syntheses routes included the use of neutral pH and ambient temperature conditions, rapid synthesis (15 min), and a considerable reduction in secondary pollution by using aqueous solutions to eliminate the need of organic solvents for the preparation method. Another aim of this work was the improvement of the physical properties (surface area) of a previously produced material (GN30-11) by modification of the concentration of silica precursor, or the ratio of Si: N, and by addition of shorter polyethylene amine, tetraethylenepentamine (TEPA) as an alternative additive. Gas adsorption application was demonstrated after materials were functionalised with organic amino groups to provide viable alteratives to mesosilica adsorbents such as MCM-41 or SBA-15.

6.2 Experimental

6.2.1 Synthesis of novel green nanomaterials (GN) adsorbents

The synthesis of bioinspired silica materials, referred to as green nanomaterials (GNs), was achieved by modifying a previously reported method [211, 213] as described briefly below. Sodium metasilicate ($Na_2SiO_3.5H_2O$, Fisher Scientific) was used as the silica source whereas tetraethylenepentamine (TEPA, $C_8H_{23}N_5$, ACROS ORGANICS) or pentaethylenehexamine (PEHA, $C_{10}H_{28}N_6$, ACROS ORGANICS were used as bioinspired additives at different molar ratios of Si: N.

The procedure for synthesising GN at a silica source concentration of 30 mM and using PEHA as the additive at a Si: N molar ratio of 1: 1 was as follows: To provide solution A, 6.5 g of sodium metasilicate was dissolved in 500 cm^3 of deionized water in a 1000 cm^3 polyethylene bottle. 1.1 g of PEHA was dissolved in 400 cm^3 of deionized water in a 500 cm^3 polyethylene bottle to provide solution B. Then, 70 cm^3 of 1 M hydrochloric acid (HCl, Fisher Scientific) was added to solution A to produce an acidified solution (solution C) which was shaken for 1 min before adding solution B. The pH of final mixture was immediately adjusted to pH 7 $\pm$ 0.1 by adding a few

drops of 1 M HCl and rapid precipitation of silica was visible within 1 – 2 min. The resultant as-synthesised precipitate was collected after 15 min (hereafter referred to 'as-GN30-11') by filtration, washing three times with deionized water, and drying in air at room temperature before calcination at 500 °C for 5 h to produce GN30-11.

To study the effect of silica precursor concentration and the molar ratio of Si: N on the material's resultant physical properties, the synthesis procedure described above was repeated using the altered conditions outlined in Table 6.1.

Table 6.1 GNs produced to study textural properties and VOC or H_2CO scavenging efficiencies

Sample ID	Additives	Conc. Of silica precursor (mM)	Mass of silica precursor (g)	Mass of additive (g)	Ratio of Si: N
GN30-11	PEHA	30	6.5	1.1	1: 1
GN30-12	PEHA	30	6.5	0.55	1: 2
GN30-21	PEHA	30	6.5	2.2	2: 1
GN20-11	PEHA	20	4.34	0.74	1: 1
GN40-11	PEHA	40	8.67	1.47	1: 1
GN30-11T	TEPA	30	6.5	1.14	1: 1

6.2.2 Functionalization of GN adsorbents by organic amine group

GN adsorbents (GN30-11, GN30-21, GN40-11 and GN30-TEPA) were modified by the addition of chelates onto the silica surface to enhance the material's ability to target pollutants by selective adsorption. Functionalisation was achieved by post synthesis grafting (described in Section 3.1.3) using 3-aminopropyltrimethoxysilane to produce NH_2- GN30-11, NH_2-GN30-21, NH_2-GN40-11 and NH_2-GN30-T. The efficiency of the modified GN materials for H_2CO vapour removal from a contaminated air stream was examined and compared to the efficacy of NH_2-MCM-41.

6.2.3 Characterisation of GN adsorbents

To determine the physiochemical properties of calcined and modified GN adsorbents, characterisation was achieved using experiments as described in Section 3.2. The nitrogen adsorption-desorption isotherms (BET isotherm) was used to measure surface area, pore sizes and pore size distribution whereas SAS-XRD was used to examine the nature of pore structure/ordering. ATR-FTIR spectroscopy and microanalysis were also used to confirm the removal of organic templates from the as-made materials and presence of amino groups after functionalisation.

6.2.4 Set up of VOCs and H_2CO dynamic atmospheric chambers

Before using calcinced or modified GNs adsorbents to extract the selected VOCs or H_2CO vapour, two dynamic atmospheric systems were set up to generate constant pollutant concentrations in separate sampling chambers as illustrated in Figure 3.1 (see Section 3.3.1). The first sampling chamber contained 34, 18, 12 or 7.8 mg cm^{-3} of toluene, ethylbenznene (EB), cumene or dichlorobenzene (DCB), respectively, whereas the second chamber contained 1.4 mg cm^{-3} of H_2CO vapour.

6.2.5 VOCs sampling method set up

Sampling tubes were filled with 100 mg of each adsorbent (GN30-11, GN30-12, GN30-21, GN20-11, GN40-11 or GN30-TEPA) and conditioned by the thermal desorption unit (TDU) as described in Section 3.3.3 prior to use for VOCs collection. The flow rate of contaminated air sampled from chamber was adjusted to 100 cm^3 min^{-1} for all experiments. Tenax TA sampling tubes were placed at the chamber outlet and the air was sampled for 1 min collecting experimental, 'reference', masses of 2109, 404, 479 or 494 ng for toluene, EB, cumene or DCB, respectively. To study the adsorption performance of GNs adsorbents, the chamber was resampled after sorbent filled tubes were placed between the chamber outlet and a Tenax TA sampling tube. The difference in masses trapped by the Tenax TA before and after addition of the sorbent used to assess extraction efficiency. Sorbent tubes filled with

MCM-41 were also prepared and assessed to compare with GN adsorbent efficiencies.

6.2.6 H_2CO sampling method set up

Calcined and modified GN adsorbents were conditioned at 120 ^{0}C for 2 h prior to being mixed with glass bead and loading into glass tubes; these sorbent tubes are described further in Section 3.3.3. GNs adsorbents were assessed for the extraction of H_2CO vapour from contaminated air using the previously described exposure chamber (see Section 3.3.1.). The air sampling was adjusted at 100 cm^3 min^{-1} and a sampling time of 60 min was used in all experiments. Initial experiments, run with no sorbent tubes in-line, used silica cartridges impregnated with 2,4-dinitrophenyl hydrazine to determine the masses of H_2CO collected in the 6 dm^3 of contaminated air. The collected masses were determined by the LC-UV-vis chromatography after elution of trapped formaldehyde-dinitrophenyl hydrazine (F-DNPH) using acetonitrile. An average (n = 3) mass of 8.1 µg was measured and used as a 'reference' mass. The experiment was repeated with GN adsorbents placed between the chamber outlet and the DNPH sampling cartridge. The reduction in trapped F-DNPH masses were attributed to extraction by of the studied GN adsorbents. NH_2-MCM-41 was also assessed as a reference adsorbent.

6.3 Results and discussions

6.3.1 Characterisation of GNs materials by N_2 adsorption isotherm and XRD

Nitrogen sorption isotherms were used to provide information on the physical properties including surface area and pore diameter of the novel synthesized GNs adsorbents (collected data is summarised in Table 6.2). Results demonstrated that the first material prepared via the rapid, environmentally friendly synthesis route, GN30-11, produced a material with a surface area of 58 ± 0.5 m^2 g^{-1}. This is significantly lower than for MCM-41 or SBA-15 at 1014 ± 4.6 or 644 ± 7.9 m^2 g^{-1}, however, the

mesosilica materials were prepared via a sol-gel method under harsh conditions and using longer multistep synthesis procedures (see Section 5.3.1). In an attempt to increase the surface area of GN adsorbents, different GNs were prepared as described in Section 6.2.1 and the results are given in Table 6.2. No significant enhancement in surface area was obtained when the Si : N ratio was altered from 1:1 to 1:2 (see GN30-12 at 49 ± 0.4 m^2 g^{-1}), however, alteration of the Si: N ratio to 2:1 (GN30-21) resulted in a significant increase in surface area to 355 ± 6.3 m^2 g^{-1}; which is approximately 7 times that of GN30-11. Interestingly a comparable enhancement in surface area was obtained by changing the concentration of silica precursor (sodium silicate originally at 30 mM) to 20 or 40 mM even when the Si:N ratio was held to 1:1 (see GN20-11 or GN40-11 which had surface areas of 363 ± 7.4 or 260 ± 4.5 m^2 g^{-1}). An increase in surface area was also achieved when a shorter additive (TEPA) was used instead of PEHA, even with the concentration of silica precursor remained at 30 mM and the Si:N ratio at 1: 1 (GN30-11T at 268 ± 4.8 m^2 g^{-1}). It was also observed that the pore volume was similar for most GN adsorbents (0.13 – 0.28 cm^3 g^{-1}), however GN40-11 had the highest pore volume measured at 0.59 cm^3 g^{-1}.

Table 6.2 Physical characterisation data for GNs adsorbents

Sample	**BET surface area (m^2 g^{-1})[a]**	**Pore size (nm)[b]**	**Pore volume (cm^3 g^{-1})[c]**
GN30-11	58 ± 0.5	N/A	0.20
GN30-12	49 ± 0.4	N/A	0.13
GN30-21	355 ± 6.3	N/A	0.28
GN20-11	363 ± 7.4	N/A	0.26
GN40-11	260 ± 4.5	N/A	0.59
GN30-11T	268 ± 4.8	N/A	0.25

[a] Calculated by BET model from sorption data in relative pressure range from 0.05- to 0.25.

[b] Calculated by BJH model from the adsorption branches of isotherm.

[c] Calculated from N_2 amount adsorbed at a relative pressure P/P_0 of 0.99.

N/A: no clear size seen, only broad line, See Figure 6.7.

The similar isotherm shapes measured for all GN adsorbents (illustrated in Figure 6.6) were thought to reflect combined features of type I and type II IUPAC isotherms. Very little or no hysteresis was observed for any of the GN sorption isotherms, while the sharps rise at low partial pressure and overall isotherm shape suggested the presence of micropores. GN adsorbents possessed low pore volumes and the data did not permit the calculation of an average pore size within the mesoporous range since the micropore size range is not compatible with N_2 sorption experiments used here (see Figure 6.7). The microporosity of the GN materials was consistent with the small molecular size of the additives used in GNs formation. However, the materials exhibited reasonable pore volumes measured between 0.20 – 0.59 cm^3 g^{-1} which exceed that expected from conventional microporous materials.

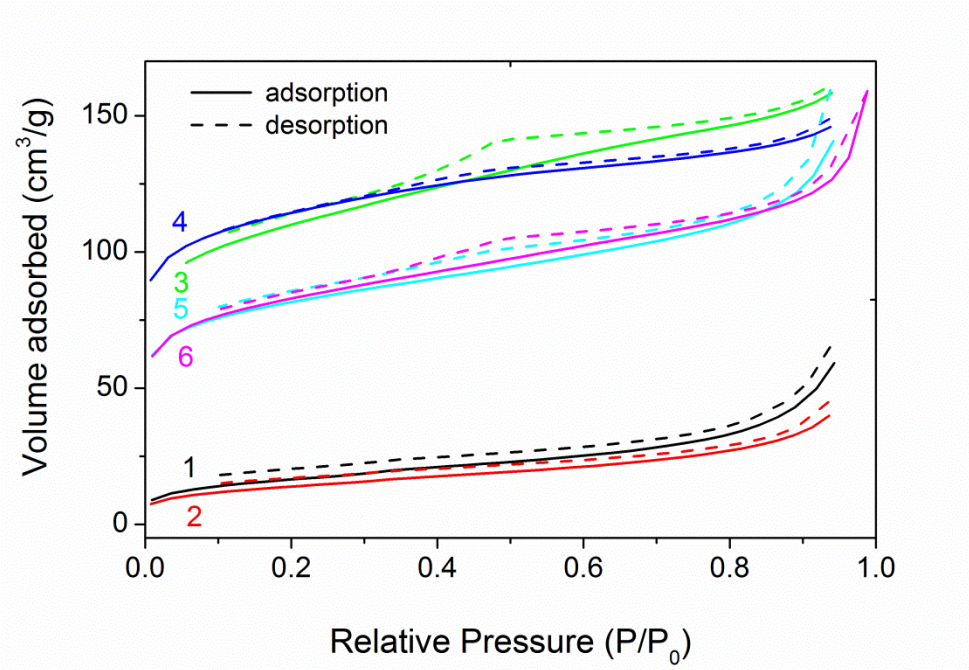

Figure 6.6 Nitrogen adsorption isotherms of 1) GN30-11, 2) GN30-12, 3) GN30-21, 4) GN20-11, 5) GN40-11 and 6) GN30-11T

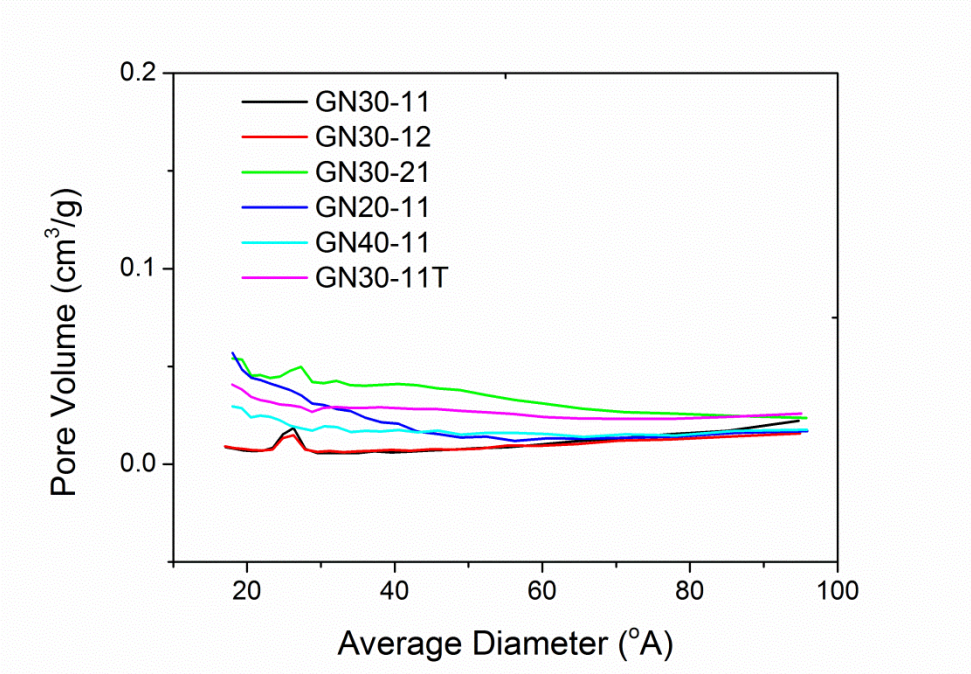

Figure 6.7 BJH pore size distribution patterns of GN adsorbents

To confirm the presence of microporosity in GNs materials, further analysis using the t-method of Halsey was performed for GN30-11. The adsorption/desorption isotherms of GN30-11 (see Figure 6.8) showed a significant adsorption of nitrogen at very low pressure consistent with the presence of micropores. The gradual slope between 0.1 and 0.8 indicates the filling of non-specific diameter mesopores, resulting in very broad pore size distributions for GN30-11 (see Figure 6.7). The large volume adsorbed between 0.9 and 1 represented the filling of the inter-particle spaces. The corresponding t-plots shown in Figure 6.9 are illustrative of micropores in the presence of mesopores. The upper linear region represents the mesopore slope from which the mesopore surface area can be determined using the Halsey equation (See Equation 2.6 in Section 2.1.1.2). The lower linear region represents the total pore slope which can be also used to obtain total surface area of sample. Since the total surface area from the lower liner cannot be calculated easily and it should be the same as the BET surface area, the micropores surface area can be calculated by Equation 2.7 outlined in section 2.1.1.2. The micropore surface area of GN30-11 was determined to be 9.4 m^2/g and pore size of 7Å.

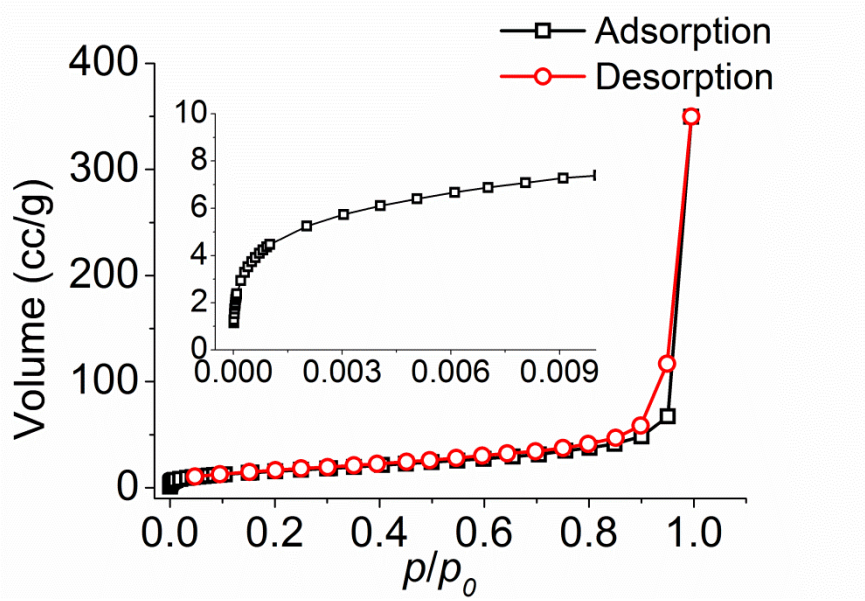

Figure 6.8 Nitrogen adsorption isotherms of GN30-11

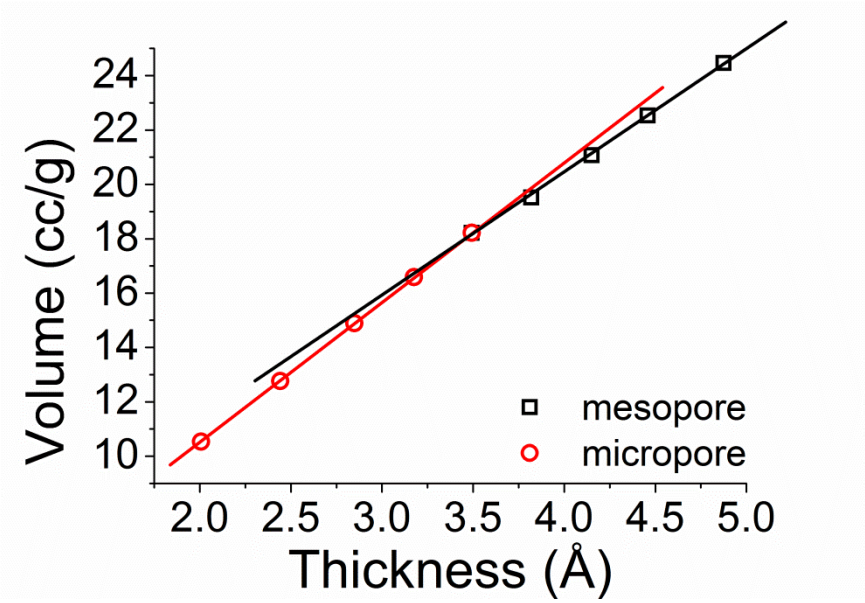

Figure 6.9 The V-t plot for the nitrogen gas adsorption analysis used for micropore measurement

The GN adsorbents' SAS-XRD patterns (see Figure 6.10) indicated that all of the newly prepared GNs adsorbents were amorphous with no pore ordering, confirming a network of branched pores. However the TEM image of GN adsorbents (see Figure 6.11) showed some ordered pores in their structures which were thought to be unusual for these materials. The discrepancy between the XRD and TEM results need further work to determine the correct topography of the GNs.

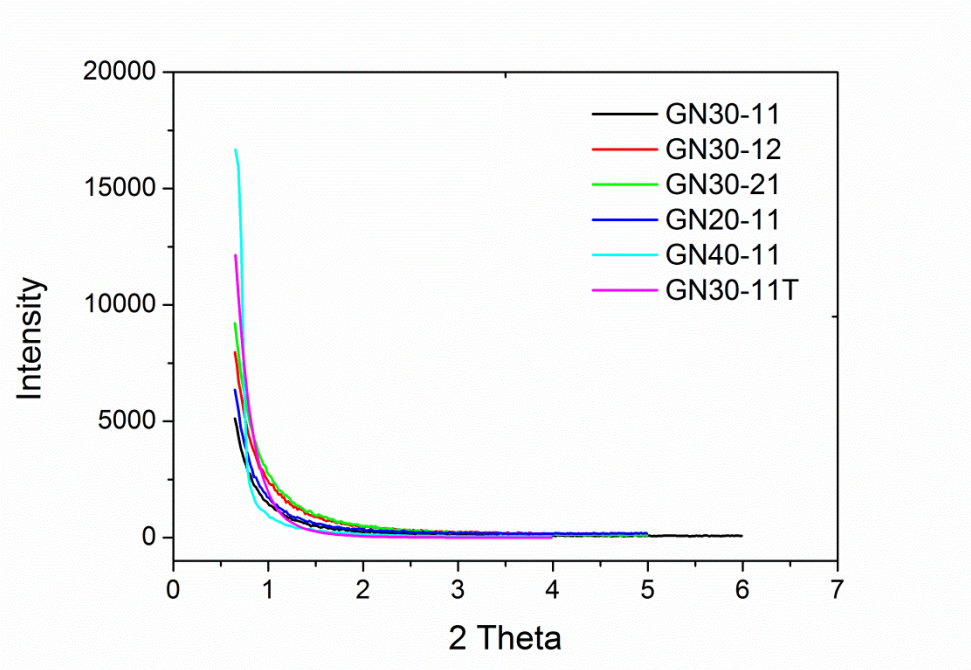

Figure 6.10 SAS-XRD patterns of GN adsorbents

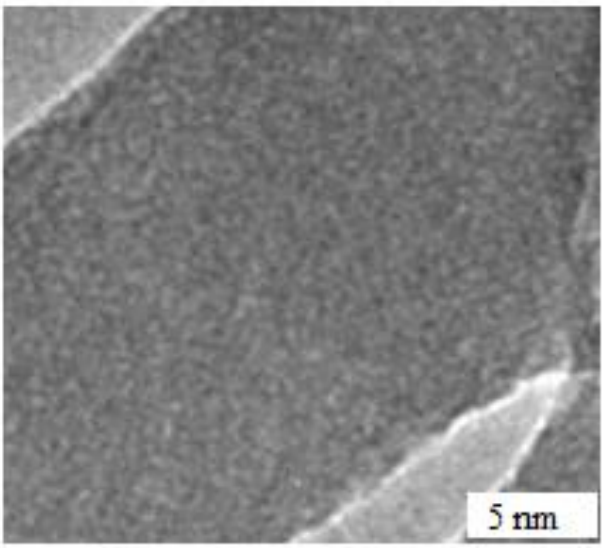

Figure 6.11 Representative TEM image of GN

6.3.2 ATR-FTIR spectra and elemental analysis of GN adsorbents

The ATR-FTIR spectra of calcined and modified GN materials (Figure 6.12), confirmed the formation and functionalisation of silica materials by a bioinspired synthesis route. The appearance of peaks labelled i-iii in Figure 6.12a, confirmed the formation of Si-O-Si bonds: Si–O–Si stretching bands were assigned to a large broad band between 1000 and 1250 cm^{-1} (i) and band at 800 cm^{-1} (iii) and Si-OH band was observed at 950 cm^{-1} (ii). Further, the appearance of peaks in modified GN adsorbents at 1560 cm^{-1} and 1480-1490 cm^{-1} (v and vi in Figure 6.12b) were assigned to N-H and C-N respectively, confirming the successful functionalisation of GN adsorbents by amino groups. Finally, bands measured between 1635-1645 cm^{-1} (iv), present in both calcined and modified GN adsorbents were assigned to water bending modes.

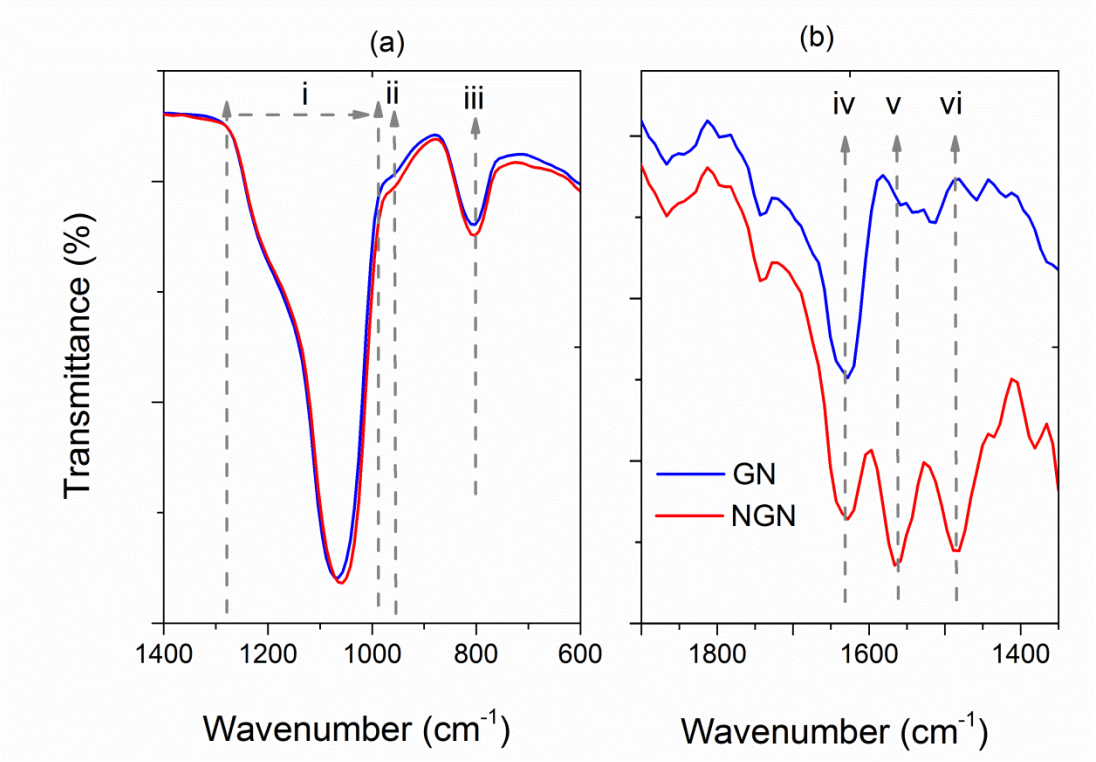

Figure 6.12 FT-IR spectra of GN and NH_2-GN adsorbents showing silica formation (a) and amine functionalisation (b)

The spectroscopic results were supported by microanalysis as summarised in Table 6.3. The data confirmed successful template removal from as-made GNs; no carbon or nitrogen atoms were measured in the calcined products. The percentage of nitrogen (% N) present in NH_2-GN30-11, NH_2-GN40-11 or NH_2-GN30-11T was measured at 1.71, 2.1 or 2.36 %, respectively. These percentages were used to estimate the degree of surface functionalisation (L_0) using the equation reported by Damian *et al.* [191]. The calculated values of L_0 (Table 6.3) indicated that similar degrees of functionalisation for GNs adsorbents; with slight higher degree (L_0 = 1.69) for GN30-11T, followed by GN40-11 (L_0 = 1.5). Interestingly the results demonstrated that even GN30-11, with the lowest surface area, was successfully grafted with amine groups giving a reasonably large surface coverage (L_0 = 1.2).

Table 6.3 Elemental microanalysis data recorded for the samples

Sample ID	% C	% H	% N	Lo / mmol g^{-1}
As-GN30-11	10.28	3.53	6.57	
GN30-11	Nil	Nil	Nil	
NH2- GN30-11	6.22	1.74	1.71	1.2
As- GN40-11	7.91	2.62	4.73	
GN40-11	Nil	Nil	Nil	
NH2- GN40-11	4.94	1.10	2.1	1.5
As- GN30-11T	6.28	2.61	3.76	
GN30-11T	Nil	0.36	Nil	
NH2- GN30-11T	5.82	1.11	2.36	1.69

6.3.3 Applications of GN adsorbents for VOCs and H_2CO extraction

6.3.3.1 Use GN adsorbents for VOCs extraction

To examine the extraction efficiencies or dynamic capacities of GN adsorbents for VOCs, sampling tubes loaded with Tenax TA were used to calibrate the TDU-GC-MS for a range of analyte masses. Details of the calibration by standard solution experiments are described in Section 4.2.1. For all experiments, the flow rate of air contaminated by VOCs was adjusted to 100 cm^3 min^{-1} for 1 min and the experimental masses of VOCs expected to be trapped in a 100 cm^3 aliquot of contaminated air were determined by using sampling tubes loaded with Tenax TA and the calibration curve of each VOC as described in Section 4.2.5. Average of masses 2109, 404, 479 and 494 ng of toluene, EB, cumene and DCB, respectively, were used as "reference masses" to examine extraction efficiencies or dynamic capacities of GN adsorbents. Sampling tubes loaded with GN adsorbents (GN-30-11, GN30-12, GN30-21, GN20-11, GN40-11 or GN30-11T) were used to sample VOCs from sampling chamber then were analysed by calibrated TDU-GC-MS. The

collected masses of VOCs were calculated using their calibration curves and used to examine their performances toward VOCs extraction.

6.3.3.1.1 Effect of methanolic solution on masses of VOCs trapped

Masses of VOCs trapped on sorbent tubes loaded with GN30-11 detected with or without adding a methanolic solution of the IS, and masses recovered by methanolic solution were plotted as illustrated in Figure 6.13. The results demonstrated that VOC masses were significantly higher than that masses detected after the IS was spiked onto the sorbent tube. The displacement of trapped VOCs by methanol was also confirmed by injecting the IS onto tubes loaded with VOCs; higher recoveries were obtained (labelled as recovered masses in Figure 6.13).

The results indicated that toluene was the most affected by methanol which recovered more than 95 % of toluene trapped on sorbent tube followed by EB, approximately 75 % masses were recovered, whereas 50 % of cumene or DCB. These results confirmed that calibration tubes loaded with silica could not be used in the direct injection calibration method, as noted previously for MCM-41 or SBA-15) developed for the TDU-GC-MS. Displacement problems were not observed for VOC trapping from air (as not methanol was present).

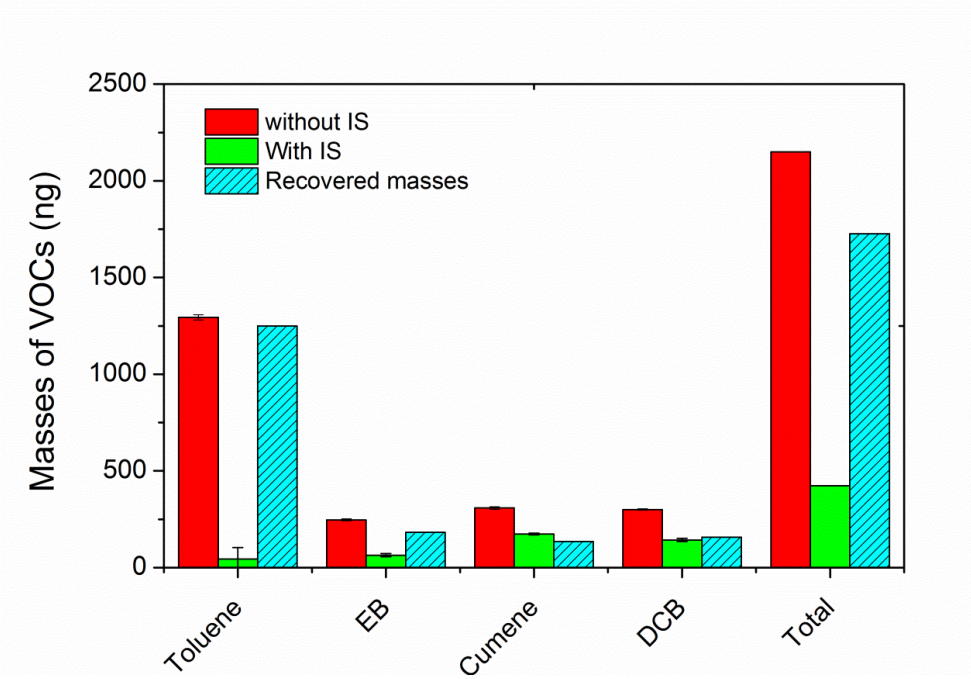

Figure 6.13 Effect of methanolic solution on masses of VOCs trapped on GN adsorbents

6.3.3.1.2 Examination of extraction efficiency of GN adsorbents

To examine the performance of GN adsorbents for adsorption of toluene, EB, cumene or DCB, sampling tubes loaded with GN30-11, GN30-12, GN30-21, GN20-11, GN40-11 or GN30-11T were conditioned prior to sampling (n=3) 100 cm^3 of contaminated air at flow rate of 100 cm^3 min^{-1}. The average masses of VOCs collected by each GN adsorbent (with acceptable % RSD values 2-15.6) are summarised in Table 6.4, and the 'references masses' collected by calibrant Tenax-TA tubes were used to calculate the GN adsorbent extraction efficiencies using Equation 3.6 as described in Section 3.6. The performances of GN adsorbents for VOCs extraction were compared to MCM-41 as illustrated in Figure 6.14.

Table 6.4 Average masses of VOCs adsorbed on GNs materials

Sorbents	VOCs	T	EB	Cumene	DCB	Total
GN30-11	Masses (ng) ±SD	1294 ±124	247 ±21	308 ±14	300 ±7	2149
	% RSD	9.6	8.5	6.4	2.3	
GN30-12	Masses (ng) ±SD	1095 ±95	242 ±24	324 ±35	364 ±57	2025
	% RSD	8.7	10	10.9	15.6	
GN30-21	Masses (ng) ±SD	1345 ±69	231 ±7	259 ±8	285 ±18	2120
	% RSD	5.1	3.2	3	6.3	
GN20-11	Masses (ng) ±SD	1222 ±39	230 ±9	281 ±6	267 ±21	2000
	% RSD	3.2	4.1	2	8	
GN40-11	Masses (ng) ±SD	1427 ±123	243 ±10	301 ±24	336 ±51	2307
	% RSD	8.6	4.1	8.1	15.2	
GN30-11T	Masses (ng) ±SD	1814 ±107	355 ±21	477 ±33	381 ±27	3027
	% RSD	5.9	5.8	7	7	

The results demonstrated that GNs, synthesised with a longer additive (PEHA), removed similar masses of VOCs regardless of their differing surface areas. In contrast GN30-11T, prepared using the shorter poly ethylene amine, TEPA, as an additive removed significantly higher masses from the contaminated air stream. One key observation was that similar extraction efficiencies were obtained for GNs

adsorbents prepared via PEHA addition as MCM-41, despite the lower surface area and pore volume of GNs (49 – 363 m^2 g^{-1} and 0.13 – 0.59 cm^3 g^{-1}) compared to MCM-41 (1014 m^2 g^{-1} and 0.82 cm^3 g^{-1}). Although GN30-11T demonstrated highest extraction efficiencies in this study it had lower surface area and pore volume (268 m^2 g^{-1} and 0.25 cm^3 g^{-1}), than two comparative GNs. Thus adsorption performance was not correlated to surface area or pore volume; rather it was thought that better performance was observed for GN30-11T due to the presence of micropores in the structure; which was expected due to the shorter chain length of the additive used during the synthesis. These results highlight the high selectivity of GNs materials in VOCs removal and strongly support the potential of GNs as greener alternatives of more expensive, less environmentally friendly porous materials.

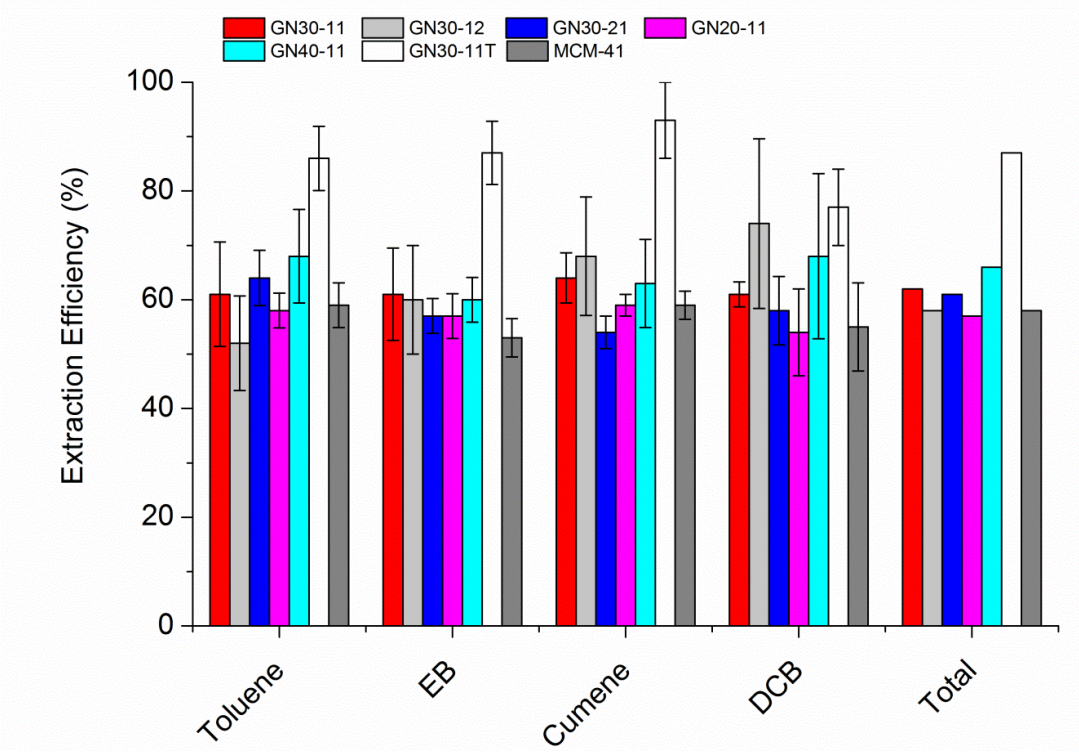

Figure 6.14 Extraction efficiency of GNs adsorbents and MCM-41 for VOCs adsorption. Error bars indicate the % RSD value (n = 3)

The importance of the presence of micropores in silica for optimum VOC extraction has been reported previously. When compared to microporous materials, the decrease in efficiency of mesoporous materials, such as MCM-41, for VOC extraction is related to its gas adsorption performance as illustrated by its Type IV isotherm. In one study [239] microporous materials outperformed mesosilica when analytes were present at low vapour phase concentrations; not until the adsorbates were present at high vapour phase concentrations did MCM-41 performed better than microporous zeolites. It has further been recognised that pore tailoring could enhance MCM-41 VOC extraction efficiencies for benzene adsorption at low concentration [240], when the pore opening was narrowed (from an average pore size of 3.0 to 1.4 nm). The mesosilica produced retained 80 % of its pore volume, exhibited a type I isotherm and the adsorption capacity value increased by 35 %. This correlation between microporosity and VOC adsorption at low concentration has since been recognised in further studies which compared VOC capacity performance of SBA-15 to MCM-41; in each case higher dynamic adsorption capacities observed for SBA-15 (for example for toluene and benzene [91] and light hydrocarbons [241]) with increased performance being attributed to the presence and number of micropores in SBA-15. Thus control of microstructure, such as the availability and number of micropores present in a material, are now thought to be key factors to consider when optimising materials for gas adsorption and selectivity [242]. The success of microstructure adjustment was shown also demonstrated for SBA-15; when the pore size was adjusted to be approximately 0.6 nm (to match the size of a benzene molecule) benzene was selectively removed from toluene [243]. Contrasting reports [157, 243] however indicating a decrease in benzene sorption capacity with decreasing pore diameter of MCM-41 or a decrease in adsorption capacity of *N*-nitrosodimethylamine [244] with MCM-48, suggesting that in addition to tailoring pore size, the role of the micropore-mesopore system must also be considered when optimising the adsorbent for selective adsorbate extraction. Rather it might be that the micropores in SBA-15 act as adsorption sites but do not act efficiently on their own and require easy access routes which are facilitated by the mesopores [241]. Such interactions were shown for the diffusion of *n*-heptane and cumene onto SBA-15; the adsorption results indicated that intrawall micropores played a major role in

molecular transport at low analyte concentration. Indeed it was shown that diffusion of *n*-heptane was controlled by a combination of micropore and mesopore diffusion resistances [245].

6.3.3.1.3 Dynamic adsorption capacity of GN materials (Breakthrough)

Further experiments were conducted to examine the breakthrough and dynamic capacity of GN adsorbents for VOC adsorption by passing contaminated air through the sorbent tubes at 100 cm^3 min^{-1} for longer sampling times. Sampling tubes containing GN30-11, GN30-12, GN30-21, GN20-11, GN40-11 or GN30-11T (100 mg of sorbent in each tube) were used to sample VOCs. Tenax-TA sampling tubes were positioned after sorbent tubes to collect masses that passed over the sorbent and the masses of VOCs were analysed as outlined in Section 3.4.1. The breakthrough values were calculated by Equation 3.7 (see Section 3.6) as the mass of VOC not adsorbed on the sorbent tube divided by the mass of VOC trapped by the sampling tube, and the breakthrough was measured when percentage values were greater than 5%.

The calculated dynamic capacities of all GN adsorbents were compared with that of MCM-41 (see Figure 6.15) and the results demonstrated that the toluene exceeded the breakthrough value for all sorbents under study first. GN30-12 had the lowest capacities; breakthrough rapidly occurred with a high value (of approximately 50 %) after sampling 0.1 dm^3 of contaminated air, followed by GN30-11 which had slight higher capacity (after 0.2 dm^3) in spite of their similar surface areas (49 ± 0.4 or 58 ± 0.5 m^2 g^{-1}). Capacities of GNs were increased by altering the Si: N ratio to 2: 1, increasing the concentration of silica precursor to 40 mM or using a shorter additive TEPA; breakthrough of VOCs occurred after sampling 0.5 dm^3 of polluted air for GN30-21, GN40-11 or GN30-11T.

Interestingly, GN-20-11 had the highest adsorption capacity of the GNs materials studied here, which was similar to that of MCM-41, in spite of its lower surface area and pore volume (363 m^2 g^{-1}, 0.26 cm^3 g^{-1}) compared to MCM-41 (1014 m^2 g^{-1}, 0.82 cm^3 g^{-1}). However, toluene breakthrough was observed when sampling 1 dm^3 of

polluted air by GN20-11 or MCM-41, it was dramatically increased at this point to be over 30 % for GN20-11. On the other hand, breakthrough of EB, cumene or DCB did not occur until longer sampling times. The VOC trapped at the point of toluene breakthrough for GNs or MCM-41 (summarised in Table 6.5) demonstrated that MCM-41 had a significantly higher capacity with a total capacity of 25917 ng compared to GN20-11 which had a capacity of 15313 ng; the highest value of all the GN adsorbents. Since sorbent tubes contained the same weight (100 mg) of GNs or MCM-41 and were used to sample VOCs under the same condition, it was thought that the delay in breakthrough for MCM-41 was due to its higher surface area and larger pore volume.

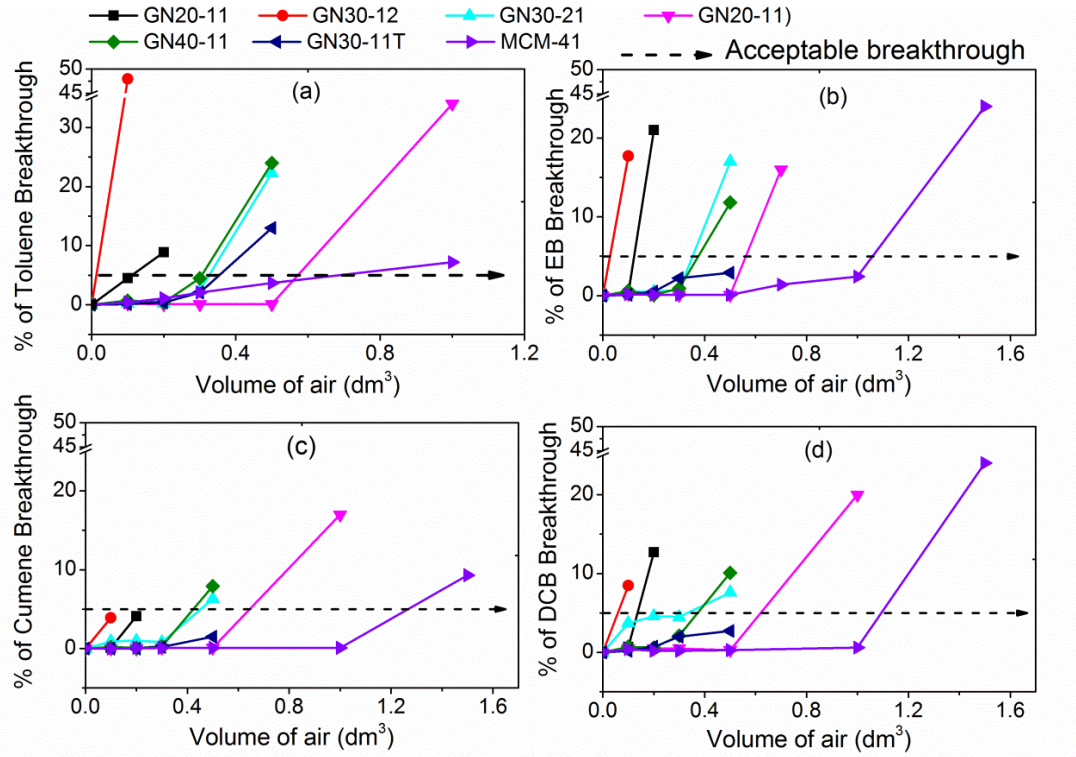

Figure 6.15 Calculated breakthrough volumes for toluene (a), EB (b), cumene (c) and DCB (d) on MCM-41 and GN adsorbents

Table 6.5 Masses of VOCs trapped at point of toluene breakthrough on sorbents

Sorbents	Toluene Masses (ng)	EB Masses (ng)	Cumene Masses (ng)	DCB Masses (ng)	Total Masses (ng)
GN30-11	2623	485	644	637	4389
GN30-12	1008	266	362	421	2057
GN30-21	5726	964	1243	1356	9289
GN20-11	8408	2095	2410	2400	15313
GN40-11	5681	1159	1468	1180	9488
GN30-11T	8029	1755	2195	1876	13855
MCM-41	16796	3368	2980	2773	25917

Although from a commercial standpoint, higher capacity per unit weight is ideal, in order to understand the relationship between the physical properties of these materials with their functional performance, VOC extraction capacities were normalised with respect to their surface areas (SA), in addition to normalising the capacities with air volume sampled at point of breakthrough (see Figure 6.16). When normalised capacities per unit of surface area (ng/m^2) the results showed that GN adsorbents significantly outperformed MCM-41 despite their low surface areas, confirming the effect of microporosity on VOC extraction.

In contrast GN adsorbents had lower capacities when normalised per unit of air volume (ng/cm^3), even lower than capacity of MCM-41 except GN30-11T which was only slightly higher. These results indicated that GNs adsorbents had the best short-term performance for VOCs extraction despite their lower surface area but if analytes are to be scrubbed from larger volumes of air MCM-41 would be required to extract higher masses of VOCs over longer period of time.

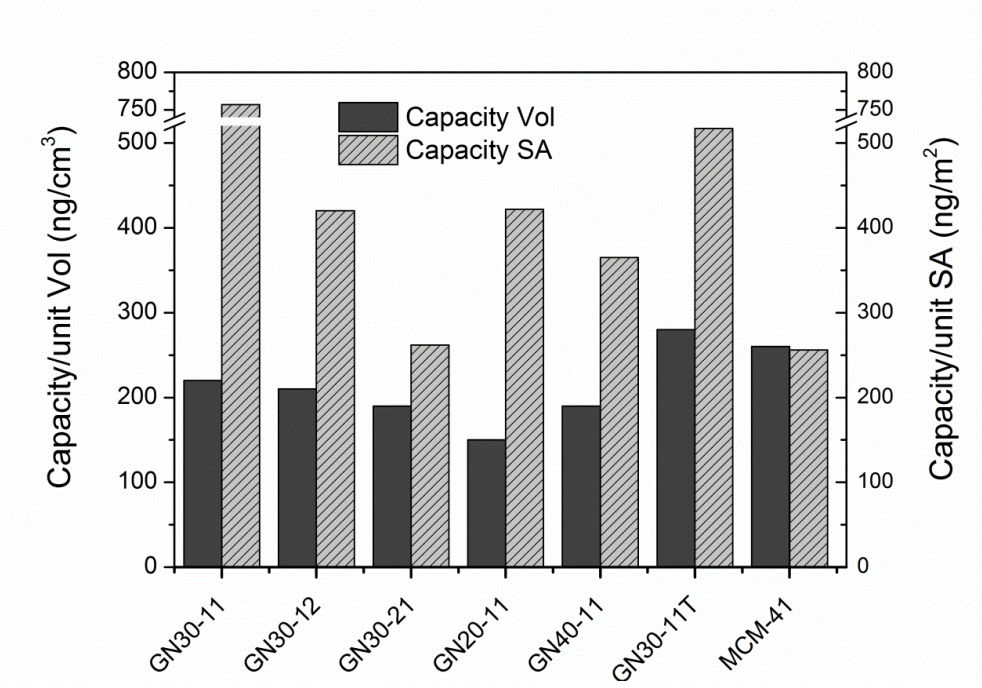

Figure 6.16 Normalised capacities per unit volume or per unit surface area (SA) of GN adsorbents and MCM-41

6.3.3.2 Use modified GN adsorbents for chemisorption of H_2CO

After examining the performance of GN adsorbents for VOCs adsorption and to enhance their selective adsorption of H_2CO, these adsorbents were successfully functionalized by organic amine groups. Herein GN30-11, GN40-11 and GN30-11T were selected to study their efficacy for H_2CO extraction before and after grafting by organic amine groups.

6.3.3.2.1 GNs extraction efficiencies and capacities for H_2CO adsorption

To examine the extraction efficiencies of GN30-11, NH_2-GN30-11, GN40-11, NH_2-GN40-11, GN30-11T or NH_2-GN30-11T for H_2CO adsorption, hydrazine trapping cartridges were immediately positioned after sorbent tubes to collect masses of H_2CO passed over sorbents (see Figure 3.11 in Section 3.6). Contaminated air was sampled at a rate of 100 cm^3 min^{-1} for 60 min with sorbent in-line and the masses collected by hydrazine sampling cartridges were determined as described in Section 3.5.2 and

used to calculate masses trapped by sorbents in-line (wt_{sorb}); experiments were repeated (n= 3). Extraction efficiencies for GN adsorbents were calculated using measured masses (wt_{nosorb} and wt_{sorb}) as given in the equation 3.6 in Section 3.6 and compared with efficacy of mesoporous adsorbents MCM-41 (see Figure 6.17).

The results showed that functionalised GN adsorbents (NH_2-GN30-11, NH_2-GN40-11 or NH_2-GN30-11T) had significantly higher performances when used to sample 6 dm^3 of H_2CO contaminated air (1.4 mg m^{-3}). NH_2-GNs removed approximately 97 % of H_2CO vapour which was similar in efficiency of NH_2-MCM-41 despite their physical properties differences. Non-functionalised GNs and MCM-41 adsorbents had lowest extraction efficiencies at approximately 70 %, in addition the lowest efficacy was measured for GN30-11 at 10 % as expected due to its surface area which was approximately 5 times lower than of other GNs adsorbents.

Dynamic capacities of selected GN adsorbents were determined by measuring the H_2CO breakthrough of each adsorbent and again were compared with the NH_2-MCM-41 capacity (see Figure 6.18). The results indicated that non-functionalised GNs and MCM-41 adsorbents had lower dynamic adsorption capacities for H_2CO vapour as breakthrough was rapidly measured at values of 90, 25, 25 or 31 % for GN30-11, GN40-11, GN30-11T or MCM-41, respectively. In stark contrast no breakthrough were observed for functionalised GNs or MCM-41 adsorbents. GN adsorbents grafted with organic amine groups had a similar performance to NH_2-MCM-41. When the sample volume was increased to 12, 18 or 24 dm^3, breakthrough occurred for NH_2-GN30-11 after sampling an air volume of 18 dm^3 whereas no breakthrough was measured for GN40-11 or GN30-11T; even when the sample volume increased to 24 dm^3. Overall, the NH_2-GN adsorbents performed as well as NH_2-MCM-41 despite their low surface areas and pore volumes. Considering the advantages of production (including lower cost, pH neutral synthesis, green chemistry, speed of synthesis) these results demonstrate that GN adsorbents provide an exciting novel platform that can be used in pollution extraction or gas separation (e.g. for the targeted removal of formaldehyde vapour).

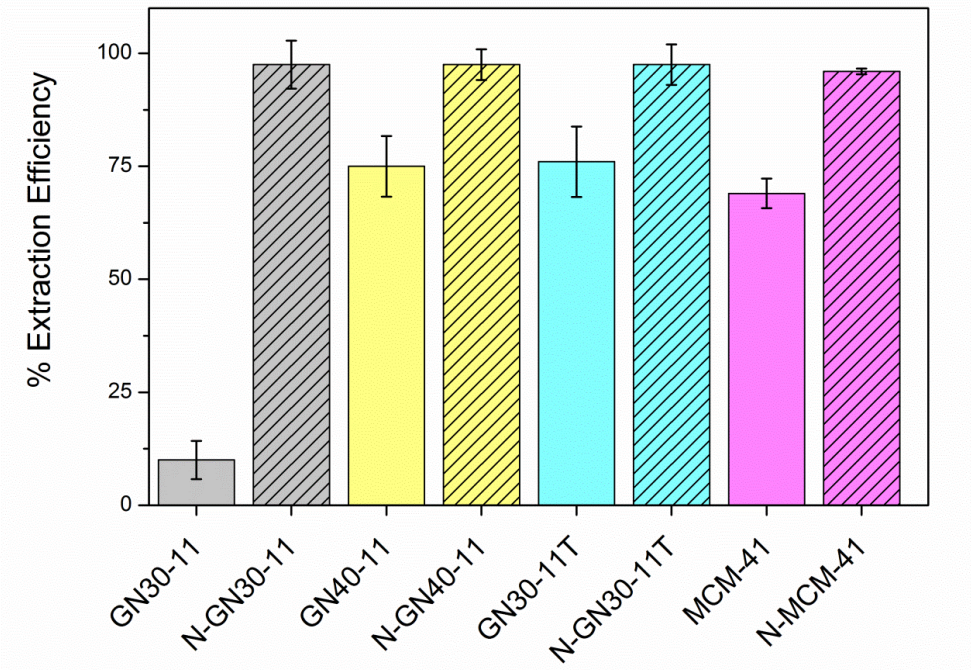

Figure 6.17 Extraction efficiency of GN adsorbents for H_2CO adsorption and comparison them to MCM-41. Error bars indicate the % RSD value (n = 3)

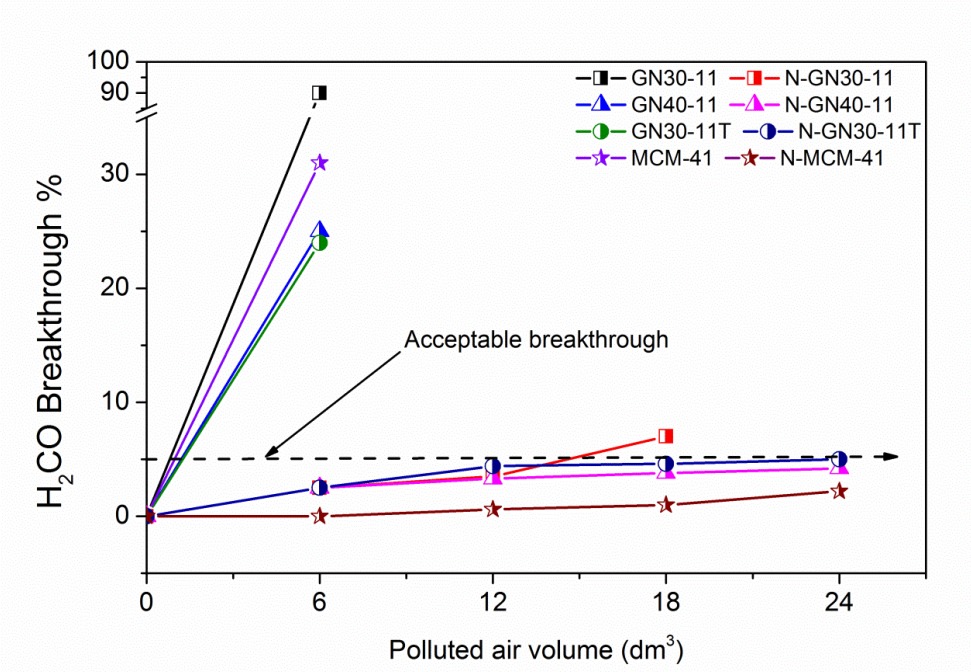

Figure 6.18 Calculated breakthrough volumes for H_2CO on GN adsorbents and MCM-41

6.3.3.2.2 Examination of chemisorption removal of H_2CO

To ensure that H_2CO was removed by GN adsorbents from the contaminated air by chemisorption, loaded sorbents tubes were back flushed with air at 100 cm^3 min^{-1} for 60 min. Any H_2CO removed during this process were recovered using hydrazine sampling cartridges and masses were determined by LC-UV-vis (see Figure 6.19). GN adsorbents which had not been functionalised retained only a very small mass of VOCs and during the air flush 25 % or 43 % of loaded H_2CO was lost from GN30-11 or GN40-11 (Figure 6.14);. This suggests that the formaldehyde molecules are partly retained by physical adsorption processes In stark contrast NH_2- GN adsorbents retained > 95 % of trapped analytes during the back flush indicating a strong interaction (chemisorption) between the surface of the adsorbent and the adsorbate due to the strong bound formed between with amine group and formaldehyde (see Figure 5.17 in Section 5.3.4.1.2). These results showed that GN adsorbents had a high performance for chemisorption of H_2CO which further supports the potential of GNs as greener alternatives pollution platforms

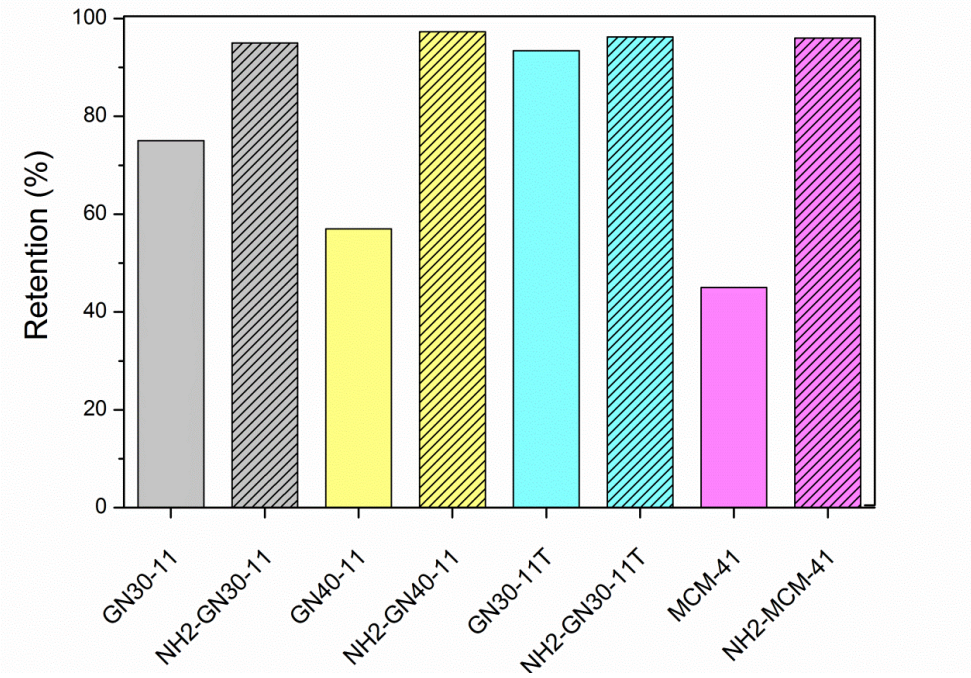

Figure 6.19 Retention of H_2CO adsorbed on GNs and MCM-41 adsorbents

6.3.3.2.3 Effects of VOCs on H_2CO extraction

To assess the potential efficacy of the NH_2-GNs for H_2CO removal in the presence of VOCs, sampling tubes loaded with a known mass of H_2CO (each sorbent tube used to sample 6 dm^3 of contaminated air containing 1.4 mg m^{-3} of H_2CO vapour), was then exposed to a VOC contaminated air stream (34.05, 18.02, 12.38, or 7.81, mg m^{-3} of toluene, EB, cumene or DCB, respectively). The recovered masses were collected by hydrazine sampling cartridges and analysed by LC-UV-vis. The results (see Figure 6.20) demonstrated that approximately 37, 30 or 50 % of masses trapped on sorbents were recovered from GN40-11, GN30-11T or MCM-41, respectively, whilst NH_2-sorbents retained > 90 % of the H_2CO during the VOC purge. These results supported the previous theory of chemisorption and that that VOCs significantly displaced H_2CO form unmodified sorbents whereas they have no competitive detrimental effect on the masses of H_2CO trapped NH_2-sorbents.

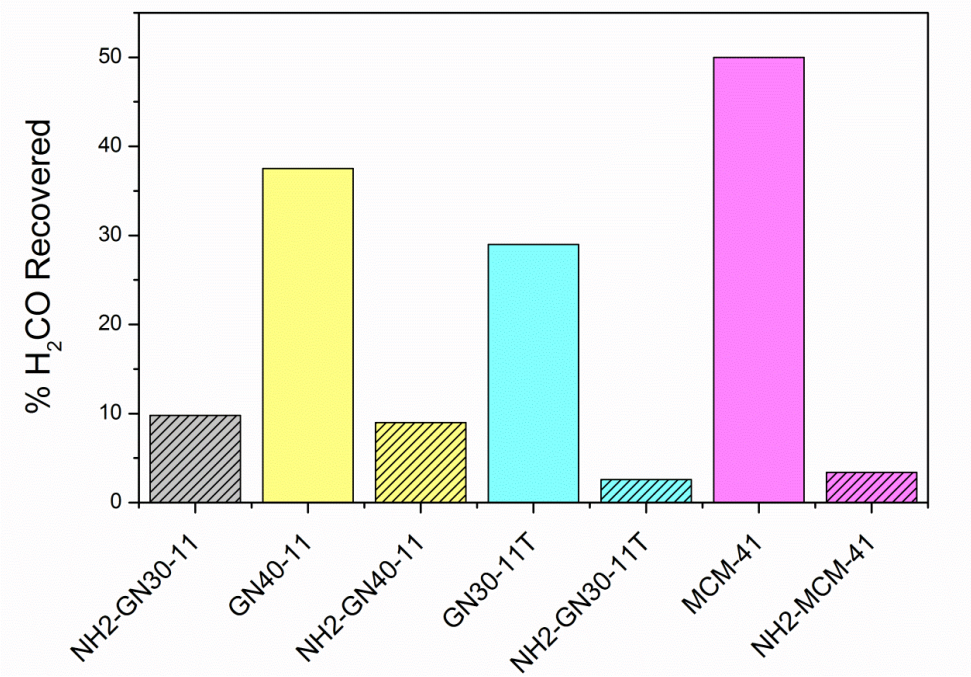

Figure 6.20 Displacement of pre-adsorbed H_2CO by VOC (% H2CO recovered)

The efficacies of GN30-11T and NH_2-GN30-11T were also assessed for H_2CO extraction when in the presence of selected VOCs. The chamber conditions were altered so that the environment contained mixture of 17.03, 9.1, 6.2, 3.9 or 0.7 mg m-3 of toluene, EB, cumene, DCB or H_2CO respectively. The polluted air was sampled by sorbent tubes at a flow rate 100 cm^3 min^{-1} for 60 min. Adsorbent breakthrough values were compared to MCM-41 measured under the same conditions (see Figure 6.21). The results showed that no breakthrough was observed for NH_2-sorbents, indicating that the presence of VOCs in the flowing stream had no detrimental effect on the selective extraction of H_2CO vapour.

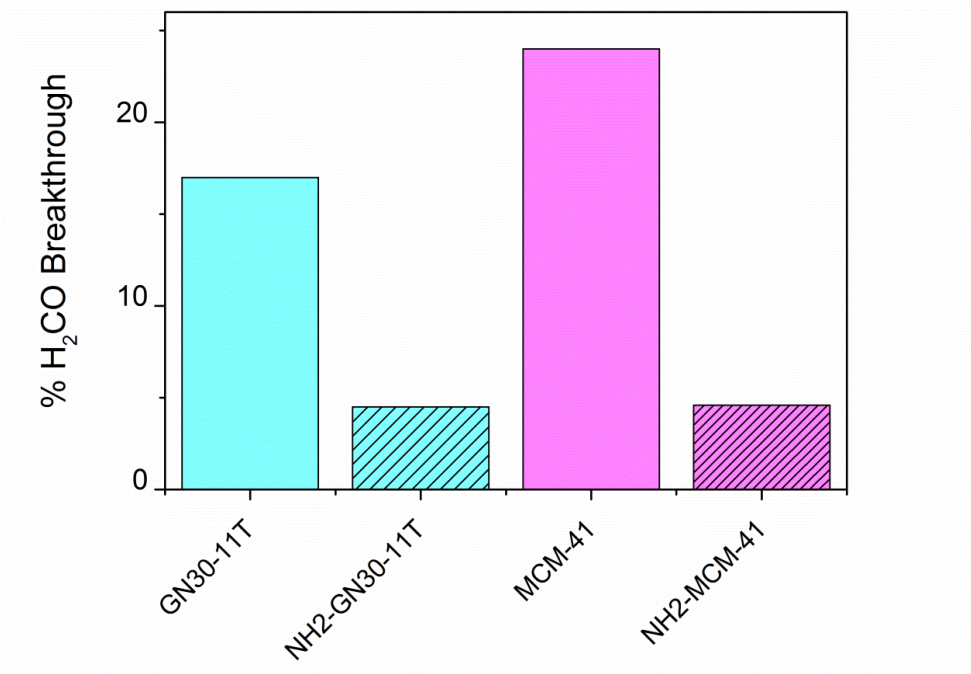

Figure 6.21 Selective removal of H_2CO (% breakthrough) from a mixture of H2CO and VOC

6.4 Conclusions

This work presents the production of novel silica green nanomaterials (GNs) using a bioinspired synthesis route. The preparation of GNs exhibits a range of advantages including the use of neutral pH and room temperature conditions, rapid synthesis (15

min), and a considerable reduction in secondary pollution by using aqueous solutions by eliminating use of organic solvents in the preparation method. These advantages represent a significant progress since the complex and lengthy process of preparation of MCM-41 materials has been a major roadblock in delivering these materials to market in a cost-effective manner. The physical properties of produced GNs possess features such as a unique porous network including micropores which are advantageous in a number of applications such as gases adsorption.

The present study also reports developments of synthetic conditions in order to improve the physical properties of the first synthesised GN adsorbent (GN30-11) such as increasing surface area by alteration of silica precursor concentration, Si: N ratio or the use of shorter poly ethylene amine as additive. These promising results indicate that GNs can be tailored to provide ideal physical properties to suit specific applications. Although the concept of designer platforms has been proven here, more work is required to optimise the material to ensure maximum VOC adsorption capacity.

This work also reports the first application of GN adsorbents for VOC removal from contaminated air and compares their efficiencies to the traditional mesoporous material MCM-41. The results demonstrated that GN adsorbents were comparable, or in some examples, better than the benchmark MCM-41 silica in terms of extraction efficiencies and capacity per unit surface area. The results suggested that the performance of GNs was related to their unique physical properties, which can be easily tailored. This work also presents the first application of GNs adsorbents as H_2CO scavengers after successful grafting by organic amine groups. Herein the performance and dynamic adsorption capacity of these adsorbents for H_2CO extraction were examined and compared with grafted MCM-41. The results indicated high performance of modified adsorbents compared to unmodified adsorbents, confirming that active sites (amine groups) were necessary before silica materials could extract H_2CO from air permanently. Interestingly chemisorption was evident in displacement experiments ensuring that H_2CO was removed from the air even in presence of other VOCs. By highlighting the strengths of GNs, considering the cost, time and environmental implications alone (when preparing silica materials) it is

suggested here that GNs provide an exciting new platform for adsorption and can rival more expensive meso-silica materials for environmental remediation of VOCs and H_2CO from indoor air.

7 A novel preparation route for mesoporous materials

7.1 Introduction

As reported previously, mesoporous materials possess high thermal and chemical stability, controllable composition as well as being flexible via functionalization permitting the grafting of specific functional moieties onto the silica surface for specific applications [246]. They have found use in a wide range of potential applications including heterogeneous catalysts or catalyst supports [247], separation process, sensors [248] and environmental pollution control [151, 249]. Moreover functionalisation of these materials by specific chelates is often used to improve the selectivity, stability and activity in a large number of catalytic reactions and sorption processes [159, 166]. Arguably the most important ordered mesoporous materials belong to the M41S family (MCM-41 or SBA-15) as previously reported in the introduction of chapter 5 (See section 5.1 for more information of their properties, synthesis methods and applications). Generally, MCM-41 has been synthesised using a sol-gel method with tetraethylorthosilicate (TEOS) or sodium silicate as a silica precursor and organic surfactant such as cetyltrimethylammonium bromide (CTAB) as the template, which is removed from the silica by calcination, solvent extraction or microwave digestion.

Numerous researcher studies (summarized in in Table 5.1 in Section 5.1.1) have modified the original preparation method reported in reference [81] to enhance the physicochemical properties of MCM-41. Despite the increased attention of researchers studying the preparation of MCM-41, only a few of them focussed on the modification of as-made MCM-41 preparation conditions. Attempts have been made to decrease the preparation time, permit synthesis at ambient temperature, or to reduce the cost by using an inexpensive silica precursor. Therefore it is thought that the main disadvantages of the current preparation method, which limits the industrial usage of mesosilica materials in industrial and environmental applications include:

- Long preparation times (2 – 7 days).
- The use of an expensive silica precursor (TEOS) which requires a co-solvent to solublise it in the reaction mixture.
- The use the harsh conditions such as high temperature and pH in preparation.

- The production of only small quantities of material in the final production (few grams).

Consequently researchers have tried to produce larger quantities of MCM-41 with short preparation times and the less expensive sodium silicate salt as the silica precursor. For example, Climent *et al.* [170] reported shorter preparation times (1 h) of MCM-41 synthesis under basic conditions using TEOS as silica precursor and CTAB as a surfactant. Huang *et al.* [162] prepared MCM-41 in two steps; first sodium silicate was used to produce a gel within a mixture of surfactants (CTAB and tetraethylammonium hydroxide TEAOH) in a short preparation time (2 h) at room temperature at pH (9.5 – 10), then the gel was aged by heating at 96 ^{0}C for 4 days under auto-generated pressure. In another example, Tang *et al.* [250] used ultrasound irradiation to prepare highly ordered MCM-41 by sonicating a mixture of sodium silicate, CTAB, ethyl acetate and distilled water for 3.5 h under ambient conditions. Although the ultrasound method produced a highly ordered MCM-41 material under ambient conditions the mass of material produced was limited due to the small capacity of the sonication cell used (50 cm^3).

Most MCM-41 modified preparation methods (Table 5.1 in Section 5.1.1) used a Teflon lined autoclave at the intermediate stage (the condensation stage) to control the pressure and temperature of the reaction. This stage of preparation also involves heating the gel to approximately 100 ^{0}C for long periods (1 to 7 d), which leads to increased overall preparation times even when initial preparation stages were short.

More recently attention has been focussed on the production of large quantities of MCM-41. For example Ritter *et al.* [141] reported a scale-up, room temperature procedure for MCM-41. The gel was prepared using the conventional reagents of TEOS and CTAB but crucially the synthesis was prepared at room temperature and the reagents were mixed for only 4 h before being aged at room temperature for 24 h. The final MCM-41 product was obtained by filtration, washing with copious amounts of distilled H_2O and drying in air at room temperature prior to calcination in air at 550 ^{0}C for 16 h. Finally, Idris *et al.* [153] recently reported a new procedure for template removal by microwave digestion which is faster than the traditional

calcination method. In addition it can be used to produce MCM-41 with larger average pore size and greater amounts of surface silanol groups.

As discussed in Chapter 6, "bio-inspired silica" materials are growing in popularity due to the use of environmental friendly synthesis routes and rapid preparation times [125]. The results provided in Chapter 6 also support the theory that the textural properties of GN, such as surface area and particle size, can be controlled by selecting appropriate additives or changing the chemistry of silica precursor and additives. As an example GN has been synthesised using poly ethylene amines as an additive to precipitate silicic acid in a short time and under mild conditions [213, 251].

As reported in Section 6.1 numerous research groups are developing synthetic routes to prepare bio-inspired silica materials. Additionally there are numerous methods of preparation which describe the synthesis of MCM-41 (see section 5.1.1). Using the bioinspired synthesis route materials can be produced economically, quickly and at near neutral pH. Using the conventional MCM-41 method silica can be prepared with high surface area and mesopores. It is recognised that by combining the advantages of the bioinspired silica synthesis route with the templating mechanism of MCM-41, materials can be prepared quickly, efficiently, economically and with the required high surface area and mesopore volume. Therefore this chapter reports the development of such a method' where CTAB will be introduced into the bioinspired silica method to examine the materials that can be produced. This will permit, for the first time; the preparation of mesoporous silica with high surface area in short periods of time using green synthetic routes and as yet this combination of methods has yet to be explored.

The work in this Chapter reports a novel route for the synthesis of mesoporous materials by combining the knowledge from conventional MCM-41 preparation with that of a bio-inspired silica synthesis route. Ordered mesoporous materials were prepared using sodium silicate as a silica precursor and CTAB as an organic surfactant under mild conditions (ambient temperature and natural pH) in an environmentally friendly aqueous solution with short preparation times (15 min). This work aims to:

- Synthesis ordered mesoporous silica materials with a high surface area, large pore size and pore distribution.
- Produce large quantities of mesoporous materials in a short preparation time (15 min).
- Reduce the cost of synthesis by using a less expensive silica precursor (sodium silica) instead of TEOS and avoid the use of co-solvents.
- Compare the physiochemical properties of the new materials with MCM-41, prepared via conventional methods under harsh conditions.
- Compare the performance of the new material with MCM-41 for the extraction of selected VOCs and H_2CO adsorption from contaminated air streams.

7.2 Experimental

7.2.1 Synthesis of mesoporous adsorbents

In a typical synthesis, a mixture of 208 cm^3 distilled water and 96 cm^3 of ammonia solution (NH_3, 35 %, Fisher Scientific) was warmed to 35 ^{0}C, and 5.5 g of (CTAB was added under stirring to provide a clear solution. To provide a solution of silicic acid, 6.5 g of sodium metasilicate ($Na_2SiO_3.5H_2O$, Fisher Scientific) was dissolved in 250 cm^3 of distilled water in a 500 cm^3 of polyethylene bottle. Then a small amount of concentrated hydrochloric acid (HCl, Fisher Scientific), 75 cm^3, was added to the silica solution 1 min prior to the addition of the surfactant solution. The pH of the final mixture was measured by a pH-meter and quickly adjusted to pH = 7 ± 0.2 by adding a few drops of 1M HCl.

The produced gel was aged for 15 min at room temperature. To assess the influence of aging time, the above procedure was repeated with an increased aging time of 18 h. The final materials were obtained after filtration, washing 3 times with distilled water and drying in air at room temperature. The materials will hereafter be referred to as ‘as-USG-S or as-USG-L’ according to laboratory preparation in University of Strathclyde Glasgow (USG) whereas S and L indicate short (15 min) and long (18 h) aging times, respectively. Finally, the as-made materials were calcined at 500 ^{0}C for

5 h, producing 'USG-S or USG-L' respectively. A further batch of As-USG-S was prepared where the surfactant was removed by microwave digestions using a MARS microwave digestion unit with an operating power of approximately 1600 W; the pressure and temperature inside the microwave were controlled to be lower than 1.3 MPa and 200 ^{0}C, respectively. This material will be referred to as MWD-USG-S. A summary of the factors altered during samples preparation is given in Table 7.1.

Table 7.1 Samples of USG materials prepared under mild conditions

Sample ID	Precursor conc. (mM)	Precursor mass (g)	CTAB mass (g)	Ratio of Si: N	Aging time
USG-S	40	6.5	5.5	2: 1	15 min
USG-L	40	6.5	5.5	2: 1	18 h
MWD-USG-S	40	6.5	5.5	2: 1	15 min

The extraction efficiencies of the new mesoporous materials (USG-S and USG-L) were examined for the adsorption of selected VOCs and were compared to MCM-41. To increase the application of the materials they were modified to selectively target H_2CO from air. Post synthesis grafting was used to functionalize the materials with anorganic amine group (3-aminopropyltrimethoxysilane); the post synthesis grafting process is described in detail in Section 3.2. Modified materials are labelled NH_2-USG-S or NH_2-USG-L.

7.2.2 Characterisation and assessment of USG materials

To characterise the physiochemical properties of the new USG materials SAS-XRD or nitrogen adsorption-desorption isotherms were used to examine nature of structure, the surface area, pore size and pore size distribution of the materials; experimental details are as described in Section 3.3. In addition ATR-FTIR spectroscopy and microanalysis were used to confirm the successful

functionalization of NH_2-USG-S and NH_2-USG-L. The materials were tested for VOC or H_2CO extraction as described previously.

7.3 Results and discussion

7.3.1 USG materials characterisation by N_2 adsorption isotherm and XRD analysis

The SAS-XRD patterns of USG materials obtained after calcination or microwave digestion are shown in Figure 7.1a. For comparison, the SAS-XRD pattern for MCM-41 is given in Figure 7.1b. The patterns indicated that the calcined USG adsorbents had a typical (100) diffraction peak at a 2 θº angle of 1.87 or 1.97 for USG-L or USG-S, respectively, with similar intensity of approximately 13200. Moreover their patterns also showed weaker reflections which were assigned to the (110) or (200) reflections. Calcined USG and MCM-41 adsorbents demonstrated a similarity long range ordering, with slightly higher intensities measured for the USG materials indicating a longer range order of pores. The SAS-XRD pattern of MWD-USG-S indicated that the use of harsh microwave digestion conditions led to destruction of the pore order in the silica framework producing an amorphous material. These results were confirmed by transmission electron microscopy (TEM), the micrographs are illustrated in Figure 7.2. Interestingly MWD-MCM-41 still had limited pore ordering as demonstrated by the SAS-XRD peak at a 2 θº angle of 2.1. Again the use of the microwave to remove the organic template resulted in lower pore ordering compared to the calcined sample, but a clear (100) reflection peak was noted with similar intensity to MCM-41. These exciting results indicated that if calcination is used to remove the organic template from USG materials an ordered porous material can be produced using a 15 min synthesis under green conditions with comparable ordering to MCM-41.

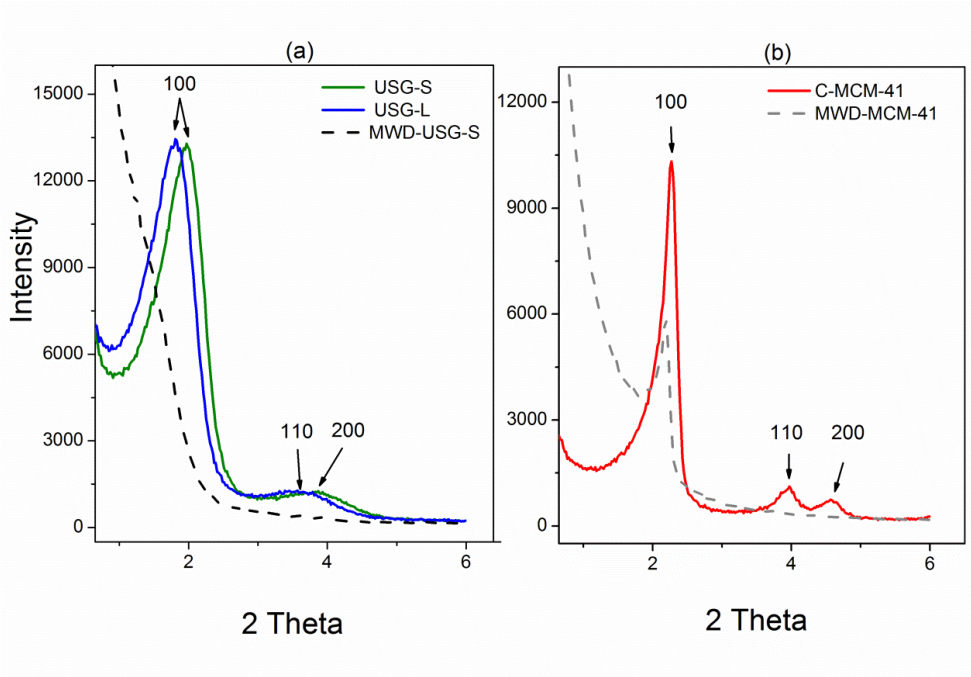

Figure 7.1 SAS-XRD patterns of (a) USG and (b) MCM-41 adsorbents

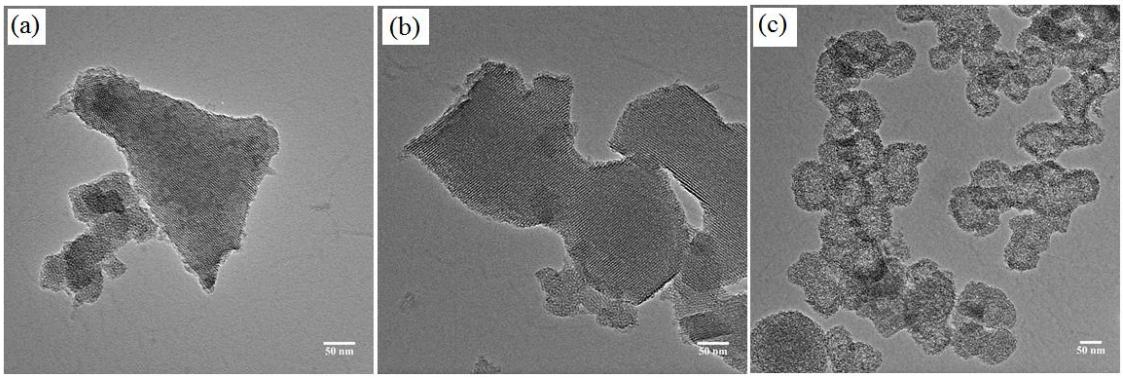

Figure 7.2 Representative TEM images of (a) USG-S, (b) USG-L and (c) MWD-USG

The physicochemical properties of USG materials were measured by nitrogen sorption isotherms and the collected data is summarised in Table 7.2. Results show that rapid synthesis of USG-S material, aged for 15 min, had significantly higher surface area (1140 ± 58.8 $m^2 g^{-1}$) than the USG-L material aged for 18 h at 730 ± 3.4 $m^2 g^{-1}$. A slight increase in average pore size from 2.6 to 3.1 nm was measured for USG-L although the pore volumes were similar at 1.00 or 0.99 $cm^3 g^{-1}$. One notable

observation was that USG-S had a slightly higher surface area and pore volume than MCM-41. Interestingly the surface area of USG-S was significantly reduced (from 1140 ± 58.8 to 412 ± 1.5 m^2 g^{-1}) when the template was removed by MWD and the reduction in surface area was greater than experienced for MWD-MCM-41 (760 ± 1.1 m^2 g^{-1}). It was observed that the use MWD produced MWD-USG-S with variety of pore sizes (from 2.6 to 3.9 nm) and lower pore volume (0.65 cm^3 g^{-1}). In contrast MWD caused an increase in the average pore size (6.74 nm) and pore volume (0.99 cm^3 g^{-1}) of MWD-MCM-41.

Table 7.2 Physical properties of USG mesoporous adsorbents

Sample ID	Surface area (m^2 g^{-1})[a]	Pore size (nm)[b]	Pore volume (cm^3 g^{-1})[c]
USG-S	1140 ± 58.8	2.6	1.00
USG-L	730 ± 3.4	3.1	0.99
MCM-41	1014 ± 4.6	2.7	0.82
MWD-USG-S	412 ± 1.5	(2.6-3.9)	0.654
MWD-MCM-41	760 ± 1.1	6.74	0.99

[a] Calculated by BET model from sorption data at range 0.05-0.25 of relative pressure.

[b] Calculated by BJH model from the adsorption branches of isotherm.

[c] Calculated from N_2 adsorbed at a relative pressure P/P_0 of 0.99.

The N_2 sorption isotherms of USG materials and MCM-41 as illustrated in Figure 7.3 were indicative of type IV isotherms according to IUPAC classification, confirming the mesoporous nature of the newly prepared USG materials. USG isotherms had similar capillary condensation steps to MCM-41 at relative pressures of 0.31–0.38 with little-no hysteresis loop indicating a narrow range of well-defined pores. This was confirmed by examination of the pore size distribution plots of USG and MCM-41 as shown in Figure 7.4.

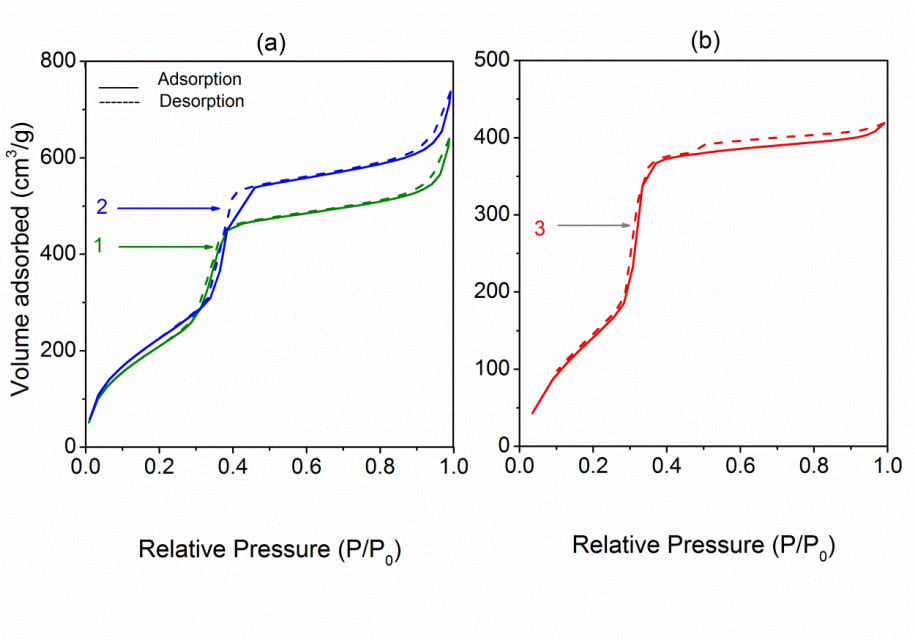

Figure 7.3 Nitrogen adsorption isotherms of (1) USG-S, (2) USG-L and (3) MCM-41

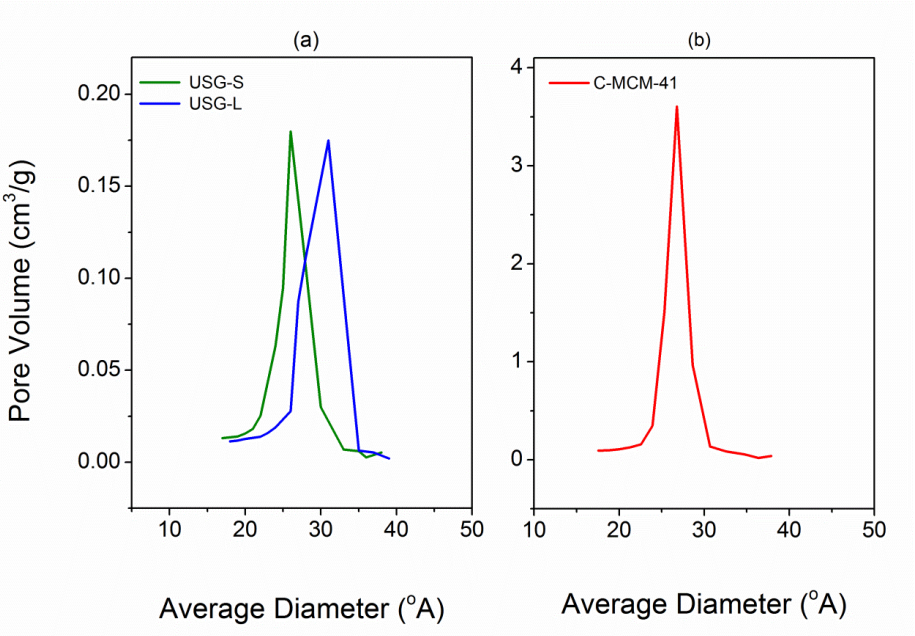

Figure 7.4 BJH pore size distribution patterns of (a) USG adsorbents and (b) MCM-41

The N_2 sorption isotherms for MWD-USG-S and MWD-MCM-41, shown in Figure 7.5, also indicated a mesoporous structure was obtained. However compared

to the calcined materials, the capillary condensation step at higher relative pressures of (0.55 – 0.70) indicated the production of larger pores in the material by the microwave digestion method. Moreover the hysteresis loop was broader for the MWD material suggesting that it contained pores of different shape and size; as confirmed by plotting the pore size distribution plot, shown in Figure 7.6, which gives a pore size distribution range of 2 to 12 nm (with an average of 2.74 nm). Use of MWD to remove the template from USG-S also induced changes in the structure of the final product. In addition to the reduced surface area and pore volume noted above the isotherm shows a gradual condensation step for MWD-USG-S at relative pressures of (0.50 – 0.98). Indeed the isotherm shape is not common and less representative of a type IV classic isotherm. It was concluded that the harsh conditions of the MWD method caused significant disruption of the silica framework of USG-S with a loss of pore ordering, reduction of surface area and pore volume and is therefore not recommended for use with this material.

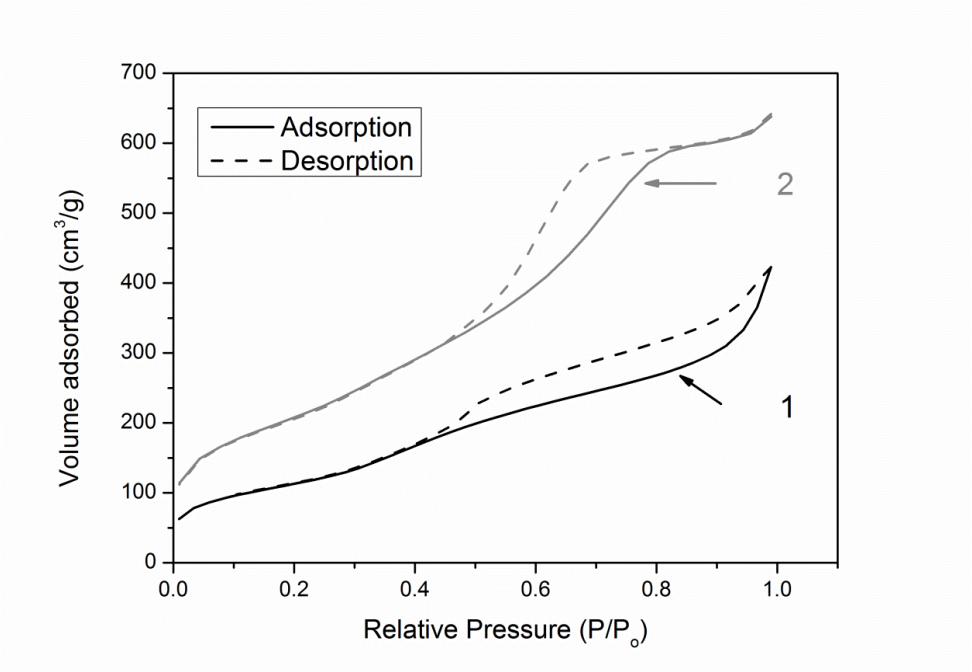

Figure 7.5 Nitrogen adsorption isotherms of (1) MWD-USG-S and (2) MWD-MCM-41

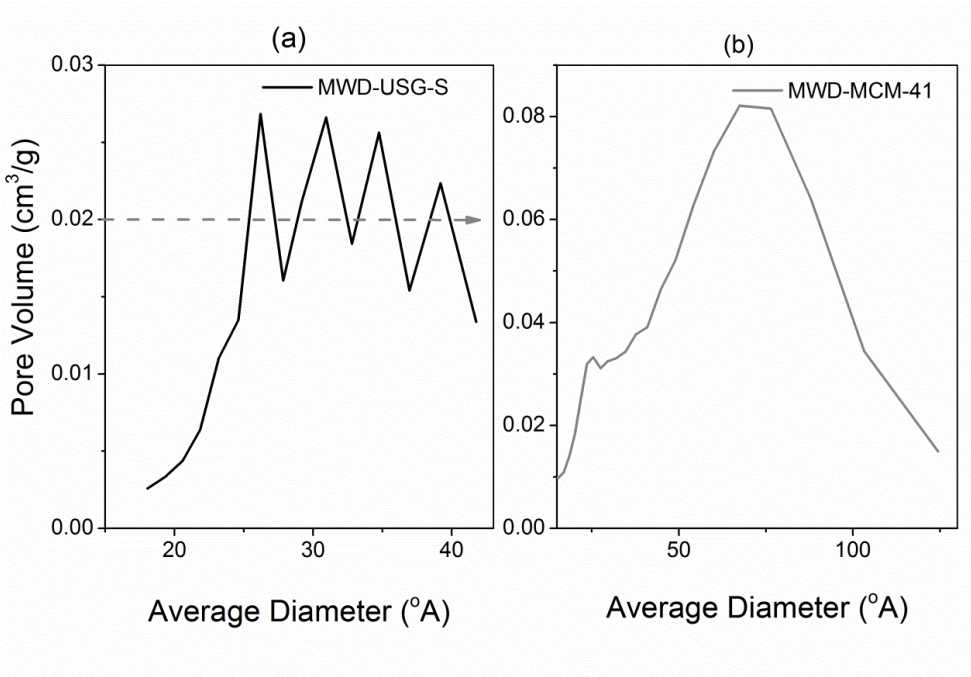

Figure 7.6 BJH pore size distribution patterns of (a) MWD-USG –S and (b) MWD-MCM-41

7.3.2 ATR-FTIR spectra and elemental analysis of USG samples

The ATR-FTIR spectra of USG-S and USG-L samples before and after functionalisation by organic amine groups are shown in Figure 7.7. The formation of silica was apparent from peaks i-iii in Figure 7.7a, indicating that all USG adsorbents had similar features which were thought to be related to the inorganic backbone such as the Si–O–Si stretch. A large broad band between 1000 and 1260 cm^{-1} (i) and the band at 800 cm^{-1}(iii) were assigned to the Si–O–Si stretching, whereas a band at 950 cm^{-1} (ii) could be assigned to the Si-OH. The spectra (illustrated in Figure 7.7b) also provided evidence that USG materials were successfully functionalised by organic amine groups. It was shown that peaks at 1560 cm^{-1} (v) and 1480-1490 cm^{-1} (vi) in Figure 7.7b, which are assigned to N-H and C-N, respectively, were observed only in modified USG adsorbents. Finally, the band measured between 1635-1645 cm^{-1} (iv) was assigned to a water bending mode and was present in all spectra.

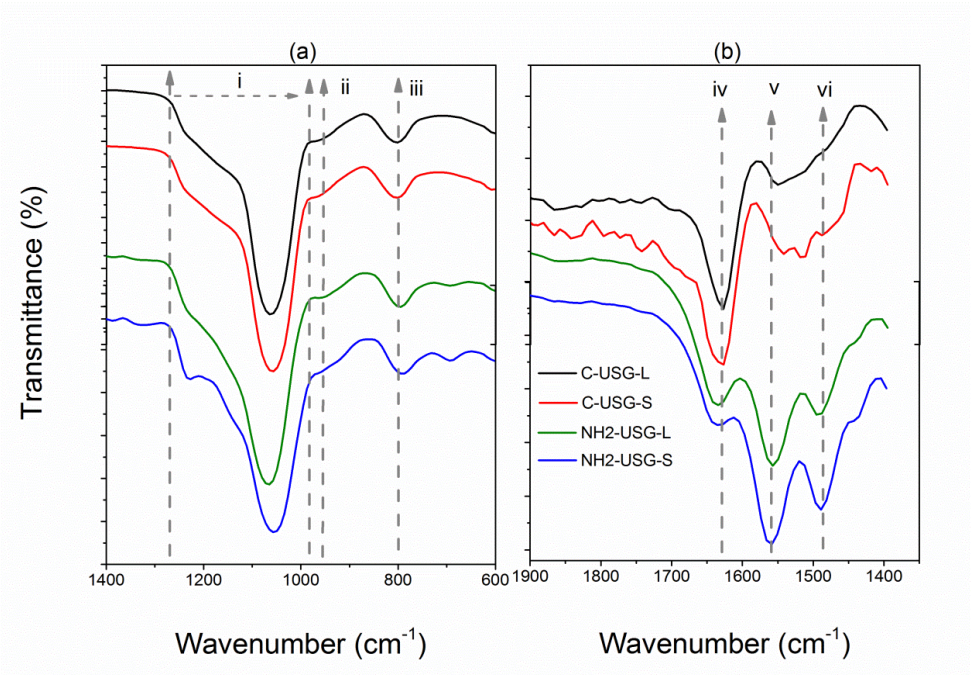

Figure 7.7 FT-IR spectra of USG and NH2-USG materials showing silica formation (a) and amine grafting (b)

These results were supported by elemental microanalysis; the result of which are summarised in Table 7.3. Comparison of % C and % N values for as-USG-S with USG-S demonstrated the complete removal of CTAB by calcination. Further the NH2-USG-S results indicate successful grafting of 3-aminopropyltrimethoxysilane onto the surface of the silica. The measured percentage values of nitrogen (% N) at 3.58 or 2.77 % for NH_2-USG-S or NH_2-USG-L, respectively, were used to calculate the degree of surface functionalisation (L_0) using the equation reported by Damian *et al.* [191]. The calculated values of L_0 (reported in Table 7.3) indicated the slightly higher loading was measured (L_0 = 2.6 mmole g^{-1}) for USG-S compared to USG-L (L_0 = 2.0 mmole g^{-1}). Interestingly the USG-S had a significantly higher degree of functionalisation degree compared to MCM-41 (1.29 mmole g^{-1}) in spite of both materials possessing similar surface area and pore size distribution.

Table 7.3 Elemental microanalysis data recorded for the USG samples

Sample ID	% C	% H	% N	Lo (mmol g^{-1})[a]
As-USG-S	28.93	5.57	0.77	
USG-S	Nil	0.62	Nil	
NH_2-USG-S	9.96	2.89	3.58	2.6
As-USG-L	26.47	5.47	1.09	
USG-L	Nil	0.57	Nil	
NH_2-USG-L	7.78	1.70	2.77	2.0

[a] Functionalisation degree (L_0 mill moles of nitrogen per gram of functionalised silica).

7.3.3 Application of USG materials for VOC and H_2CO adsorption

To examine the ability of USG materials for adsorption of selected VOCs or H_2CO from indoor air, contaminated environments were generated into two separate sampling chambers as described in section 3.4.1. The first sampling chamber contained concentrations of toluene, EB, cumene or DCB at 34, 18, 12 or 7.8 mg cm^{-3}, respectively, whereas H_2CO was generated in a second chamber at a concentration of 1.4 mg cm^{-3}.

7.3.3.1 Use USG-S adsorbent for VOC adsorption

Sampling tubes containing 100 mg of USG-S or MCM-41 were prepared and conditioned as described in Section 3.4.3. The TDU-GC-MS instrument was calibrated by standard solutions as described in Section 4.2.1. The flow rate of contaminated air was adjusted at 100 cm^3 min^{-1} for a sampling time of 1 min and Tenax TA was used to determine the experimental masses (n = 3) of toluene, EB, cumene or DCB using these sampling conditions: 2109, 404, 479 or 494 ng, respectively (see Section 4.2.5). The averages masses were used as "reference masses" to examine the extraction efficiency, or dynamic capacity, of USG-S or MCM-41 adsorbents.

Conditioned sampling tubes loaded with USG-S or MCM-41 adsorbent were used to sample 100 cm^{-3} of contaminated air for 1 min, and the experiment was repeated 3 times (n=3). Analyte masses trapped by the adsorbents were determined and the results are given in Table 7.4. The results demonstrated that a higher average mass for toluene was trapped by USG-S whilst similar masses of EB or cumene were trapped on both adsorbents. In contrast, the average mass of DCB trapped on USG-S was lower than for MCM-41 as was the total VOC mass. The performances of both adsorbents were repeatable with % RSD values for all VOCs in the range 5.92 – 9.57 or 2.52 – 8.13 for USG-S or MCM-41.

The VOC masses collected by each adsorbent were compared to expected "references masses" to calculate the extraction efficiency values (using Equation 3.6 as described in Section 3.6). Remarkably, calculated extraction efficiencies for the new mesoporous USG-S material made under environmentally friendly conditions and with a rapid 15 min synthesis time were comparable to the well-used, but more expensive and time-consuming (by preparation) MCM-41 adsorbent, as shown in Figure 7.8. Thus the new preparation method for a mesoporous material using a rapid, green synthesis route, and less expensive silicate source, performed extremely well when compared to the benchmark MCM-41.

Table 7.4 Average masses of VOCs adsorbed USG-S and MCM-41

Adsorbents	USG-S		MCM-41	
VOC	Masses (ng)	% RSD	Masses (ng)	% RSD
Toluene	1358 ± 80	5.92	1263 ± 52	4.13
EB	240 ± 23	9.57	247 ± 10	4.00
Cumene	295 ± 23	7.90	321 ± 8	2.52
DCB	296 ± 27	9.12	414 ± 34	8.13
Total	2189		2245	

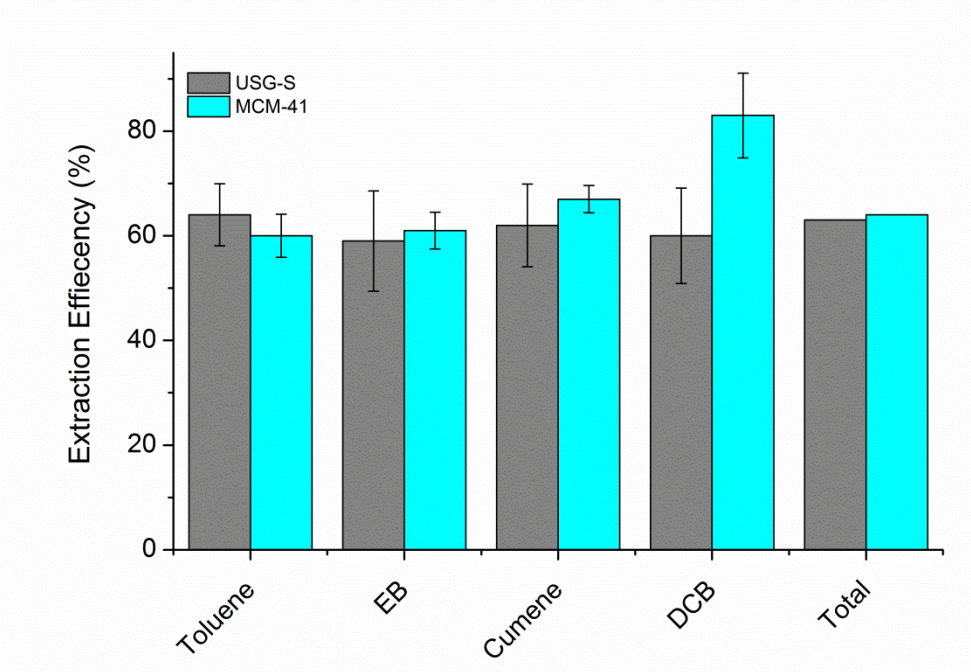

Figure 7.8 Extraction efficiency of USG-S and MCM-41 adsorbents for VOCs adsorption. Error bars indicate the % RSD value (n = 3)

Further experiments were conducted in order to examine the breakthrough and dynamic capacity of USG-S by increasing sampling times. Tenax-TA was placed after the sorbent tube to collect masses that passed through the sorbent tube to determine the masses of VOC not adsorbed by USG-S (experimental details are given in 3.5.1). Breakthrough values were calculated using Equation 3.7 (see Section 3.6). The results (see Figure 7.9), demonstrated that the first analyte to breakthrough both adsorbents was, as expected, toluene which passed through MCM-41 more quickly than USG-S at an approximate sample volume of 1 dm^3. Breakthrough of EB, cumene or DCB occurred after sampling 1.5 dm^3 of contaminated air where again USG-S performed as well as MCM-41.

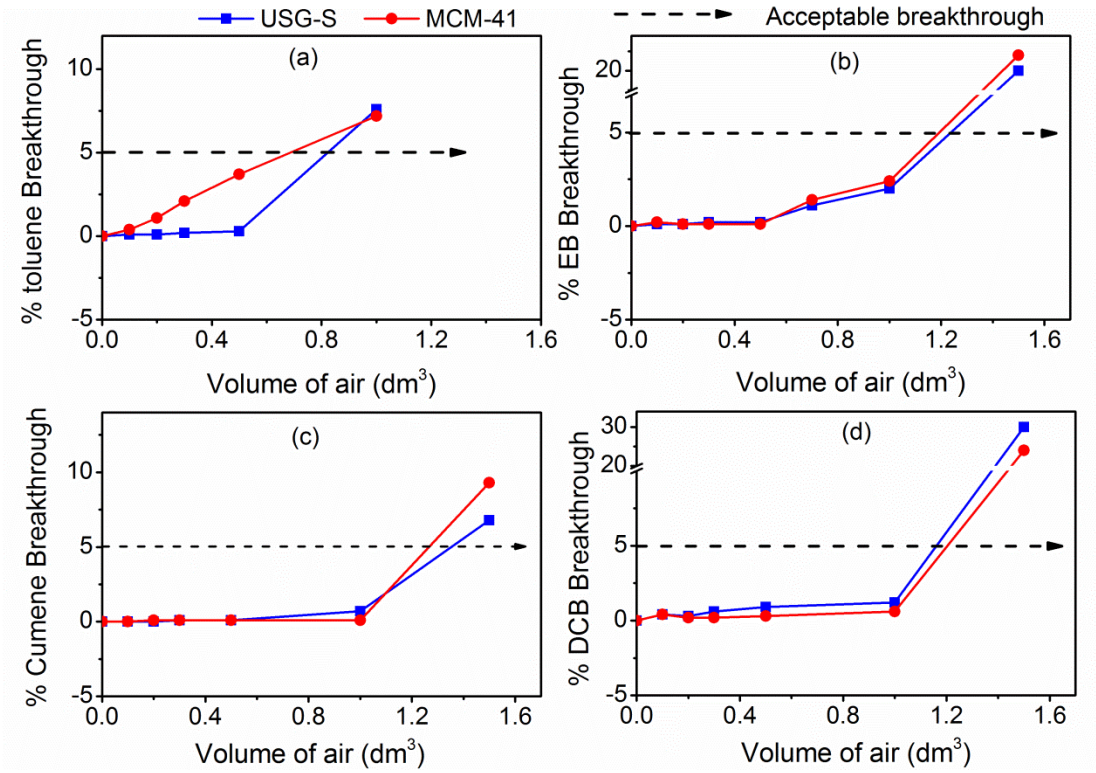

Figure 7.9 Calculated breakthrough volumes for toluene (a), EB (b), cumene (c) and DCB (d) on USG-S and MCM-41 adsorbents

The trapped VOC masses at the point of toluene breakthrough were calculated and are listed in Figure 7.10. Although both adsorbents demonstrated a similar breakthrough performance for all VOCs, MCM-41 had slightly higher capacity when compared to USG-S: total VOC masses trapped onto MCM-41 were 25917 ng compared to 18766 ng for USG-S. This overall higher capacity for MCM-41 was attributed to the collection of a higher mass of toluene at 16796 ng compared to 10684 ng for USG-S. Otherwise the absorbents had similar capacity at the point of breakthrough.

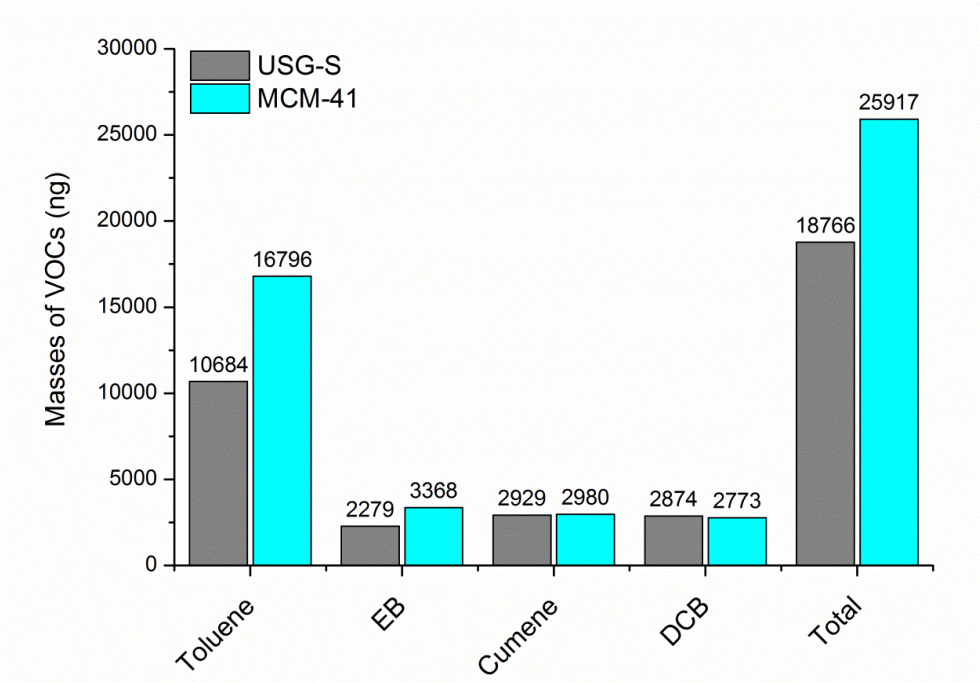

Figure 7.10 Total masses of VOCs trapped on adsorbents at point of toluene breakthrough

7.3.3.2 Use mesoporous sorbents for H_2CO extraction

USG-S and USG-L were assessed to determine their selectivity towards H_2CO vapour before and after grafting by 3-aminopropyltrimethoxysilane. For comparison the performance of NH_2-MCM-41 was also reassessed. Full experimental details are reported in Sections 3.4.6, 3.5.2 and 4.4.2.2. Extraction efficiencies were calculated as describe in Equation 3.6, Section 3.6. The H_2CO breakthrough values for each adsorbent are given in Figure 7.11.

The results demonstrated that USG-S and USG-L had significantly lower extraction efficiencies for H_2CO with rapid breakthrough measured when sampling 6 dm^3 of contaminated air (1.4 mg m^{-3}). Without amine functionality the adsorbents are not capable of trapping H_2CO vapour which quickly passes through the sorbent tube. In contrast NH_2-USG adsorbents removed approximately 96 % of H_2CO vapour from 6 dm^3 of contaminated air, confirming their high performance. Interestingly no breakthrough were observed for NH_2-USG-(S or L) after sampling up to 24 dm^3 of air contaminated with 1.4 mg m^{-3} H_2CO vapour. Significantly, NH_2-USG-S had

comparable performance to NH_2-MCM-41, indicating that modified USG-S provides an appropriate platform for H_2CO trapping.

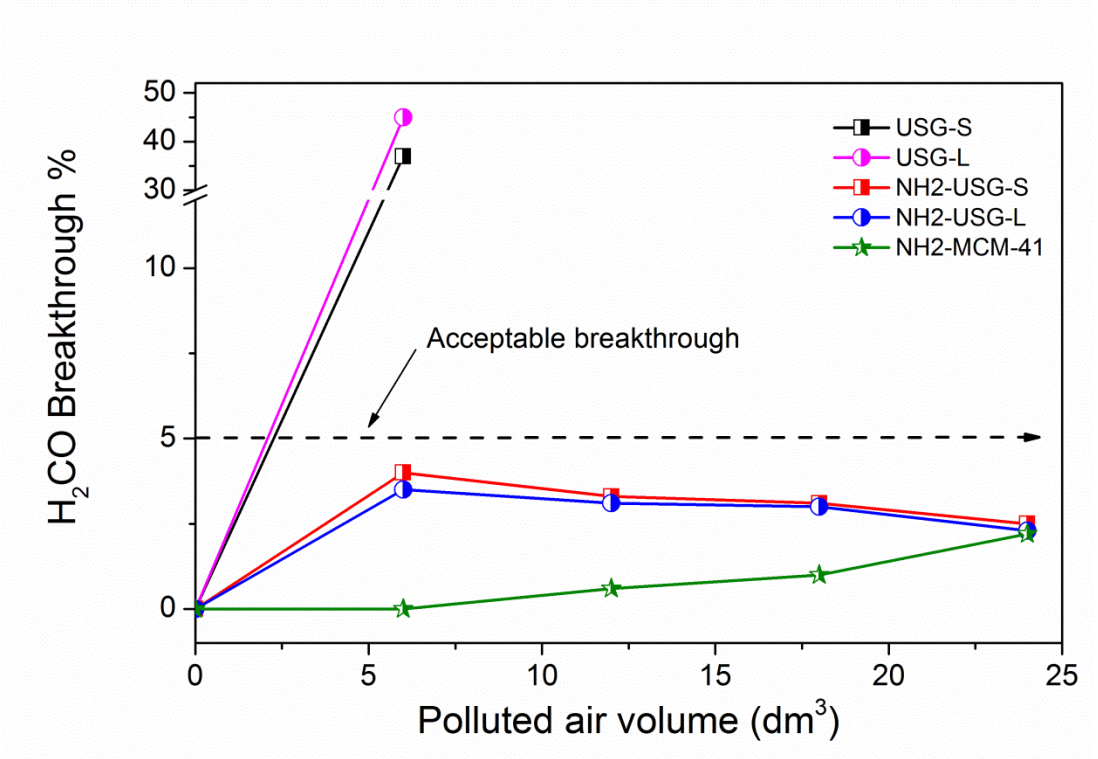

Figure 7.11 Calculated breakthrough volumes for H_2CO on USG adsorbents and compared to NH_2-MCM-41

H_2CO trapped onto modified or non-modified USG adsorbents were back flushed with air at 100 cm^3 min^{-1} for 60 min. The results (see Figure.11) confirmed that, as expected, any small amounts of H_2CO trapped by unmodified adsorbents were quickly released into the flushing air stream. However, in stark contrast modified adsorbents NH_2-USG-S or NH_2-USG-L retained > 95 % of the H_2CO loaded masses and no further H_2CO was released when the tubes were flushed with up to 24 $dm^3$of air. These results support the chemisorption theory of H_2CO with the laminated surfaces of NH_2-USG adsorbents; which performed as well as NH_2-MCM-41.

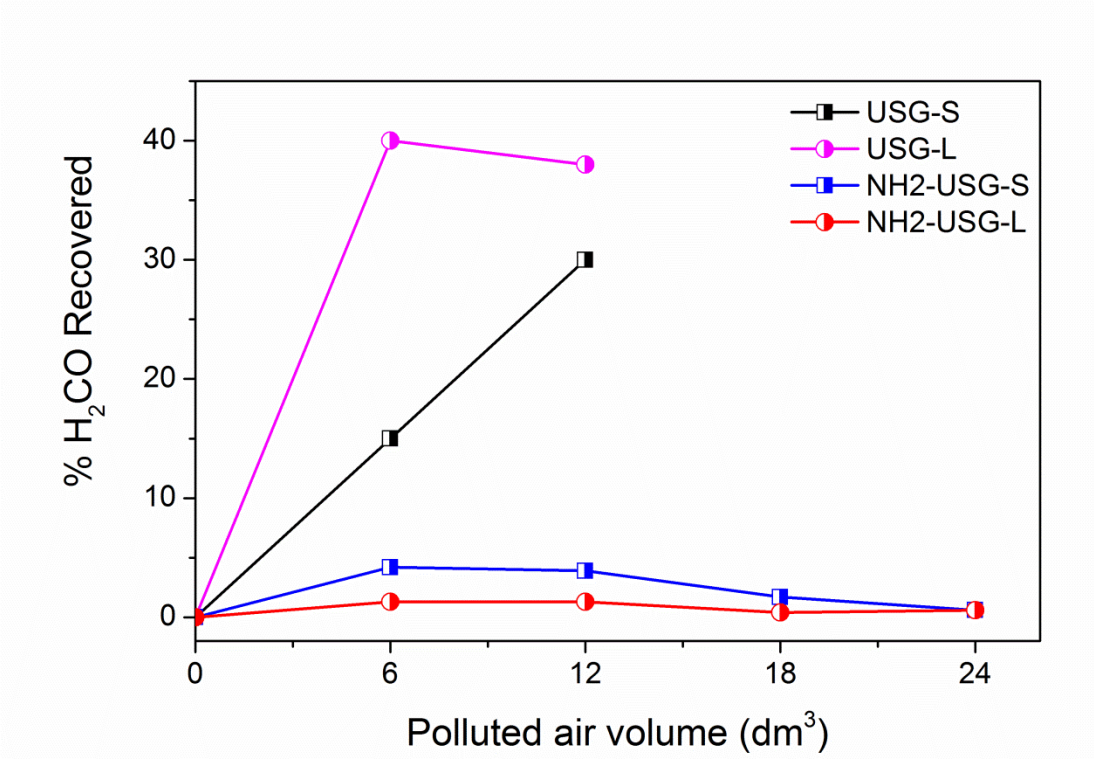

Figure 7.12 Recovery of trapped H_2CO on USG adsorbents by air

7.4 Conclusions

The work in this chapter reports a novel method for synthesising mesoporous silica materials. The main advantages of this method are; (i) the rapid production of mesoporous silica in 15 min (ii) the use of mild conditions of neutral pH, (iii) use of room temperature, (iv) the use of a cheaper silica source and (v) the use of environment-friendly "green reagents". These combined advantages represent an important step change for the preparation of mesoporous silica compared to conventional MCM-41 preparation methods which are complex, expensive, create secondary pollutants and are lengthy in comparison.

This material, reported here for the first time, combined bioinspired synthesis routes with the self-assembly templating mechanism of conventional mesoporous systems. The textural properties of the material USG-S were extremely encouraging with higher surface area, similar long range pore order, pore volume and pores size distribution when compared to MCM-41. The adsorbents lend themselves to post-

synthesis grafting which, in this study, was successful with 3-aminopropyltrimethoxysilane. Functionalisation by other groups is possible extending the potential adsorption targets of the material. Although MCM-41 lends itself well to template removal by MWD, here it was demonstrated that best performance is given for calcined USG materials.

This first reported application of USG for adsorption indicates, significantly, similar performance with MCM-41 whether for removal of selected VOC or H_2CO vapour from contaminated air. The USG adsorbents had high performance and dynamic capacities for VOCs or H_2CO adsorption opening new opportunities for adsorption platform preparation.

8 Preliminary assessment of TiO_2 Photocatalysts for VOC degradation

8.1 Introduction

8.1.1 Photocatalysis

There are many definitions of the term "photocatalysis"; it can be defined as the conceptual name for a photocatalytic reaction, which is the chemical reaction induced by photo-absorption of a photocatalyst that remains unchanged during a reaction. Most definitions describe a solid material that acts catalytically (without change) under the influence of light [252, 253]. In general, photocatalysis is defined as the catalysis of photochemical reactions at a solid surface, usually a semiconductor such as TiO_2, ZnO or WO_3 [94, 254]. Ollis *et al.* reported that the active catalysts of metal oxides for hydrocarbon partial oxidation in the gas phase were ranked in the activity sequence: TiO_2 (anatase) > ZnO > WO_3 [255].

8.1.2 Titanium dioxide polymorphs

Titanium dioxide, TiO_2, is an ideal photocatalyst widely used in applications due to its relatively low cost, physicochemical stability and highly oxidizing potential due to photogenerated holes [256]. In addition it is non-toxic and has a the ability to oxidize several compounds under irradiation of UV light [257]. Titanium dioxide exists in one of three polymorphic forms (rutile, anatase, or brookite) that are naturally occurring at atmospheric pressure. The photocatalytic behaviour of these polymorphs depends on their crystalline form, which has made them extremely suitable for a diverse range of applications [258]. The stable phase is rutile, whereas anatase and brookite are metastable and can be transformed to rutile by heating [259]. Anatase is generally produced at low temperatures whilst brookite is difficult to synthesise and so is rarely studied [260]. The anatase and rutile polymorphs both have tetragonal crystal structures with energy band-gaps of 3.23 or 3.02 eV, respectively [260, 261]. The anatase phase is usually regarded as the more photochemically active titania phase; probably due to the combined effect of lower rates of recombination and higher surface adsorptive capacity for organic compounds [262]. However, anatase has higher photocatalytic activities in the presence of O_2 whereas rutile has significant catalytic activities in the presence of other oxidants such as H_2O_2 [263, 264].

8.1.2.1 Synthesis of TiO_2 photocatalystic particles

Preparation methods for TiO_2 photocatalysts can be divided into two main categories; gas-phase or liquid-phase. In the gas-phase methods, TiO_2 can be synthesised by three different pathways:

- Gas-phase flame hydrolysis of $TiCl_4$. This route involves mixing reactants gases (hydrogen and oxygen) with $TiCl_4$ at high temperature to burn the reactant gas by high temperature hydrolysis [265]. TiO_2 prepared by this method includes anatase and rutile phases such as the commercial product Degussa P25 (see Section 8.2.1).
- Gas-phase oxidation of $TiCl_4$. TiO_2 powders can be formed by oxidizing $TiCl_4$ using flame-aerosol reactors at high temperature and near atmospheric pressure [266].
- Gas-phase hydrolysis of titanium alkoxides. It used to form spherical TiO_2 particles by spraying vapours of water and titanium alkoxides ($Ti(OR)_4$) with nitrogen gas into a hydrolysis chamber [267].

Liquid-phase methods include preparation of TiO_2 materials in solution. There are four liquid-phase methods;

- A sol-gel method based on the hydrolysis and condensation of titanium alkoxides in solution to prepare a porous TiO_2 [268]. The sol-gel process can be used to form TiO_2 powders, thin films, or fibers directly from the solution at low temperature [269].
- Liquid-phase hydrolysis of $TiCl_4$. TiO_2 can also be formed by a liquid-phase hydrolysis reaction which is used commercially to produce TiO_2 into a fine particulate form that includes both polymorphs of anatase and rutile [266].
- Hydrothermal. In this method, TiO_2 powder was prepared using liquid solutions as solvents to produce the precursors under high temperature (< 250 ^oC) and high-pressure conditions [270]. This technique is widely employed to form crystalline powder products of TiO_2 with different composition, structure, and morphology using $TiCl_4$ and ($Ti(SO_4)_2$) as the precursors with a solution of NaOH, or ethanol and water, as solvents [271, 272]. However, the crystallisation process may be affected by the type of precursor, reaction

temperature and time used. The method is usually used to enhance crystallisation in both laboratory synthesis and in commercial production [273].

- Water-in-oil micro emulsion. This method is used to prepare monodispersed nanoparticles due to the thermodynamic stability, optically isotropic dispersion of surfactant stabilised micro droplets of water in an external oil phase. However the surface of the resultant particles may be polluted by the oil phase and a post-treatment has been developed to avoid adverse effects to the performance of catalysts [274].

8.1.2.2 Methods used to produce TiO_2 photocatalyst films

TiO_2 film has demonstrated higher photocatalytic activities when compared to the most active commercial TiO_2 powder [275]. Two main coating mechanisms are used to produce TiO_2 films; forming a film on a support or handle catalyst powder. In the first method, a film of TiO_2 can be formed on a support by different pathways; using sol-gel [268], spray coating [276], chemical vapour deposition (CVD) [277] or metal-organic chemical vapour deposition (MOCVD) [278]. The other method involves sintering TiO_2 powder [270] or dip-coating [279, 280]. The TiO_2 films can be prepared by coating its solution onto quartz or glass substrates [281]. The photocatalytic activity of TiO_2 film depends on several parameters such as crystallinity, density of TiO_2, film thickness and the topography of the thin film [282].

8.1.3 General mechanisms for the photocatalytic decomposition of VOCs

Photocatalytic oxidation (PCO) is one the advanced technologies developed for the rapid and inexpensive removal of VOCs from indoor air [283]. Most PCO techniques commonly use TiO_2 as the catalyst, activated by ultraviolet (UV) light to convert VOCs into odourless constituents; water vapour (H_2O) and carbon dioxide (CO_2) as illustrated in Figure 8.1[96].

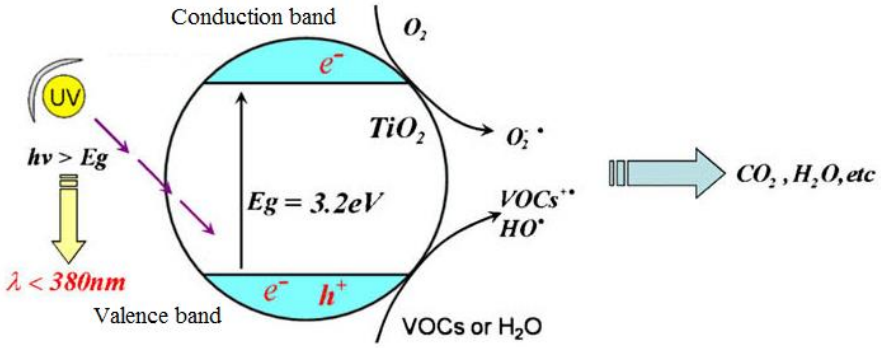

Figure 8.1 Schematic of photocatalytic oxidation process of VOCs by TiO_2/UV [96].

When TiO_2 is exposed to radiation exceeding its band gap, such as UV irradiation, the photo-irradiation excites an electron from an electron-filled valence band (VB) to a vacant conduction band (CB), leaving a positive hole in the VB. These excited electrons (e^-) facilitate reduction of electron acceptors and resultant positive holes (h^+) facilitate oxidation of electron donors of compounds adsorbed on the surface of TiO_2 [284, 285]. The activation equation is shown in Equation 8.1 [286].

$$TiO_2 + hv \rightarrow h^+ + e^- \qquad \textbf{Equation 8.1}$$

The oxidation and reduction reactions can be expressed as shown in Equation 8.2 and Equation 8.3 respectively, [287, 288].

$$h^+ + OH^- \rightarrow OH^* \qquad \textbf{Equation 8.2}$$

$$e^- + O_{2\,adsorbed} \rightarrow O^-_{2\,adsorbed} \qquad \textbf{Equation 8.3}$$

When VOCs are chemically transformed by a PCO, the hydroxyl radical is the dominant strong oxidant and the general degradation reaction of VOCs can be expressed in Equation 8.4 [96].

$$OH^* + VOCs + O_2 \rightarrow nCO_2 + mH_2O$$ **Equation 8.4**

The PCO mechanism possesses several advantages for VOCs degradation [255]:

- Generally Recognized As Safe (GRAS): the common photocatalyst is anatase TiO_2.
- Mild oxidant: Kinetic studies demonstrate that molecular oxygen is the source of oxygen during oxidation, which is milder oxidant than hydrogen peroxide or ozone, etc.
- Ambient temperature: the catalyst appeared to be active at room temperature.
- In general: the strength of hydroxyl radical (or some other equally strong oxidant) photo-generated on the TiO_2 surface is responsible for the titanium's broad activity toward VOCs degradation.

The reaction rate of PCO may be affected by such factors as the ultraviolet (UV) source and intensity, humidity, contaminant concentrations, flow rate and oxygen concentration. It was reported that TiO_2 photocatalysts could be activated by UV light with wavelength < 380 nm and that the reaction rate was increased by increasing light intensity [289]. However, for reactions between molecular water adsorbed on a photocatalyst surface with holes generating free radical (OH^*) which in turn oxidises the pollutant, the rate of PCO may be decreased at high humidity levels due to ''competitive adsorption'' between water vapour and the pollutant. For example Ao *et al.* [290] reported that conversion of formaldehyde was decreased with increasing humidity levels. On the other hand, Luo *et al.* [291] reported no degradation of toluene in the absence of water vapour and that the PCO rate increased at a humidity of 20 % and decreased thereafter.

It has been found that the rate of PCO was influenced by pollutant concentration and usually there is an optimal concentration which maximises the reaction rate [292, 293]. The PCO rate also depends on the environment temperature; it was increased with increasing temperature and then decreased, therefore an optimal temperature should be determined to obtain maximum PCO rate [294]. The effect of PCO rate was investigated for various VOCs at different temperatures. It was shown that the

PCO rate for acetaldehyde and toluene decreased with increasing temperature [295] whilst it increased for ethylene and formaldehyde [279, 296, 297]. Although the increase of temperature enhances the PCO rate for some VOCs, high temperatures have a negative effect on the adsorption of pollutants on the surface of the PCO [279]. Finally, the concentration of oxygen has also been shown to affect completion of pollutant decomposition, it was found that the PCO rate increased by increasing the concentration of oxygen [298].

8.1.4 Applications of TiO_2 photocatalysts for VOCs degradation

Photocatalytic oxidation of VOCs usually occurs at room temperature and pressure and, as a result, may be more inexpensive than other conventional techniques such as adsorption or chemical scrubbers used in air purification systems [68]. In the past two decades, several types of TiO_2 photocatalyst systems have been developed and assessed for the photocatalytic oxidation of VOCs [94]. One of the first investigations was reported by Obee and Brown [279] using Degussa P25 TiO_2 as a catalyst for formaldehyde, toluene, and 1,3-butadiene oxidation. The commercial TiO_2 powder, Degussa P25, demonstrated highest activities when compared to TiO_2 powders [299-301]. Stevens *et al.* [302] reported successful PCO of low molecular weight carbonyl compounds (formaldehyde, acetaldehyde, and acetone) in the ppb concentration range using P25 TiO_2, demonstrating that the PCO of acetaldehyde was lower than that of formaldehyde and acetone which was approximately 100 %.

8.1.4.1 Improvements to enhance the photocatalytic activity of TiO_2 for VOC degradation

Numerous studies have reported that the photocatalytic activity of TiO_2 for VOC degradation can be improved by doping metal ions into TiO_2. Doping TiO_2 with transition metal ions or nitrogen are commonly used to extend the photo-response of the catalyst into the visible range [303]. For example Bosc *et al.* [304] reported that the high photocatalytic efficiency of TiO_2 on toluene was obtained under both UV and visible light when the catalyst was coupled with WO_3. Catalyst doping with

metal ions such as Li^{+}, Zn^{2+}, Cd^{2+}, Ce^{3+}, Co^{3+}, Cr^{3+}, Fe3þ, Al^{3+}, Mn^{2+} has extended the useable activity into the visible light range, however photocatalytic activities were significantly reduced in the UV region [305].

On the other hand, nitrogen-doped TiO_2 (film or powder) had higher photocatalytic activity than TiO_2 under visible light irradiation for the degradation of various VOCs such as formaldehyde, acetaldehyde [306], acetone [307], 2-propanol [308] and toluene [309]. The PCO of benzene, toluene, ethylbenzene and o-xylene (BTEX) was improved by Ln^{3+} ion-doped TiO_2 due to the enhanced electron–hole pairs separation on the surface [310]. Further improvements in photocatalytic activity can be achieved by compositing the catalyst with metal ions and adsorption materials since the photocatalyst efficiency strongly depends on the adsorption ability of VOCs and the efficiency of electron–hole pair separation [311]. The low adsorption ability of non-porous TiO_2 particles, especially for non-polar substances, can be improved by the production of TiO_2-adsorbent composites with supports such as alumina, silica and activated carbon [290, 312]. A list of PCO applications for VOCs decomposition is given in Table 8.1.

Table 8.1 Various TiO_2 photocatalysts for VOCs degradation

Catalyst	Preparation method	Type	VOCs	Ref.
Commercial Degauss P25	Flam hydrolysis Dip- Coating	powder Powder	formaldehyde, toluene, butadiene formaldehyde toluene 2-Propanol ethylene dichloroethylene acetaldehyde, acetone	[279] [280, 290, 302, 313] [313] [299] [297] [289] [302]

Pure TiO_2	Dip- Coating Sol–gel Sol–gel/ dip-glass fibre Sol–gel	Powder Film Film Powder	trichloroethylene tetrachloroethylene Trichloroethylene Toluene ethylene, toluene, propylene	[293] [293] [265] [314] [315]
Doped N-TiO_2	Hydrothermal Hydrothermal Hydrolysis Hydrolysis Hydrothermal Hydrothermal	Film Powder Powder Powder Powder Powder	Acetone 2-Propanol Formaldehyde Acetaldehyde Toluene 2-Propanol	[307] [308] [306] [306] [309] [308]
WO_3–TiO_2	Sol-gel/dip-coating	Film	Toluene	[304]
Pd–TiO_2	Hydrothermal/sintering	Powder	Toluene	[316]
Fe-TiO_2	Sol-gel Sol-gel/dip-coating	Powder Film	Toluene benzene, toluene, ethylbenzene	[317] [318]
Ln^{3+}–TiO_2	Sol-gel	Film	Benzene, toluene, EB, o-xylene	[310]
TiO_2/SiO_2	Hydrothermal	Powder	Toluene	[319]
$TiO_2/SiO_2/ZrO_2$	Sol-gel	Powder	Ethylene	[296]
In-TiO_2	Sol-gel	Powder	EB	[320]

8.1.4.2 Deactivation of TiO_2 photocatalysts

TiO_2 photocatalytic activity for VOCs degradation has been reported to decrease with time due to the deactivation of catalytic sites on the reaction surface [321]. The deactivation can be caused by several mechanisms such as the generation of by-products or intermediates which may be adsorbed onto the active sites, this type of

deactivation is very common and reported for degradation of VOCs such as toluene [322] and ethanol [323]. Photo-polymerization of species on the surface of the catalyst can also lead to a reduction in activity, especially in the absence of water as was demonstrated for benzene conversion [255]. A strong photo-oxidation of heteroatoms species such as N and S, can also lead to oxidized inorganic forms which accumulate on the surface, reducing activity [321]. Finally, pore blocking may also lead to a change in the catalytic surface [69].

In addition to enhancing photocatalytic performance, metal ion doping has also been shown to decrease the deactivation of photocatalysts. Belver *et al.* [316] reported a considerable increase in the conversion of toluene under UV irradiation by Pd-TiO_2. The binary SiO_2–TiO_2 photocatalysts have significantly higher photocatalytic oxidation and a slower rate of deactivation than TiO_2 due to their higher surface acidity [296, 319].

8.1.5 Aims and Objectives

This chapter of work aims to examine the photochemical degradation of selected VOCs (toluene, EB, cumene and DCB) by TiO_2 photocatalyst (powder or films) under UV irradiation.

- The commercial powder Degaussa P25 was used as a pure TiO_2 photocatalyst, or as a composite with MCM-41 at ratio of 80 to 20 %, to compare degradation efficacies of the selected VOCs.
- Thin films of TiO_2 coated onto small or big glass bead (Ti-SGB or Ti-BGB) were examined for VOCs degradation.
- The effect of films thickness on the performance of VOCs degradation was assessed.
- Finally, the effect of flow rate over the TiO_2 coated catalyst beds was studied.

8.2 Experimental

8.2.1 Preparation of TiO_2 materials

Degussa P25 TiO_2 was obtained by a commercial supplier. The powder is generally prepared by the gas-phase flame hydrolysis of $TiCl_4$ and produces a power which contains both anatase and rutile in the ratio 70:30 %. The P25 TiO_2 was used to degrade selected VOCs as a pure adsorbent, or it was mixed with MCM-41 at a mass ratio of 80:20.

TiO_2 films were prepared using a modified sol-gel method as described briefly. First a solution of TiO_2 was prepared as described below:

A 4.2 g mass of titanium (IV) isopropoxide (Sigma Aldrich, 97 %) was dissolved in 3.06 g of concentrated hydrochloric acid (Sigma Aldrich, HCl, 36.5-38 %) and the solution was stirred at room temperature for 10 min. 1.3 g of co-polymer P123 (Sigma Aldrich) was dissolved in 12 g of ethanol (Sigma Aldrich) and the P123 solution was added to the titanium solution. The mixture was continuously stirred for 15 min. This final solution of TiO_2 was used to coat quartz tubes (10 cm in length and 6 mm internal diameter), 1 mm dia glass beads (SGB) or 2 mm glass beads (BGB) Prior to coating, quartz tubes and glass bead were cleaned by washing with ethanol and drying in air at room temperature prior to being immersed into the TiO_2 solution for 2-3 min. The coated quartz tubes and glass bead were left overnight in a fridge before calcination at 400 °C for 10 min (heated at 25 ^{0}C min^{-1} to 400 ^{0}C, held at 400 ^{0}C for 10 min).

The coating and calcination steps were repeated (n) times to increase the thickness of the thin film layer on the quartz tubes or glass beads. The final materials will be referred to as Ti-SGB-n or Ti-BGB-n; where Ti indicates thin films of TiO_2, SGB or BGB indicates small (1 mm dia) or big (2 mm dia) glass beads, and n indicates the number of coats applied. For example sample Ti-SGB-1 indicates thin films of TiO_2 were coated once onto small glass bead packed into a quartz tube. The values of (n) were 1, 2, 3 or 4.

8.2.2 Preparation of packed sampling tubes

Quartz tubes were used to prepare sorbent packed tubes following the preparation procedure described in Section 3.3.3. Two types of sorbents were packed into sampling tubes; pure TiO_2 sorbent (each sampling tube contained 100 mg of P25) or 100 mg of TiO_2: MCM-41 at 80:20 w/w. The packed sampling tubes will be referred to as Ti-P25 or Si-Ti-P25, respectively. Quartz tubes were also used to support coated glass beads. A 2 g mass of coated glass beads (SGB and BGB) was packed into coated quartz tubes and held between two plugs of glass wool to produce Ti-SGB-n or Ti-BGB-n sampling tubes.

8.2.3 Set up dynamic atmospheric systems

The dynamic atmospheric system described in Section 3.3.1 (see Figure 3.1) was used to generate constant concentrations of the selected VOCs in a sampling chamber. The air outlet contained 34.0, 18.0, 12 or 7.8 mg cm^{-3} of toluene, EB, cumene or DCB, respectively. In the photocatalysis experiments, a photocatalysis unit was constructed and connected to the outlet of the sampling chamber (see Figure 8.2). The photocatalysis unit consisted of a UV source (UV lamp, Uvitec VL 204 BLB, 2 x 4 W, 365 nm, tube power low), sampling tubes loaded with control quartz tubes of tubes loaded with TiO_2 photocatalyst (powder or thin films glass coated beads) inside a dark box. The titanium loaded sampling tube was positioned at a distance of 7 cm from the UV lamp. To examine VOC breakthrough a Tenax-TA sampling tube was connected to the system immediately before the vent (as shown in Figure 8.2) which was used to collect VOCs that had not been degraded by the UV irradiation photocatalytic material inside the dark box.

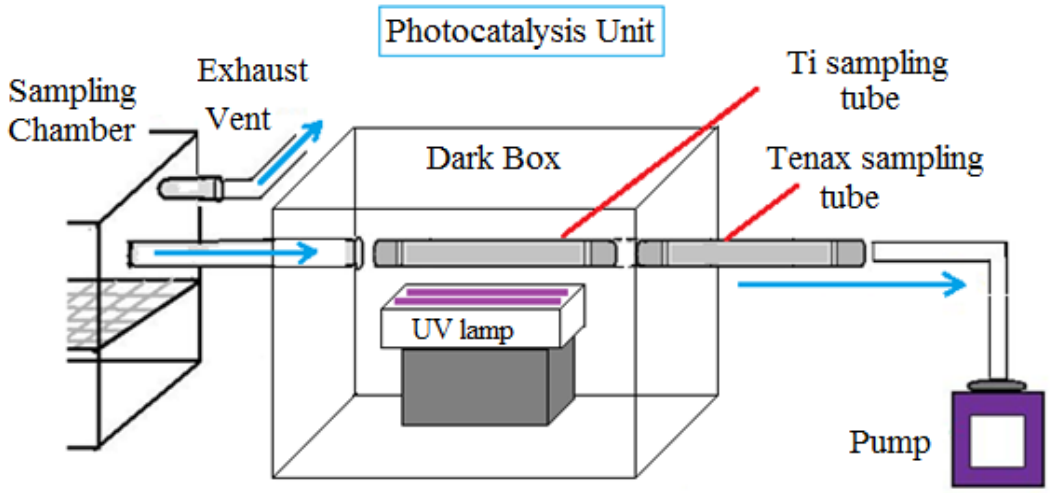

Figure 8.2 Dynamic atmospheric chamber system contains photocatalysis unit

8.2.4 VOCs sampling method set up

Before the assessment of photocatalytic materials control experiments were run using empty quartz tubes and the UV lamp was switched off. Experimental conditions are given in Section 3.4. The control experiment was repeated (n =3) and the average masses of VOCs trapped by Tenax TA tubes were determined as described in Section 3.4. The average masses (ng) of each VOC (thereafter referred to as "$masses_{no\text{-}sorb}$) were used as reference masses to determine the efficiency of the photocatalytic material.

In addition to assess whether VOCs were being adsorbed onto the materials held in the quartz tube, or if photochemical reaction was taking place, experiments were run with the sorbents in-line but the UV lamp switched off. The average masses collected by Tenax-TA sampling tubes in these experiments are referred to "$masses_{UVoff}$". The VOC masses adsorbed by materials were calculated as: $masses_{no\text{-}sorb}$ - $masses_{UVoff}$. The experiments were repeated with sorbents in-line and the UV lamp On. VOC masses collected by Tenax-TA tubes in these experiments are referred to as "$masses_{UVon}$". Finally, the amount of VOCs degraded (ng) were calculated using the

calculation: $masses_{no\text{-}sorb}$ - masses $_{UVon}$. The percentage of degradation (%) by photocatalysis was calculated using Equation 8.5:

$$\%\ Degradation\ of\ VOC\ masses = \frac{degraded\ masses\ (ng)}{masses_{no-sorb}\ (ng)} \times 100 \qquad \textbf{Equation 8.5}$$

8.3 Results and discussion

8.3.1 Calibration of TDU-GC-MS

Before the TDU-GC-MS was used to determine VOC masses trapped by Tenax-TA sampling tubes, the instrument was calibrated using the standard solutions of VOCs prepared as described in section 3.4.2. The data was used provide regression data for toluene (y= 11764x +44766, R^2 = 0.9972), ethylbenzene (y= 12543x + 71434, R^2 = 0.9845), cumene (y= 9809x – 17260, R^2 = 0.9464) and dichlorobenzene (y= 4173x + 52076, R^2 = 0.8296).

8.3.2 Determination of references masses, flow rate and sampling times for quartz tubes containing powdered catalytic material

Using an air flow rate of 100 cm^3 min^{-1}, a sampling time of 2 min and an empty quartz catalyst tube, the VOC masses that passed onto Tenax-TA sampling tubes were determined when the UV lamp was switched off. The VOC reference masses ($masses_{no\text{-}sorb}$) are given in the second column of Table 8.2. The experimental conditions remained the same and experiments were performed when quartz tubes were loaded with Ti-P25 but the UV lamp was switched off. This allowed determination of VOC masses that had adsorbed ($masses_{no\text{-}sorb} - masses_{UVoff}$) onto the surface of the Ti-P25 powder without any photoactivity. Results are given in the third column of Table 8.2, with adsorption efficiency % values listed in column 4. Finally the experiment was repeated with the UV lamp on to provide the degradation masses and % degradation values (see columns 5 and 6 in Table 8.2).

The results demonstrated that using these experimental conditions degradation percentages were not much better than adsorption percentages. Interestingly, degradation values were significantly increased to approximately 70 or 80 % when the sampling times were increased to 4 or 6 min as shown in Figure 8.3. These results indicated that Ti-P25 sorbent had high photocatalysis efficiency for VOCs degradation at longer sampling time. Reasons why were not clear; it may simply be that the catalyst was warmed when exposed to UV radiation for longer time which lead to higher photocatalytic activation.

Table 8.2 Comparison of adsorption and degradation of VOCs from 200 cm^3 of contaminated air by Ti-P25

VOCs	References masses (ng)	Adsorbed masses (ng)	% Adsorption	Degraded masses (ng)	% Degradation
Toluene	14734	1203	8	3288	22
EB	3603	1134	31	1345	37
Cumene	2338	1214	52	1046	45
DCB	1310	327	25	330	25
Total	21985	3878	18	6009	27

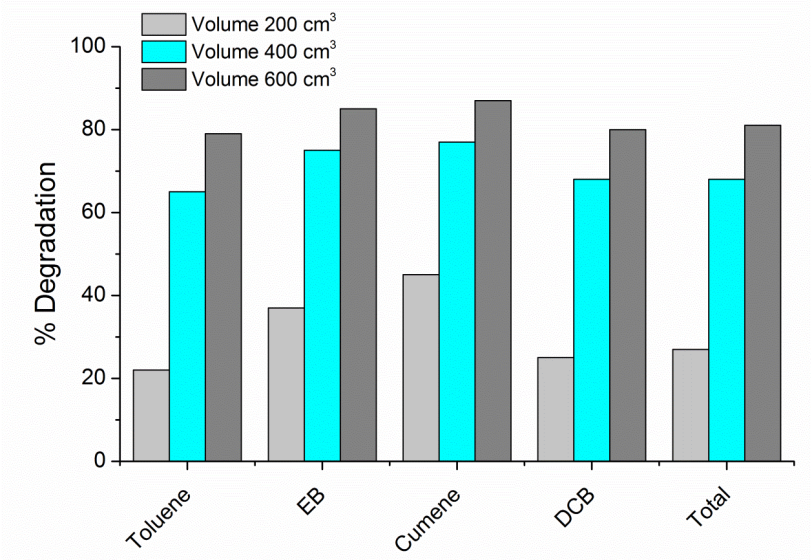

Figure 8.3 Comparison of VOCs degradation on Ti-P25 at different sampling times

Further experiments were conducted where the air flow rate was reduced to 50 cm^3 min^{-1} to double the residence time of the VOCs in the catalyst bed. Using a sampling time of 8 min, 400 cm^3 of contaminated air flowed through the Ti-P25 catalyst bed. The results (see Figure 8.4) showed a similar degradation percentage for VOCs whether the air flowed through the catalyst bed at 100 or 50 cm^3 min^{-1}.

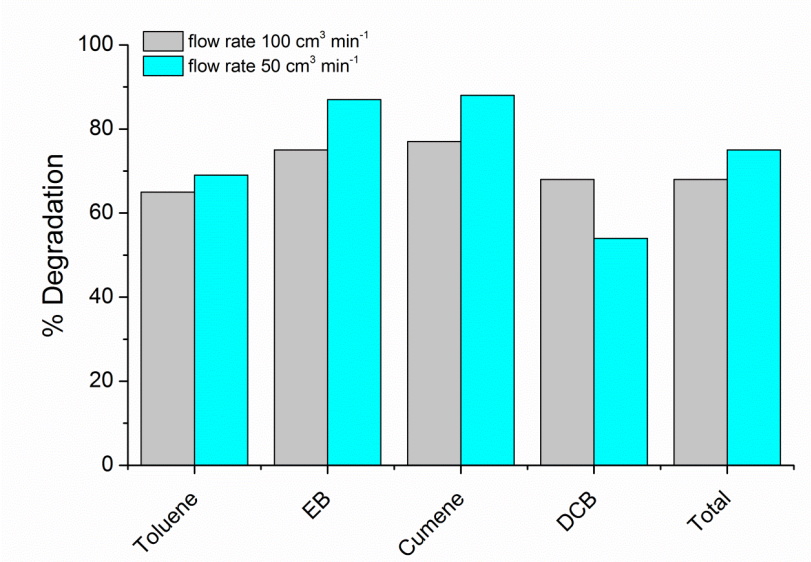

Figure 8.4 Comparison of VOCs degradation at different flow rate of contaminated air

8.3.2.1 Comparison of the performance of Ti-P25 with Si-Ti-P25

Quartz catalyst tubes containing 100 mg of Ti-P25 or Si-Ti-P25 were placed into the chamber to compare their performance for VOC extraction and/or decomposition. The results, presented in Figure 8.5, demonstrated that VOC masses adsorbed onto Si-Ti-P25 were significantly higher than for Ti-P25. This was expected due to presence of MCM-41 which previously demonstrated high capacity for VOC adsorption. In contrast both catalysts had high VOC degradation efficiencies of approximately 80 – 85 % for the selected VOCs presented in 400 cm^3 of contaminated air. The experiments were repeated (n=3) using the same catalyst tubes and the results are given in Table 8.3. These results indicate that the catalysts can be reused efficiently to extract and degrade VOCs from contaminated air.

To further assess the material performances the volume of contaminated air passing over the quartz catalyst tubes was increased to 800, 1200 or 1600 cm^3. The VOC degradation values (%) (See Figure 8.6) indicated that VOC degradation by Ti-P25 was again enhanced as the exposure time to UV radiation increased. Degradation values were between 50 – 90 % for toluene, 65 – 100 % for ethyl benzene, 80 – 100 % for cumene with lowest performance (30 – 70 %) for dichlorobenzene. There appeared to be a trend between performance and exposure time. Slightly different results were obtained for Si-Ti-P25, there appeared to be no improvement in performance when MCM-41 was combined with TiO_2. It was thought that adsorption of VOCs by MCM-41 was taken place simultaneously with degradation.

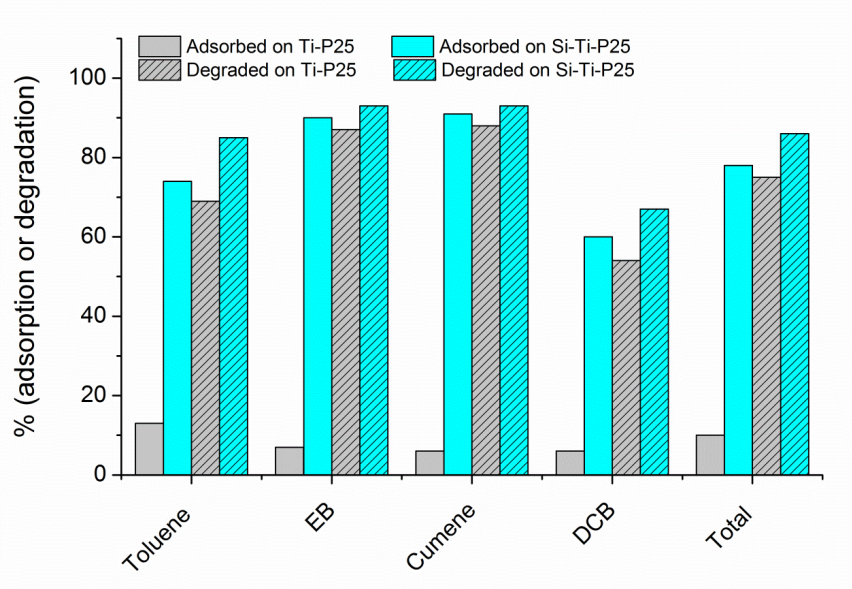

Figure 8.5 Comparison of VOCs masses adsorbed or degraded on Ti-P25 or Si-Ti-P25

Table 8.3 Degradation of VOCs by Ti-P25 or Si-Ti-P25 sorbents with repeated sampling

Sorbent	Ti-P25			Si-Ti-P25		
VOCs	Exp.1	Exp.2	Exp.3	Exp.1	Exp.2	Exp.3
Toluene	69	91	99	85	81	79
EB	87	92	98	90	93	93
Cumene	88	90	97	93	94	93
DCB	54	64	78	67	74	73
Total	74	88	96	86	85	83

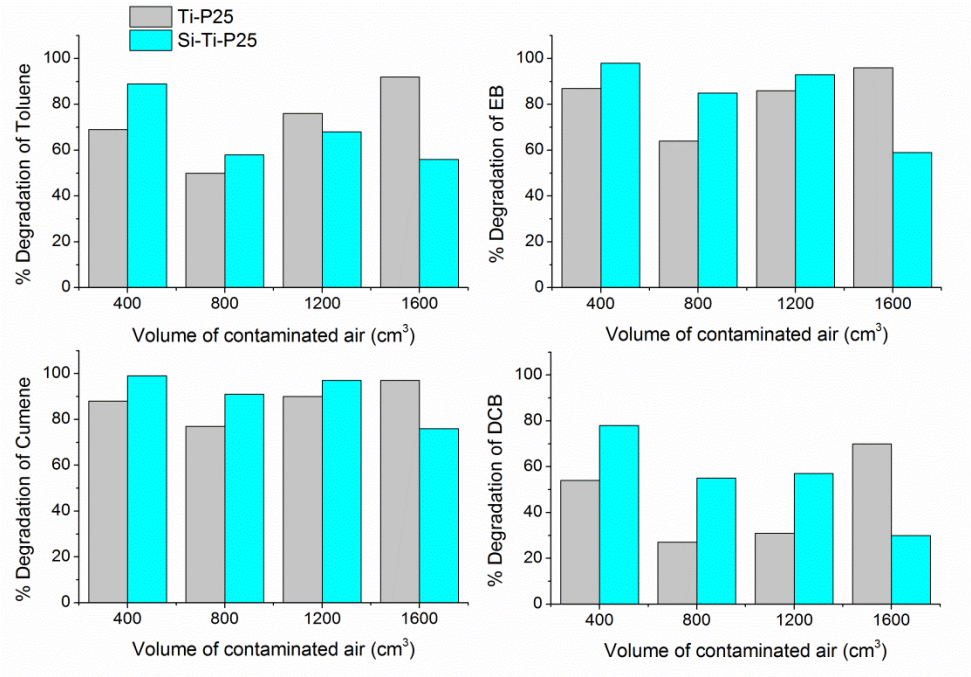

Figure 8.6 Degradation of VOCs by Ti-P25 or Si-Ti-P25 using increasing volumes of contaminated air

8.3.3 Use of TiO_2 coated glass beads for VOC photocatalysis

Before examining the photo-degradation of VOCs a control experiments were run using quartz sampling tubes loaded with uncoated glass bead (GB) with the UV lamp (Off) to obtain VOC "references masses", which were required to calculate the degradation percentages. The VOC masses collected by Tenax-TA sampling tubes, calculated by calibration, are given in Table 8.4. Results showed averages masses (n=3) of VOCs with acceptable values of % RSD (0.50 – 5.48) which could be used as references to calculate degraded masses and degradation percentages of VOCs.

Table 8.4 Average of VOCs masses "references masses" at 50 cm^3 min^{-1}

VOC	Toluene / ng	EB / ng	Cumene /ng	DCB / ng	Total / ng
Exp.1	18637	10404	5684	6104	40829
Exp.2	19424	10343	5746	6071	41584
Exp.3	19951	10296	6273	6218	42738
Average	19337	10348	5901	6131	41717
STDEV	661	54	324	77	961
% RSD	3.42	0.52	5.48	1.26	2.31

8.3.3.1 Initial experiments to assess the performance of glass beads coated with porous TiO_2 catalyst

Quartz TiO_2 coated sampling tubes loaded with TiO_2 coated (n = 1-4) glass beads (1 mm dia or 2 mm dia) were used to examine the photocatalysis of VOCs. In the first set of experiments, quartz coated catalyst tubes containing big glass bead coated one or two times (Ti-BGB-1 or Ti-BGB-2) were used to sample contaminated air at a flow rate of 50 cm^3 min^{-1} for 8 min. The degradation values (%) for the first 2 catalyst tubes are given in Figure 8.7. Similar results were obtained for glass beads whether they were coated once or twice with the porous TiO_2 catalyst, with degradation values ranging from 45 – 70 %.

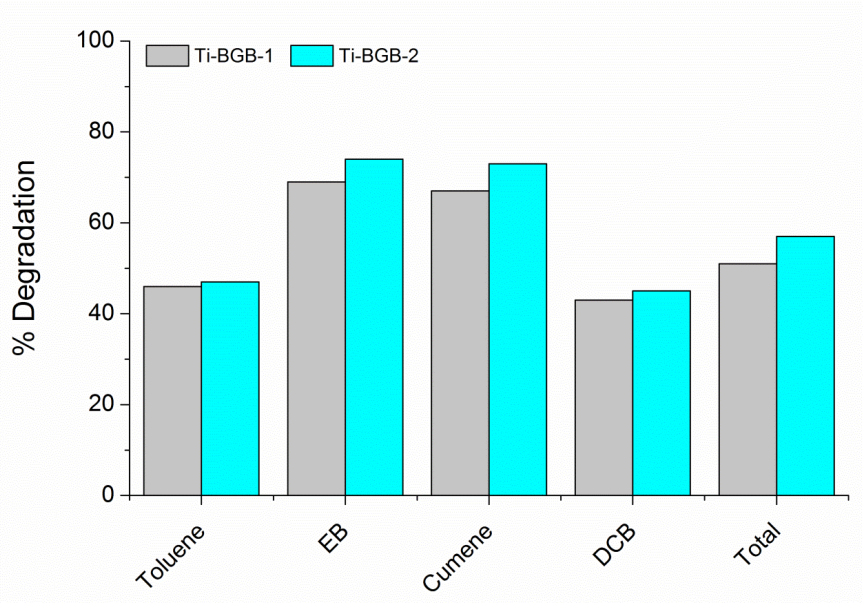

Figure 8.7 Degradation of VOCs by Ti-BGB-1 or Ti-BGB-2 presented in 400 cm^3 of contaminated air

The flow rate of contaminated air was reduced to 25 cm^3 min^{-1} and again control experiments (n = 3) were undertaken with quartz sampling tubes loaded with uncoated GB and with the UV lamp (Off). Reference masses for toluene, EB, cumene or DCB were 7735, 2729, 1260 or 317 ng with acceptable RSD values of 15, 12, 13 or 15 %, respectively. Quartz catalyst tubes loaded with Ti-BGB-2 or Ti-SGB-2 were used to sample contaminated air at 25 cm^3 min^{-1} for 8 min (with the UV lamp (On)) and VOCs passing through the catalyst bed were collected by a Tenax-TA sampling tube. The amounts of VOC masses degraded by the catalysts are given in Figure 8.8, No change in performance was observed for Ti-BGB-2 when the air flow was reduced from 50 to 25 cm^3 min^{-1}. Arguably slightly better performance was observed for Ti-SGB-2 indicating that the higher catalytic surface area has improved the performance of the catalyst bed. Approximately 80 % of total VOC masses were degraded by Ti-SGB-2 compared to approximately 50 % for Ti-BGB-2, confirming the enhancement of photocatalysis of VOCs by increasing the surface area of porous TiO_2 coated glass beads.

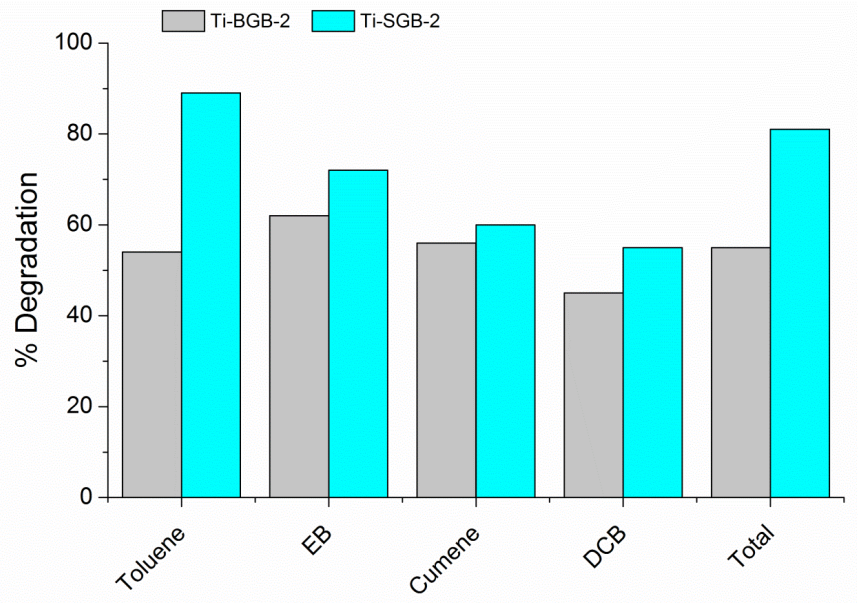

Figure 8.8 comparison degradation of VOCs by Ti-BGB-2 and Ti-SGB-2 when used to sample contaminated air at 25 cm^3 min^{-1}

8.3.3.2 Assessment of the number of porous TiO_2 coats used to cover glass beads

To examine the influence of film thickness layer of the coated porous TiO_2 films on the surface of the glass beads the TiO_2 dipping process was repeated several times. Quartz sampling tubes containing big glass beads Ti-BGB-1, Ti-BGB-2, Ti-BGB-3 or Ti-BGB-4) or small glass beads (Ti-SGB-1, Ti-SGB-2, Ti-SGB-3 or Ti-SGB-4) were used to sample contaminated air at a flow rate of 25 cm^3 min^{-1} for 2 min. As before control experiments, n = 3, were run (with uncoated GB and the UV lamp switch off) to determine reference masses, which are given in Table 8.5. Results showed that average masses of all VOCs were higher for uncoated SGB compared with uncoated BGB and by factor 2 in total masses.

Table 8.5 Averages of references masses of VOCs presented in 50 cm^3 of contaminated air.

Glass bead	Uncoated BGB		Uncoated SGB	
VOCs	Average masses / ng	% RSD	Average masses / ng	% RSD
Toluene	4497	6.10	5835	2.75
EB	1219	6.41	2366	9.65
Cumene	487	8.59	1725	6.79
DCB	146	6.34	1131	5.08
Total	6349		11057	

Small glass beads were used to determine the effect of the thickness coating on the surface of the beads. Quartz catalyst tubes contained Ti-SGB-1, Ti-SGB-2, Ti-SGB-3 or Ti-SGB-4 and the contaminated air was passed through the catalyst bed at 25 cm^3 min^{-1} for 2 min. The results, illustrated in Figure 8.9, demonstrate that the degradation of all VOCs was significantly increased when the glass beads were coated twice with the porous TiO_2 catalyst (see Ti-SGB-1 c.f. Ti-SGB-2). The degradation of total VOC masses increased from 50 to 80 %. In addition the degradation was slightly increased when the number of coatings increased to 3 or 4, confirming that the coating of glass bead should be undertaken at least twice to ensure a high performance of VOC photocatalysis.

Furthermore the performance of Ti-SGB for VOCs degradation was compared with Ti-BGB (see Figure 8.10), further confirming that Ti-SGB had significantly higher performance for the degradation of VOCs at all coating values, compared to Ti-BGB.

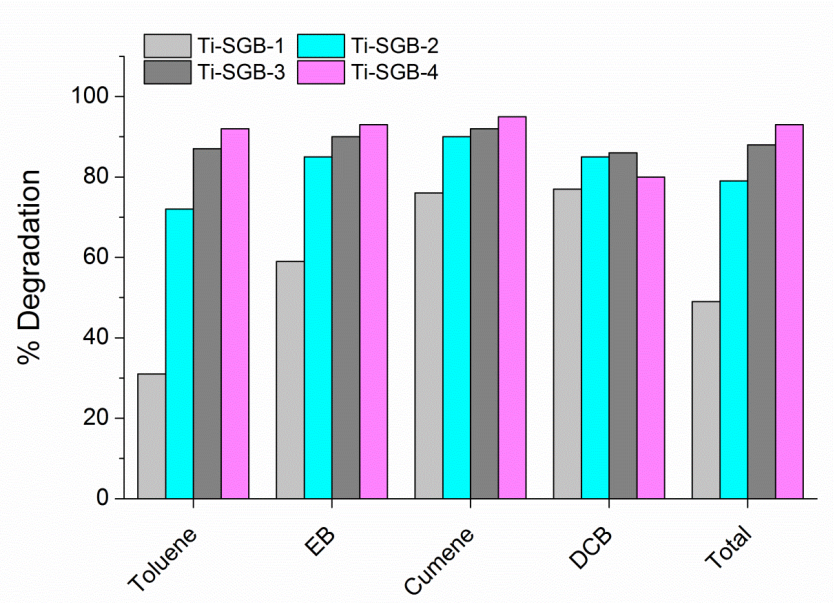

Figure 8.9 Degradation of VOCs by Ti-SGB coated different times when used to sample 50 cm^3 of contaminated air

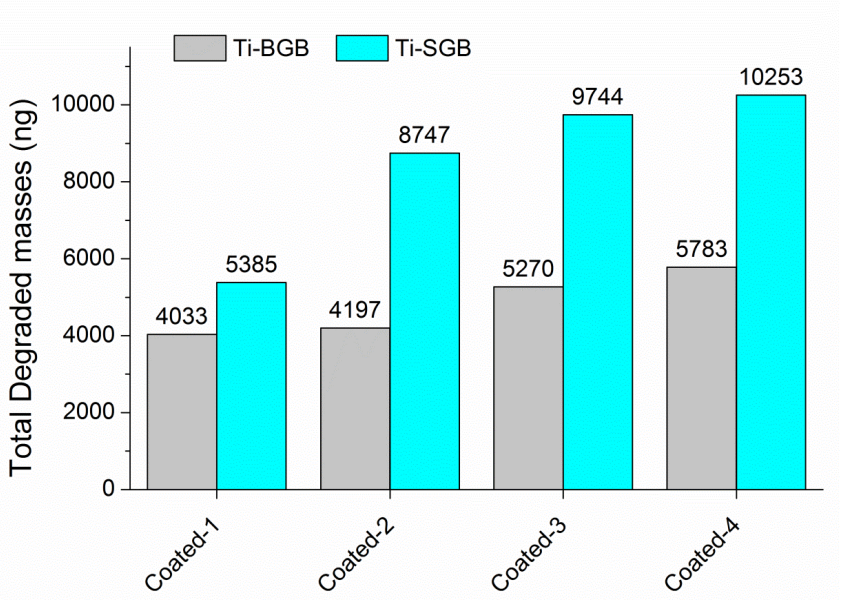

Figure 8.10 Comparison total masses of VOCs degraded by Ti-BGB or Ti-SGB when used to sample 50 cm^3 of contaminated air

8.3.3.3 Reduction of air flow rate to 15 cm^3 min^{-1}

To further increase VOC residence time in the catalyst bed the flow rate of contaminated air was reduced to 15 cm^3 min^{-1}. The VOC masses "reference masses" for both Ti-BGB and Ti-SGB were again measured using uncoated-BGB or uncoated-SGB, respectively, as outlined in Table 8.6. The results showed that the VOC masses trapped by Tenax-TA sampling tubes decreased by a factor 4 or 3, respectively, by decreasing the flow rate of contaminated air from 25 to 15 cm^3 min^{-1} (see also Table 8.5). On the other hand the total masses of VOCs collected by Tenax TA tube with uncoated-SGB in-line were higher (by factor 2) than masses that collected when uncoated-BGB in-line. Therefore the average of VOCs masses for each type of glass bead were used to calculate degraded masses and degradation percentages for each coated glass bead. The degradation percentages of VOCs by Ti-BGB or Ti-SGB sampling tubes when used to sample 30 cm^3 contaminated air were shown in Figure 8.11 and Figure 8.12 respectively.

Table 8.6 Averages of references masses of VOCs presented in 30 cm^3 of contaminated air.

Glass bead	Uncoated BGB		Uncoated SGB	
VOCs	Average masses (ng)	% RSD	Average masses (ng)	% RSD
Toluene	1156	7.24	1805	1.8
EB	222	7.48	560	7.59
Cumene	78	5.5	296	8.83
DCB	64	7.32	640	9.29
Total	1520		3301	

Results illustrated in Figure 8.11 demonstrated that the degradation of all VOCs was increased as the number of porous TiO_2 coats increased from 1 to 4. In addition the total VOC degradation value increased 20 to 60, 80 or 90 % by increasing coats from 1 2, 3 or 4 times, respectively. Similar degradation performances were obtained for Ti-SGB thin films (see Figure 8.12); however, they had slightly higher efficiencies according to their total reference masses (3301 ng) compared with (1150 ng) for Ti-BGB (see Figure 8.13). These results confirmed again that Ti-SGB thin films had significantly higher degradation efficiency compared to Ti-BGB thin films for VOCs photocatalysis. It was shown that Ti-SGB-1 had performance greater than Ti-BGB thin films which were coated many times.

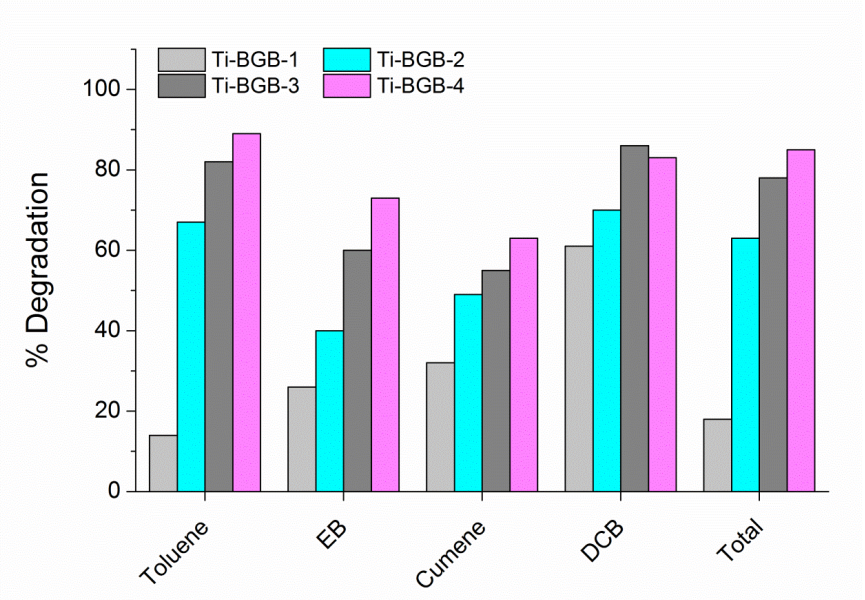

Figure 8.11 Degradation of VOCs by Ti-BGB coated different times when used to sample 30 cm^3 of contaminated air

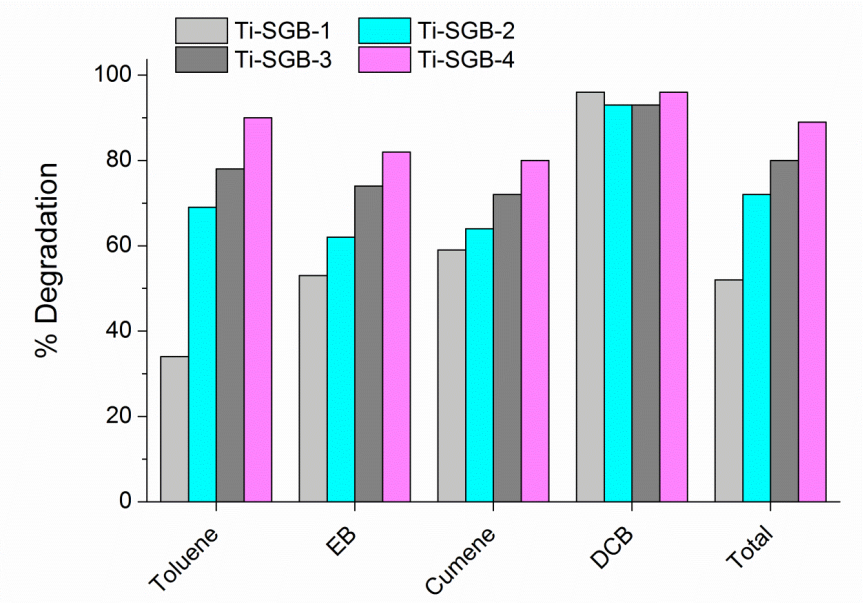

Figure 8.12 Degradation of VOCs by Ti-SGB coated different times when used to sample 30 cm^3 of contaminated air

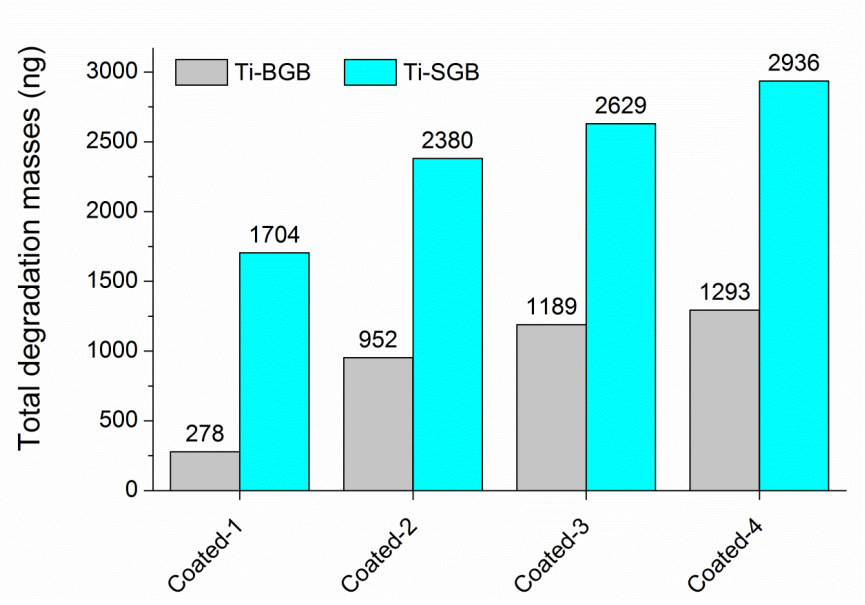

Figure 8.13 Comparison total masses of VOCs degraded by Ti-BGB or Ti-SGB when used to sample 30 cm^3 of contaminated air

Finally to examine the effect of contaminated air flow rate on degradation efficiency of titanium thin films used for VOCs degradation, masses of VOCs degraded by Ti-SGB-2 at different flow rates of contaminated air were normalized to be masses/ unit volume of air (ng/cm^3). Normalization of degraded masses when contaminated air was sampled at flow rates of 25 or 15 cm^3 min^{-1} for 2 min by Ti-SGB-2 thin films are illustrated in Figure 8.14. The normalization values indicate that the degradation efficiency of Ti-SGB-2 was higher when used to sample the contaminated air at flow rate of 25 cm^3 min^{-1} for 2 min for most of the VOCs. These results indicated that total degraded masses were increased by factor 2 when flow rate increased from 15 to 25 cm^3 min^{-1}, confirmed the high performance of Ti-SGB thin films for VOCs degradation even when present at high concentrations (approx. 180 ng cm^{-3}).

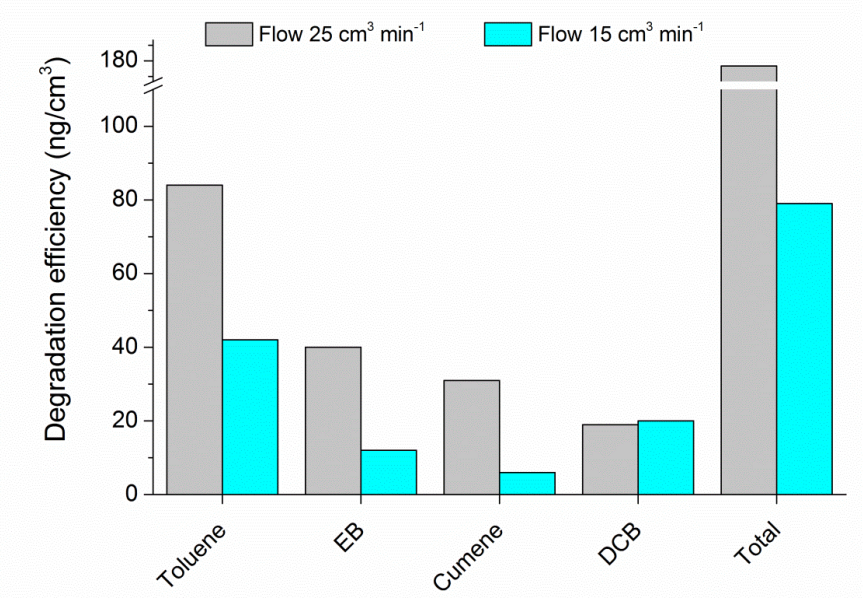

Figure 8.14 Normalisation the degradation efficiency of Ti-SGB-2 thin films for VOCs

8.4 Conclusions

In this work, porous TiO_2 photocatalyst materials (powder or thin films) were used to degrade selected VOCs (toluene, EB, cumene and DCB). The results obtained when

Ti-P25 sorbent was used to sample contaminated air at flow rate of 100 cm^3 min^{-1} demonstrated that the degradation of VOCs was significantly increased with increased sampling time. It was though that photocatalytic activation of the sorbent was increased by increasing sampling time which led to warmed active sites more suitable for degradation. Similar degradation values were obtained when the flow rate was reduced to 50 cm^3 min^{-1} with double sampling times, confirming the positive effect of longer sampling time on the VOCs degradation. Comparison of Ti-P25 and Si-Ti-P25 sorbents indicated that no improvement of degradation efficiencies was achieved after mixing MCM-41 with the TiO_2 catalyst. However the adsorption efficiency of VOCs by Si-Ti-P25 were significantly higher than that of P25 as expected due to high capacity of MCM-41 for VOCs adsorption. The effect of adsorption can be confirmed by repeating the sample of contaminated air many times by using the same sampling tubes of both sorbents; it was observed that the degradation efficiency of Si-Ti-P25 was similar for all repeated experiments while it was significantly increased for Ti-P25.

This work reported the first use of porous TiO_2 thin films coated onto glass beads for VOC degradation. The results indicated that the air flow rate passing through the catalyst bed is of great importance and must be optimised to ensure best degradation efficiencies. Using a flow rate 50 cm^3 min^{-1} approximately 50 % of VOCs in the air stream were degraded. Performance was improved at lower flow rates and using smaller glass beads, with degradation values increasing to 80 %. The number of times the glass beads are coated with the porous TiO2 catalyst is also of primary importance as the coating number significantly influences decomposition efficiencies. In these experiments best performance was achieved when the beads were coated 4 times, although arguably the performance was only slightly higher than beads which were coated twice. One coat is not recommended. Finally the residence time of VOCs in the catalytic bed was also shown to influence the performance; with best results being achieved for a low flow rate 15 cm^3 min^{-1}, the normalization of degraded masses (mass/volume) indicated that the total degraded masses were higher by factor 2 with flow rate of 25 cm^3 min^{-1}.

9 Conclusions and future work

9.1 Validation methods used to determine VOCs or H_2CO

The results obtained during this research demonstrated successful generation of constant concentrations of VOCs and H_2CO in laboratory dynamic air sampling chambers using in-house built permeation vials and permeation devices. Constant emission rates of VOCs were provided by permeation vials for up to 6 weeks. A permeation device was also shown to provide a constant emission rate of H_2CO for even longer times, and H_2CO could be generated at high or low concentrations (17 or 1.4 mg m^{-3}) by controlling the oven temperature to 80 or 25 °C, respectively.

Direct injection of VOCs onto calibrant tubes loaded with Tenax TA was shown to be the best calibration method for the TDU-GC-MS instrument which was used to determine the concentration of trapped VOCs. The calibration method was shown to be repeatable and reproducible. In contrast, the direct injection method could not be used for instrument calibration when silica calibrant tubes were used due to the potential adsorption competition of methanol and analytes with the silica surface. Significant breakthrough of injected VOCs was observed. Therefore Tenax TA was recommended as the calibrant material used to obtain all calibration curves in this work, regardless of which sorbent is used to collect VOCs from contaminated air. Furthermore Tenax TA sampling tubes were used to determine experimental masses of VOCs collected in the contaminated air stream. The results indicated that the air sampling method was repeatable and reproducible with average of measured masses of toluene, ethylbenzene, cumene or dichlorobenzene of 2109, 404, 497 or 494 ng, respectively. These masses were used as "reference masses" to examine the extraction efficiency and dynamic adsorption capacity of all silica adsorbents studied through this research.

The developed colorimetric method was used to determine H_2CO vapour generated at high concentration. The results demonstrated the high stability of coloured solution was obtained after 1 h after addition of the Schiff's reagents to an aqueous solution of H_2CO, whereas no stability was observed when the method was used to determine H_2CO generated at low concentration. Therefore the developed colorimetric impinge method was recommended for air sampling only when the

H_2CO concentration was high. Silica C18 cartridges loaded with a 2,4-DNPH trapping solution were used to collect H_2CO vapour at lower concentration. The results demonstrated successfully validation of collected and detected method used to determine H_2CO vapour when generated at low concentration with repeatability and reproducibility. The average of detected masses (8.1 μg) was chosen as the "reference mass" for examination of extraction efficiency of silica adsorbents used for H_2CO adsorption.

9.2 Synthesis of silica adsorbents used for VOCs and H_2CO extraction

Two mesoporous silica adsorbents, MCM-41 and SBA-15, were synthesised under conventional preparation methods using harsh conditions and a long condensation step. Calcination was applied to remove the organic template from the silica framework to provide MCM-41 and SBA-15 materials which possessed high surface areas (1014 and 644 $m^2 g^{-1}$) and large pore volumes (0.82 $cm^3 g^{-1}$) as required for adsorption processes. Moreover, microwave digestion was used to remove the organic template to produce MWD-MCM-41 giving a significant increasing of the pore size from 2.7 to 6.74 nm, a larger number of silanol groups and a lower surface area (760 $m^2 g^{-1}$). The performance of these mesoporous adsorbents for VOC extraction was examined and compared to Tenax TA. The results demonstrated similar performance of MCM-41 adsorbents and a slight different performance of SBA-15 as described in Section 9.3.

This work also reports on the production of novel silica green nanomaterials (GNs) using a bioinspired synthesis route. The main advantages of this synthesis route were; rapid production of material (15 min), use of mild conditions such as neutral pH and ambient temperature, and use of environmentally-friendly solutions (all aqueous solutions) which led to considerable reduction of secondary pollution. The produced GN adsorbents with physical properties possess important features such as the presence of micropores in their structures, which an advantage for gases adsorption. However, the surface area of the initial GN material produced (58 $m^2 g^{-1}$) was significantly lower than that of MCM-41 and SBA-15 which were prepared

under harsh conditions and longer multistep condensation. An increasing of surface area was achieved by an alteration of silica precursor concentration, Si: N ratio or by using the shorter poly ethylene amine additive. The results showed that surface area was significant increased to 363 or 260 $m^2 g^{-1}$ by changing the original concentration (30 mM) of silica precursor to 20 or 40 mM, respectively. Furthermore surface area was successful enhanced (355 $m^2 g^{-1}$) by altering the Si: N ratio to 2:1, or (268 $m^2 g^{-1}$) when shorter additive was used. Therefore an optimisation of preparation conditions of GN materials required more work to provide ideal properties for specific applications. According to features of GN adsorbents which include the advantages of synthesis conditions and their micropores structures, they can be used as alternative adsorbents for VOCs extraction. The obtained results indicated that GN adsorbents had performances which are comparable to that of MCM-41, confirming their ability to use as VOCs scavengers.

Furthermore, this work also presents a novel preparation method of mesoporous silica materials (USG). These materials were successfully produced by using green route; rapid synthesis (15 min), neutral pH, ambient temperature, use of aqueous solution "green reagents" and cheaper silica precursor. The calcined USG adsorbents possess a high surface area, large pore volume and narrow pore distribution which are comparable with conventional mesoporous silica (MCM-41). The results demonstrated a higher surface area (1140 $m^2 g^{-1}$) of USG-S, aged for 15 min, compared to USG-L (730 $m^2 g^{-1}$), which was aged for longer time (18 h). However they have similar pore size of 2.6 or 3.1 nm and pore volumes 1.00 or 0.99, respectively. In contrast a significant reduction of surface area was observed when microwave digestion was applied to produce MWD-USG instead of calcination (1140 to 412 $m^2 g^{-1}$) compared to MCM-41. On the other hand MWD-MCM-41 showed an important increasing of pore size (6.74 nm) whereas MWD-USG was produced with variety of pore sizes (2.6 to 3.9 nm). The results showed the best results were obtained for calcined USG-S, aged for 15 min, which produced by green routes, with similar physical properties of MCM-41. In addition results demonstrated that adsorbent (USG-S) had similar extraction efficiency and dynamic capacity for VOCs as well as MCM-41.

Finally all silica adsorbents (MCM-41, SBA-15, GNs or USG) were successfully functionalised with an organic amine group in order to examine their performance for H_2CO extraction. The functionalisation process of these adsorbents was confirmed by results obtained from microelemental and ATR-FTIR analysis. These results showed that MWD-MCM-41 had higher functionalisation degree (1.99) than SBA-15 (1.58), however, they have similar pore sizes (≈7 nm); confirming that microwave digestion produced large silanol groups. Whereas MCM-41 had a lower degree due to smaller pore size (2.7 nm) in spite of its higher surface area (1014 m^2 g^{-1}). Interestingly GNs showed significant degree (1.2) in spite of its lower surface area (58 m^2 g^{-1}) and no measurable pore size. The highest functionalisation degree (2.6) was reported for USG-S adsorbent in spite it has pore size as similar as MCM-41. These results demonstrated that the new adsorbents, GNs and USG, can be provided an exciting platform for grafting by variety functional groups which were required for specific adsorption applications. Moreover the BET and SAS-XRD analysis were used to study the effect of grafting on the physical properties of functionalised MCM-41 and SBA-15. The BET results indicated that calcined adsorbents retained their structure after grafting; the SAS-XRD patterns demonstrate a new and similar structure for all functionalised adsorbents.

In this work, performances of all grafting silica adsorbents were examined for H_2CO extraction and to investigate that it was removed permanently from indoor air by chemisorption as reported in Section 9.3.

9.3 Use silica adsorbents for VOCs and H_2CO extraction

Extraction efficiencies of MCM-41 and SBA-15 adsorbents were measured for VOCs adsorption and compared to reference masses collected by Tenax TA under selected sampling conditions. The results showed that both MCM-41 and SBA-15 had a similar performance for extraction most of VOC (64 to 69 %) except a higher performance of MCM-41 for DBC (83 to 85 %) and of SBA-15 for EB and cumene (80, 96). However, SBA-15 possessed a lower surface area compared to C-MCM41; it had a slight higher adsorption capacity as results of the presence of micropores in its bimodal pore structure which are favourable for VOCs adsorption.

Furthermore the performance of GN adsorbents (prepared by green route) for VOCs extraction was reported as the first application of these materials. Efficiencies and adsorption capacities of these adsorbents were compared with conventional mesoporous materials (MCM-41). The results demonstrated that GN adsorbents had similar extraction efficiencies (60 %) for VOCs adsorption compared with MCM-41 in spite of their lower surface area, and again it is due to their micropores structure. In addition, results demonstrated that GN adsorbent (prepared using the shorter poly ethylene amine) had the highest extraction efficiency (80 %) in this comparison, confirming an increase of performance due to presence of micropores. Furthermore the GN adsorbents had similar adsorption capacities with MCM-41 for VOCs extraction when normalised per unit of surface area (ng/m^2).

This work also reports the first application of USG adsorbents for VOCs extraction. Interestingly results indicated that the USG adsorbents, which rapidly produced by using the green synthesis route, had extraction efficiencies (60 %) as similar as that of MCM-41 prepared under harsh conditions with higher value of DCB (80 %) for MCM-41.

Finally, all functionalised silica adsorbents (NH_2-MCM-41, NH2-SBA-15, NH_2-GNs or NH_2-USG) were examined for the extraction of H_2CO from contaminated air by dynamic (active) sampling mode. The results demonstrated that all these functionalised adsorbents successfully extracted H_2CO by chemisorption ensuring it was removed from contaminated air permanently. On the other hand NH_2-MCM-41 and NH_2- SBA-15 were chosen to extract H_2CO in passive sampling mode. The results showed a significant reduction of H_2CO vapour but not to a zero level; therefore dynamic mode is recommended as the best method for removal of H_2CO from indoor air.

In general, the new GNs and USG adsorbents, prepared by the green synthesis route, provided exciting new platforms for the environmental remediation of VOCs and H_2CO from indoor air.

9.4 Degradation of VOCs by TiO_2 catalysts

Herein, porous TiO_2 photocatalyst as powder or thin films were used to degrade selected VOCs (toluene, EB, cumene and DCB) that generated in contaminated air. Degussa P25 TiO_2 (Ti-P25) was used as a pure powder to sample contaminated air at different flow rates and for a variety of sampling times. The results demonstrated that a similar degradation performance (65 to 70 %) of these materials even when the air flow rate was decreased from 100 to 50 cm^3 min^{-1}. In contrast the best degradation performance was achieved by increasing sampling times to 4 or 6 min (70 or 80 %). On the other hand, it was observed that no improvement of degradation of VOCs by combination of MCM-41 and TiO_2 (Si-Ti-P25), and both catalysts had degradation efficiencies (80 – 85 %) for VOCs presented in 400 cm^3 of contaminated air.

TiO_2 thin films coated on a glass beat were used for VOCs degradation as the first applications. Glass beat coated (1-4) times were used to sample contaminated air at different flow rates and for variety of sampling times. The results showed that the degradation efficiency of catalyst bed is significantly affected by surface area of porous, air flow rate and coating times. The degradation performance can be enhanced by increasing surface area of coated porous, the results showed that degradation of VOCs collected by bigger glass bead (50 %) was increased to 80 % when collected by smaller glass bead under the sampling conditions. In addition the degradation efficiency was significantly increased from 50 to 80 % when glass bead was coated twice and slight increased when coated 3 or 4 times. Furthermore normalization of degraded masses (masses/volume) demonstrated that the total degraded masses collected at flow rate at 25 cm^3 min^{-1} were higher by factor 2 than that collected at 15 cm^3 min^{-1}. The best performance was obtained when the smaller glass bead were coated 3 or 4 times and at lower flow rate (25 cm^3 min^{-1}) of contaminated air.

9.5 Future work

Some points of this project need more investigation as described below:

In this work, silica adsorbents were successfully functionalised with organic amine groups to target the removal of H_2CO from indoor air by chemisorption. The obtained results of the new materials, GNs and USG, were encouraging indicating successful grafting. It is possible therefore those other chelates could be grafted onto their surface potentially expanding their applications, for example they could be used to remove potentially toxic elements from aqueous streams. More work is also required to better understand the structure of these new materials. Characterisation of functionalised mesoporous adsorbents by BET indicated a significant reduction of surface area after grafting. However, N_2 sorption isotherms showed that the materials retained their pore structure after grafting, especially the calcined materials, the corresponding SAS-XRD patterns indicated that the functionalised materials had different pore ordering. This is an exciting observation which needs further investigation.

The synthesis of new GN adsorbents using bioinspired synthesis routes produced adsorbents that possessed unique physical properties which could be easily tailored. It was reported that the surface area of the first GN adsorbent could be improved by increasing of silica precursor, alteration of Si: N ratio or by using shorter ethylene amine. These results open further exciting opportunities for different preparation methods producing a variety of tailored silica materials. Furthermore the promising results demonstrate that GNs adsorbents had a significantly high performance for VOCs and H_2CO extraction, but it is possible that better results would be obtained with further optimisation.

The photocatalysis work reported that glass bead could be coated by TiO_2 thin films and successfully used to degrade VOCs. The results indicated that approximately 90 % of VOCs were degraded on coated glass bead when one UV lamp was used for activation. Therefore to ensure that the performance of TiO_2 photocatalyst was up to 100 %, the sampling conditions should be optimised and two UV lamps should be used to ensure the activation of all the photocatalyst sites.

References

[1] D. Won, R.J. Magee, W. Yang, E. Lusztyk, G. Nong, C.Y. Shaw, Indoor Air 2005: Proceedings of the 10th International Conference on Indoor Air Quality and Climate, Vols 1-5, (2005) 2070-2075.

[2] L. Molhave, G. Clausen, B. Berglund, J. de Ceaurriz, A. Kettrup, T. Lindvall, M. Maroni, A.C. Pickering, U. Risse, H. Rothweiler, B. Seifert, M. Younes, Indoor Air-International Journal of Indoor Air Quality and Climate, 7 (1997) 225-240.

[3] M.E. Heroux, D. Gauvin, N.L. Gilbert, M. Guay, G. Dupuis, M. Legris, B. Levesque, Indoor and Built Environment, 17 (2008) 128-137.

[4] S.J. Solomon, G.W. Schade, J. Kuttippurath, A. Ladstatter-Weissenmayer, J.P. Burrows, Indoor and Built Environment, 17 (2008) 260-268.

[5] IARC, International Agency for Research on Cancer, Lyon, France. Ludin, L., 1993, (2004).

[6] U.S.E.P. Agency, Report to congress on indoor air quality, Washington, D.C., (1989.).

[7] Who, Environmental Health Criteria, 89 (1989) 1-219.

[8] H. Canada, H128-1/05-432E. Health Canada, (2005).

[9] S. Kim, Bioresource Technology, 100 (2009) 744-748.

[10] A.P. Jones, Atmospheric Environment, 33 (1999) 4535-4564.

[11] S.C. Lee, W.M. Li, C.H. Ao, Atmospheric Environment, 36 (2002) 225-237.

[12] W.M. Li, S.C. Lee, L.Y. Chan, Science of the Total Environment, 273 (2001) 27-40.

[13] S. Halvarsson, H. Edlund, M. Norgren, Industrial Crops and Products, 28 (2008) 37-46.

[14] M. Guerue, S. Tekeli, I. Bilici, Materials & Design, 27 (2006) 1148-1151.

[15] L. Allou, C. Marchand, P. Mirabel, S. Le Calve, Indoor and Built Environment, 17 (2008) 138-145.

[16] B. Zabiegala, M. Partyka, B. Zygmunt, J. Namiesnik, Indoor and Built Environment, 18 (2009) 492-504.

[17] P. Wolkoff, T. Schneider, J. Kildeso, R. Degerth, M. Jaroszewski, H. Schunk, Science of the Total Environment, 215 (1998) 135-156.

[18] A.L. Clobes, G.P. Ananth, A.L. Hood, J.A. Schroeder, K.A. Lee, Human Activities as Sources of Volatile Organic-Compounds In residential Environments, 1992.

[19] B.P. Leaderer, S.K. Hammond, Environmental Science & Technology, 25 (1991) 770-777.

[20] C. Marchand, B. Buillot, S. Le Calve, P. Mirabel, Atmospheric Environment, 40 (2006) 1336-1345.

[21] A. Baez, H. Padilla, R. Garcia, M.D. Torres, I. Rosas, R. Belmont, Science of the Total Environment, 302 (2003) 211-226.

[22] P. Pluschke, The Handbook of Environmental Chemistry (Indoor air pollution), Springer, Berlin Heidelberg, (2004).

[23] S. Batterman, T. Metts, P. Kalliokoski, E. Barnett, Journal of Environmental Monitoring, 4 (2002) 361-370.

[24] J. Namiesnik, B. Zabiegala, A. Kot-Wasik, M. Partyka, A. Wasik, Analytical and Bioanalytical Chemistry, 381 (2005) 279-301.

[25] B. Lundgren, D. Crump, R., H. Knoppel, A. Laurent, E. Lebret, H. Rothweiler, B. Seifert, P. Wolkoff, D. Cavallo, , Sampling strategies for volatile organic compounds (VOCs) in indoor air, in, European union, 1994.

[26] I.M. D. Crump, Daily variations of volatile organic compound concentrations in residential indoor air, in: Proceedings of Indoor Air 93, Helsinki, (1993) 15-20.

[27] P. Wolkoff, Indoor Air, 5 (1995) 5-73.

[28] E. Woolfenden, Journal of Chromatography A, 1217 (2010) 2685-2694.

[29] E. Woolfenden, Journal of Chromatography A, 1217 (2010) 2674-2684.

[30] R.H. Brown, Pure and Applied Chemistry, 65 (1993) 1859-1874.

[31] E.D. Pamles, A.F. Gunnison, Am. Ind. Hyg. Assoc, 34 (1973) 78-81.

[32] B. Oury, F. Lhuillier, J.-C. Protois, Y. Morele, Journal of Occupational and Environmental Hygiene, 3 (2006) 547-557.

[33] R. H. Brown, J. Chalton, K.J. Suanders, Am. Ind. Hyg. Assoc. J, 42 (1981) 865-869.

[34] C. Thammakhet, V. Muneesawang, P. Thavarungkul, P. Kanatharana, Atmospheric Environment, 40 (2006) 4589-4596.

[35] A. Kumar, I. Viden, Environmental Monitoring and Assessment, 131 (2007) 301-321.

[36] S. Krol, B. Zabiegala, J. Namiesnik, Trac-Trends in Analytical Chemistry, 29 (2010) 1101-1112.

[37] A. Guenther, C. Geron, T. Pierce, B. Lamb, P. Harley, R. Fall, Atmospheric Environment, 34 (2000) 2205-2230.

[38] S. Krol, B. Zabiegala, J. Namiesnik, Trac-Trends in Analytical Chemistry, 29 (2010) 1092-1100.

[39] F.J. Santos, M.T. Galceran, Trac-Trends in Analytical Chemistry, 21 (2002) 672-685.

[40] S.K. Pang, J.S. Lee, H. Cho, J.Y. Sohn, S. Cho, Indoor and Built Environment, 17 (2008) 552-561.

[41] M. Rosa Ras, F. Borrull, R. Maria Marce, Trac-Trends in Analytical Chemistry, 28 (2009) 347-361.

[42] K. Badjagbo, P. Picard, S. Moore, S. Sauve, Journal of the American Society for Mass Spectrometry, 20 (2009) 829-836.

[43] M.L. Mattinen, J. Tuominen, K. Saarela, Indoor Air-International Journal of Indoor Air Quality and Climate, 5 (1995) 56-61.

[44] F.J. Santos, M.T. Galceran, D. Fraisse, Journal of Chromatography A, 742 (1996) 181-189.

[45] P. Bruno, M. Caputi, M. Caselli, G. de Gennaro, M. de Rienzo, Atmospheric Environment, 39 (2005) 1347-1355.

[46] Q. Li, P. Sritharathikhum, M. Oshima, S. Motomizu, Analytica Chimica Acta, 612 (2008) 165-172.

[47] A. Pretto, M.R. Milani, A.A. Cardoso, Journal of Environmental Monitoring, 2 (2000) 566-570.

[48] L.T. Gibson, W.J. Kerr, A. Nordon, J. Reglinski, C. Robertson, L. Turnbull, C.M. Watt, A. Cheung, W. Johnstone, Analytica Chimica Acta, 623 (2008) 109-116.

[49] A. Buldt, R. Lindahl, J.O. Levin, U. Karst, Journal of Environmental Monitoring, 1 (1999) 39-43.

[50] W.H. Chan, S.M. Shuang, M.M.F. Choi, Analyst, 126 (2001) 720-723.

[51] L.B. Coyne, R.E. Cook, J.R. Mann, S. Bouyoucos, O.F. McDonald, C.L. Baldwin, American Industrial Hygiene Association Journal, 46 (1985) 609-619.

[52] R. Otson, P. Fellin, Science of the Total Environment, 77 (1988) 95-131.

[53] J.R. Hopkins, T. Still, S. Al-Haider, I.R. Fisher, A.C. Lewis, P.W. Seakins, Atmospheric Environment, 37 (2003) 2557-2565.

[54] E. Fagnani, C.B. Melios, L. Pezza, H.R. Pezza, Talanta, 60 (2003) 171-176.

[55] A.C. Gigante, M.A. Gotardo, J.O. Tognolli, L. Pezza, H.R. Pezza, Microchemical Journal, 77 (2004) 47-51.

[56] Y.Y. Maruo, J. Nakamura, M. Uchiyama, M. Higuchi, K. Izunli, Sensors and Actuators B-Chemical, 129 (2008) 544-550.

[57] Y. Chi, Y. Feng, S. Wen, H. Lu, Z. Yu, W. Zhang, G. Sheng, J. Fu, Talanta, 72 (2007) 539-545.

[58] W.H. Chan, T.Y. Xie, Analytica Chimica Acta, 349 (1997) 349-357.

[59] A. Altshuller, D.L. Miller, S.F. Sleva, Analytical Chemistry, 33 (1961) 621-&.

[60] E. Sawicki, W. Elbert, T.R. Hauser, T.W. Stanley, Analytical Chemistry, 33 (1961) 93-&.

[61] R.R. Miksch, D.W. Anthon, L.Z. Fanning, C.D. Hollowell, K. Revzan, J. Glanville, Analytical Chemistry, 53 (1981) 2118-2123.

[62] K. Motyka, P. Mikuska, Analytica Chimica Acta, 518 (2004) 51-57.

[63] L.T. Gibson, A.W. Brokerhof, Studies in Conservation, 46 (2001) 289-303.

[64] S.S.H. Ho, K.F. Ho, W.D. Liu, S.C. Lee, W.T. Dai, J.J. Cao, H.S.S. Ip, Atmospheric Environment, 45 (2011) 261-265.

[65] P. Bruno, M. Caselli, G. de Gennaro, S. Iacobellis, M. Tutino, Indoor Air, 18 (2008) 250-256.

[66] S. Li, S. Chen, L. Zhu, X. Chen, C. Yao, X. Shen, Science of the Total Environment, 407 (2009) 2004-2011.

[67] M.M. Loh, E.A. Houseman, G.M. Gray, J.I. Levy, J.D. Spengler, D.H. Bennett, Environmental Science & Technology, 40 (2006) 6903-6911.

[68] S. Wang, H.M. Ang, M.O. Tade, Environment International, 33 (2007) 694-705.

[69] J. Zhao, X.D. Yang, Building and Environment, 38 (2003) 645-654.

[70] S.E. Roark, J. Cabrera-Fonseca, M.C. Milazzo, J.H. White, J.D. Wander, Journal of Environmental Engineering-Asce, 130 (2004) 329-337.

[71] O. Carp, C.L. Huisman, A. Reller, Progress in Solid State Chemistry, 32 (2004) 33-177.

[72] M. Harper, Analyst, 119 (1994) 65-69.

[73] K.S.W. Sing, D.H. Everett, R.A.W. Haul, L. Moscou, R.A. Pierotti, J. Rouquerol, T. Siemieniewska, Pure and Applied Chemistry, 57 (1985) 603-619.

[74] B. Seifert, D. Ullrich, Atmospheric Environment, 21 (1987) 395-404.

[75] N. Yalcin, V. Sevinc, Carbon, 38 (2000) 1943-1945.

[76] R. Stroebel, J. Garche, P.T. Moseley, L. Joerissen, G. Wolf, Journal of Power Sources, 159 (2006) 781-801.

[77] R.K. Iler, The Chemistry of Silica, Jonh Willey & Sons, New York, (1979).

[78] P. Kustrowski, R. Janus, A. Kochanowski, L. Chmielarz, B. Dudek, Z. Piwowarska, M. Michalik, Materials Research Bulletin, 45 (2010) 787-793.

[79] N.L. Dias, D.R. Filho, D. Carmo, Adsorption at silica, alumina and related surfaces, in: Encyclopedia of Surface and Colloid Science, Marcel Dekker, New York, (2004) 1-20.

[80] J.Y. Ying, J.B. Benziger, Colloids and Surfaces a-Physicochemical and Engineering Aspects, 74 (1993) 23-31.

[81] J.S. Beck, J. C. Varuli, W. J. roth, M. E. Leonowicz, C. T. Kresge, K. D. Schmitt, C. T-W. Chu, D. H. Olson, E. W. Sheppard, S. B. McCullen, J. B. Higgins, a.J.L. Schlenker, J. Am. Chem. Soc, 114 (1992) 10834-10843.

[82] F.-Y. Wei, Z.-W. Liu, J. Lu, Z.-T. Liu, Microporous and Mesoporous Materials, 131 (2010) 224-229.

[83] U. Ciesla, F. Schuth, Microporous and Mesoporous Materials, 27 (1999) 131-149.

[84] D.H. Everett, *International Union of pure and applied chemistry* (1971) 579-638.

[85] K.A. Jan-Olof Levin, Roger Lindahl, and Carl-Axel Nilsson, *Anal. Chem.*, 57 (1985) 1032-1035.

[86] A. Matsumoto, H. Chen, K. Tsutsumi, M. Grun, K. Unger, Microporous and Mesoporous Materials, 32 (1999) 55-62.

[87] W. Xuan, C. Zhu, Y. Liu, Y. Cui, Chemical Society Reviews, 41 (2012) 1677-1695.

[88] R. Schmidt, M. Stocker, E. Hansen, D. Akporiaye, O.H. Ellestad, Microporous Materials, 3 (1995) 443-448.

[89] R. Tian, H. Zhang, M. Ye, X. Jiang, L. Hu, X. Li, X. Bao, H. Zou, Angewandte Chemie-International Edition, 46 (2007) 962-965.

[90] L. Zhao, H. Qin, R.a. Wu, H. Zou, Journal of Chromatography A, 1228 (2012) 193-204.

[91] K. Kosuge, S. Kubo, N. Kikukawa, M. Takemori, Langmuir, 23 (2007) 3095-3102.

[92] S.Z. Qiao, S.K. Bhatia, D. Nicholson, Langmuir, 20 (2004) 389-395.

[93] J. Garcia-Martinez, Nanotechnology for the Energy Challenge, John Wiley & Sons, Weinheim (1st Ed.) (2010).

[94] M.R. Hoffmann, S.T. Martin, W.Y. Choi, D.W. Bahnemann, Chemical Reviews, 95 (1995) 69-96.

[95] A. Fujishima, K. Honda, Nature, 238 (1972) 37-+.

[96] J. Mo, Y. Zhang, Q. Xu, J.J. Lamson, R. Zhao, Atmospheric Environment, 43 (2009) 2229-2246.

[97] R. Meininghaus, S. Kirchner, F. Maupetit, H. Sallee, D. Quenard, Indoor and Built Environment, 9 (2000) 277-283.

[98] D.B.M. colombo. A, a.T.B. A Indoor Air, 3 (1993) 276-282.

[99] J. Popa, F. Haghighat, Building and Environment, 38 (2003) 959-964.

[100] H. Huang, F. Haghighat, P. Blondeau, Indoor Air, 16 (2006) 236-247.

[101] D. Won, R.L. Corsi, M. Rynes, Indoor Air-International Journal of Indoor Air Quality and Climate, 11 (2001) 246-256.

[102] Zhang. J, Zhang. J. S, a.C. Q, ASHRAE Trans, 108 (2002) 273-282.

[103] Z.G. B. Tichenor, J. Dunn, Indoor Air 1(1991) 23-25.

[104] Y. An, J.S. Zhang, C.Y. Shaw, Hvac&R Research, 5 (1999) 297-316.

[105] J.C.S. Chang, Z. Guo, Indoor Air-International Journal of Indoor Air Quality and Climate, 4 (1994) 35-39.

[106] P.K. S. Kirchner, P. Rouxel, CSTB Report EAE/SB-96059, (1996).

[107] F. Rouquerol, J.Rouquerol, K.Sing, Adsorption by powders and porous solids : principles, methodology, and applications San Diego : Academic Press, 1999.

[108] R. Dales, L. Liu, A.J. Wheeler, N.L. Gilbert, Canadian Medical Association Journal, 179 (2008) 147-152.

[109] H. Naono, M. Hakuman, T. Tanaka, N. Tamura, K. Nakai, Journal of Colloid and Interface Science, 225 (2000) 411-420.

[110] P.I. Ravikovitch, D. Wei, W.T. Chueh, G.L. Haller, A.V. Neimark, Journal of Physical Chemistry B, 101 (1997) 3671-3679.

[111] M. Kruk, M. Jaroniec, A. Sayari, Langmuir, 13 (1997) 6267-6273.

[112] F. Rouquerol, J. Rouquerol, K. Sing, Adsorption by powders and porous solids: Principles, Methodology and Applications, San Diego : Academic Press 1999.

[113] S. Brunauer, P.H. Emmett, E. Teller, Journal of the American Chemical Society, 60 (1938) 309-319.

[114] A.K. Ladavos, A.P. Katsoulidis, A. Iosifidis, K.S. Triantafyllidis, T.J. Pinnavaia, P.J. Pomonis, Microporous and Mesoporous Materials, 151 (2012) 126-133.

[115] E.P. Barrett, L.G. Joyner, P.P. Halenda, Journal of the American Chemical Society, 73 (1951) 373-380.

[116] W. Thomson, (Lord Kelvin), Philos. Mag., 42 (1871) 448-452.

[117] S. Lowell, J.E. Shields, M.A. Thomas, M. Thommes, Characterization of Porous Solids and Powders: Surface Area, Pore Size and Density, Kluwer Academic Publishers, Corr, 2004.

[118] D. A. Skoog, D. M. West, F.J. .Holler, Fundamentals of Analytical Chemistry, 7th ed., Saunder College Publishing, Philadelphia, 1996.

[119] D.K. Nguyen, A. Bruchet, P. Arpino, Hrc-Journal of High Resolution Chromatography, 17 (1994) 153-159.

[120] B.D. Kruschel, R.W. Bell, R.E. Chapman, M.J. Spencer, K.V. Smith, Hrc-Journal of High Resolution Chromatography, 17 (1994) 187-190.

[121] K. Villberg, A. Veijanen, Analytical Chemistry, 73 (2001) 971-977.

[122] M. Harper, Journal of Chromatography A, 885 (2000) 129-151.

[123] N.E. Rabaud, S.E. Ebeler, L.L. Ashbaugh, R.G. Flocchini, Journal of Agricultural and Food Chemistry, 50 (2002) 5139-5145.

[124] E. De Hoffman, J. Charette, V. Stroobant, Mass Spectrometry, Principles and Applications, John Wiley & Sons Ltd, Chichester, UK, 1996.

[125] J.B. Fenn, M. Mann, C.K. Meng, S.F. Wong, C.M. Whitehouse, Science, 246 (1989) 64-71.

[126] G.M. Message, Practical Aspects of Gas Chromatography/Mass Spectrometry, John Wiley & Sons, New York, 1984.

[127] L.D. Rothman, S.R. Crouch, J.D. Ingle, Analytical Chemistry, 47 (1975) 1226-1233.

[128] G.D. Christian, Analytical chemistry Fifth edition John Wiley & Sons, INC. New York, 1994.

[129] R. J. Hamilton, P.A. Sewell, Itroduction to high performance liquid chromatography, Second Ed. London New York Champan Hall, 1982.

[130] F.C. Strong, Analytical Chemistry, 24 (1952) 338-342.

[131] M. Otto, W. Wegscheider, Analytical Chemistry, 57 (1985) 63-69.

[132] R.B. Bilhorn, J.V. Sweedler, P.M. Epperson, M.B. Denton, Applied Spectroscopy, 41 (1987) 1114-1125.

[133] H.M. .McNair, Basic Gas Chromatography John Wiley & Sons, New York, 1997.

[134] P.W. Atkins, Physical Chemistry, 6th ed.,, Oxford University Press, Oxford, 1998.

[135] W.D. Callister, Materials science and engineering - An introduction, 4th ed., John Wiley & Sons, Inc: USA, 1997.

[136] V. Meynen, P. Cool, E.F. Vansant, Microporous and Mesoporous Materials, 125 (2009) 170-223.

[137] B. Fultz, J.M. Howe, Transmission Electron Microscopy and Diffractometry of Materials. , 3rd ed. Berlin ; New York : Springer., 2008.

[138] N.B. Colthup, L.H. Daly, S.E. Wiberley, Introduction to Infrared and Raman Spectroscopy, 3rd ed. , Academic Press, Boston, 1990.

[139] I. Antal, Á.Z. Dávid, Fundamentals and pharmaceutical applications of near-infrared spectroscopy, in, http://www.glatt.com 2007.

[140] M. Thompson, CHNS Elemental Analysers,The Royal Society of Chemistry, Analytical Methods Committee, (2008).

[141] H. Ritter, M. Nieminen, M. Karppinen, D. Bruehwiler, Microporous and Mesoporous Materials, 121 (2009) 79-83.

[142] B.Z. Tian, X.Y. Liu, C.Z. Yu, F. Gao, Q. Luo, S.H. Xie, B. Tu, D.Y. Zhao, Chemical Communications, (2002) 1186-1187.

[143] D.Y. Zhao, Q.S. Huo, J.L. Feng, B.F. Chmelka, G.D. Stucky, Journal of the American Chemical Society, 120 (1998) 6024-6036.

[144] M.H. Lim, A. Stein, Chemistry of Materials, 11 (1999) 3285-3295.

[145] S.A. Idris, C. Robertson, M.A. Morris, L.T. Gibson, Analytical Methods, 2 1803-1809.

[146] Sigma Aldrich.

[147] K.N. Brewer, R.S. Herbst, I.Y. Glagolenko, T.A. Todd, Solvent Extraction and Ion Exchange, 16 (1998) 487-504.

[148] R. V. Nauman, P. W. West, F. Tron, G.C.G. Jr., Anal. Chem., 32 (1960) 1307-1311.

[149] S. Idris, Department of Pure and Applied Chemistry, University of strathclyde, Glasgow, (2009).

[150] Y.-C. Su, H.-M. Kao, J.-L. Wang, Journal of Chromatography A, 1217 (2010) 5643-5651.

[151] A. Corma, Chemical Reviews, 97 (1997) 2373-2419.

[152] H. Ji, Y. Fan, W. Jin, C. Chen, N. Xu, Journal of Non-Crystalline Solids, 354 (2008) 2010-2016.

[153] S.A. Idris, C.M. Davidson, C. McManamon, M.A. Morris, P. Anderson, L.T. Gibson, Journal of Hazardous Materials, 185 (2011) 898-904.

[154] M. Kruk, M. Jaroniec, C.H. Ko, R. Ryoo, Chemistry of Materials, 12 (2000) 1961-1968.

[155] D.Y. Zhao, J.L. Feng, Q.S. Huo, N. Melosh, G.H. Fredrickson, B.F. Chmelka, G.D. Stucky, Science, 279 (1998) 548-552.

[156] J. Liu, X. Zhang, Y. Han, F.S. Xiao, Chemistry of Materials, 14 (2002) 2536-2540.

[157] J.S. Beck, J.C. Vartuli, W.J. Roth, M.E. Leonowicz, C.T. Kresge, K.D. Schmitt, C.T.W. Chu, D.H. Olson, E.W. Sheppard, S.B. McCullen, J.B. Higgins, J.L. Schlenker, Journal of the American Chemical Society, 114 (1992) 10834-10843.

[158] N. Igarashi, K.A. Koyano, Y. Tanaka, S. Nakata, K. Hashimoto, T. Tatsumi, Microporous and Mesoporous Materials, 59 (2003) 43-52.

[159] F. Hoffmann, M. Cornelius, J. Morell, M. Froeba, Angewandte Chemie-International Edition, 45 (2006) 3216-3251.

[160] C.F. Cheng, Z.H. Luan, J. Klinowski, Langmuir, 11 (1995) 2815-2819.

[161] C.T. Kresge, M.E. Leonowicz, W.J. Roth, J.C. Vartuli, J.S. Beck, Nature, 359 (1992) 710-712.

[162] L. Huang, J.C. Wu, S. Kawi, Journal of Molecular Catalysis a-Chemical, 206 (2003) 371-387.

[163] L. Huang, S. Kawi, C. Poh, K. Hidajat, S.C. Ng, Talanta, 66 (2005) 943-951.

[164] T. Yasmin, K. Mueller, Journal of Chromatography A, 1217 (2010) 3362-3374.

[165] S.-Y. Park, M. Barton, P. Pendleton, Colloids and Surfaces a-Physicochemical and Engineering Aspects, 385 (2011) 256-261.

[166] C.D. Nunes, A.A. Valente, M. Pillinger, A.C. Fernandes, C.C. Romao, J. Rocha, I.S. Goncalves, Journal of Materials Chemistry, 12 (2002) 1735-1742.

[167] C. Cai, H. Wang, J. Han, Applied Surface Science, 257 (2011) 9802-9808.

[168] S. Jana, B. Dutta, H. Honda, S. Koner, Applied Clay Science, 54 (2011) 138-143.

[169] S.E. Park, D.S. Kim, J.S. Chang, W.Y. Kim, Catalysis Today, 44 (1998) 301-308.

[170] M. Grun, K.K. Unger, A. Matsumoto, K. Tsutsumi, Microporous and Mesoporous Materials, 27 (1999) 207-216.

[171] A. Marcilla, M. Beltran, A. Gomez-Siurana, I. Martinez, D. Berenguer, Chemical Engineering Research & Design, 89 (2011) 2330-2343.

[172] L. Huang, Q. Huang, H. Xiao, M. Eic, Microporous and Mesoporous Materials, 98 (2007) 330-338.

[173] Z. Huang, L. Huang, S.C. Shen, C.C. Poh, K. Hidajat, S. Kawi, S.C. Ng, Microporous and Mesoporous Materials, 80 (2005) 157-163.

[174] Dong Gu, Fuqiang Zhang, Yifeng Shi, Fan Zhang, Zhangxiong Wu, Yonghui Deng, Lijuan Zhang, Bo Tu, D. Zhao, journal of Colloid and Interface Science, 328 (2008) 338-343.

[175] B.L. Newalkar, J. Olanrewaju, S. Komarneni, Chemistry of Materials, 13 (2001) 552-557.

[176] S. Kubo, K. Kosuge, Langmuir, 23 (2007) 11761-11768.

[177] J. Izumi, Mitsubishi Heavy Industries, Ltd, (1996).

[178] H. Hori, I. Tanaka, T. Akiyama, American Industrial Hygiene Association Journal, 50 (1989) 24-29.

[179] T.M. Wu, G.R. Wu, H.M. Kao, J.L. Wang, Journal of Chromatography A, 1105 (2006) 168-175.

[180] D.P. Serrano, G. Calleja, J.A. Botas, F.J. Gutierrez, Industrial & Engineering Chemistry Research, 43 (2004) 7010-7018.

[181] M.H. Lim, C.F. Blanford, A. Stein, Chemistry of Materials, 10 (1998) 467-+.

[182] C.W. Purnomo, Asean Journal of Chemical Engineering,, 7 (2007) 43-48.

[183] D.I. Kim, J.H. Park, S.D. Kim, J.-Y. Lee, J.-H. Yim, J.-K. Jeon, S.H. Park, Y.-K. Park, Journal of Industrial and Engineering Chemistry, 17 (2011) 1-5.

[184] J.-H. Yim, D. Il Kim, J.A. Bae, Y.-K. Park, J.H. Park, J.-K. Jeon, S.H. Park, J. Song, S.-S. Kim, Journal of Nanoscience and Nanotechnology, 11 (2011) 1714-1717.

[185] S. Sae-ung, V. Boonamnuayvitaya, Environmental Engineering Science, 25 (2008) 1477-1485.

[186] M. Jaroniec, Design, synthesis and characterization of ordered mesoporous materials for environmental applications, in: J.M. Loureiro, M.T. Kartel (Eds.) Combined and Hybrid Adsorbents: Fundamentals and Applications, 2006, pp. 23-36.

[187] R. Serna-Guerrero, A. Sayari, Environmental Science & Technology, 41 (2007) 4761-4766.

[188] B.L. Newalkar, N.V. Choudary, U.T. Turaga, R.P. Vijayalakshmi, P. Kumar, S. Komarneni, T.S.G. Bhat, Chemistry of Materials, 15 (2003) 1474-1479.

[189] H.-P. Cong, S.-H. Yu, Current Opinion in Colloid & Interface Science, 14 (2009) 71-80.

[190] Q. Hu, J. Li, S. Qiao, Z. Hao, H. Tian, C. Ma, C. He, Journal of Hazardous Materials, 164 (2009) 1205-1212.

[191] D. Perez-Quintanilla, I. del Hierro, M. Fajardo, I. Sierra, Journal of Hazardous Materials, 134 (2006) 245-256.

[192] C. Exley, Progress in molecular and subcellular biology, 47 (2009) 173-184.

[193] N.P. Hughes, C.C. Perry, O.R. Anderson, R.J.P. Williams, Proceedings of the Royal Society B-Biological Sciences, 238 (1989) 223-+.

[194] M. Hildebrand, Chemical Reviews, 108 (2008) 4855-4874.

[195] S.V. Patwardhan, Chemical Communications, 47 (2011) 7567-7582.

[196] N. Kroger, R. Deutzmann, M. Sumper, Science, 286 (1999) 1129-1132.

[197] N. Kroger, R. Deutzmann, C. Bergsdorf, M. Sumper, Proceedings of the National Academy of Sciences of the United States of America, 97 (2000) 14133-14138.

[198] S.V. Patwardhan, S.J. Clarson, Polymer Bulletin, 48 (2002) 367-371.

[199] R.L. Brutchey, D.E. Morse, Chemical Reviews, 108 (2008) 4915-4934.

[200] S.V. Patwardhan, S.J. Clarson, C.C. Perry, Chemical Communications, (2005) 1113-1121.

[201] V.V. Annenkov, S.V. Patwardhan, D. Belton, E.N. Danilovtseva, C.C. Perry, Chemical Communications, (2006) 1521-1523.

[202] D. Belton, S.V. Patwardhan, C.C. Perry, Chemical Communications, (2005) 3475-3477.

[203] N. Poulsen, M. Sumper, N. Kroger, Proceedings of the National Academy of Sciences of the United States of America, 100 (2003) 12075-12080.

[204] N. Poulsen, N. Kroger, Journal of Biological Chemistry, 279 (2004) 42993-42999.

[205] C.C. Perry, T. Keeling-Tucker, Journal of Biological Inorganic Chemistry, 5 (2000) 537-550.

[206] T. Coradin, O. Durupthy, J. Livage, Langmuir, 18 (2002) 2331-2336.

[207] J.N. Cha, G.D. Stucky, D.E. Morse, T.J. Deming, Nature, 403 (2000) 289-292.

[208] K. Shimizu, D.E. Morse, In Vitro Cellular and Developmental Biology Animal, 36 (2000) 4.A-4.A.

[209] S.V. Patwardhan, S.J. Clarson, Materials Science & Engineering C-Biomimetic and Supramolecular Systems, 23 (2003) 495-499.

[210] M. Sumper, E. Brunner, G. Lehmann, Febs Letters, 579 (2005) 3765-3769.

[211] D.J. Belton, S.V. Patwardhan, V.V. Annenkov, E.N. Danilovtseva, C.C. Perry, Proceedings of the National Academy of Sciences of the United States of America, 105 (2008) 5963-5968.

[212] T. Coradin, J. Livage, Colloids and Surfaces B-Biointerfaces, 21 (2001) 329-336.

[213] D.J. Belton, S.V. Patwardhan, C.C. Perry, Journal of Materials Chemistry, 15 (2005) 4629-4638.

[214] M.R. Knecht, D.W. Wright, Chemistry of Materials, 16 (2004) 4890-4895.

[215] A. Rai, C.C. Perry, Silicon, 1 (2009) 91-101.

[216] R.-H. Jin, J.-J. Yuan, Advanced Materials, 21 (2009) 3750-3753.

[217] J.-J. Yuan, P.-X. Zhu, N. Fukazawa, R.-H. Jin, Advanced Functional Materials, 16 (2006) 2205-2212.

[218] Q.S. Huo, D.I. Margolese, G.D. Stucky, Chemistry of Materials, 8 (1996) 1147-1160.

[219] Q.Y. Sun, T.P.M. Beelen, R.A. van Santen, S. Hazelaar, E.G. Vrieling, W.W.C. Gieskes, Journal of Physical Chemistry B, 106 (2002) 11539-11548.

[220] T. Coradin, C. Roux, J. Livage, Journal of Materials Chemistry, 12 (2002) 1242-1244.

[221] F. Noll, M. Sumper, N. Hampp, Nano Letters, 2 (2002) 91-95.

[222] T. Mizutani, H. Nagase, N. Fujiwara, H. Ogoshi, Bulletin of the Chemical Society of Japan, 71 (1998) 2017-2022.

[223] D. Belton, G. Paine, S.V. Patwardhan, C.C. Perry, Journal of Materials Chemistry, 14 (2004) 2231-2241.

[224] N. Nassif, J. Livage, Chemical Society Reviews, 40 (2011) 849-859.

[225] R.H. Meinhold, H.P. Rothbaum, R.H. Newman, Journal of Colloid and Interface Science, 108 (1985) 234-236.

[226] T. Tarutani, Analytical Sciences, 5 (1989) 245-252.

[227] J. Schlomach, M. Kind, Journal of Colloid and Interface Science, 277 (2004) 316-326.

[228] H.P. Rothbaum, A.G. Rohde, Journal of Colloid and Interface Science, 71 (1979) 533-559.

[229] R.K. Iler, Journal of Colloid and Interface Science, 75 (1980) 138-148.

[230] S.V. Patwardhan, G.E. Tilburey, C.C. Perry, Langmuir, 27 (2011) 15135-15145.

[231] C. De Stefano, C. Foti, A. Gianguzza, S. Sammartano, Analytica Chimica Acta, 418 (2000) 43-51.

[232] D.J. Belton, O. Deschaume, S.V. Patwardhan, C.C. Perry, Journal of Physical Chemistry B, 114 (2010) 9947-9955.

[233] L. Sudheendra, A.R. Raju, Materials Research Bulletin, 37 (2002) 151-159.

[234] M.A. Brook, Y. Chen, K. Guo, Z. Zhang, J.D. Brennan, Journal of Materials Chemistry, 14 (2004) 1469-1479.

[235] W. Yang, P.J. Lopez, G. Rosengarten, Analyst, 136 (2011) 42-53.

[236] N.A. Pchelintsev, F. Neville, P.A. Millner, Sensors and Actuators B-Chemical, 135 (2008) 21-26.

[237] K.-I. Sano, T. Minamisawa, K. Shiba, Langmuir, 26 (2010) 2231-2234.

[238] M. Hatzimarinaki, V. Vamvakaki, N. Chaniotakis, Journal of Materials Chemistry, 19 (2009) 428-433.

[239] X.S. Zhao, Q. Ma, G.Q.M. Lu, Energy & Fuels, 12 (1998) 1051-1054.

[240] X.J. Hu, S.Z. Qiao, X.S. Zhao, G.Q. Lu, Industrial & Engineering Chemistry Research, 40 (2001) 862-867.

[241] B.L. Newalkar, N.V. Choudary, P. Kumar, S. Komarneni, T.S.G. Bhat, Chemistry of Materials, 14 (2002) 304-309.

[242] Y. Ueno, A. Tate, O. Niwa, H.S. Zhou, T. Yamada, I. Honma, Chemical Communications, (2004) 746-747.

[243] Y. Ueno, T. Horiuchi, A. Tate, O. Niwa, H. Zhou, T. Yamada, I. Honma, New Journal of Chemistry, 29 (2005) 504-508.

[244] J.H. Zhu, S.L. Zhou, Y. Xu, Y. Cao, Y.L. Wei, Chemistry Letters, 32 (2003) 338-339.

[245] V.T. Hoang, Q.L. Huang, M. Eic, T.O. Do, S. Kaliaguine, Langmuir, 21 (2005) 2051-2057.

[246] A. Stein, B.J. Melde, R.C. Schroden, Advanced Materials, 12 (2000) 1403-1419.

[247] Y.S. Tao, H. Kanoh, L. Abrams, K. Kaneko, Chemical Reviews, 106 (2006) 896-910.

[248] M. Tiemann, Chemistry-a European Journal, 13 (2007) 8376-8388.

[249] A. Berggren, A.E.C. Palmqvist, K. Holmberg, Soft Matter, 1 (2005) 219-226.

[250] X.H. Tang, S.W. Liu, Y.Q. Wang, W.P. Huang, E. Sominski, O. Palchik, Y. Koltypin, A. Gedanken, Chemical Communications, (2000) 2119-2120.

[251] A.M. Ewlad-Ahmed, M.A. Morris, S.V. Patwardhan, L.T. Gibson, Environmental Science & Technology, 46 (2012) 13354-13360.

[252] B. Ohtani, Chemistry Letters, 37 (2008) 217-229.

[253] P.V. Kamat, Chemical Reviews, 93 (1993) 267-300.

[254] A. Mills, S. LeHunte, Journal of Photochemistry and Photobiology a-Chemistry, 108 (1997) 1-35.

[255] D.F. Ollis, Comptes Rendus De L Academie Des Sciences Serie Ii Fascicule C-Chimie, 3 (2000) 405-411.

[256] A. Fujishima, X.T. Zhang, Comptes Rendus Chimie, 9 (2006) 750-760.

[257] N. Negishi, K. Takeuchi, Journal of Sol-Gel Science and Technology, 22 (2001) 23-31.

[258] D.C. Hurum, A.G. Agrios, K.A. Gray, T. Rajh, M.C. Thurnauer, Journal of Physical Chemistry B, 107 (2003) 4545-4549.

[259] J.A. Gamboa, D.M. Pasquevich, Journal of the American Ceramic Society, 75 (1992) 2934-2938.

[260] A. Beltran, L. Gracia, J. Andres, Journal of Physical Chemistry B, 110 (2006) 23417-23423.

[261] N. Serpone, Journal of Physical Chemistry B, 110 (2006) 24287-24293.

[262] G. Riegel, J.R. Bolton, Journal of Physical Chemistry, 99 (1995) 4215-4224.

[263] A. Sclafani, L. Palmisano, E. Davi, New Journal of Chemistry, 14 (1990) 265-268.

[264] R.W. Matthews, Journal of Catalysis, 97 (1986) 565-568.

[265] A.J. Maira, K.L. Yeung, C.Y. Lee, P.L. Yue, C.K. Chan, Journal of Catalysis, 192 (2000) 185-196.

[266] L. Zeatoun, D. Feke, Particle & Particle Systems Characterization, 22 (2006) 276-281.

[267] J. Rubio, J.L. Oteo, M. Villegas, P. Duran, Journal of Materials Science, 32 (1997) 643-652.

[268] N.V. Golubko, M.I. Yanovskaya, I.P. Romm, A.N. Ozerin, Journal of Sol-Gel Science and Technology, 20 (2001) 245-262.

[269] J. Livage, Chemistry of Materials, 3 (1991) 578-593.

[270] H.M. Cheng, J.M. Ma, Z.G. Zhao, L.M. Qi, Chemistry of Materials, 7 (1995) 663-671.

[271] Y.Q. Zheng, S. Erwei, S.X. Cui, W.J. Li, X.F. Hu, Journal of Materials Science Letters, 19 (2000) 1445-1448.

[272] Z. Wu, Z. Gu, W. Zhao, H. Wang, Chinese Science Bulletin, 52 (2007) 3061-3067.

[273] W.L. Guo, Z.M. Lin, X.K. Wang, G.Z. Song, Microelectronic Engineering, 66 (2003) 95-101.

[274] L.M. Qi, J.M. Ma, H.M. Cheng, Z.G. Zhao, Colloids and Surfaces a-Physicochemical and Engineering Aspects, 108 (1996) 117-126.

[275] A.M. Huang, L.X. Cao, J. Chen, F.J. Spiess, S.L. Suib, T.N. Obee, S.O. Hay, J.D. Freihaut, Journal of Catalysis, 188 (1999) 40-47.

[276] J. Drelich, Y.Q. Lu, L.Y. Chen, J.D. Miller, S. Guruswamy, Applied Surface Science, 125 (1998) 236-244.

[277] H.M. Yates, M.G. Nolan, D.W. Sheel, M.E. Pemble, Journal of Photochemistry and Photobiology a-Chemistry, 179 (2006) 213-223.

[278] X.W. Zhang, M.H. Zhou, L.C. Lei, Catalysis Communications, 7 (2006) 427-431.

[279] T.N. Obee, R.T. Brown, Environmental Science & Technology, 29 (1995) 1223-1231.

[280] J. Mo, Y. Zhang, R. Yang, Indoor Air, 15 (2005) 291-300.

[281] H. Tada, M. Tanaka, Langmuir, 13 (1997) 360-364.

[282] M.L. Kaariainen, T.O. Kaariainen, D.C. Cameron, Thin Solid Films, 517 (2009) 6666-6670.

[283] D.T. Tompkins, ASHARE Research Project RP-1134., (2001).

[284] A. Fujishima, X. Zhang, D.A. Tryk, Surface Science Reports, 63 (2008) 515-582.

[285] J.M. Herrmann, Catalysis Today, 53 (1999) 115-129.

[286] D.A.H. Hanaor, C.C. Sorrell, Journal of Materials Science, 46 (2011) 855-874.

[287] A. Sclafani, J.M. Herrmann, Journal of Physical Chemistry, 100 (1996) 13655-13661.

[288] U.I. Gaya, A.H. Abdullah, Journal of Photochemistry and Photobiology C-Photochemistry Reviews, 9 (2008) 1-12.

[289] K.H. Wang, Y.H. Hsieh, C.H. Lin, C.Y. Chang, Chemosphere, 39 (1999) 1371-1384.

[290] C.H. Ao, S.C. Lee, J.Z. Yu, J.H. Xu, Applied Catalysis B-Environmental, 54 (2004) 41-50.

[291] Y. Luo, D.F. Ollis, Journal of Catalysis, 163 (1996) 1-11.

[292] J. Peral, D.F. Ollis, Journal of Catalysis, 136 (1992) 554-565.

[293] S. Hager, R. Bauer, Chemosphere, 38 (1999) 1549-1559.

[294] N. Serpone, Pelizzetti, E., Wiley, New York, (1989) pp. 217–250.

[295] T. Sano, N. Negishi, K. Takeuchi, S. Matsuzawa, Solar Energy, 77 (2004) 543-552.

[296] X.Z. Fu, L.A. Clark, Q. Yang, M.A. Anderson, Environmental Science & Technology, 30 (1996) 647-653.

[297] T.N. Obee, S.O. Hay, Environmental Science & Technology, 31 (1997) 2034-2038.

[298] V. Augugliaro, S. Coluccia, V. Loddo, L. Marchese, G. Martra, L. Palmisano, M. Schiavello, Applied Catalysis B-Environmental, 20 (1999) 15-27.

[299] S.A. Larson, J.A. Widegren, J.L. Falconer, Journal of Catalysis, 157 (1995) 611-625.

[300] J. Kirchnerova, M.L.H. Cohen, C. Guy, D. Klvana, Applied Catalysis a-General, 282 (2005) 321-332.

[301] A.L. Linsebigler, G.Q. Lu, J.T. Yates, Chemical Reviews, 95 (1995) 735-758.

[302] L. Stevens, J.A. Lanning, L.G. Anderson, W.A. Jacoby, N. Chornet, Journal of the Air & Waste Management Association, 48 (1998) 979-984.

[303] P.V. Kamat, D. Meisel, Current Opinion in Colloid & Interface Science, 7 (2002) 282-287.

[304] F. Bosc, D. Edwards, N. Keller, V. Keller, A. Ayral, Thin Solid Films, 495 (2006) 272-279.

[305] V. Brezova, A. Blazkova, L. Karpinsky, J. Groskova, B. Havlinova, V. Jorik, M. Ceppan, Journal of Photochemistry and Photobiology a-Chemistry, 109 (1997) 177-183.

[306] R. Asahi, T. Morikawa, T. Ohwaki, K. Aoki, Y. Taga, Science, 293 (2001) 269-271.

[307] T. Ihara, M. Miyoshi, Y. Iriyama, O. Matsumoto, S. Sugihara, Applied Catalysis B-Environmental, 42 (2003) 403-409.

[308] H. Irie, Y. Watanabe, K. Hashimoto, Journal of Physical Chemistry B, 107 (2003) 5483-5486.

[309] Y. Irokawa, T. Morikawa, K. Aoki, S. Kosaka, T. Ohwaki, Y. Taga, Physical Chemistry Chemical Physics, 8 (2006) 1116-1121.

[310] F.B. Li, X.Z. Li, C.H. Ao, S.C. Lee, M.F. Hou, Chemosphere, 59 (2005) 787-800.

[311] W.Y. Choi, A. Termin, M.R. Hoffmann, Journal of Physical Chemistry, 98 (1994) 13669-13679.

[312] H. Yoneyama, T. Torimoto, Catalysis Today, 58 (2000) 133-140.

[313] T.N. Obee, Environmental Science & Technology, 30 (1996) 3578-3584.

[314] Y.S. You, K.H. Chung, J.H. Kim, G. Seo, Korean Journal of Chemical Engineering, 18 (2001) 924-929.

[315] M. Hussain, N. Russo, G. Saracco, Chemical Engineering Journal, 166 (2011) 138-149.

[316] C. Belver, M.J. Lopez-Munoz, J.M. Coronado, J. Soria, Applied Catalysis B-Environmental, 46 (2003) 497-509.

[317] S. Sun, J. Ding, J. Bao, C. Gao, Z. Qi, X. Yang, B. He, C. Li, Applied Surface Science, 258 (2012) 5031-5037.

[318] C.A. Korologos, M.D. Nikolaki, C.N. Zerva, C.J. Philippopoulos, S.G. Poulopoulos, Journal of Photochemistry and Photobiology a-Chemistry, 244 (2012) 24-31.

[319] R. Mendez-Roman, N. Cardona-Martinez, Catalysis Today, 40 (1998) 353-365.

[320] M. Hinojosa-Reyes, V. Rodriguez-Gonzalez, S. Arriaga, Journal of Hazardous Materials, 209 (2012) 365-371.

[321] M.L. Sauer, D.F. Ollis, Journal of Catalysis, 163 (1996) 215-217.

[322] J. Blanco, P. Avila, A. Bahamonde, E. Alvarez, B. Sanchez, M. Romero, Catalysis Today, 29 (1996) 437-442.

[323] E. Piera, J.A. Ayllon, X. Domenech, J. Peral, Catalysis Today, 76 (2002) 259-270.

Publications from this work

There are three papers will be published from this work. Three are already published:

[1] L.T. Gibson, A. Ewlad-Ahmed, B. Knight, V. Horie, G. Mitchell, C.J. Robertson, Measurement of volatile organic compounds emitted in libraries and archives: an inferential indicator of paper decay? Chemistry Central Journal, 6 (2012).

[2] A.M. Ewlad-Ahmed, M.A. Morris, S.V. Patwardhan, L.T. Gibson, Removal of Formaldehyde from Air Using Functionalized Silica Supports.Environmental Science & Technology, 46 (2012) 13354-13360.

One paper has been already submitted:

[1] Abdunaser Mabruk Ewlad-Ahmed, Michael Morris, Justin Holmes, David Belton, Siddharth Patwardhan and Lorraine Teresa Gibson. Novel green nanomaterials for selective gas separations.